THE HIGH TEMPERATURE PROPERTIES OF Fe-Ni-Cr ALLOYS

A thesis submitted to the Council for National Academic Awards for the degree of

DOCTOR OF PHILOSOPHY

in

THE SHEFFIELD CITY POLYTECHNIC

by

ASHOK KUMAR KOUL, B.Sc. Met. Eng.

March 1979

SYNOPSIS

A literature review has been presented concerning the influence of the common alloying additions in Austenitic Stainless Steels and Ni-Fe Base Superalloys on their grain coarsening characteristics, precipitation hardening and recrystallization behaviour. The effects of various microstructural features on the high temperature properties of Austenitic Stainless Steels and Ni-Fe Base Superalloys have also been reviewed.

The work discribed has shown the grain coarsening characteristics to depend on the type and amount of alloying addition, which influences undissolved particle size and volume fractions. An attempt has been made to compare various mathematical models of the effect of second phase particles on the grain size, using observed data.

The age-hardening characteristics of Ni-Fe Base Superalloys have been shown to vary with the morphology of the different types of precipitate such as $M_{23}C_6$, TiC and γ', and their nucleation at different sites. The precipitation kinetics have been explained in terms of the relative diffusion rates of the various alloying additions present.

The effect of cold working on the relative kinetics of precipitation and recrystallization have been shown to vary with the type of alloying addition . In steels precipitating $M_{23}C_6$, precipitation precedes recrystallization, whereas in γ' forming alloys, cold working prior to ageing significantly increases the rate of zone formation and growth, thus retarding the recrystallization processes.

Both high temperature tensile and creep properties of Ni-Fe Base Superalloys, at varying strain rates, have been shown to depend on the microstructure. Tensile strength increases with increasing volume fraction of

precipitating phase, whereas the overall creep strength has been shown to be dependent upon the relative strength of the grain boundaries and the matrix. The variation of high temperature ductility of the different initial microstructures at varying strain rates have been explained in terms of the qualitative influence of predominant microstructural features on the deformation and fracture mechanism maps.

Serrated yielding has been shown to be a common phenomenon in all steels tested at 700°C at strain rates of 10^{-2}/s and 10^{-3}/s, and substitutional solutes have been shown to be responsible for this effect. Also, the stress dependence of the creep rate varies with different microstructural features in Ni-Fe Base Superalloys, and the prominence of deformation mechanism controlled by a marked interface reaction has been indicated.

Dedicated

to

KALHANA PANDITA

The author of RAJATARANGANI, a great 12th century historian cum research worker, who used Sanskrit, the mystical language of Indian epics to write this fascinating historical record and conducted research in accordance with the modern treatise.

THE HIGH TEMPERATURE PROPERTIES OF Fe-Ni-Cr ALLOYS

This thesis is based on an investigation sponsored by United Kingdom Atomic Energy Authority, Harwell, and carried out at Sheffield City Polytechnic between October 1974 and April 1978. During this period regular meetings were held with the internal and industrial supervisors to discuss the progress of the work, and also the following lectures and conferences were attended.

(1) "High Strength Steels" - Series of seminars held at Sheffield City Polytechnic, 1975, 30 hours.

(2) "High Strength Alloys" - Advanced topic in Module 3 of the M.Sc. in Industrial Metallurgy, Sheffield City Polytechnic, 1975, 24 hours.

(3) "Crack Initiation During Creep" - A Conference organised by the Metals Society at Sheffield University, May 1975.

(4) "The Use of Electron Techniques in the Study of Materials" - A course held at Sheffield City Polytechnic, 1976, 90 hours.

(5) "Numerical Methods and Programming" - Part of M.Sc. in industrial Metallurgy at Sheffield City Polytechnic, 1976, 56 hours.

The results obtained in this investigation and the theories developed are, to the best of my knowledge, original except where reference is made to authors. No part of this thesis has been submitted for a degree at any other college or university.

ACKNOWLEDGEMENTS

I would like to express my gratitude to Dr F. B. Pickering for the invaluable help and guidance so freely given during the course of this work. Thanks are due to Mr David Marriott and other technical staff members of the Department of Metallurgy, Sheffield City Polytechnic for their continuous practical assistance. The constructive criticism and help offered by Dr D. R. Harries and Mr R. M. Boothby is also acknowledged. I am indebted to Prof. A. W.D. Hills, Sheffield City Polytechnic, to have given me the opportunity to participate in this useful piece of work.

Thanks are also due to my ex-flatmates Mr Andrew Biglin and Miss Christine Walsh for being so understanding during my stay with them. Last but not least, words cannot express my appreciation for the patience and tolerance shown by Miss Judith K. McCann and my parents, towards the unpredictability of a researching mind.

	Page
SYNOPSIS	(i)
Aims and Objectives of the Investigation	(iii)
1. INTRODUCTION	(iv)
2. LITERATURE REVIEW	1
2.1 General Metallurgy of Austenitic Stainless Steels and Iron-Base Superalloys	1
2.1.1 Composition	1
2.1.1.1 Austenitic Stainless Steels	1
2.1.2.2 Iron Base Super Alloys	2
2.1.2 Microstructures	2
2.1.2.1 Austenitic Stainless Steels	2
2.1.2.2 Iron-Base Superalloys	6
2.1.3 Effect of Alloying additions on the Microstructural Features	9
2.1.4 Effect of Alloying Additions on Properties	14
2.2 High Temperature Strengthening Mechanisms	17
2.2.1 Solid Solution Hardening	18
2.2.2 Precipitation Hardening	19
2.2.2.1 Clustering and the Kinetics of Clustering	20
2.2.2.2 Nucleation	21
2.2.2.3 Growth of the Precipitates	23
2.2.2.4 Factors affecting age-hardening of Austenitic Steels	24
2.2.2.5 Strengthening mechanisms by ordered precipitates in Austenite	25
2.2.2.6 Grain boundary strengthening	28
2.3 Grain Coarsening Characteristics and the Influence of Second Phase Particles	29
2.3.1 Types of grain growth	30
2.3.2 Basic theory of grain growth	30
2.3.3 The effect of dissolved impurities and second phase particles on grain growth	32
2.3.3.1 Zener's model	32
2.3.3.2 Hillert's Analysis	33
2.3.3.3 Gladman's model	34
2.3.3.4 Hellman and Hillert's correction	36
2.3.3.5 Critical assessment of grain growth	36

	Page
2.4 Precipitation in Austenite	37
2.4.1 Carbides	38
2.4.2 $M_{23}C_6$ precipitation	38
2.4.2.1 $M_{23}C_6$ precipitation at grain-boundaries and grain boundary junctions	39
2.4.2.2 $M_{23}C_6$ on incoherent twin-boundaries	40
2.4.2.3 Matrix precipitation of $M_{23}C_6$	41
2.4.2.4 $M_{23}C_6$ precipitation on coherent twin boundaries	
2.4.2.5 General sequence of precipitation	42
2.4.3 TiC precipitation and its sites	42
2.4.4 Combined $M_{23}C_6$ and TiC precipitation	44
2.4.5 Precipitation of γ'	44
2.4.5.1 Precipitation sites for γ'	46
2.4.5.2 Effect of Al and Ti content on precipitation of γ' in Austenite	47
2.4.6 Combined precipitation of $M_{23}C_6$ and γ'	49
2.5 Cold work, Recrystallization and Precipitation	50
2.5.1 Nucleation mechanisms of recrystallization	50
2.5.1.1 General comparison of nucleation mechanisms	53
2.5.1.2 Factors influencing primary recrystallization	55
2.5.2 Separate and combined effect of precipitation and recrystallization	57
2.5.3 Influence of cold work on precipitation kinetics	60
2.5.3.1 Effect on zone formation	60
2.5.3.2 Effect on intermediate precipitation	61
2.5.3.3 Effect on carbide precipitation	61
2.5.4 Effect of cold work, in the presence of a fine dispersion of a precipitate on recrystallization and further precipitation	63
2.6 High temperature properties of Austenitic Steels and Iron-Base Superalloys	65
2.6.1 High temperature deformation mechanisms	65
2.6.1.1 Combined dislocation glide and climb	66

Page

2.6.1.2 Non Uniform Shear (sliding) 67
2.6.1.3 Diffusional flow 69
2.6.2 Deformation mechanism maps 73
2.6.2.1 Ashby's maps 73
2.6.2.2 Effect of microstructure on Ashby's maps 74
2.6.2.3 Langdon's maps 75
2.6.2.4 Comparison of Langdon's and Ashby's maps 75
2.6.3 High temperature tensile properties 76
2.6.3.1 Effect of temperature and Strain Rate on the Strength of Austenitic Steels 77
2.6.3.2 Serrated yielding 79
2.6.3.3 Effect of microstructural features on high temperature tensile strength 79
2.6.3.4 Effect of strain rate and temperature on tensile ductility 80
2.6.3.5 Effect of microstructural features on high temperature tensile ductility in Austenitic Steels 82
2.6.4 Creep properties in precipitation hardened Austenite 83
2.6.4.1 Stress dependence of minimum creep rate/rupture life 84
2.6.4.2 On the value of stress exponent n 85
2.6.4.3 Tertiary creep 87
2.6.4.4 Influence of second phase particles on creep properties 87
2.6.4.4.1 Effect of $M_{23}C_6$ precipitates on creep properties 89
2.6.4.4.2 Effect of TiC precipitates on creep properties 90
2.6.4.4.3 Effect of γ' precipitates on creep properties 90
2.7 High temperature Fracture 91
2.7.1 Transgranular creep fracture 92
2.7.2 Intergranular creep fracture 93
2.7.2.1 Nucleation and growth of w-type cracks 93
2.7.2.1.1 Effect of microstructure on w-type cracks 95

Page

2.7.2.2 Nucleation and growth of r-type cracks 96
2.7.2.1.2 Effect of microstructure on r-type cracks 97
2.7.3 Rupture 97
2.7.4 Fracture maps 98
2.7.4.1 Effect of microstructure on fracture maps 98
2.7.4.2 Application 99

3. EXPERIMENTAL METHODS 100
3.1 Manufacture of alloys 100
3.2 Processing, hot-rolling and heat-treatment 100
3.2.1 Solution treatments 101
3.2.2 Ageing treatments 101
3.3 Cold-rolling and ageing 102
3.4 Specimen preparation 102
3.5 Experimental technique 103
3.5.1 Grain size measurements 103
3.5.1.1 The accuracy of the mean linear intercept 103
3.5.1.2 Measurement of grain size 104
3.5.2 Hardness testing 104
3.5.3 High temperature tensile testing 105
3.5.3.1 Specimen preparation and heat-treatment 105
3.5.3.2 The High Temperature Tensile Test 105
3.5.4 Creep testing 106
3.5.5 Electron microscopy 107
3.5.6 Scanning electron microscopy 108
3.5.7 Chemical analysis of carbides 109
3.5.8 Quantitative metallography 109
3.5.8.1 Volume fraction measurement 109
3.5.8.2 Crack counting 110

4. EXPERIMENTAL RESULTS 111
4.1 The effect of solution treatment on grain coarsening characteristics 111

		Page
4.1.1.	Low carbon Fe-Ni-Cr Alloy No. 1	111
4.1.2	Medium carbon Fe-Ni-Cr Alloy No. 2	112
4.1.3	High carbon Fe-Ni-Cr Alloy No. 3	112
4.1.4	High carbon Molybdenum Alloy No. 4	113
4.1.5	High carbon Mo-Ti alloy. Alloy No. 5	113
4.1.6	Extra high carbon Mo-Ti steel Alloy No. 6	114
4.1.7	Low carbon PE16 composition Alloy No. 7	114
4.1.8	High carbon PE16 composition Alloy No. 8	115
4.1.9	General comparison of all alloys	115
4.2	Age Hardening Characteristics	115
4.2.1	Low-carbon base composition Alloy No. 1	115
4.2.2	Medium carbon base composition Alloy No. 2	116
4.2.3	High carbon base composition Alloy No. 3	116
4.2.4	High carbon Mo-steel Alloy No. 4	116
4.2.5	High carbon Mo-Ti steel Alloy No. 5	117
4.2.6	Extra high carbon Mo-Ti steel Alloy No. 6	118
4.2.7	Low carbon PE16 composition Alloy No. 7	118
4.2.8	High carbon PE16 composition Alloy No. 8	119
4.2.9	General comparison of ageing characteristics	119
4.3	Combined effect of cold work and ageing on precipitation and Recrystallization characteristics	119
4.3.1	Medium carbon base composition Alloy No. 2	121
4.3.2	High carbon base composition Alloy No. 3	121
4.3.3	High carbon Mo-steel Alloy No. 4	122
4.3.4	High carbon Mo-Ti steel Alloy No. 5	122
4.3.5	PE16 compositions Alloy No. 7 and 8	123
4.3.6	General comparison of all alloys	123
4.4	Microstructural Features	124
4.4.1	Solution treated structures	124
4.4.2	Aged microstructures	126

		Page
4.4.2.1	Low carbon base composition	126
4.4.2.1	Medium carbon base composition	126
4.4.2.3	High carbon base composition	127
4.4.2.4	High carbon Mo-alloy	127
4.4.2.5	High carbon Mo-Ti alloy	128
4.4.2.6	Extra high carbon Mo-Ti alloy	129
4.4.2.7	Low carbon PE16 composition	129
4.4.2.8	High carbon PE16 composition	130
4.4.3	Cold worked and aged structures	131
4.4.3.1	Medium carbon base composition	132
4.4.3.2	High carbon base composition	133
4.4.3.3	High carbon Mo-Alloy	133
4.4.3.4	High carbon Mo-Ti alloy	134
4.4.3.5	Low and high carbon PE16 compositions	134
4.4.4	Selection of Heat-Treatments for producing various microstructural features	136
4.5	High Temperature Properties	138
4.5.1	Tensile Properties	138
4.5.1.1	Base composition with no grain-boundary precipitates	138
4.5.1.2	Base composition with $M_{23}C_6$ at grain boundaries	139
4.5.1.3	$M_{23}C_6$ at grain boundaries and within the matrix	139
4.5.1.4	Comparison of $M_{23}C_6$ precipitating alloys	140
4.5.1.5	Mo-rich $M_{23}C_6$ at grain-boundaries	140
4.5.1.6	Combined effect of Mo and Ti.	141
4.5.1.7	Low carbon PE16	142
4.5.1.8	High carbon PE16	143
4.5.1.9	General comparison of all alloys	143
4.5.2	Creep Properties	145
4.5.2.1	Base composition	145
4.5.2.2	Base composition with $M_{23}C_6$ at grain boundaries	146
4.5.2.3	$M_{23}C_6$ at grain boundaries and within the grains	146

Page

4.5.2.4 Mo-rich $M_{23}C_6$ at grain-boundaries 147
4.5.2.5 $M_{23}C_6$ and TiC at the Grain Boundaries and in the Grains 148
4.5.2.6 Low carbon PE16 composition 148
4.5.2.7 High carbon PE16 149

4.6 Microstructural Features of Tested Materials 150
4.6.1 Transmission electron microscopy after creep testing 150
4.6.1.1 $M_{23}C_6$ carbide forming alloys 150
4.6.1.2 Effect of Mo and Ti 151
4.6.1.3 PE16 compositions 151
4.6.2 Fracture characteristics 152
4.6.2.1 Base composition 152
4.6.2.2 Base composition with $M_{23}C_6$ at grain boundaries 153
4.6.2.3 $M_{23}C_6$ at grain boundaries and within the grains 154
4.6.2.4 Mo-rich $M_{23}C_6$ at grain boundaries 154
4.6.2.5 Combined effect of Mo and Ti 155
4.6.2.6 Low carbon PE16 composition 156
4.6.2.7 High carbon PE16 composition 157

5. DISCUSSION OF RESULTS 158
5.1 Grain Coarsening Characteristics 158
5.1.1 The grain size below the grain coarsening temperature 158
5.1.2 The grain size above the grain coarsening temperature 161
5.1.3 The grain coarsening temperature 164
5.1.4 Comparison of various mathematical models on the effect of second phase particles on grain coarsening 165
5.2 Age Hardening and Precipitation Mechanisms 166
5.2.1 Low carbon base composition 166
5.2.2 Medium carbon base composition 166
5.2.3 High carbon base composition 167
5.2.4 Comparison of the effect of carbon 168
5.2.5 Effect of Mo 168

	Page
5.2.6 Effect of Ti	170
5.2.7 The effect of combined Al and Ti additions	171
5.3 Cold Work, Recrystallization and Precipitation	173
5.3.1 Medium carbon base composition	173
5.3.2 High carbon base composition	175
5.3.3 Effect of Mo	176
5.3.4 Effect of Ti	177
5.3.5 PE16 compositions	178
5.4 High Temperature Properties	179
5.4.1 Expected effects of various microstructural features on the deformation and fracture mechanism maps	179
5.4.2 Alloys forming $M_{23}C_6$	182
5.4.2.1 Base composition with no grain-boundary precipitates	182
5.4.2.2 Base composition with $M_{23}C_6$ at grain boundaries	186
5.4.2.3 $M_{23}C_6$ at grain boundaries and within the grains	188
5.4.3 Effect of Mo and Ti additions	191
5.4.3.1 Mo-rich $M_{23}C_6$ at grain boundaries	191
5.4.3.2 $M_{23}C_6$ at grain boundaries in a Ti-rich matrix	193
5.4.3.3 $M_{23}C_6$ and TiC at the grain-boundaries and within the grains	194
5.4.4 Gamma-prime (γ') forming alloys	196
5.4.4.1 γ' zones with virtually no $M_{23}C_6$ at grain boundaries	196
5.4.4.2 Semicoherent γ' and virtually no $M_{23}C_6$ at grain boundaries	199
5.4.4.3 Matrix γ' zones and grain-boundary $M_{23}C_6$	202
5.4.4.4 Matrix semicoherent γ' and large grain boundary $M_{23}C_6$ precipitates	203
5.4.5 Serrated Yielding	204
5.4.5 Microstructural dependence of the stress exponent n	207

Page

6. CONCLUSIONS:-

6.1 Grain Coarsening Characteristics 210

6.2 Age Hardening and Precipitation Kinetics 210

6.3 Cold-work, Recrystallization and Precipitation 212

6.4 High Temperature Properties 213

6.5 Suggestions for Further Work 216

7. REFERENCES 217

TABLES I - XVII

FIGURES 1 - 92

PLATES 1 - 20

CHAPTER ONE

SYNOPSIS

A literature review has been presented concerning the influence of the common alloying additions in Austenitic Stainless Steels and Ni-Fe Base Superalloys on their grain coarsening characteristics, precipitation hardening and recrystallization behaviour. The effects of various microstructural features on the high temperature properties of Austenitic Stainless Steels and Ni-Fe Base Superalloys have also been reviewed.

The work discribed has shown the grain coarsening characteristics to depend on the type and amount of alloying addition, which influences undissolved particle size and volume fractions. An attempt has been made to compare various mathematical models of the effect of second phase particles on the grain size, using observed data.

The age-hardening characteristics of Ni-Fe Base Superalloys have been shown to vary with the morphology of the different types of precipitate such as $M_{23}C_6$, TiC and γ', and their nucleation at different sites. The precipitation kinetics have been explained in terms of the relative diffusion rates of the various alloying additions present.

The effect of cold working on the relative kinetics of precipitation and recrystallization have been shown to vary with the type of alloying addition . In steels precipitating $M_{23}C_6$, precipitation precedes recrystallization, whereas in γ' forming alloys, cold working prior to ageing significantly increases the rate of zone formation and growth, thus retarding the recrystallization processes.

Both high temperature tensile and creep properties of Ni-Fe Base Superalloys, at varying strain rates, have been shown to depend on the microstructure. Tensile strength increases with increasing volume fraction of

precipitating phase, whereas the overall creep strength has been shown to be dependent upon the relative strength of the grain boundaries and the matrix. The variation of high temperature ductility of the different initial microstructures at varying strain rates have been explained in terms of the qualitative influence of predominant microstructural features on the deformation and fracture mechanism maps.

Serrated yielding has been shown to be a common phenomenon in all steels tested at 700°C at strain rates of 10^{-2}/s and 10^{-3}/s, and substitutional solutes have been shown to be responsible for this effect. Also, the stress dependence of the creep rate varies with different microstructural features in Ni-Fe Base Superalloys, and the prominence of deformation mechanism controlled by a marked interface reaction has been indicated.

AIMS AND OBJECTIVES OF THE INVESTIGATION

Age-hardening austenitic iron-nickel-chromium alloys containing additions of titanium and aluminium have potential for fuel element cladding in fast reactors. The advantages of this type of alloy over the conventional molybdenum bearing stainless steels (Type 316) are that it has superior high temperature strength so that the target fuel burn-up can be achieved before the can fails, and it does not suffer to the same extent from swelling introduced by irradiation. A major problem with the age hardening alloy is that it exhibits very low ductility when deformed at high temperatures and very low strain rates, especially after irradiation. Many different heat-treatments have been used in attempts to improve the ductility and to eliminate or minimise the ductility trough which occurs over a specific range of strain rates and temperatures.

The aim of the present investigation was therefore to examine the effect of microstructure on the low strain rate, high temperature properties in general and high temperature ductility in particular, in Fe-Ni-Cr alloys of base composition 35%Fe, 45%Ni, 20% Cr. The separate effects of molybdenum, which is present in the commercial age hardening alloy, grain-boundary precipitates of $M_{23}C_6$ and TiC, and the age-hardening precipitates of the γ' type were also investigated. The mechanisms of high temperature deformation and fracture were examined.

1. INTRODUCTION

The role of different types and morphologies of precipitates on the high temperature properties of Fe-Ni-Cr base superalloys of the PE16 type, and in particular the effects of these microstructural variations on high temperature ductility, have been studied. Whilst, there are several deformation and fracture mechanisms associated with hot working and low strain rate creep testing, an attempt has been made to bridge the gap between these two extremes, and the influence of various microstructural features have been studied. The microstructural features investigated were:-

(i) The precipitation of $M_{23}C_6$ carbides on grain boundaries, the matrix being free from such precipitates.
(ii) The absence of any carbide precipitates either on grain-boundaries or within the grains.
(iii) The precipitation of $M_{23}C_6$ carbides both on grainboundaries and within the grains.
(iv) The precipitation of molybdenum rich grainboundary $M_{23}C_6$.
(v) The precipitation of $M_{23}C_6$ carbides on grainboundaries in a titanium rich matrix.
(vi) The precipitation of $M_{23}C_6$ and TiC carbides on grain-boundaries.
(vii) The precipitation of varying dispersions of γ' in the matrix, both in the presence and absence of grain-boundary $M_{23}C_6$ carbides.

The special features studied include the locking of dislocations generated during and prior to deformation, by carbides and γ' precipitates; the effect of grain boundary precipitates on grain boundary deformation processes; the formation of dislocation cell structures in different initial microstructures, and finally the formation and growth of grain-boundary cracks during the high temperature deformation of different microstructures at different strain rates. The experimental work was designed in four major stages:-

(i) To establish the effect of solution treatment temperature on the grain size of each alloy, in order to determine

that most appropriate for the subsequent ageing and high temperature testing. It was believed necessary to use as a criterion for solution treatment, that the maximum amount of carbon and alloy content should be dissolved with a minium of grain growth. The establishment of as fine a grain size as possible prior to high temperature testing is important, as coarse grain sizes can lead to low and very variable high temperature ductility.

(ii) To establish the ageing characteristics using the requisite solution treatment temperature, and the kinetics of the ageing processes, using hardness testing. Optical and electron microscopical results, were used, together with the hardness results to select heat-treatments to provide the initial structures required for the high-tempera ture testing programme.

(iii) To study the effect of cold work prior to ageing, which introduces some new microstructural features due to the relative kinetics of the precipitation and recrystallization reactions, thus helping to develop the desired high temperature properties. This was carried out on the basis of hardness data, optical and electron metallography, on six alloys out of the eight alloys used in the investigation.

(iv) To establish the effect of the various microstructural features outlined previously on the high temperature properties at 700°C. Various strain rates, were used and the high temperature strength and ductility received particular attention. In order to assess the micro-structural changes accompanying the high temperature deformation, interrupted creep tests were used for electron microscopical examination of the creep tested specimens.

2. LITERATURE REVIEW

The primary concern of this investigation was to correlate the high temperature properties of Fe-base superalloys with different microstructural variables in an austenitic matrix. In general, when reference is made to any type of superalloy, the high temperature strength is considered to be derived from a gamma-prime type of precipitation within a stable matrix. The series of alloys investigated in this work comprised both gamma-prime and non-gamma-prime forming alloys with stable austenite as matrix. It was felt that the work would be inadequate if it did not include a brief review of the stabilized Austenitic Stainless Steels together with iron-base superalloys, therefore, a review of the literature concerning the properties and topics of interest also includes austenitic stainless steels. The austenitic stainless steels discussed in this literature survey include only stainless steels that remain austenitic (ie do not undergo an austenite-to-martensite transformation at any stage).

2.1 GENERAL METALLURGY OF AUSTENITIC STAINLESS STEELS AND IRON-BASE SUPERALLOYS

2.1.1 Composition

2.1.1.1 Austenitic Stainless Steels

These are high chromium-nickel alloys of iron which are austenitic at and above room temperature, and essentially non-magnetic in the annealed condition. Stabilized austenitic stainless steels contain 18-25% Cr with 8-20% Ni and low carbon contents. The primary function of nickel is to retain austenite at room temperature and retard its transformation during cold working[1]. The main function of chromium is to increase corrosion resistance in atmospheric conditions, and at elevated temperatures. It does so by formation of an inert film of chromic-oxide over the entire metal surface and confers upon it the phenomenon of passitivity.[2] Passitivity is a phenomenon of super-normal corrosion resistance occurring at room temperature, not essentially a condition of non-corrosion, but of negligible corrosion.

These steels also often contain additions of molybdenum, niobium, titanium, aluminium and other elements such as nitrogen and phosphorus.[3] The amount of these alloying additions may vary from the property requirement point of view (ie the application requirements which are discussed in detail under the effect of alloying additions).

2.1.1.2 Iron-Base Superalloys

Nickel-iron-base superalloys were developed primarily from the austenitic stainless steels.[4] This group of superalloys includes those alloys with an austenite matrix hardened by an intermetallic or carbide precipitate, and contain approximately 25-60% nickel and intentional amounts of 14-60% and 10-25% of iron and chromium respectively. Generally the major strengthening constituent in these alloys is an intermetallic precipitate rather than solid-solution strengthening, strain hardening or carbide precipitation.[5]

These alloys invariably contain molybdenum and tungsten as solid-solution strengtheners; titanium, aluminium and niobium to combine with nickel as precipitation strengtheners; and carbon, boron, cobalt, zirconium, vanadium and other elements for various complex effects.[4]

Thse use of chromium is mainly to combat oxidation and corrosion in aggressive environments.[5] Most of these superalloys contain relatively low carbon, less than 0.10% and relatively large amounts of ferrite stabilizers such as chromium and molybdenum. The minimum level of nickel to maintain an austenite matrix in a nickel-iron base superalloy is about 25 wt %[4]. The addition of cobalt or other austenite stabilizers can lower this requirement. The intentional addition of elements other than iron, nickel and chromium will be discussed later in this review.

2.1.2 Microstructures

2.1.2.1 Austenitic Stainless Steels

Stabilized austenitic stainless steels can be broadly classified in two major groups from the point of view of microstructures.

(a) This group involves an austenite matrix without any second phase precipitates or segregates present in the microstructure. The microstructural variables in such steels would be the control of grain-size and the twin frequency within the grains themselves. It has been demonstrated that twin-frequency largely depends upon the stacking fault energy of the lattice, but twinning also is influenced by the grain size and the amount of deformation before recrystallization.(6)

Generally the higher the stacking fault energy the lower is the twin frequency and vice-versa. The control of stacking fault energy also affects the cross-slip during deformation and thus the work-hardening rate, and the higher the stacking fault energy the easier the occurrence of cross-slip resulting in lower work-hardening rates.(7)

(b) The second group of austenitic stainless-steels is the age-hardening type where the strength and other desirable properties can be derived from the precipitation of different type of precipitates at various microstructural sites in a polycrystalline austenitic matrix.(8) Some of the common micro-structural sites mentioned in the literature are grain-boundaries, incoherent twin boundaries, quenched in dislocations and vacancies within the grains, and lastly coherent twin boundaries. Depending upon the energy changes involved in the formation of a particular type of precipitate, one microstructural site could be more favourable for precipitation than the other. A brief summary of the morphology of different types of precipitates is as follows.

(i) Carbides and Nitrides

Commonly these are formed as a continuous grain-boundary precipitate but can be found within the grains in the form of a general precipitation and lamellar grain-boundary reaction products. Particularly in the case of $M_{23}C_6$ the general precipitation is characterised by a widmanstatten precipitation of fine carbides and is associated with the crystallographic relationship between

the carbides and the matrix austenite. The grain-boundary reaction is characterised by the formation of lamellar nodules of a depleted and recrystallized austenite plus $M_{23} C_6$ or $Cr_2 N$, from a super saturated austenitic matrix at the ageing temperature. Some other important sites for carbide and nitride precipitation are incoherent twin boundaries and the quenched in dislocations.

(ii) Inter-metallic Compound Formations

Useful generalizations have been found to predict the occurrence and structure of different inter-metallic compounds, and are used to predict the phases present in commercial alloys.(9) Some of the factors considered to be most important have been the changes in the electron/atom ratio, the atomic size and the compressibility of the alloying elements. Also, in recent years, through computer programming a method of prediction of different types of phases has been developed on the basis of electron hole concentration (Nv) called PHACOMP. Some of the commonly found phases are:-

Gamma Prime (γ')

Technically $B_3 A$ is considered to be a major hardening phase in austenitic matrices. It has a fcc lattice based on ordered $Ni_3 Al$, $Ni_3 (Al, Ti)$ and most uniquely it is only a transition phase of hexagonal $Ni_3 Ti$. The importance of γ' arises from its natural spherical low misfit morphology with small inter-particle spacing, large volume fractions, and preference for general precipitation. The microstructure shows a very fine general precipitate, barely discernible in peak age-hardened conditions and observed as a general distribution of spheroids in the over-aged condition.

Eta (η)

The γ' transition phase is replaced by eta phase, hexagonal $Ni_3 Ti$, and the transformation has been associated with over ageing of γ'. Microstructurally it can exist

in two different modes. One mode of precipitation, namely cellular precipitation, is nucleated at the grain boundaries in the form of Ni_3 Ti lamellae, leaving a semi-coherent eta-gamma interface. The second mode, widmanstatten inter-granular eta, is nucleated on stacking faults in the γ' and on several co-planar γ' particles and on co-planar (111) γ' plates. The eta nuclei then join up to form a plate of eta phase with complete transformation of the γ'.

Laves Phase

Laves phase can occur in austenitic stainless steel as cubic Mg Cu_2 type structures and as hexagonal Mg Zn_2 type structures. The latter form of hexagonal phase is more common in austenitic stainless steels. Generally it has been noticed that if the e/a is <8 the steels are more prone to laves phase formation and any alloying addition which increases this number can effectively suppress the formation of this phase. The phase has abnormally small inter-atomic spacings and appears as a massive grain-boundary phase or plates in the microstructure.

Beta Phase

Beta phase is a Cs Cl typephase which has a bcc lattice. In the microstructure it appears as a very fine general precipitate at peak hardness and as large plate-like structures in the over-aged condition.

Sigma Phase

Sigma has a tetragonal lattice and is considered to be the most common minor phase in austenitic stainless steels. This phase is found over the e/a range of 5.6 - 7.6 and stoichiometry range of B_4 A to BA_4. A large difference in atomic size of A and B suppresses the formation of σ phase. It has been observed as a continuous and massive grain-boundary angular constituent and large widmanstatten platelets. Generally it is considered very detrimental to properties but a blocky morphology within a fine grained austenite has been

reported to have beneficial effects on creep ductility.[9]

Chi Phase (χ)

This is a cubic phase, generally stabilized by electron acceptors such as silicon and chromium. According to Beattie and Hagel[10], its unit cell structure is $(Fe_{27}Ni_8Cr_{13})(Mo_{5.5}Ti_{0.5})$. It appears in a massive, blocky morphology at grain-boundaries and has effects similar to σ phase.

Mu Phase (μ)

This has a trigonal lattice, is generally designated as $B_7\ A_6$ and found in the e/a range of 7.1-8.0. The precipitates are relatively large irregular intragranular platelets, parallel to $\{0001\}\gamma$, and occur during over-ageing of the major hardening precipitate, γ'.

G Phase

G phase has a fcc lattice and is found as a ternary silicide in austenitic stainless steels. It is generally designated as $A_6\ B_{16}\ C_7$, where silicon replaces the C atom. Its morphology is generally massive and globular at grain-boundaries.

Ni_3 Nb

Ni_3 Nb has an orthorhombic lattice and is used as a major age-hardening and strengthening phase in high Nb + Ta alloys. It appears as an extremely fine precipitate at the lower ageing temperatures and as coarse acicular precipitates at higher ageing temperatures.

2.1.2.2 Iron-Base Superalloys

Microstructurally nickel-iron base superalloys can be subdivided into four main groups, according to the major precipitation - strengthening mechanism involved in a particular system.[4] Typical microstructural features of each group are as follows:-

(a) Those alloys with little or no precipitation strengthening. The major structural variable in these alloys is the grain-size, apart from other strengthening effects exerted through solid-solution hardening. Generally finer grain sizes are preferred for better creep ductility.

(b) The second group of alloys employs major precipitation strengthening from carbides, nitrides and/or carbo-nitrides. Phases such as carbonitrides and nitrides usually form during solidification and occur as discrete particles, distributed heterogeneously throughout the alloy, both in intergranular and transgranular positions. These have generally a fcc structure with little or no misfit with the matrix austenite. The microstructural control available in these types of alloys is achieved by controlling the precipitation of different types of carbides at various microstructural sites. The common classes of carbides are MC, $M_{23}C_6$, M_7C_3 and M_6C. The morphology of each type of carbide is as follows:-

(i) MC Carbides

These are usually formed in superalloys slightly below the freezing temperatures with a coarse random cubic or script like morphology. However, it has been shown that these carbides have a temperature dependent solubility during solution treatment and can be reprecipitated on further ageing treatments. The solution treated alloy is quenched rapidly to retain a high solute concentration in the matrix.[11,12] MC type carbides of exact stoichiometry may also precipitate at grain-boundaries during heat treatment or service. They can form both as globular particles or a thin film at grain-boundaries.[4] Furthermore, a high dislocation density in the matrix can assist the precipitation within the grains.[12]

(ii) $M_{23}C_6$ Carbides

These carbides have a complex cubic structure and form in

Ni-Fe-base superalloys during lower-temperature heat-treatments and service, both from degeneration of MC carbides and from soluble carbon residual in the alloy matrix. These carbides are usually seen at grain-boundaries but can occasionally occur along twin-boundaries, stacking faults, and at twin ends. Usually these take the shape of globular or blocky particles but thin films may also be formed, and sometimes a fine, cellular form of $M_{23} C_6$ has also been observed.

(iii) M_7C_3 Carbides

These carbides have been found as irregular blocky particles in simple alloys but are not stable in more complex superalloys. When an $M_7 C_3$ carbide can form, it usually transforms on ageing to $M_{23} C_6$.

(iv) M_6 C Carbides

These carbides are very similar to $M_{23} C_6$ type carbides with a similar complex cubic structure but form at higher ageing temperatures and with a higher refractory metal content in the alloy. M_6 C has been generally observed on grain boundaries, usually with $M_{23} C_6$.[13]

(c) The third and largest group of nickel-iron base alloys includes those strengthened by the precipitation of ordered fcc gamma prime (γ'). This group can be further subdivided into two sub-groups on the basis of service temperature. One contains lesser amounts of nickel and is used at lower service temperatures. The second group contains higher nickel for use at higher servic temperatures. The γ' particles in both these groups of alloys are usually spherical and homogeneously distributed throughout the matrix. Titanium is the major γ' forming element and the lattice misfit is less than $\sim$0.5%.[14]

γ' in nickel-iron alloys is coherent with the matrix over a wide range of (γ') sizes, and coherency is only partially lost on further ageing.

(d) The fourth group of nickel-iron base superalloys comprises the alloys which are primarily hardened by ordered b.c.t. (γ'') precipitate. These alloys solely depend upon (γ'') precipitation strengthening instead of, or in conjunction with, (γ') strengthening. The precipitate is principally based on the Ni_3Nb type of precipitate and appears usually in the shape of discs, uniformly throughout the matrix. The effective hardening is the result of coherency strains,[15] and the precipitate has an orientation relationship of $\{100\}\gamma'' // \{100\}\gamma$; $\langle 001\rangle\gamma'' // \langle 001\rangle\gamma$.

2.1.3 Effect of Alloying Additions on the Microstructural Features

Both nickel-iron base superalloys and stabilized austenitic stainless steels have a common austenite matrix, so the role of all the alloying additions is similar in both cases. The effect of each alloying addition is as follows:-

(a) Effect of Chromium

Additions of small amounts of chromium act as an austenite stabilizer by expanding the gamma phase up to the minimum in the gamma loop, and thereafter acts as a ferrite stabilizer. At 18% Cr, a minimum nickel content is required to promote a fully austenite structure which is stable at room temperature, and with more than 18% Cr, the ferrite-forming tendency of chromium predominates and increasing nickel is required to eliminate delta ferrite.[16] With regard to the effect of chromium on the stacking fault energy, there have been contradictory observations reported. Dulieu and Nutting[17] indicated that increasing chromium increased the stacking fault energy, whereas on the basis of available twinning frequency data, increasing chromium lowers the stacking fault energy.[7] Nevertheless, it is generally felt that increasing chromium lowers the stacking fault energy.

Chromium is used as one of the most potent carbide forming elements in austenite matrices, and one of the important

carbides formed is $Cr_{23}C_6$, particularly on grain-boundaries and incoherent twin boundaries. It can lead to the formation of certain other types of carbides like Cr_7C_3 and has been known to enter the M_6C unit cell.[4]

In the case of γ' forming alloys, chromium has been known to enter γ' unit cell thereby increasing the hardening by increasing the γ'-matrix misfit.

The presence of sigma phase, due to excessive amounts of chromium present in an austenitic stainless steel, is well established, so a limiting amount of chromium is preferred in an alloy to minimize this tendency. An excessive amount of chromium has been noticed to accelerate the formation of σ-phase induced by the presence of $Cr_{23}C_6$.[18] Also chromium, being an electron acceptor, promotes the formation of chi phase.

(b) Effect of Nickel

The major effect of nickel on the microstructure is to stabilize austenite by decreasing the M_s temperature to well below room temperature, and thus retaining a completely austenitic structure even after a very fast quench from the solution treatment temperature to room temperature.[19]

Nickel has been shown to increase the stacking fault energy of austenite.[20] There are certain other beneficial affects exerted by nickel on various types of phase formation, eg increasing nickel content suppresses the formation of the undesirable β and σ phases in favour of γ'. This has been largely attributed to the incompressibility of the nickel atom due to its 3d electron state, thus favouring precipitation of γ', which requires little size differences in comparison with β or σ formation.[4, 9]

(c) Effect of Carbon, Nitrogen and Phosphorus

Carbon is a powerful austenite forming element and also lowers the stacking fault energy, although direct evidence of this effect is very limited.[7] An austenitic solid solution super-saturated with carbon can lead to precipitation of carbides on further ageing after solution treatment of the alloy. With increasing carbon a higher solution treating temperature is required, and also the solution treatment temperature increases as the chromium content of the alloy is increased.[8] The most common carbide precipitated in austenitic matrices is $M_{23}C_6$ which precipitates at grain boundary triple point junctions, high angle boundaries and incoherent twin boundaries. It can form intergranularly with increasing carbon content, mainly on dislocations and vacancies.[21]

Generally nitrogen is added to steels in combination with carbon. Thermodynamically nitrogen is very similar to carbon, eg. has similar effects on the stacking fault energy and also is a very potent austenite stabilizer. The usual maximum level of nitrogen added to steels is about 0.2%, as higher amounts lead to problems such as ingot porosity.[3] The combined effect of (C + N) on precipitation is that along with $M_{23}C_6$ some Cr_2N can form as a grain boundary cellular precipitate, and the tendency for cellular precipitation is increased with increasing amounts of nitrogen in the steel.[8]

Phosphorus is added to steels in combination with carbon and can be an intentional alloying addition in (C + N) austenitic stainless steels.[3] Phosphorus is regarded as a strong ferrite stabilizer and decreases the stacking fault energy of austenite.[7] Phosphorus in combination with carbon increases the amount of general carbide precipitate within the matrix. There are still disagreements over the composition of the precipitating phase.[3] The precipitating phase has been designated

as $M_{23}(CP)_6$, or $(Cr\ Fe\ P)_{23}\ C_6$, and also Cr_3P in certain cases. Higher phosphorus in the alloy leads to the formation of an undesirable grain boundary cellular precipitate ; therefore there is a limitation on the amount of phosphorus that can be added to steel.

(d) Effect of Molybdenum, and Tungsten

Both molybdenum and tungsten are strong ferrite formers, thereby demanding an increased amount of austenite stabilizers. Molybdenum decreases the stacking fault energy, whereas the effect of tungsten has yet to be determined. Both these elements are very strong carbide formers and replace chromium in $M_{23}\ C_6$ so that the composition changes to $Cr_{21}\ (Mo, W)_2\ C_6$. It has been reported that when an alloy contains more than about 6 - 8 at % molybdenum or tungsten, $M_6\ C$ forms on grain boundaries, usually with $M_{23}\ C_6$, and with typical formulae for $M_6\ C$ of $(Ni, Co)_3\ Mo_3\ C$, and $(Ni\ Co)_2\ W_4\ C$. Also $M_6\ C$ has been found to replace $M_{23}\ C_6$ totally if the W or Mo content is high enough. The presence of these elements has certain other effects such as promoting the formation of Laves, mu and chi phases which impart undesirable effects to the properties.(9)

(e) Effect of Titanium, Aluminium and Niobium

All these elements are very strong ferrite formers, and both titanium and niobium remove carbon and nitrogen from solution as insoluble carbides and nitrides. This further stabilizes the ferrite, and therefore higher amounts of nickel are required to retain an austenitic structure.(3)

One of the major reasons for titanium additions has been to strengthen the alloy by γ' precipitation based on fcc $Ni_3\ Ti$. It was found that $Ni_3\ Ti$ overages rapidly to hcp η-$Ni_3\ Ti$, forming either as widmanstatten laths or a grain boundary cellular precipitate, and this tendency increases with increasing titanium in the alloy.(3,4,8)

Instead of increasing the titanium content of the alloy, some replacement by aluminium markedly retards the overageing associated with the $\gamma' \rightarrow \eta$ transformation and the precipitating phase formed is fcc Ni_3 (Al, Ti).[8] Also, higher titanium contents have been reported to increase the tendency for the formation of Laves and G phases, but excessive aluminium can form undesirable σ phase.[9] Control of Ti and Al is needed to obtain only the desirable γ' and generally, equal amounts of Ti and Al are added to obtain the optimum microstructural features.

The primary aim of niobium additions is to combine with carbon to form NbC for combating sensitization to intergranular corrosion. In the case of precipitation hardening the function of Nb is to combine with carbon thereby leaving titanium available for increased γ' precipitation. Recently, higher niobium contents of the order of approximately 2 -6 wt % have been added to iron base superalloys to form b.c.t γ'' within the matrix either as a major phase or in conjunction with γ' [4]. The limitations on the use of niobium arise from the overageing of $\gamma'' \rightarrow \delta$ (orthorhombic Ni_3 Nb), rather like $\gamma' \rightarrow \eta$; which can form both as intergranular platelets and cellular grain-boundary precipitate[4]. Also, niobium has been reported to increase the formation of undesirable laves, mu and G phases.[9]

Both Nb and Ti lower the stacking fault energy, titanium having a larger effect than niobium.[7]

(f) Effect of Trace Elements Boron and Zirconium

Trace levels of boron are commonly added to commercial austenitic stainless steels and nickel-iron base superalloys to retard the transformation of $\gamma' \rightarrow \eta$ (cellular), by segregating to grain boundaries.[22] More than 120 ppm boron in an alloy reacts to form two types of $M_3 B_2$ borides depending on the thermal history.[4]

Borides are hard refractory particles observed generally at grain boundaries . They often appear to grow from a grain boundary into the grain and act as a supply of boron for the grain boundary.

The effect of zirconium is not well understood. Nevertheless it is thought that its effect is limited to a grain boundary effect.[4] Because of its atomic size it tends to segregate at grain boundaries, thus increasing the structural perfection. It is added to nickel-iron base superalloys in the range 0.003-0.30% for improving the high temperature ductility and as a carbide former, and also prevents (σ) phase formation in austenitic stainless steels.[9] A few Russian workers have related the effect of zirconium to the grain-boundary interfacial energy that favours coalescence and spheroidization of grain boundary precipitate phases, thus helping to produce a more ductile material compared with the presence of continuous films at grain boundaries.[23]

2.1.4 Effect of Alloying Additions on Properties

Austenitic stainless steels and nickel-iron base superalloys are widely used because of their outstanding forming characteristics, elevated temperature (650°-800°C) strength, oxidation and corrosion resistance, mechanical properties at low temperatures (particularly ductility) and non-magnetic properties.

(a) Carbon, Nitrogen and Phosphorus

Increasing additions of carbon and nitrogen impart hardening through the precipitation of carbides and nitrides. Generally increasing carbon content increases the tensile strength but decreases the ductility and impact strength; especially if there is cellular precipitation of $M_{23}C_6$. Increasing nitrogen is even more detrimental, for it enhances the tendency for cellular precipitation at grain boundaries, and the formation of lamellar grain-boundary reaction products are detrimental to elevated temperature strength[8]. Also, both carbon and nitrogen

are very potent solid solution strengtheners in austenite apart from their precipitation hardening effects.[24]

Increasing phosphorus in combination with carbon increases the hardness, tensile and yield strength through age-hardening, but decreases the ductility[24]. The maximum amount of P in an alloy is normally $\sim$ 0.3%, because any higher amounts lead to the formation of embrittling grain-boundary cellular precipitates which drastically reduce ductility.[3] Also, phosphorus imparts beneficial effects on creep-rupture properties, providing the solution-treatment temperatures and the amount of phosphorus are carefully controlled[8]. Apart from these beneficial effects of phosphorus, it is generally considered to be one of the factors responsible for the poor weldability of austenitic steels.

(b) Molybdenum and Tungsten

Molybdenum and tungsten cause solid solution strengthening of austenite apart from their carbide forming tendency. These elements markedly increase both the room temperature and high temperature strength of the alloy, but reduce the impact strength at room temperature after ageing.[8] The beneficial effects of molybdenum and tungsten additions become more evident in superalloys, for at higher service temperatures the strengthening of austenite is diffusion dependent, and because of their slow diffusivity these prove to be potent hardeners.[4]

Also, through its carbide forming tendency, molybdenum, dissolves in $M_{23}C_6$ which significantly increases the rupture strength by inhibiting grain boundary sliding, although rupture failure usually initiates either by fracture of these same grain boundary $M_{23}C_6$ particles, or decohesion of the $M_{23}C_6 - \gamma$ interface. Larger amounts of molybdenum or tungsten are beneficial in wrought superalloys by controlling the grain size through the

precipitation of M_6C, which is more stable at higher temperatures than $M_{23}C_6$[4]. The presence of molybdenum in austenite also improves the general corrosion resistance, particularly in chloride media.[3]

(c) Titanium, Aluminium and Niobium

The basic intention of adding titanium and niobium to austenitic stainless steels is to stabilize C in the form of TiC or NbC and prevent the formation of $Cr_{23}C_6$, in order to combat intergranular corrosion. These stabilizing elements also produce finer grain sizes, thereby improving the strength of the steel[25].

During the development of high strength austenitic stainless steels through precipitation of γ', the effect of varying additions of Ti and Al on the properties was a subject of intensive study. In steels age hardened with only aluminium the high temperature rupture strength increases to a maximum with increasing aluminium and decreases significantly after this limit because of the formation of β phase, although room temperature yield and tensile strengths have been noted to remain unaffected[8]. Similarly, in steels hardened with only titanium, the room temperature yield and tensile strengths show a linear increase with increasing titanium , without any significant change in rupture-strength, although both the room temperature and high temperature ductility are greatly reduced if cellular Ni_3Ti occurs.[3] The combined addition of titanium and aluminium has been observed to result in better properties through the precipitation of $Ni_3(Al\ Ti)$, compared with alloys containing titanium or aluminium alone. General strengthening of the alloy increases with increasing (Al + Ti) content, and shows a further increase by increasing the Ti/Al ratio.[3] The amount of (Al + Ti) which can be used is limited, as too much Al results in σ phase formation, while too high Ti/Al ratio results in the undesirable cellular Ni_3Ti, both of which reduce the strength and ductility. Therefore

within the confines imposed by the above conditions, the steel should have maximum response to age-hardening, and should contain a maximum (Ti + Al) content and a maximum Ti/Al ratio. In general, compared with the Ni - Al and Ni - Ti steels, the Ni - Al - Ti steels give the best combination of strength, ductility, and toughness, particularly at the higher strength levels.(3)

Niobium additions to nickel-iron base alloys as a major strengthening alloying addition, are very recent, and strengthening occurs through the precipitation of γ'' within a niobium range of 2 - 6%, but only in the presence of some iron in the alloy.(4) The major advantage of niobium containing alloys comes from the much higher strenghtening potentional of γ'' compared with γ', and a sluggish ageing response which may contribute to a reduced tendency to crack in weld heat-affected zones. Alloys containing niobium overage during service to form δ, which may degrade the strength, although the heat-treatments designed to produce globular grain-boundary δ have been shown to lead to optimum stress-rupture ductility. Nevertheless δ formation is still considered to be undesirable. Also, with increasing Nb the tendency to form δ increases and some substitution of Nb by Al and Ta inhibits this tendency. However, γ'' has limitations compared with γ', as it appears to be less stable than γ' and the service temperature of the alloys is limited to 650°C maximum.

(d) Boron and Zirconium

Boron is believed to improve the hot workability and stress rupture properties of austenite, probably through delaying rupture failure. Zirconium is also added for similar reasons, although the literature available on the effect of zirconium is very limited.

2.2 HIGH TEMPERATURE STRENGTHENING MECHANISMS

The main purpose of alloy design is to suppress as many flow mechanisms as possible. Some of the principal methods

for doing this are:-

a) solid solution hardening
b) precipitation hardening

Precipitation mechanisms can be subdivided into two major groups, namely:-

i) grain boundary hardening
ii) matrix hardening

An attempt will be made to discuss the effects of these hardening mechanisms in austenite matrices.

2.2.1 Solid Solution Hardening

This can be defined as an increase in the resistance to deformation obtained by dissolving one element in another. Any lattice disturbance that hinders the movement of dislocations reduces the rate of plastic deformation, thus strengthening the alloy. The introduction of dissimilar (solute) atoms causes the crystal lattice of solvent either to expand or contract. This change is lattice parameter causes a disturbance, which takes the form of a strained condition within the crystal structure of the alloy. Small areas of localised strain surround each of the solute atoms. It is these strained areas that retard the movement of dislocations and strengthen the alloy.

The beneficial effects of solid solution hardening are valid for ternary and more complex solutions and the effects are additive.[30] Consequently, maximum solid solution strengthening is obtained when a large number of elements are dissolved to form an extremely complex solid solution. Obviously, maximum benefits are obtained when elements are dissolved which have the greatest possible difference in atomic size from that of the matrix. The different mechanisms operative in solid solution strengthening can be briefly listed as :-

a) Solute-dislocation interactions - Cottrell theory of yield point
b) Solute - stacking fault interaction - Suzuki locking of stacking faults.

c) Dislocation - Moduli interactions
d) Substitional solid solution hardening
e) Interstitial solid solution hardening

Most of the contemporary theories developed by Cottrell, Suzuki, Fleisher and others, postulate the existence of a localised segregation of solute atoms. The presence of these segregates is necessary to explain the strengthening effects obtained by the interaction of dislocations and the locally strained areas. The localised segregations occur in the form of clusters, "atmospheres", or as the result of short range ordering. When a dislocation line intercepts the strained area surrounding the localised segregation of solute atoms, the movement of the dislocation is retarded.

The role of interstitial solutes, such as carbon and nitrogen, in raising the strength of austenitic stainless steel is well established particularly at low temperatures.(31) Such effects are, however, overshadowed because of the precipitation of carbides and/or carbonitrides in complex systems such as iron-base superalloys, either during ageing treatments or at service temperatures. Therefore, to obtain solid-solution strengthening in such systems is possible only by the addition of substitutional solutes such as, chromium, vanadium, tungsten, molybdenum, cobalt and sometimes phosphorus. However, the strengthening effects of these elements can be markedly influenced by the interstitial content of the solid solution, i.e. how much of the substitutiona alloying addition is removed as carbides and how much is left in the solution to produce strengthening in the alloy.

2.2.2 Precipitation Hardening

Generally, steels for high temperature service are strengthened by precipitation. The basic principle as presented by Merica, was that precipitation hardening depended upon a solid solution showing decreasing solubility of the solute in the solvent with decreasing temperature. Thus the firat step in precipitation hardening is solution treatment, which involves heating a solid-solution above the solvus

temperature, holding for a suitable length of time, then cooling to room-temperature at such a rate to retain the elevated temperature structure. This treatment results in a super-saturated solution. The next step involved is the ageing treatment which results in the formation of a dispersed second phase by precipitation from the super-saturated solid solution. The selected ageing temperature represents a compromise between diffusion rate and degree of super saturation. The sequence of steps in the precipitation reaction may be characterised by:-

i) clustering
ii) nucleation
iii) growth

2.2.2.1 Clustering and the Kinetics of Clustering

Solute diffusion is a vital phenomenon in precipitation because the clustering of solute atoms in a pre-requisite for precipitation.[32] The solute atoms must migrate, by diffusion, to concentrate or cluster at locally favourable sites and initiate the formation of second phase particles.

It is accepted that a much higher diffusion co-efficient than normal is necessary to explain the formation of clusters.[32] The solute diffusion coefficient required for clustering is anomalously high in quenched dilute alloys. There have been two basic attempts to explain this effect; in one it is proposed that diffusion takes place along dislocation lines and in the other the effect is attributed to a non-equilibrium concentration of vacancies. The dislocation mechanism gives a reasonable explanation of the absolute value of the anomalous diffusion coefficient, but does not explain why the coefficient should be so sensitive to quenching rate, homogenization temperature, etc. Consequently this theory has been superceded by the excess vacancy mechanism.

The excess vacancy theory explains most of the experimental facts concerning the kinetics of clustering. It predicts that diffusion is governed by a vacancy concentration which would

be in equilibrium at the solution temperature, T_H, rather than at, T_A, the ageing temperature. For the diffusion of Cu in Al it has been shown that:-

$$D_{Cu} = A.\exp\left(\frac{-E_M}{K\,T_A}\right).\exp\left(\frac{-E_F}{K\,T_H}\right) \quad \ldots\ldots \quad (1)$$

where E_F and E_M are the activation energies for the formation and migration of vacancies respectively, and A is a constant. Equation (1) explains why the rate of quenching has such a marked effect on the kinetics of clustering. If the quench is slow some vacancies have time to migrate to sinks during quenching and the retained concentration is not associated with T_H but with some lower temperature. Also this equation predicts that the clustering process should be governed by an activation energy, E_M, for the migration of vacancies.

These clusters are no different from zones except that during or immediately after quenching, the solute atoms segregate to form clusters, but these clusters grow until they give rise to the x-ray diffraction effects typical of G.P. zones.[32] When there is no atomic size difference between the solute and the solvent, the shape of the zones is spherical but where there is a size difference the zones, and probably the first clusters, are assymetrical and may take the form of plates and rods[32].

In the case of alloys showing precipitation in the matrix, the clusters or zones may not form above a well defined temperature, called the G.P. solvus temperature[33]. Below this temperature G.P. zones form spontaneously and above this temperature zones are unstable and are replaced by hetrogeneous precipitation. This effect has been attributed to the energy barrier for nucleation of zones, which is zero below the G.P. solvus temperature, and the reaction rate is then solely controlled by solute diffusion. Above this temperature, the retardation in the rate of zone formation indicates that the energy barrier becomes positive and increases progressively with increasing temperatures.

2.2.2.2 Nucleation

The clusters often act as nucleation sites for further

precipitation because the energy required for solute atoms to add to the clusters is much less than for their precipitation at new nucleation sites. These nuclei contribute stable regions having a chemical composition different from the composition of the matrix. As precipitation proceeds the aggregates grow and may undergo internal ordering to produce a precipitate with a crystal structure quite different from that of the matrix.

The shape of the precipitate particles and the nature of the interface between the precipitate and the matrix are of interest and have a great influence on the mechanical properties of the final structure. The shape of the precipitate is greatly influenced by the nature of the interface between the precipitate and the matrix.[32] A fully coherent interface is defined when the crystals are placed in contact such that the plane of the atoms constituting the interface has an atomic arrangement, irrespective of the chemical species of the atoms, which is common to both crystal structures. In general , the interplanar spacing of the atoms in a coherent interface is not quite the same in both the matrix and the precipitate, so that only when the interface is small in area can it be fully coherent, and misfit must then be accommodated by elastic strains. If the interface becomes large in area the strain energy can be reduced by the introduction of dislocations lying in the interface.[34] Such an interface is not fully coherent . Thus a completely coherent precipitate is one in which all interfaces with the matrix are coherent and the bravais lattices in the two crystal structures are identical, if differences in chemical species, and consequent changes in atomic spacings are neglected, e.g. gamma prime in austenite matrices. A partially coherent precipitate is defined as one which has an interface in which there are interface dislocations. A non-coherent precipitate is one in which none of the interfaces with matrix exhibit even partial coherency.

Nabarro showed that if the precipitate remains completely coherent with the matrix, the strain energy of the particle increases as the precipitate increases in size.[35] If a

sphere of unstrained radius $(1+\delta)r_o$ is inserted into a spherical hole of radius r_o in the matrix, the total elastic energy of a sphere of volume $v = 4/3\pi r_o^3$ and bulk modulus K, in the matrix of rigidity modulus G , is:-

$$W = 6 G v \delta^2 / \left(1+\frac{4G}{3K}\right) \qquad \ldots\ldots\ldots\ldots \qquad (2)$$

The energy thus increases as the volume of the precipitate particle increases. If the precipitate breaks away from the matrix and forms a non-coherent interface of such a type that the shear strain in the precipitate vanishes, and if all the strain occurs in the matrix, the energy is given by:-

$$W = 6 G v \delta^2 f(c/a) \qquad \ldots\ldots\ldots\ldots \qquad (3)$$

where f(c/a) is a function of the shape of the spheroid. A more recent calculation by Brown and Ham [36] on the effect of coherent precipitates on the shear stress, τ gives:-

$$\tau = 4.1 G \epsilon^{3/2} f^{1/2} \left(\frac{r_o}{b}\right)^{1/2} \qquad \ldots\ldots\ldots \qquad (4)$$

for small precipitates

and $$\tau = 0.7 G f^{\frac{1}{2}} \left(\frac{\epsilon b^3}{r_o^3}\right)^{\frac{1}{4}} \qquad \ldots\ldots\ldots \qquad (5)$$

for large precipitates.

where f = the volume fraction of precipitate,

b = Burger's Vector of dislocations

and ϵ = is a measure of the Shear Strain due to mis-match of the precipitate with the matrix.

2.2.2.3 Growth of the Precipitates:

As the precipitate grows, so does the localised internal strain. In time, these strains build up to the point where local shearing takes place and the precipitate becomes an isolated particle of the second phase. When shearing occurs, there is a definite release of internal strain and a decrease in the size of the strain affected region .[30] Subsequent agglomeration of the second phase particles further reduces the effectiveness of the strained regions because fewer precipitates are present, and dislocations can travel greater distances between them.

It has been shown[37] that the isothermal growth of gamma prime precipitates in nickel-base alloys can be represented by a relationship of the form

$$D = Q\, t^{n} + C \qquad \ldots\ldots\ldots \quad (6)$$

where D = diameter of the precipitate in angstrom units, t is the time and Q and n are constants. Mitchell has stated that the value of n is about 1/3.[38] The growth of the precipitates is diffusion controlled, and the rate of growth increases with increasing supersaturation and increasing ageing temperatures.[39]

2.2.2.4 Factors Affecting Age-Hardening of Austenitic Steels

The intensity of age-hardening in austenitic steels depends upon:-

i) volume fraction of the precipitate
ii) the coherency strains around the precipitated particles, as influenced by the precipitate/matrix misfit.
iii) the internal ordering of precipitates, and
iv) the ageing temperature

In general the greater the volume fraction of the precipitate the more rapid and intense is the age-hardening.[33] However, it has been shown in Ni-base alloys that the hardness increment during ageing is also a function of the lattice misfit between the matrix and intermediate precipitate.[40] The larger the misfit the higher are the coherency strains, with the result that a higher hardness is observed for a constant volume fraction of the precipitate. If a larger misfit occurs between a precipitate and matrix, although the tendency to harden will be more pronounced, overageing will also occur more rapidly and some of the benefit of the large increase in hardness may be lost.[39] There is therefore an optimum lattice mismatch at which the intensity of age-hardening is high but is not so large that it results in too rapid overageing.[33] Also it has been observed in austenitic steels hardened by gamma-prime, that the maximum increase in hardness is directly related to the rate of overageing.[33]

An increase in volume fraction of the precipitate as a consequence of increasing super-saturation, increases both the rates of ageing and overageing. Overageing also depends upon the mismatch, increasing with increasing mismatch, or when there is an unfavourable orientation relationship between the equilibrium precipitate and the matrix.[33] That is why the b.c.c. Ni (Al Ti) and Ni_2(Al Ti) phases overage more rapidly than does f.c.c. Ni_3 (Al, Ti).

The ageing temperature also plays an important role, for increasing the temperature usually increases the solubility of the precipitating phase[30]. Because the amount of second phase precipitated is related to its solubility, an increase in ageing temperature decreases the amount of second phase. Also, as already mentioned, if the ageing temperature is above the G.P. solvus , an intermediate precipitate nucleates directly from the austenite, giving non-uniform precipitation, which may reduce the intensity of age-hardening[33,41].

2.2.2.5 Strengthening Mechanisms by Ordered Precipitates in Austenite

Several theories of strengthening by ordered precipitates have appeared in the literature. In all cases the variation of the critical resolved shear stress with particle size derives from a Friedel-type relationship[5, 42-46]. In such systems it has been assumed that macroscopic flow is governed by the stress to move a dislocation pair.

In cutting through a particle, the first dislocation creates an antiphase boundary, the second dislocation is pulled forward by the antiphase boundary energy and is generally straight[43]. The dependence of the $\Delta\tau_c$, increase in critical resolved shear stress, on the particle radius, r , and volume fraction, f, has been shown to be:-

$$\Delta\tau_c = 0.2\ \gamma^{3/2}\ T^{-\frac{1}{2}}\ b^{-1}\ f^{\frac{1}{3}}\ r^{\frac{1}{2}} \qquad \ldots\ldots\ldots (7)$$

Raynor and Silcock[42] found that :-

$$\Delta\tau_c = A\ \gamma^{3/2}\ T^{-\frac{1}{2}}\ b^{-1}\ f^{\frac{1}{3}}\ r^{\frac{1}{2}} - \gamma f/2b \qquad \ldots\ldots\ (8)$$

γ is the antiphase boundary energy, T the dislocation line tension, and b the burger's vector. Gleiter and Hornbogen[47] used $T = Gb^2/2$, where G is the shear modulus. Raynor and Silcock[42] estimated the line tension while taking into account the variation of energy as the dislocation bows and also the effects of other parts of the dislocation on the line tension at any point. Their estimate for line tension T is given by:-

$$T = \frac{Gb^2}{4\pi} \cdot \frac{1+\nu - 3\nu \sin^2\theta}{1-\nu} \cdot \ln \lambda/b$$

where, ν, is the Poissons ratio, λ = outer cut off radius, in the case of PE16 equal to the particle spacing along the dislocations and θ is the bowing angle of the first dislocation. Equations (7) and (8) are very similar except for the term $\gamma f/2b$. Evidently, equation (8) does not hold for r approaching zero, since $\Delta\tau_c$ must not become negative. In reality, $\Delta\tau_c$ approaches zero for very small particles. For such particles, some of the assumptions made in deriving equation (8) are not valid. For very large particles $\Delta\tau_c$ decreases with increasing r because the Orowan looping process operates[44]. Martens and Newbach[43] found that for $r \leq 120A^o$, the Raynor and Silcock theory describes the dependence of $\Delta\tau_c$ on r and f in PE16. For $r > 120\ A^o$ the Orowan looping process operates.

Equations (7) and (8) treat the antiphase boundary energy as the only resistance to dislocation movement, There is considerable doubt on the relative importance of misfit and antiphase boundary energy. Wilson carried out an analysis of the intensity of age-hardening as a function of the degree of misfit between the precipitate and the matrix and of the precipitate particle size at constant volume fraction in an austenitic steel. He found:-

$$\Delta H = K R^{\frac{1}{2}} \delta^{\frac{1}{4}} \qquad \ldots\ldots\ (9)$$

ΔH = Intensity of age-hardening,
R = Radius of particle,
δ = Misfit in % and K is a constant

The relationship is similar to the equation developed by Gleiter and Hornbogen[47] for coherency hardening, which has the form

$$\Delta\tau = K\delta^{m} f^{n} R^{\frac{1}{2}} \qquad \ldots\ldots\ldots\ldots \quad (10)$$

where $\Delta\tau$ = increase in critical resolved shear stress,

δ = misfit,

f = is the volume fraction

R = radius of spherical precipitate

K, m and n are constants.

In reviews[30] on the strengthening mechanisms in Ni-base superalloys, the main cause of strengthening is generally regarded as the result of interactions between the strain surrounding a particle of second phase and the movement of dislocations. As a particle of second phase is formed it produces elastic strains in its immediate vicinity. As dislocations move through the crystal they cannot continue along the easiest path of slip when they intersect the strained region, thereby strengthening the alloy. When contact is made between dislocations and the strain field, the dislocations pile up against this barrier. This description provides an explanation of strengthening effects before the appearance of an observable second phase. When the second phase is observable microscopically, then other processes of strengthening such as antiphase boundary energy and Orowan looping occur. In the case of a semi-coherent precipitate Singhal and Martin[48] simply added the equations given by different authors for anti-phase boundary energy and the misfit, and obtained a reasonable comparison with their results. Raynor and Silcock[42] considered the value of misfit as zero in Nimonic PE16 and attributed the strengthening to antiphase boundary energy alone. But White et al[49] have shown a negative misfit of γ' with the matrix of the order of 0.03%, although these authors quote the same volume fraction of precipitate. Therefore, there is a considerable doubt as to which theory should be applied to a particular alloy system.

After the precipitate has lost coherency with the matrix and starts overageing, Orowan looping is the dominant method of strengthening. The flow stress in this case is given by the

stress required to bow a dislocation between precipitates.[36] The original equation was modified by Ashby, to give the following formula:-

$$\tau = A \cdot \frac{Gb}{2\pi} \cdot \frac{1}{L} \cdot \ln\left(\frac{r}{b}\right) \qquad \ldots\ldots\ldots\ldots (11)$$

where A = 1, for an edge dislocation and $A = \frac{1}{(1-\nu)}$ for a screw dislocation.

Recent studies in some nickel-iron base superalloys have shown that ordered b.c.tet. γ'' produces effective hardening by coherency strains.[45,46] Available data suggests that a strengthening mechanism based on dislocations cutting through the γ'' precipitate in a manner analogous to γ' alloys is dominant.[5]

2.2.2.6 Grain-Boundary Strengthening

Grain-boundaries, like dislocations are often a source of considerable strengthening, while in other circumstances they are regions of weakness, which leads to premature failure or to selective corrosive attack. Particularly when it is realised that many high temperature creep and rupture failures initiate at grain-boundaries and propogate along the grain-boundaries, the importance of suppressing these effects becomes clear.[50] One of the most common methods of strengthening grain-boundaries has been through precipitation and segregation of different solutes or compounds to suppress grain-boundary sliding. The energetics and kinetics of nucleation, reviewed recently by Russell[51] show that grain-boundaries are expected to be preferred sites for incoherent and semi-coherent particles, but not for fully coherent particles.

The classical theory of heterogeneous nucleation can be applied to the precipitation at a grain-boundary. The free energy equation for homogeneous nucleation[52] at a grain-boundary is:-

$$\Delta F = \Delta F_{volume} + \Delta F_{surface} + \Delta F_{strain} \quad \ldots\ldots (12)$$

For nucleation at a grain-boundary, the term $\Delta F_{surface}$

in equation (12), is reduced because of the presence of the grain-boundary. There may also be some reduction in the ΔF_{strain} term. These effects result in a lower value of ΔF which makes possible the nucleation of an equilibrium phase at grain-boundaries even at low temperatures. The grain-boundary precipitate is then in a lower energy state than the zones or intermediate precipitates formed within the grain and it will therefore tend to increase in size during ageing at the expense of the intragranular precipitate, and is able to draw solute from within the grains.

The theoretical estimation of the solute concentration at the grain-boundary in a solid solution, X_{GB}, is based on the deformation energy of the lattice caused by the presence of a foreign atom and, can be written as:- [53,54]

$$X_{GB} = \frac{X.\exp\,(Q/RT)}{1 + \exp\,(Q/RT)} \qquad \ldots\ldots\ldots\ldots \qquad (13)$$

where X is the concentration of solute within the grains. The higher the value of X_{GB}, the more dominant the segregation to the grain boundaries. Equation (13) shows that with increasing amount of precipitate forming elements, e.g. C,N,B,Zr,Mo, W, Ti, etc. in the solid solution, the amount of precipitate formed at the grain-boundary increases. Russell and Aaronson[55] have shown that the kinetics of precipitation at grain-boundaries is affected by the solution annealing temperature. When the binding energy, Q, of the solute to the grain-boundary is sufficiently high, the nucleation rate at these boundaries is sensitive to the solution annealing temperature. When quenching to the ageing temperature is rapid, the nuclei are able to form at the ageing temperature before the solute concentration at the grain-boundary rises above that inherited from the solution annealing temperature .

2.3 GRAIN COARSENING CHARACTERISTICS AND THE INFLUENCE OF SECOND PHASE PARTICLES

The dependence of the yield stress on grain size is well established[52] in f.c.c. materials and also grain size has

been noticed to have an appreciable effect on high temperature properties such as creep elongation and high temperature fracture mechanisms.[56] Particularly when creep is controlled by diffusion processes and not by the movement of dislocations, the grain size of the material is of great importance and there is usually a rapid increase in creep rate with a decrease in grain size. In single phase materials the micro-structural variations are limited to grain size, grain shape and grain orientation. Thus the control of grain size in metals plays an important part in developing the required mechanical properties.

2.3.1 Types of Grain Growth

The term grain growth is used to embrace those phenomena which involve an increase in grain size of strain-free single phase polycrystalline microstructures, and second phases are considered only in so far as they modify the basic pattern of these events. The two major forms of grain-growth can be described as follows:-

a) Normal grain growth

This process involves the maintenance during grain-growth of equiaxed grains with a similar size distribution throughout the microstructure. This process necessarily involves the disappearance of some grains, usually the smaller ones, which has led to grain-growth being described as a "cannibalistic" process.

b) Abnormal grain-growth

This involves the growth of very few selected grains in a relatively fine grained matrix, at the expense of the remainder that do not grow pending their consumption by the relatively few growing grains. It thus requires inhibition of normal grain-growth, usually by precipitate particles,[57] and results in the development of an abnormal distribution of grain size.

2.3.2 Basic Theory of Grain Growth

Grain growth in crystalline solids occurs by the migration

of grain boundaries, with the free energy of the boundaries acting as the driving force.

The basic equation for grain growth can be simply derived following a procedure used by Beck et al[58-61] in which it is assumed that the velocity, V, of a grain-boundary is proportional to the driving force, F, acting on it, i.e.:-

$$V = M.F. \qquad \ldots\ldots\ldots\ldots\ldots (14)$$

where M denotes the grain-boundary mobility. In the absence of restraining effects due to dissolved impurities or second phases, the force F is given by $2\gamma_B/r$, where γ_B is the grain boundary tension and r is the grain radius. The mobility, M, under the same condition is given by $M_o \exp(-Q/RT)$ where Q is the activation energy for grain-boundary migration, R is the gas constant and T is the absolute temperature. Thus:-

$$V = M_o \exp(-Q/RT) \cdot 2\gamma_B/r \qquad \ldots\ldots\ldots\ldots (15)$$

Assuming that $V \approx dD/dt$ and $r \propto D/2 = KD/2$ where D is the grain diameter, then equation (15) leads to:-

$$\frac{dD}{dt} = M_o \exp(-Q/RT) \frac{4K\gamma_B}{D} \qquad \ldots\ldots\ldots\ldots (16)$$

$$= K' \cdot \frac{1}{D} \text{ at constant T} \qquad \ldots\ldots\ldots\ldots (17)$$

where dD/dt is the rate of grain growth and depends on temperature and grain size of the material.

Integrating equation (17) gives:

$$\int_{D_o}^{D} D.dD = \int_{t_o}^{t} K' . dt$$

i.e. $$\left[D^2/2\right]_{D_o}^{D} = K'(t - t_o) \qquad \ldots\ldots\ldots\ldots (18)$$

and:-

$$D^2 - D_o^2 = 2K'(t - t_o)$$

where D_o is the grain size at the start of grain growth, at time t_o. A generalised form of equation (18) is:-

$$D^{n'} - D_o^{n'} = 2K'(t - t_o) \qquad \ldots\ldots\ldots (19)$$

where n' is the grain size exponent. This gives the empirical equation formulated by Beck et.al, i.e:-

$$D = (At)^{1/n'} = Kt^{n} \qquad \ldots\ldots\ldots (20)$$

where $A = Ao \exp(-Q/RT)$. The material parameters, n, Ao and Q depend upon temperature, composition and material history. Equation (20) can be regarded as a limiting form of equation (19), valid at prolonged annealing times, when D_o and t_o both become increasingly negligible with respect to D and t.

2.3.3 The effect of dissolved impurities and second phase particles on grain growth

The derivation of equations (17) - (20) implicitly assumes that the grain-boundary driving force is unimpeded by any opposing drag effects. Such drag effects may arise in practice from interactions of moving grain-boundaries with a free surface, second phase particles and dissolved impurities.

Mullins[62] showed that a thermal grain-boundary groove, of magnitude less than $\gamma_B/2\gamma_s$, developing at the intersection of a grain boundary with a free surface, would effectively lock any grain boundary inclined at an angle h/2r to the surface normal, (where h is the sheet thickness, r(> h) is the grain-boundary radius, γ_s is the surface energy). Thus the effective restraining force on grain-boundary motion, $2\gamma_B/r$, amounts to $\gamma_B^2/\gamma_s.h$ in this case, and Mullins concluded that grain growth would stop where the grain size reached $\sim$ 2h. With regard to the effect of second phase particles on grain growth, there have been several models proposed, and it is worth while to discuss each of them in detail.

2.3.3.1 Zener's Model

Zener[63] considered the relation between the size of

spherical grains of radius R, and the size of spherical precipitate particles of radius r. He showed that the restraining force (B) exerted on a grain-boundary by a spherical inclusion would be:-

$$B = \pi . r . \gamma \qquad \ldots\ldots\ldots (21)$$

Where the grain-boundary meets the particle at an inclination 45^{o} to the direction of boundary motion, and γ is the surface-energy per unit area of the boundary. The driving force for grain growth was assumed to be $2\gamma/Ro$. This force, however, relates to a contracting spherical surface with no attached interfaces. Zener's ultimate criterion was:-

$$R = 4/3 \cdot r/f \qquad \ldots\ldots\ldots\ldots (22)$$

where f is the volume fraction of second phase particles, and R_o is the initial grain size.

2.3.3.2 Hillert's Analysis

Hillert[64] suggested a growth equation for individual grains in single phase materials and used it to calculate a rate equation for normal grain growth, and the grain size distribution in the material. It predicted the maximum size of twice the average size, and he also modified this equation to take into account the effect of second phase particles. The basic expression for the growth rate was of the form:-

$$\frac{dR}{dt} = \alpha M \sigma \left(\frac{1}{R_{cr}} - \frac{1}{R}\right) \qquad \ldots\ldots\ldots (23)$$

where $\frac{dR}{dt}$ = grain growth rate

M = grain boundary mobility

and σ = grain boundary pinning force,

α = a dimensionless constant

R_{cr} is the critical grain size which neither grows nor shrinks and

R = average grain size

Taking the second phase particles into account the growth rate equation was:-

$$\frac{dR}{dt} = \alpha M \sigma \left(\frac{1}{R_{cr}} - \frac{1}{R} \pm \frac{Z}{\alpha}\right) \quad \ldots\ldots\ldots (24)$$

where $z = \frac{3f}{4r}$, f and r having the same meaning as in Zener's equation.

In general he considered the relation between the rate of growth of metal grains and the energy changes involved. It was assumed that large grains would grow at the expense of small grains, and a simple model of the energy change, E, was assumed, in which:-

$$-E = K\left(\frac{1}{R_{cr}} - \frac{1}{R}\right) \quad \ldots\ldots\ldots\ldots (25)$$

This model indicates that grains larger than the critical size would cause a decrease in energy, whereas grains smaller than R_{cr} would cause an increase in energy and therefore be prevented from growing.

2.3.3.3 Gladman's Model

Gladman[57] attributed the pinning mechanism between a grain boundary and a particle to the reduction in grain-boundary area, when a grain-boundary intersected the particle. He considered two factors that would affect the grain-boundary area viz:-

a) the curvature of the boundary
b) a particle occupying a position on the boundary.

On the basis of these assumptions there are two principal sources of energy changes. First, the energy of the system is increased by the expansion of the interface of the growing grain, and, secondly, the energy of the system is decreased by the elimination of grain-interfaces of grains which are absorbed by the growing grains. These assumptions led to the derivation of the energy change during simple grain growth as:-

$$E_n = \frac{s}{R_o} \gamma \left(\frac{2}{Z} - \frac{3}{2} \right) \qquad \ldots\ldots\ldots\ldots (26)$$

Z = Ratio of the radii of the growing grain to its neighbour and is $\sim$1.33-2, R_o is the matrix grain size, s is the boundary displacement and γ is the surface energy per unit area.

To assess the energy change accompanying grain growth in the presence of second phase particles, he combined the energy change in equation (26) with the unpinning energy. The total energy change associated with the unpinning of a single particle, E_T, is:-

$$E_T = E_P + E_I \qquad \ldots\ldots\ldots\ldots (27)$$

where E_P is the unpinning energy and E_I is the energy released per particle due to grain growth, or:-

$$E_I = En/2\, r\, n_v$$

where En is the energy change during simple grain growth, n_v is the number of particles per unit volume and r the particle radius.

$$\therefore \quad E_I = \frac{2 s \pi r^2 \gamma}{3 R_o f} \left(\frac{2}{Z} - \frac{3}{2} \right)$$

where f = volume fraction of particles

By calculating these energy changes he estimated the critical particle radius, at which grain growth would occur, which was defined by the activation energy barrier being reduced to a level at which thermally activated boundary release could occur. This occurs when:-

$$\left[\frac{d_{EP}}{ds} \right]_{max} = - \left[\frac{d_{EI}}{ds} \right] \qquad \ldots\ldots\ldots (28)$$

$\left[\frac{d_{EP}}{ds} \right]_{max}$ is the maximum rate of increase in energy involved in the unpinning process, and $\left[\frac{d_{EI}}{ds} \right]$ is the rate of change of energy due to grain growth.

Substituting these values in equation (28) gives:-

$$r^* = \frac{6 R_o f}{\pi} \cdot (3/2 - 2/Z)^{-1} \qquad \ldots\ldots\ldots (29)$$

where r^* = critical particle radius.

2.3.3.4 Hellman and Hillert's Correction:-

Recently these authors[65] ascribed a macroscopic curvature ρ to the boundary, and suggested that the ratio between the macroscopic curvature of the boundary and the particle size, ρ/r, has a strong influence on the ability of the boundary to stay in contact with the particle. In effect they have tried to improve Zener's treatment and suggest that his expression for the net effect should be multiplied by the ratio between the area under the curve (Fig. 1) for the appropriate value of ρ/r, and the area of the dashed square. This ratio is denoted as β, where:-

$$\beta = 0.125 \cdot \ln 40\rho/r \qquad \ldots\ldots\ldots\ldots (30)$$

where ρ/r equals $6R_o/r$. This modifies the Zener's equation to the form:-

$$R_o/r = 4/9\, \beta f \qquad \ldots\ldots\ldots\ldots (31)$$

2.3.3.5 Critical Assessment of Grain Growth

Some authors[57,66] have shown that Zener's model over-estimates the driving force for grain growth, because the diminution of one interface usually involves an expansion of some other attached interface. Gladman and Pickering[66] substituted typical precipitate particle sizes and volume fractions into Zener's equation, which indicated a much larger equilibrium grain size than actually observed. These observations confirm that the driving force was over-estimated. Hellman and Hillert[65] suggest that Zener gave a total restraining force as $\sigma\pi\sum r$ where the summation is carried out over all the particles situated in a unit area of the boundary. This is an over-estimation since it is not likely that the particles are arranged in such a way that they can all exert their maximum effect simultaneously. But at the same time they suggest that Zener replaced the summation $\sum r$ by nr^2,

where n is the number of particles per unit volume of the material. They show that this method yields an increasing underestimation of the number of particles in contact with the boundary as increasing values of ρ/r are considered, because a boundary can stay in contact with a particle over a longer distance. The larger the value of ρ/r, the more the approximations used by Zener tend to offset each other, but still his equation is not in agreement with the experimental observations. That is why Hellman and Hillert[65] have introduced a factor β, which according to their analysis gives a reasonable fit.

Hillert[64] considered the growth rate and energy changes involved, and developed a general treatment for the effect of second phase particles, but he did not consider the effect of the precipitate distributions in detail, i.e. the volume fraction, particle size, and number of particles were not treated individually.[66]

Gladman's approach[57] seems more practical and fits the observed data[67]. But Hellman and Hillert[65] argue that he has limited his treatment to macroscopically flat boundaries, in other words the shape of an imaginary surface which approximates to the real boundary but neglects all local variations in shape caused by the presence of second phase particles.

2.4 PRECIPITATION IN AUSTENITE

There can be many types of precipitates present in austenitic matrices, but the precipitates of major interest in this work are $M_{23}C_6$, TiC and Gamma-prime. The presence of a variety of nucleation sites, and the preference of the individual type of precipitate for a specific type of site, results in a considerable range of precipitate nucleation mechanisms, and these nucleation sites can control the mechanical properties of precipitation hardened alloys to a great extent. It will be worthwhile discussing the kinetics of each type of precipitate with reference to their nucleation sites individually.

2.4.1 Carbides

The common types of carbides in nickel-iron base superalloys are, MC, $M_{23}C_6$, M_7C_3 and M_6C.[4] $M_{23}C_6$ is formed in alloys with moderate to high chromium contents, during lower-temperature heat-treatment and service, both from degeneration of MC carbides[4] and from soluble carbon residual in the alloy matrix.

$M_{23}C_6$ carbides can also form at temperatures in the range 595-760°C, due to the solubility of carbon being exceeded.

M_7C_3 carbides are formed as irregular blocky particles in simple alloys with low chromium contents and low refactory element contents. They are not usually stable in the more complex superalloys, for they usually transform to $M_{23}C_6$[4].

There is evidence that, unlike other nimonic alloys where M_7C_3 is the first carbide to form at high temperatures, transforming subsequently at lower temperatures to $M_{23}C_6$, in nimonic PE16 the $M_{23}C_6$ is the main carbide formed on heat-treatment and M_7C_3 is precipitated principally on prolonged exposures at temperatures in the range 500°-750°C.

The MC carbides are believed to form in superalloys shortly after freezing; and occur from simple combination of carbon with the more refractory metals. Many atoms can dissolve in MC phases. Mo or W substitution weakens the binding forces of MC so that degenerations to $M_{23}C_6$ becomes easier.[4]

M_6C carbides form at higher temperatures, in the range 815-980°C, and usually occur where the refractory metal content is high. They tend to be the grain-boundary precipitate, usually with $M_{23}C_6$.

2.4.2 $M_{23}C_6$ precipitation

The structural relationships between the parent austenite and any carbide precipitation should have two consequences[21], namely:-

1) Precipitation of carbides with an orientation parallel to that of parent austenite should be energetically favourable, and

2) A high vacancy concentration in the austenite should facilitate carbide precipitation and growth.

On the basis of these two principles the kinetics of precipitation of any carbide can be conveniently discussed with special reference to any precipitation site.

2.4.2.1 $M_{23}C_6$ Precipitation at Grain-Boundaries and Grain-Boundary Junctions

Precipitation of $M_{23}C_6$ has been observed by many workers on grain boundaries[21,23,69]. Massive precipitation of $M_{23}C_6$ usually occurs at triple points[69] because ΔF surface in equation (12) is greatly reduced due to the larger surface, area of grain-boundary. According to Mott[70], grain-boundaries may be considered to have regions of alternately good and bad atomic fit. Regions of bad atomic fit must be associated with space , i.e. atomic density is less in the grain-boundary than it is in the perfect crystal. Nucleation of $M_{23}C_6$ in these regions should thus be facilitated. In addition high angle grain-boundaries are good sources and sinks for vacancies. As a result vacancies are available for the growth of carbide particles.

$M_{23}C_6$ has been observed to nucleate on defects such as dislocations lying in the grain-boundary plane with an orientation of $\{111\}\langle 110\rangle$ with the matrix.[69] An increase in the dislocation density around the grain-boundaries increases the amount of precipitate formed. On ageing at lower temperatures, $M_{23}C_6$ precipitates are more closely spaced than after ageing at higher temperatures, because nucleation is more copious due to the greater super-saturation, whilst growth is less rapid.

Taking the orientation relationship into account, $M_{23}C_6$ precipitation at grain-boundaries should provide a good lattice match on only one side of the carbide[21]. Evidence

for this was observed by Kinzel[71] who showed that the knife edge attack by HNO_3 occurred only on one side of the carbide particles in the austenite grain boundary, but never on both sides. This effect has been interpreted by assuming the carbide particles to be in atomic registry with one grain, but having a high energy boundary with the other, thus facilitating corrosion.

Precipitation of $M_{23}C_6$ at grain boundaries has been reported to produce a denuded zone adjacent to the grain-boundary, which has been attributed to the loss of solute concentration near the grain-boundary, e.g. chromium, which has been concluded to be the most likely explanation for the sensitization of austenitic steels[72]. Recently Pande et al[73] have produced the first direct evidence to this effect with the help of STEM, and proved that in austenitic stainless steels, free from any other types of precipitates other than $M_{23}C_6$ at grain-boundaries, the corrosion is definitely through chromium depleted regions.

2.4.2.2. $M_{23}C_6$ On Incoherent Twin Boundaries

$M_{23}C_6$ forms on incoherent twin boundries, as in the case of grain-boundary precipitation. The rate of precipitation is higher at higher ageing temperatures than at lower ageing temperatures[69]. As for grain-boundary carbide precipitation, the precipitate at incoherent twin boundary leaves a solute denuded zone adjacent to the boundary.

Lewis and Hattersley[74] demonstrated that $M_{23}C_6$ had the same orientation as the matrix on one side of boundary. They observed that during the later stages of ageing, lamellae of $M_{23}C_6$ grew into the grains along $\langle 110 \rangle$ directions parallel to the twin plane. The nucleation was suggested to occur at an early stage on the non-coherent boundary, which consists of an array of Shockley partial dislocations. They also considered the possibility of growing particles repelling some of the partial dislocations or nucleating new dislocations at the interface. These would glide along $\langle 110 \rangle$ and further precipitation could occur on them, i.e. in the grain.

2.4.2.3 Matrix Precipitation of $M_{23}C_6$

Broadly there are two types of intragranular precipitates of $M_{23}C_6$ that can occur in austenite matrices.[48,74]

(i) Stringers of carbides
(ii) Widmanstatten precipitation

The stringers of carbides have been observed to nucleate on dislocations which have been "grown in" or formed during the quench[74]. During the growth of $M_{23}C_6$, dislocations, by the "prismatic punching" mechanism, are generated due to the large atomic volume of $M_{23}C_6$ compared with the parent austenite, and these newly generated dislocations may act as sites for further nucleation of $M_{23}C_6$.[69]

The second type of precipitate has been observed to appear as dot like particles, which give rise to coherency strain contrast in the matrix.[48] As the particles grow along $\langle 110 \rangle$, they loose coherency and lead to the formation of a Widmanstatten type structure. The presence of vacancies has been said to play an important role in the formation of such precipitates, because regions near the grain boundaries have been noticed to be free from such precipitates; grain boundaries being a good source of vacancy sinks, decrease the nucleation sites for the initial dot like particles.

The amount of precipitate largely depends upon the amount of carbon in solution and the time and temperature of ageing. For both types of $M_{23}C_6$ precipitates the orientation relationship with the matrix is:-

$$(111)_{M_{23}C_6} \parallel (111)_\gamma \quad \text{and} \quad [110]_{M_{23}C_6} \parallel [110]_\gamma \quad [48,74]$$

2.4.2.4 $M_{23}C_6$ Precipitation on Coherent Twin Boundaries

The amount of $M_{23}C_6$ precipitation on coherent twin boundaries is far less than observed on grain-boundaries or incoherent twin boundaries.[69] Nucleation of $M_{23}C_6$ on coherent twin boundaries is thought to be as a result of

dislocations present in the boundary plane. Nucleation proceeds after long ageing times, and growth takes place more rapidly at higher ageing temperatures. Straining the alloy, or increasing the dislocation density at coherent twin-boundaries, causes the amount of precipitation to increase. Generally, in an unstrained matrix, dislocations are produced during quenching and can be held up at such boundaries. The precipitates have a parallel orientation relationship with the matrix. Growth of $M_{23}C_6$ on coherent twin-boundaries is attributed to the role of vacancies in the precipitation process. It has been shown[69] that coherent twin boundaries could act as sinks for vacancies and hence provide a flux of vacancies to the boundary. $M_{23}C_6$ needs vacancies for growth to reduce the strain energy, due to its greater atomic volume compared with parent austenite.

2.4.2.5 General Precipitation Sequence

First carbides precipitate at junctions of three grain-boundaries and fan out from there into the adjoining boundary surfaces, becoming coarser and thicker as the annealing time increases.[21]

Subsequent precipitate sites are high angle boundaries, at first as individual particles of uniform size and shape.[74] At later annealing stages, the particles grow together and form lacy sheets of single crystal orientation, and sheets in adjacent grain-boundaries are joined by coarser precipitates in the junctions.

While precipitation in high angle grain boundaries is in progress, carbides start to precipitate on incoherent twin boundaries, in the shape of long ribbons composed of bands and rods in parallel arrangement.[21] The initial carbide gradually transforms into fibres of $M_{23}C_6$.

The last stage of precipitation is carbides in the matrix and coherent twin boundaries.[74]

2.4.3 TiC Precipitation

Precipitation of TiC in austenite has been observed by a number of workers, and depending upon the super-saturation different precipitating sites have been observed to be favourable in various alloys.[31] If the super-saturation

is low, the grain-boundaries are preferred as nucleating sites and sometimes dislocations also. But if the super-saturation is high an intense general precipitation has been observed, usually on defects of the matrix.(75)

Generally, TiC has been observed at grain-boundaries if the Ti:C ratio is very high. Because of the slow diffusion rate of Titanium, TiC also forms more readily at higher ageing temperatures(69). TiC particles at grain-boundaries have usually a parallel orientation with one grain. There is no great evidence for TiC being formed at incoherent twin boundaries and there is no adequate explanation for this effect.

As regards the precipitation of TiC in the matrix, dislocations are the most favourable sites, and precipitation occurs by Ti atoms segregating to the dislocation core in order to relieve the strains.(69, 75) The vacancies required for the growth of TiC are obtained by the climb of dislocations on which the precipitates have formed. The TiC particles can be seen in the form of strings in creep resisting alloys and the preference of these precipitates to nucleate on the dislocations has been attributed to their smaller unit cell, which is likely to need less surface energy to form stable nuclei.(75)

Sometimes the TiC particles are not all taken into the solution at the solution treatment temperature. The residual particles have a lower co-efficient of thermal expansion than the matrix and therefore on quenching after solution-treatment, dislocations are produced in the matrix near such particles; and these dislocations act as sites for TiC nucleation.(69)

Another important site for the precipitation of TiC in austenitic stainless steels is associated with the stacking faults. The only difference between stacking fault precipitation and matrix precipitation is that the matrix precipitate nucleates on vacancies or dislocations whilst stacking fault precipitates nucleate on partial dislocations.(76) The general reaction to create a stacking fault in f.c.c. matrix is by the dissociation of pre-existing dislocations into

partial dislocations, one at each end of the fault. It has been reported that stacking faults grow at the same time as TiC is nucleated,[75] although there are disagreements over the growth of the faults.[31] The partial dislocations have been said to move away from the particles either as a result of elastic repulsion when the particle reaches a critical size, or by climb which is achieved by the flow of vacancies to the partial dislocations.

2.4.4 Combined $M_{23}C_6$ and TiC Precipitation

In alloys where there is a possibility of formation of both $M_{23}C_6$ and TiC, $M_{23}C_6$ is formed first, but on prolonged ageing at high Ti:C ratios TiC can also form together with $M_{23}C_6$ at grain-boundaries.[69] $M_{23}C_6$ is more likely to be formed first because of the rapid rate of diffusion of chromium compared with titanium, but on prolonged ageing the stronger carbide forming elements such as Ti predominate .

The intragranular precipitation of TiC and $M_{23}C_6$ is greatly affected by the amount of titanium in the matrix, and generally occurs in alloys having a hyperstoichiometric ratio of Ti:C.[69] When this condition is not fulfilled, $M_{23}C_6$ precipitates in preference to TiC, especially on dislocations. However, if the above condition is satisfied, TiC, having a much smaller unit cell than $M_{23}C_6$, would be energetically favourable and expected to form more readily on dislocations.[31] Also, precipitation of TiC can occur at stacking faults.

2.4.5 Precipitation of γ'

In general, if the Ni content of alloys is of the order of 15-30% and with the normal Al and Ti additions of upto 4% of each element, the Ni/(Al+Ti) ratio is sufficiently high for γ' precipitation to occur.[39] Although the lattice parameter of the matrix changes slightly with small changes in composition, the difference in lattice parameter between γ' and matrix is very slight, generally not more than 0.5%[30].

Precipitation begins with the usual zone formation, coherent

with the matrix, and the normal growth mechanisms operate. Generally, in the case of a completely coherent precipitate and smaller particles, the process of coarsening has been reported to be diffusion controlled.(77) Although for semi-coherent interfaces, a simple ledge-growth mechanism has been proposed(78), it is argued that it may not necessarily be operative for coherent interfaces.(77)

Usually γ' has very small matrix misfits, but however, small this difference may seem, it creates considerable internal strain during the period of coherency, when the lattice of the matrix is forced to conform to the lattice of the precipitate.(30) The coherent particles have been reported to have symmetrical hexagonal dislocation networks at the interface, which along with the particle dimensions, have been regarded as the major factor controlling the loss of coherency between the particle and the matrix.(79) Although there have been three different mechanisms suggested for the loss of coherency of a growing particle, in the case of γ' it has been shown that coherency is lost by the absorption of matrix dislocations at its interface.(79) The operative mechanism in the case of γ' has been described by the interaction between the strain field of the dislocation and the elastic strain field of the precipitate. The precipitate is effectively metastable with respect to the dislocation if r is $> r_{critical}$ where:-

$r_{critical}$ = radius of the particle below which a precipitate cannot support a dislocation loop at its interface.

and r = actual radius of the particle at a particular stage of ageing.

The shape of the γ' precipitate depends largely upon the matrix/particle misfit.(14) The shape can be either spherical or cubic and in most cases when the misfit between γ' and austenite is quite small, a spherical precipitate is formed, which in general shows a very slow rate of growth, and has a cube-cube orientation relationship with the matrix.(30) Systems with misfits around 0.5% are at the critical stage where coherent particles can either be cubic or spherical.

The shape is also controlled by the size of the particle, although the misfit can be altered by small changes in matrix solute during ageing. Particle dimensions can also contribute to this parameter to a large extent, thereby showing the importance of particle size.[77]

2.4.5.1 Precipitation Sites for γ'

It is widely known that nucleation of solid state transformations occurs on lattice defects due to the release of the excess free energy as well as reducing the total interface energy required[80]. Some of the accepted sites of precipitation for γ' are:-[69]

a) Intragranular precipitation and
b) Precipitation on dislocations

Homogenous nucleation of γ' takes place in the absence of any pre-existing defect in the matrix, as reported by Saito and Watanabe.[81] On further ageing, ordered zones were produced by the emission of vacancies. Wilson and Pickering[41] examined the early stages of ageing of an austenitic steel which precipitated γ' and reported the hetrogeneous nucleation of γ' on pre-existing lattice defects. Recent work[82] on PE16 reports the quenched in-vacancies as the controlling factor for γ' nucleation, and also shows that the γ' particle is a vacancy source in the alloy. An increased vacancy emission was observed at the particle - matrix interface, which could increase the rate of nucleation for further precipitation.

Precipitation of γ' occurs on dislocations,[69] and nucleation has been considered for both the coherent and incoherent case[82]. In the case of incoherent nuclei an equilibrium phase will be formed, and in the case of coherent nuclei a transition phase may be the result. Nucleation may, however, be suppressed near dislocations if the precipitate has little or no misfit strain and has a higher shear modulus than the matrix, because a hard precipitate increases the strain energy associated with a dislocation. Under certain

conditions, nucleation can occur preferentially on dislocation of the edge type.[80] Dollins[83] recently presented a treatment for nuclei forming not on a dislocation line but in its vicinity, due to the catalytic effect exerted by the dislocation core.

2.4.5.2 Effect of Al and Ti Content on Precipitation of γ' in Austenite

The effect of these alloying additions on γ' precipitation can be summarised as follows:-

a) Effect of Ti

In austenitic steels containing Ti only, the rate of overageing is rapid due to the formation of cellular precipitate of Ni_3Ti when the Ti content exceeds 3%.[33] In Ni-base superalloys, the compound Ni_3Ti, usually designated eta, has a h.c.p structure in contrast to the f.c.c. of the austenite matrix. This precipitate is f.c.c. during the period of coherency with the f.c.c. matrix, but precipitates as particles of second phase which have either the h.c.p. (normal, lowest energy) or f.c.c. abnormal structure.[30] As precipitation continues the f.c.c. γ' form of Ni_3Ti phase dissolves and is replaced by the h.c.p. form. Ageing at lower temperatures allows more of the f.c.c. to be precipitated than does ageing at higher temperatures. Ni_3Ti is considered to be undesirable because it has no solubility for other elements and adheres closely to the stoichiometric composition.

b) Effect of Al

It has been observed that a relatively small amount of age-hardening is produced by Al alone in both austenitic steels[39] and Ni-base superalloys.[48]. In austenitic steels containing 25% Ni-15Cr and more than 1% Al, the age-hardening response increased, but not to a great extent. The effects of precipitatic were complex, and there was evidence that γ' was formed.[84] In Ni-base superalloys the lower intensity of age-hardening was attributed to the lower stresses associated with the γ'

precipitation containing only Al. However, there is evidence that increasing Al in austenitic steels increases the tensile strength and 0.2% P.S. but decreases ductility and impact values.[84]

c) Effect of (Al + Ti) added together

In Ni-base superalloys, the presence of both (Al + Ti) increases the hardness considerably.[85] The γ' phase is capable of taking a considerable amount of other elements into solution, namely Cr, Ti and Co. Grant et. al[85] have shown that up to 65% of the Al atoms in Ni_3 Al can be replaced by Ti. Many details are uncertain, but γ' is generally designated as Ni_3 (Al.Ti). Investigations have also revealed solubility for other elements, which results in a greater volume fraction of γ' than could be possibly formed if the composition were simply Ni_3 (Al.Ti).

In austenitic steels containing 25% Ni-15 Cr, the amount of ageing was greater in (Al + Ti) steels than could be obtained with a single addition of similar amounts of Al or Ti.[84] With low Al contents the presence of Ti changed the precipitate from Ni Al to Ni_3 (Al.Ti), so the Ti caused b.c.c. precipitate to be replaced by the f.c.c. precipitate. It is well known that the Al/Ti ratio plays a dominant role in the type of precipitate formed and its orientation relationship with the matrix.[33] In austenitic steels having Al/Ti ratios $\sim$ 2.6, the over-aged precipitate was b.c.c. Ni(Al.Ti). However, Hughes found that on decreasing this ratio to about unity the overaged precipitate was Ni_2Al Ti and with a further decrease in Al/Ti ratio, Ni_3 (Al.Ti) was found to be the over-aged precipitate but no Ni_2 Al Ti was observed.

In a report on a series of alloys having different Al/Ti ratios, and base composition of nimonic PE16,[87] an Al/Ti ratio of unity was found to produce the best age-hardening characteristics. This is because the misfit between γ' and the austenite matrix increases with increased Ti (which replaces Al in the γ') because of the larger atomic size of Ti compared with Al.[39,40] But the misfit is not as high with

Ni_3 (Al.Ti), compared with Ni_3Ti, and because of its slightly lower misfit with the matrix the rate of growth of γ' is very slow and overageing is also slow. This is considered desirable for high temperature applications.[30, 39]

2.4.6 Combined Precipitation of $M_{23}C_6$ and γ'

Different heat treatment sequences have been developed to precipitate both $M_{23}C_6$ and γ' in the same matrix, to obtain the beneficial effects of both phases.[68] In both austenitic steels and nimonic alloys a denuded zone has been observed, between the carbides at the grain-boundaries and γ' in the matrix.[30,37,69] Two mechanisms have been proposed for the formation of precipitate free regions, namely: a) solute depletion, b) vacancy depletion.[88] In the solute depletion mechanism, it is proposed that under ageing conditions in which the rate of nucleation and thickening of the $M_{23}C_6$ grainboundary precipitate is much greater than that of the intragranular γ', the growth of the grain-boundary precipitate depletes the adjacent regions of solute, relieving solute supersaturation, and thereby causing γ' in this region to dissolve.[30] In the vacancy depletion mechanism, it is postulated that in the region adjacent to the grain-boundaries, during the quench from solution treatment, excess vacancies migrate to the grain-boundaries, which serve as effective sinks for vacancies.[89] The resultant diminution in vacancy super-saturation effectively prevents, in these regions, the formation of vacancy loops and helical dislocations which often serve as the heterogeneous nucleation sites required for intragranular precipitation of γ'. Thus, by this vacancy depletion mechanism, a precipitate free but solute rich region is produced in the vicinity of the grain-boundary. However, these processes can be competitive and both occur simultaneously during the ageing of an alloy.[88] Therefore, depending upon the activation energy for solute diffusion and vacancy migration, it should be possible to predict the mechanism which dominates in a particular system, for a particular heat-treatment.

2.5 COLD WORK, RECRYSTALLIZATION AND PRECIPITATION

Precipitation phenomena are often affected by the maximum cold-worked hardness of the alloy, although the increment of hardness during ageing may be less than in the cold-worked alloy.[3] Typical curves of hardness against time of ageing at a fixed temperature, for different degrees of deformation for a nimonic alloy, can be seen in Fig. 2.[90] The effect of cold-work on the kinetics of ageing is very complex, generally the rate of hardening will depend upon the type of precipitate present and kinetics of precipitation in the undeformed structure.[91] The effect is said to be complex because a super-saturated and a deformed solid solution contains dissolved atoms and lattice defects, which are not in thermo-dynamic equilibrium, giving rise to a situation where precipitation of a second phase and the recrystallization of the deformed grains have a mutual influence on each other. Relatively little work has been done on the effect of cold work prior to ageing on precipitation hardened austenitic steels, thus the literature cited is very limited.

2.5.1 Nucleation Mechanisms of Recrystallization

The classical nucleation theory of conventional phase transformations was applied by a number of workers[92-94] to discuss the general mechanisms of recrystallization. The transforming phase (α) was represented by the strained metal and the newly formed phase (β) by the strain-free (recrystallizing) regions. It was suggested that on isothermal annealing, the strain-free regions equal to, or greater than, the critical size for stability, would form a viable nucleus to grow into the matrix surrounding it, and the total free energy change was represented by the difference in the strain energy between the cold worked and the fully recrystallized states. On this basis, it was shown that the incubation period observed during isothermal annealing was the average time required for a series of thermally activated fluctuations to give rise to the creation of viable strain free regions as nuclei for recrystallization.

Although the theory accounts for the existence of an incubation period and also predicts feasible values of the nucleation frequency, if it is assumed that nucleation occurs preferentially in regions of locally high strain (which is in accord with the experimental observations), the main objection has been that it is highly unlikely that nucleation actually occurs by homogeneously distributed, thermally activated fluctuations within the deformed metal.[95]

There have been various other mechanisms proposed to account for the formation of recrystallization nuclei, and most of these theories relate the nuclei formation to the original cell structure, produced during deformation. Some of the mechanisms proposed are outlined as follows:-

a) Polygonization

The basic theory of polygonization was first put forward by Cahn[96] and Beck[97] independently, involving dislocation free subgrains, one of which would become a viable recrystallization nucleus. The process is said to be operative in matrices where deformation creates a structure containing an excess of one type of dislocations, e.g. edge.

The mechanisms involved during annealing treatments are the gliding of dislocations in their slip planes, then climb, and arranging themselves to form segments of low angle tilt boundaries. Such boundaries then exert a small force on isolated dislocations some distance away to join the original segment. Ultimately the polygonization is said to progress by merging of pairs of adjacent segments thus giving a somewhat longer boundary which is still of a low angle tilt type.

The driving force for the segment formation has been said to be the lowering of the overall strain energy c.f with the more random dislocation arrangement existing before annealing.[96] Also, the driving force reponsible for the segment merger has been attributed to the reduction of boundary energy per dislocation (within the boundary) as the number of dislocations in the boundary increases, thereby increasing the misorientation

at the same time. Although the energy per dislocation in the boundary is reduced, the total energy of the boundary is increased, and that of the regions away from the boundary is decreased, by the conversion of the deformed structure to the polygonized one, thereby making the process energetically favourable.[97] Since dislocation climb is said to be an essential feature of the mechanism of polygonization therefore the process is said to be operative easily in matrices having a high stacking fault energy, such as some austenites.[95]

b) Sub-grain formation mechanisms

The basic difference between the polygonized grains and substructure is that polygonization occurs during annealing, where as subgrains form directly during cold-work and it is this substructure which coalesces to form a viable nucleus for recrystallization during annealing.[95] Although there are two different models developed for the coalescence of these subgrains, the model dealing with coalescence by rotation is said to be more viable than the geometric coal - escence model.[95]

The mechanism involved is the elimination of a common boundary between two misoriented subgrains by the rotation of one of the subgrains, and this is possible by the diffusion of atoms along the sub-boundaries.[98] Thermodynamically, the controlling factors for the process are the misorientation angles of these sub-boundaries and the energies associated with them. It has been shown that such a process is essentially a low-angle boundary phenomenon, and therefore occurs in regions where such boundaries exist in abundance, and the local misorientations are very large, such as in the vicinity of a grain-boundary or a deformation transition band.[95] Finally, the energy for sub-grain coalescence comes from the difference between the high energy of a dislocation in a low angle boundary and the lower energy associated with the higher-angle boundary.

c) Grain-boundary bulging mechanism

This was one of the early theories of recrystallization first put forward by Beck et. al,[99] and introducing the strain

induced boundary migration model. In this a length of grain-boundary bulges out into a neighbouring grain and leaves a strain free area between the boundary and the remaining deformed grain. These strain free areas were said to be the nucleation sites for recrystallization.

In the model it is assumed that the boundary between two deformed grains is capable of high mobility by virtue of large misorientation between the two parent grains, and secondly there is a significant strain difference in the two original grains because of different sub-grain sizes. Under these circumstances the boundary migration may be initiated by that part of the grain-boundary length which forms a boundary with one of the large sub-grains in the lesser strained grain, and the direction of migration occurs away from this less-strained grain into the more heavily strained grain. The basic driving force has been attributed to the difference in the stored energy for the two grains.(95)

2.5.1.1. General Comparison of Nucleation Mechanisms

The basic requirements, as observed by many workers, have been summarised by Mould and Cotterill(95) by saying that a viable recrystallization nucleus must be a relatively large region having an orientation similar to the same region in the deformed state, but being surrounded (at least partially) by a high misorientation, relative to its immediate surrounds, all within a wider region of generally high local misorientation.

This general description is taken into account by all the three models discussed earlier, but all these models are, 'variations on the same theme', in the very generalised sense that they describe possible ways in which a sub-grain, existing in the deformed state, can develop selectively until it becomes a viable recrystallization nucleus. The distinction between them is the specific way in which this development occurs.(98)

Generally, it is felt that the grain-boundary bulge mechanism is operative at low deformations, since the mechanism requires the presence of a significant stored energy

difference (i.e. a significant dislocation density difference) between the grains on either side of the relevant boundary, [100, 101] and such a condition is satisfied by the original boundaries of pre-deformation grains at low deformations. However, as the amount of cold-deformation is increased the general distribution of dislocations becomes more homogenous producing increasing misorientations within the original grain-interiors. Consequently this results in the preferential development of some selected sub-grains in order that they might acquire the misorientation appropriate to them becoming a viable nucleus.[101] Such development is likely to occur either by polygonization or by coalescence.[95] But the direct formation of viable nuclei by polygonization is now thought to be a much less widespread possibility, because of certain ideal conditions which are necessary such as an excess of edge dislocations etc., yet it remains an important mechanism in cases where a small number of slip systems have been involved in the deformation process.

Therefore, one of the major, and above all the most important process is the coalescence of sub-grains, although the final details on the actual mechanism still remain uncertain, mainly because of a much slower rate of recrystallization postulated by this theory than is actually observed in experiments.[98] It had been suggested that both the grain-boundary bulging mechanism and sub-grain coalescence operated in high nickel-high chromium austenitic steels, at different deformation levels.[102] But, later work by Baker et al[103] on 20 Cr - 25 Ni - Nb steel concluded that even after light deformations recrystallization occurred by sub-grain formation at original grain or twin boundaries, and after moderate and heavy deformations nucleation started at dislocation cells and deformation bands within the parent grain interiors. Therefore, there is still some doubt about the basic mechanism operating at a particular deformation level, and where exactly can be drawn a line between light and moderate deformations.

Lastly, in the case where the degree of deformation is most severe ($\sim$90%), there is a possibility of individual sub-grains acting as viable nuclei without any further development

as a sub-structure, and the final mechanism proposed has been the same as in the case of the coalescence model.[95]

2.5.1.2 Factors influencing primary recrystallization

There are three basic factors which influence recrystallization, namely:-[95]

a) Internal strain induced by deformation
b) Microstructural variables such as grain size, twin frequency, etc.
c) Specimen thickness

a) Deformation The concept of a recrystallization limit has been defined as the lowest temperature which produces complete recrystallization for a specific metal and condition, and this particular concept has been used to illustrate the effect of deformation on recrystallization[95] On the basis of this property there is a minimum strain below which recrystallization does not occur, and increasing the strain above this limit lowers the temperature of recrystallization. The variation of the recrystallization limit with strain has been interpreted in terms of variations in the rates of nucleation and growth and their activation energies. Generally, for small deformations the nucleation rate is low and rises steeply as the deformation increases, where as the growth rate increases rapidly at small strains and remains constant at greater deformations. In other words, the activation energy for nucleation is much greater than that for growth, corresponding to a low nucleation rate and a relatively high growth rate at lower strains. The activation energy for nucleation decreases at higher strains and growth is slightly decreased merely because of a large number of nuclei present which gives a lower overall grainsize. But it has been said that above a particular deformation($\sim$20%), the activation energies for nucleation and growth are approximately equal and each decreases in a similar manner with increasing strain above this limit.[95]

b) Grain size and twin frequency

The original grain size of the metal influences recrystallisation by influencing the overall dislocation density (i.e. the stored energy) of the deformed metal, which also leads to variations in the amount of grain-boundary regions (ie. the area) at which the nucleation can occur.(95) Generally the critical strain increases as the grain size increases, and for a given strain, the recrystallized grain size is finer, the finer the origina grain size.

The effect of grain size variations is generally pronounced at low strains (~ 40%) and the recrystallization phenomena are not greatly altered by such variations at higher deformation. This is because at higher deformations the dislocation density (i.e. stored energy) becomes more homogenous, and the differences in grain-boundary area/unit volume have a less marked effect. Consequently the recrystallization parameters become less dependent on the original grain size.(95)

The presence of twins within the grains has a similar effect t that of increased grain-boundary area(95).

c) Specimen Thickness

Generally, as the specimen thickness decreases, recrystallization is delayed, because of vacancy diffusion along grain-boundaries to specimen surfaces, thereby hindering the grain-boundary mobility and hence recrystallization.(62,95) The opposite effect has been attributed to the surface tension forces for grains of varying orientations, which increases the boundary mobility.(95) Therefore it is quite probable that the recrystallization behaviour of bulk specimen and a thin specimen of the same material under similar conditions may be quite different.(95)

2.5.2 Separate and Combined Effect of Precipitation and Recrystallization

Two important accounts of such conditions have appeared in the literature, earlier by Kreye et. al[104] and later on more generalised behaviour by Koster[105]. Both deal with recrystallisation involving a second phase. Kreye et. al[104] studied the effect of continuous and discontinuous precipitation on the recrystallization of a super-saturated Ni-base solid solution. They considered three possible cases:-

a) Recrystallisation starts well before precipitation
b) Recrystallization and precipitation occur at the same time.
c) Precipitation starts prior to recrystallization

All these three cases are greatly affected by a fourth variable, i.e. temperature as shown in Fig. 3[104]. To understand the mechanisms operating in different types of precipitation hardened alloys, it will be necessary to consider the basic mechanisms of precipitation of an undeformed alloy and the recrystallization behaviour of a pure deformed metal.

i) There are two types of precipitation mechanisms namely, discontinuous precipitation which occurs by nucleation of grain-boundary particles with a reaction front moving into the super-saturated solid solution, and continuous precipitation, where the second phase nucleates as small particles, which are statistically distributed in the matrix. The kinetics of the precipitation reactions are very much temperature dependent and it requires an incubation time (t_p) to create a driving force(P_c) necessary for the precipitate to form in an undeformed matrix.

$$t_p = A(c) \exp \frac{Q_{B+\Delta G(T,C)}}{RT} \qquad \ldots\ldots\ldots (32)$$

where t_p = annealing time until the start of precipitation, A is a pre-exponential factor which includes the driving force of the reaction, the entropy term, and a geometrical factor, c is the concentration of the alloying element,

R the gas constant, T the temperature in°K, Q_B is the activation energy for diffusion of dissolved solute atoms, and $\Delta G(T,C)$ is the activation energy for the nucleation of the second phase. The driving force, P_c, results from the decrease in free energy per unit volume during the reaction. For discontinuous precipitation the values will be given by the driving force per unit area of the reaction front:-

$$P_c \simeq \nu RT \ln \frac{C_1}{C_o}$$

ν = mole fraction of precipitate,
R = gas constant
C_1 = super-saturated solid solution concentration
C_o = equilibrium concentration

Similarly there are two types of recrystallization, but the predominant type is discontinuous recrystallization in which the structural defects produced by deformation are annihilated by a grain-boundary which moves as a reaction front. Such a front can be a grain-boundary which has been present before deformation. On the other hand during continuous recrystallization (in-situ recrystallization) the original and newly formed grain-boundaries are pinned by precipitating particles. They cannot move as a reaction front. Annealing out of dislocations takes place by rearrangement to form net-works and sub-boundaries which finally can lead to the formation of high angle boundaries. The recrystallization reaction is described by:-

$$t_R = B(N) \exp - \frac{Q}{RT} \qquad \ldots\ldots\ldots (33)$$

t_R = time for incubation,
B = is the driving force which includes the driving force for the reaction and the geometrical factor,
N = is the dislocation density
and Q = is the activation energy for the start of recrystallization, which decreases with increasing dislocation density or increasing cold work. For discontinuous recrystallization,

Q is of the order of magnitude of self diffusion, Q_o. This value, however, can be increased by more than one order of magnitude by segregation of impurity atoms, or by preferential precipitation of particles at dislocations, i.e. in continuous recrystallization[105]. The driving force P_N is given by:-

$$P_N = \alpha \mu b^2 (N_1 - N_2)$$

where α is a constant, μ = shear modulus, N_1 and N_2 are dislocation densities before and after recrystallization and b is the burger vector.

(ii) To understand the combined effect of recrystallization and precipitation, the following factors have to be taken into account:-

(a) Retardation of dislocation movement by already precipitated particles.
(b) Interaction of particles with grain-boundaries
(c) Changes in precipitation behaviour due to defects introduced by plastic deformation.

Kreye et al.[104] made an assumption in the case of nickel base alloys that the continuous precipitate of γ' is coherent with the matrix, so that there are only small lattice strains in the neighbourhood of the particle. Thus they concluded that deformation of super-saturated solid solutions does not measurably influence the precipitation behaviour. This assumption may or may not be true depending upon the type of alloying additions, which in effect are going to alter the misfit between the precipitate and the matrix.

(iii) The kinetics of the processes of recrystallization and precipitation can vary independently by changing the defect concentration or the supersaturation, taking into account equations (32) and (33) and Fig. 3 [104].

a) If $t_p >> t_R$, annealing out structural defects occurs in the whole temperature range before precipitation; both processes do not influence each other.

b) If $t_p \simeq t_R$, below a certain temperature T_1, a mutual influence of both reactions occurs. This general case can be caused by lowering the density of defects or increasing the supersaturation.

c) From the temperature dependence of t_p and t_R, three temperature ranges can be identified in which different phenomena can be expected, Fig. 3 .

(i) If $T > T_E$, recrystallization occurs without precipitation. In this range the structural defects which are present at the start of precipitation can change the precipitation kinetics.

(ii) If $T_E > T > T_1$ recrystallization followed by precipitation will be expected. But the precipitation behaviour will not be altered because most of the defects will have annealed out by the time precipitation begins.

(iii) If $T < T_{11}$, continuous recrystallization will occur, because of the pinning effect on boundaries by discontinuous precipitates, and defects only anneal out by a continuous process.

2.5.3 Influence of Cold Work on Precipitation Kinetics

2.5.3.1 Effect on Zone Formation

Cold work can only affect the kinetics of zone formation if the zones are formed on the dislocations.[32] The concentration of vacancies introduced by severe plastic deformation is much less than the concentration introduced by quenching from high temperatures. Reports suggest that quenched in vacancies are the controlling factor for the nucleation of zones[82]. Also resistivity measurements have shown that cold-work has no effect on the initial rate of ageing of a rapidly quenched specimen, but that the rate of

decay of vacancies is increased because of the dislocations introduced by plastic deformation which act as vacancy sinks.(32) Thus it is indicated that the initial rate of zone formation is not affected, but the zone size is limited because of less vacancies available for growth.

On the other hand precipitation of γ' on dislocations has been reported,(69) and Dollins(83) presented a treatment for nuclei of γ' forming in the vicinity of dislocation line, due to core diffusion. Therefore, considering this treatment, the initial rate of nucleation should increase with increasing cold-work (i.e. more dislocations). It suggests that the situation is far from clear in the understanding of the actual behaviour of cold-work on the initial zone formation.

2.5.3.2 Effect on intermediate precipitates

Many workers have shown that cold work prior to ageing increases the rate of nucleation of an intermediate phase.(32) In an alloy which is hardened by zone formation, cold work prior to ageing will cause rapid softening. On the other hand an alloy which can be hardened by the precipitation of a fine dispersed intermediate phase will show rapid and increased hardening when deformed before ageing.

Investigations on Rene 41 and some Ni-Al alloys have shown that the morphology of γ' is not altered by dislocations introduced by cold work prior to the ageing treatment.(91) Little work has been done on the rate of initial hardening and the final hardness in comparison with non-deformed specimens. Kreye et. al(104) have reported that with increasing amount of γ' forming elements, retardation of the start of recrystallization occurred in Ni-Al alloys.

2.5.3.3 Effect on Carbide Precipitation

It is quite evident from various investigations on the effect of cold work on carbide precipitation in an austenite matrix, that ageing intensifies the precipitation of carbides such as $M_{23}C_6$, M_7C_3 etc. (68,90,91). In Rene 41 the dislocatio

networks provide favourable nucleation sites and the density of dislocations was so great that grain-boundaries were difficult to detect.[91] The intensity of precipitation increased with increased amount of cold deformation. Investigations on a Ni-base super-alloy showed that for all ageing conditions smaller amounts of precipitation were observed on the grain-boundaries compared with the undeformed material, but a greater quantity of more uniformly distributed carbide was precipitated inside the grains.[90]

Popov et al[106] studied the effect of deformation on the precipitation of $M_{23}C_6$ in an austenitic steel and noticed that all the $M_{23}C_6$ was precipitated inside the grains at defects which had been introduced into the metal by plastic deformation. The preferred nucleation site varied according to the degree of deformation. Particles mostly appeared on dislocations and on non-coherent twin boundaries. The defect structure was observed to give a periodic arrangement of precipitates in certain crystallographic directions of the matrix, and this type of structure is called a modulated structure. In the undeformed structure, $M_{23}C_6$ precipitation was not arranged in this way, so it was concluded that defects in the crystal introduced by deformation prior to ageing, have crystallographic ordering[106]. There are three main variables which affect the structure and morphology of carbides, namely:-

(a) the amount of solute in the solution
(b) the degree of deformation
and (c) the time and temperature of ageing

In the case of dilute alloys, cold work can suppress the precipitation if the increased dislocation density is sufficient to cause most of the solute atoms to form atmospheres at the dislocations and hence reduce the super-saturation in the matrix. This phenomenon has been found in plain carbon steels[32] and is similar in principle to the detrimental effect of cold work in alloys containing trace additions. If the amount of solute and dislocations in the matrix are high enough, most of the solute may be precipitated out as is the case in austeniti steel, where the matrix can be almost denuded in carbon

because of precipitation of $M_{23}C_6$[106]. On further ageing the $M_{23}C_6$ particles were seen to grow, accompanied by the solution of fine $M_{23}C_6$ present in the matrix. The mean size of the particles increased with holding time according to:-

$$l = k.t^{0.33} \qquad \ldots\ldots\ldots\ldots\ldots (34)$$

where l is the mean particle size in A^o, t is the ageing time in hours and k is a coefficient related to the diffusion parameters. The growth of particles was observed to take place by bulk diffusion.

At very high ageing temperatures the deformed specimens show a breakdown in the dislocation structure, due to extensive rearrangement of the dislocations, which results in the rearrangement of precipitating particles more or less similar to that in undeformed specimens. However, the precipitation is more dense than in the undeformed structure.[106] At such temperatures the particles grow rapidly on coherent twin-boundaries and on slip bands, but those nucleated on individual dislocations increase very little in size due to less ready diffusion.

Prior to precipitation the structure can recover depending upon the degree of deformation. In Nimonic 75 no recovery was observed at lower deformations, but at very high deformation levels the recovery was so fast that the resulting matrix was similar to undeformed material.[90] Also as the amount of deformation increases the rate of softening increases.

2.5.4 Effect of Cold Work, in the Presence of a Fine Dispersion of a Precipitate, on Recrystallization and Further Precipitation.

This situation can arise in an alloy where certain stable carbides cannot be dissolved even on high temperature solution treatment. Such carbides are TiC, NbC or M_6C[54]. If an alloy containing second phase particles after solution treatment is plastically deformed, there are two possibilities for the behaviour of the particles.

(a) The dislocations in the matrix can shear through the particles. Due to the operation of many slip systems, and after a high degree of deformation, this can virtually lead to the solution of the particles.

(b) The particles may possess mechanical properties such that they can not be mechanically deformed.

The dispersion parameters of interest are the volume fraction of the precipitate f, the mean particle radius r, and the interparticle spacing. In the case of spherical particles the interparticle spacing is[107]:-

$$\Delta S = 0.554\ r \left(\frac{4\pi}{3f}\right)^{\frac{1}{3}} \qquad \ldots\ldots\ldots\ldots (35)$$

Brimhall et. al[53] summarised briefly the effect of cold work and annealing on the dispersed structure and found an unusually high and uniform dislocation density during the early stages of cold-work. The dislocation distribution after moderate amounts of cold-work was observed to be very random, but after severe deformation a crude cell structure appeared giving rise to the presence of distinct sub-grains.

In general, and independent of the alloy system, recrystallization is accelerated for a large interparticle spacing with large diameter particles, and retarded for a small interparticle spacing with smaller particle size[107]. Gladman et. al[108] examined the effect of several different carbides and nitrides and concluded that the interparticle spacing is the important factor in steels. They found that recrystallization was severely retarded when particles having diameters of the order of 0.05 microns (or less) were present at volume fractions in the range 0.05% to 0.10%. The retardation of recrystallization was said to be associated with a low nucleation rate and a stabilizing effect on the recovered sub-grain structure.

In general terms the effects have been explained by considering the bigger particles as a source of increasing dislocations density when the material is plastically deformed, thus giving arise to an increased driving force for recrystallization. The smaller particles have been said to hinder both

the rearrangement of dislocations and the formation of dislocation networks and mobile high angle boundaries, and the migration of these boundaries, so that recrystallization is retarded.[107,108] Depending upon the effect of particle size and distribution on recrystallization, the effects of precipitation during ageing should not be much different from those discussed previously.

2.6 HIGH TEMPERATURE PROPERTIES OF AUSTENITIC STEELS AND IRON BASE SUPERALLOYS

The properties of austenitic steels and Fe-base super-alloys are greatly affected by the service temperature of the component in which the alloy is being used. The room temperature properties of an alloy system are very different from their high temperature properties because the mechanism of strengthening the modes of fracture and of plastic flow are very temperature dependent. It would be unrealistic from the standpoint of structural stability, to study the properties of an alloy at temperatures much different from the service temperature. In this literature review, attention will mainly be focussed on the high-temperature properties, such as ductility and strength both in tensile and creep conditions, and the effect of different variables such as strain rate, microstructures and temperature on these properties.

2.6.1 High Temperature Deformation Mechanisms

The variety of defects, and the variety of ways in which they can move, gives a polycrystalline solid many distinguishable mechanisms by which it can flow - eight or more can be identified. At low temperatures dislocations glide, but at higher temperatures other mechanisms of flow are permitted; dislocations can climb as well as glide, grains slide over each other at grain-boundaries, vacancies diffuse,- all allowing a change in the shape of material, i.e. deformation. The flow mechanisms discussed here are predominantly those which operate at temperatures of $0.3T_m$ and above.

2.6.1.1 Combined Dislocation Glide and Climb

Above 0.3 T_m diffusion controlled mechanisms begin to contribute to flow and dislocations acquire a new degree of freedom i.e. they climb as well as glide. The material flow is generally associated with power-law creep and the deformation mechanisms are further divided into two subgroups with varying temperatures at moderate stresses, namely:-

(a) core-diffusion (at lower temperatures $>$ 0.3 T_m)
(b) lattice diffusion (at higher temperatures $>$ 0.6 T_m)

The basic operative mechanism of deformation is that of slip which in effect is controlled by dislocation glide.[29] But at higher temperatures a larger number of slip systems are available for deformation and thermally activated processes, like the occurrence of cross-slip, increase as the temperature of deformation is increased[109]. In practice the dislocation glide is limited by the presence of obstacles to slip, i.e. impurities, solute, other dislocations or precipitates; but at the higher temperatures mentioned above, processes such as core-diffusion and lattice diffusion of atoms and/or vacancies allows the gliding dislocations to climb if held up by obstacles.[10] Both these diffusion mechanisms for dislocation climb will be dealt with separately to visualize their importance at varying temperatures.

(a) Core Diffusion

It is known that at lower temperatures, transport of matter via dislocation core diffusion contributes significantly to the overall diffusive transport of matter, and may even become the dominant transport mechanism.[110] The contribution of core diffusion to high temperature deformation is given by defining an effective diffusion coefficient[29,111]:-

$$D_{eff} = D_v f_v + D_c f_c \qquad \ldots\ldots\ldots\ldots (36)$$

where D_v = vol. diffusion coefficient, D_c is the core diffusion coefficient, and f_v and f_c are the fractions of atom sites associated with each type of diffusion. The value of f_v is unity and the value of f_c is

determined by the dislocation density, ρ, since $f_c = a_c \rho$, where a_c is the cross-sectional area of the dislocation core in which fast diffusion is taking place. Although evidence for the effect of core diffusion being the only dominant mechanism for high temperature deformation is scarce, yet it has been shown to be a partially dominant mechanism of creep deformation in the temperature range of (0.5 - 0.6) T_m[111].

(b) Lattice Diffusion

On the basis of apparent activation energy changes with temperature it has been shown that at above 0.6 T_m lattice self-diffusion (D_v) is dominant in equation (36)[111]. At such temperatures the dislocation climb is controlled by the atom or vacancy mobility of the lattice as a whole, rather than by the dislocation core diffusion[29,111,112].

The general expression derived for high temperature deformation on the basis of dislocation glide and climb processes is given by[29,112]:-

$$\dot{\gamma} = \frac{A_s D \mu b}{KT} \left(\frac{\sigma_s}{\mu} \right)^n \qquad \ldots\ldots\ldots\ldots (37)$$

where A_s and n are material constants, D is the diffusion coefficient (usually the lattice diffusion coefficient, D_v but in the temperature range where D_c contributes to the effective diffusivity the overall value of D_{eff} is used instead of D_v), $\dot{\gamma}$ is the shear strain-rate, σ_s is the shear stress; and K and T stand for Boltzman's constant and temperature respectively. Although the intricate details of the exact temperature ranges for D_c and D_v remain uncertain, their effectiveness in controlling D_{eff}, i.e. $\dot{\gamma}$, has been clearly demonstrated[111]. Also at extremely high stresses the breakdown of power-law creep, has been attributed to the possibility of the creation of excess vacancies by plastic deformation, which increases D_v in the D_{eff} term, or the increase in dislocation density with increasing stress, which influences the $D_c f_c$ term in D_{eff}[111].

2.6.1.2 Non-Uniform Shear (Sliding)

Below about 0.3 T_m deformation occurs almost entirely

intragranularly and the presence of grain-boundaries leads to a strengthening effect.[113] At lower stresses, above 0.3 T_m, the flow becomes non-uniform, i.e. grain-boundary sliding is accommodated by power law creep, leads to sharp offsets at grain-boundaries and folds within the grains.[29] There are two points of view regarding the mechanism of grain-boundary sliding[109]. The first mechanism considers that shear takes place in a softened zone, present in each grain adjacent to the grain-boundary, that is created by subgrain formation along the grain-boundary prior to grain-boundary sliding. The more conventional viewpoint considers instead that grain-boundary sliding involves the relative movement of two grains along a grain-boundary surface by a shear translation along the common boundary[109,114]. Two types of translations have been identified. The first involves a minimum of non-homogeneous deformation near grain-boundaries, and sliding is confined to an extremely narrow zone about the boundary. In the second type, the translation occurs in the presence of intragranular slip involving a much wider deformation zone, and is often referred to as "Grain-boundary zone shear". Grain-boundary sliding involving both types is an important mode of high temperature deformation, particularly because of its prominent role in promoting the formation and growth of intercrystalline cracks and voids.[114]

The importance of grain-boundary sliding as a mode of deformation at high temperatures depends on its contribution to the total strain and on the inter-relationship between sliding and intra-granular deformation.[113] Usually associated with the phenomenon of grain-boundary sliding is the process of grain-boundary migration.[112] Initial sliding occurs in the immediate vicinity of the boundary, and with increase in time, the sliding gradually takes place over a zone of finite thickness. The material within the zone gradually shows evidence of progressive grain-boundary migration and grain distortion. More recent theoretical work by Ashby[115] developed a treatment for grainboundary sliding accompanied by grain-boundary migration without the change of boundary structure. The process assumes the concept of grain-boundary viscosity

and derives an expression on the basis of the Stokes-Einstein equation. It is said that applied stress raises the chemical potential of certain atoms in one grain and lowers that of those in another grain. Sliding is attributed to the flow of atoms from the regions of high, to the regions of low potential i.e the process being diffusion controlled. The boundary between the two grains is shown to constitute of two types of defects e.g. a boundary step and the boundary dislocation . The mechanism of sliding is said to involve the motion, in the boundary plane, of boundary dislocations and when they move they experience a viscous drag. When the dislocation density in the boundary plane is high, and nothing else impedes their motion, the atomistic and continuous models are said to coincide.

The diffusion during sliding and migration is again said to occur by two mechanisms i.e. lattice diffusion at higher temperatures and core or boundary diffusion at lower temperatures[29]. The power law followed by grain-boundary sliding is the same as in equation (37) except that the value of A_s is higher for sliding.

2.6.1.3 Diffusional Flow

At high temperatures (sintering temperatures) and at very low stresses polycrystalline materials are known to deform by the diffusional flow of matter from one set of grain-boundaries to another within it.[29] This flow requires that atoms (or vacancies) are detached from one set of the boundaries, diffuse through the grain or round its surfaces, and are attached to the other set of boundaries.

(a) Nabarro-Herring Type. It was first pointed out by Nabarro that at very high temperatures self diffusion within the grains of a polycrystalline material could cause the solid to deform under an applied stress, where the deformation was caused by a diffusional flow of matter within each grain away from boundaries where there was a normal pressure (or compression) and towards those where there was a normal tension.[11] Subsequently, Herring[117] presented a somewhat different

analysis for this process but arrived essentially at the same relation for the deformation rate. The Nabarro and Herring mechanism applies to polycrystalline metals in which all dislocation motion is assumed to be blocked and the grain-boundaries are assumed to be excellent sources or sinks for vacancies. In the presence of a stress normal to the boundary, the formation of vacancies is helped by the stress since it reduces the work necessary to form these vacancies.[113] The resulting equation for the total strain rate $\dot{\epsilon}$ is given by:-[115]

$$\dot{\epsilon} = c \frac{D_v}{KT} \frac{\sigma \Omega}{d^2} \qquad \ldots\ldots\ldots\ldots (38)$$

where D_v is the lattice diffusion coefficient, K and T are Boltzman's constant and absolute temperature, σ is the applied stress, d the grain size, c is a constant and Ω is the normal atomic volume.

(b) Coble Type Above a specific temperature, which is shown to vary inversely as the logarithm of the grain size, creep rates agree closely with the Nabarro-Herring equation, and the activation energy is identical with that for lattice self diffusion[115,116]. Below this temperature the activation energy was found to be near the value expected for grain-boundary self diffusion, and the creep rate was shown to vary inversely as the cube of the grain size, given by the equation[118]:

$$\dot{\epsilon} = c' \frac{D_B}{KT} \frac{\Omega \delta}{d^3} \sigma \qquad \ldots\ldots\ldots\ldots (39)$$

where K, T, σ, d and Ω are the same as in equation (38), but D_B is the grain-boundary diffusion coefficient, δ is the effective grain boundary thickness, and c' is a numerical constant. Therefore equation (39) suggests that grain-boundary transport of vacancies/atoms is the mechanism of high temperature deformation, where the flow of atom/vacancies occurs in the boundary separating the grains.

A more generalised treatment suggests that two diffusive

paths (i.e. lattice and grain-boundary diffusion) contribute in an additive way to the strain-rate and the expression for the strain rate takes the form[115]:-

$$\dot{\epsilon} = \frac{20\,\sigma\Omega}{KT}\,\frac{Dv}{d^2}\left(1 + \frac{\pi\delta D_B}{d D_v}\right) \qquad \ldots\ldots\ldots\ldots (40)$$

where all the variables in equation (40) mean the same as for equations (38) and (39)

(c) Interface-Reaction Control

The processes of diffusional flow by Nabarro-Herring and Coble creep assumes that the grain boundaries act as perfect sinks or sources of vacancies, and the rate of the flow is governed by the diffusion of vacancies from a source to a sink[119]. But mounting evidence suggests that the grain-boundaries are not perfect sources or sinks for most practical purposes, and the diffusional flow is not always diffusion controlled[29]. In practice such a situation is far more common where intentional carbide precipitation at the grain-boundaries is regarded as a necessary microstructural feature for most of the high temperature applications[4]. As pointed out by Ashby[115], vacancies cannot leave or join a boundary everywhere, and they can do so without changing the structure of the boundary only at the appropriate boundary dislocations i.e those dislocations in the boundary plane which can climb. When the motion of such dislocations is impeded, or their density lowered (as is done by carbide precipitation at the grain-boundaries), the boundary is said to be an imperfect sink or source i.e. diffusional flow by the Herring-Nabarro and Coble processes is then slowed or stopped. Such a process is said to be diffusional flow controlled by the interface reaction i.e. the dislocations present in the grain-boundary plane. In the mathematical model considered by Ashby[115,119] the rate of interface reaction depends on the planar density, ρ, and mobility, M, of suitable grain-boundary dislocations. Two separate cases have been considered, namely:-

(i) when the moving defect experiences a viscous drag, i.e. solute drag due to alloying, the final strain rate is given by:-

$$\dot{\epsilon} = \frac{10\ D_v}{KT\ d^2}\ \frac{\rho\, b_n^2 M}{\Omega}\left\{\frac{1}{(\rho\, b_n^2 M\Omega) + (5\ D_v/KTd)}\right\}\Delta\mu \quad \ldots\ldots (41)$$

where b_n is the relative normal displacement of two grains when one defect sweeps across the boundary separating them, and rest of the parameters mean the same as for equation (38), and $\Delta\mu$ is the difference in the chemical potential of a vacancy at a grain boundary under normal tension to that of a vacancy at a boundary under compression, (caused by the stress and is given by $\Delta\mu = 2\sigma\Omega$).

Two limiting results follow. When M or ρ, or the grain size, d, are large, or the temperature, and thus D_v, is small, the creep rate is diffusional controlled. Equation (41) reduces to equation (38) or, for boundary-diffusion to equation (39). But under the opposite set of conditions, the interface reaction becomes rate limiting, and equation (41) reduces to:-

$$\dot{\epsilon} = \frac{\rho\, b_n^2 M\ \sigma}{d} \quad \ldots\ldots\ldots (42)$$

There is every possibility that the density, ρ, of defects may increase with stress; the linear relation between $\dot{\epsilon}$ and σ is then lost.

(ii) When a dispersion of precipitate particles in the boundary is present, a threshold stress is required for defect movement. In by-passing particles of spacing, λ, the defect is forced to adopt a local curvature, and assuming the mobility of the defects is high once the obstacles can be overcome, i.e. the process becomes diffusion controlled, the creep rate is given by :-

$$\dot{\epsilon} = \frac{10\ D_v}{KT\ d^2}\left(2\sigma\Omega - \frac{4E\Omega}{b\lambda}\right) \text{ for } \sigma > \frac{2E}{b\lambda}$$

$$\dot{\epsilon} = 0 \qquad \text{for } \sigma \leq \frac{2E}{b\lambda} \qquad \ldots\ldots\ldots (43)$$

where E is the energy per unit length of the dislocation.

2.6.2 Deformation Mechanism Maps

It was first suggested by Weertman[120], that the knowledge of deformation mechanisms may be used to construct a "creep diagram", now generally known as a deformation mechanism maps. The aim was to present in a simple manner the way in which the alternative deformation mechanisms compete; i.e. the values of stress and temperature for which each controls the flow stress. This was done by plotting maps in stress- temperature space, where the space was developed into fields, and within a field, one mechanism was said to be dominant, i.e. one particular mechanism supplies a greater strain rate than any other mechanism. So far, two types of maps have appeared in the literature; one based on constant grain size[24,121] and another type based on constant temperature[125,124]. It will be worthwhile to discuss both types and compare the two.

2.6.2.1 Ashby's Maps

Ashby[29,121] used standard relations between tensile stress and tensile strain rate for most of the deformation mechanisms capable of permitting steady state flow, namely, defectless flow, dislocation glide, diffusional creep and dislocation creep.

The maps are constructed in two dimensional stress/temperature space, using normalized tensile stress, σ/μ, (where μ is the shear modulus) as a stress co-ordinate, and homologous temperature T/T_M (where T_M is the melting point of the material) as the temperature co-ordinate. The normalized tensile stress ranges from 10^{-8} to 1, and homologous temperature from 0 to 1; and these ranges cover all possible values of the variables normally found in practice. The process requires the development of a large computer programme to obtain the boundaries of the flow fields by equating pairs of constitutive equations for various deformation mechanisms and solving for stress as a function of temperature. The dominant flow mechanism can be read by locating a point in a field for the

known values of stress and temperature. The map also plots contours of constant strain rate by calculating the strain rates from appropriate constitutive equations. Typical deformation mechanism maps for nickel and austenitic stainless steel (type 304) are shown in Fig. 4 and Fig. 5 respectively[121,122].

The field boundaries are clearly marked in these figures and it is said that at such boundaries, the two mechanisms which meet contribute equally to the strain rate[121]. Also, at a point where three fields meet, three mechanisms contribute equally. Therefore, the knowledge of any pair of the three variables of strain rate, stress and temperature locates a point on the map, identifies the dominant mechanisms of flow and gives the value of the third variable.

2.6.2.2 Effect of Microstructure on Ashby's Maps

Generally one particular microstructural feature affects one of the flow mechanisms predominantly and might have only a slight effect on the other possible flow mechanisms. Therefore a strengthening mechanism is only useful if it slows the rate of deformation in the right field of the map[29,121].

One of the major microstructural features established in these maps has been the effect of grain-size, for high temperature diffusional creep strength is proportional to the square or the cube of the grain size; therefore in the case of nickel it has been shown that decreasing the grain size increases the area covered by the diffusional flow field in Fig. 4. Decreasing the grain-size has a small effect on the glide field of the map, causing a slight strengthening i.e. a shrinkage in the glide field.

The precipitation hardening obstacles within the matrix act as a strengthening mechanism for dislocation glide, and the smaller the interparticle spacing the less prominant will dislocation glide be, i.e. it will make the glide field shrink. Such obstacles also alter the dislocation creep field and have a similar effect on this flow mechanism as that on dislocation glide, but it has other repercussions

such as the expansion of the diffusional flow field[121]. Also, increasing the dislocation density acts as a strengthening mechanism for dislocation glide and dislocation creep, thereby shrinking these fields.

Solid solution strengthening also exerts similar effects to those of precipitation hardening, but the situation seems to be rather doubtful as to whether solid solution strengtheners like Mo, W, etc. will have a decreasing effect on the diffusional flow field because of their lower diffusivities, or the opposite effect because of the reduction of melting point of the material due to alloying.

2.6.2.3 Langdon's Maps

Langdon[123,124] developed a more simple form of deformation map, where the construction is performed without the use of a large computer programme. His maps involve the plots of normalized grain size, d/b, (where b is the burgers vector), against normalised stress, σ/G (where G is the shear modulus), at a constant temperature, so that the map is divided into fields of grain size/stress space wherein a single mechanism is rate controlling. A typical plot of such type of a map is shown in Figure 6 for pure aluminium.

These maps are essentially constructed on the basis of flow rates for high temperature deformation mechanisms, and the various fields are separated by straight lines. The slopes of these lines are calculated by considering that the lines are the loci of points where two adjacent mechanisms have equal strain rate; thereby, equating the two appropriate equations allows the slope to be found.

2.6.2.4 Comparison of Langdon's and Ashby's Maps

A major draw-back of Ashby's maps is that they must be prepared for one specific grain-size, whereas Langdon's maps are plotted for a specific temperature at varying grain sizes [29,121-124]. However, in practice the operating temperature in an engineering application is usually specified fairly exactly, so that grain size and stress are more permissible

variables, as in the case of Langdon's maps. Although contours for different grain-sizes can be drawn on a single Ashby map, the various flow fields tend to become obscured.[123] On the contrary, Langdon's maps separate individual fields by straight lines, thereby easing the plotting procedure for such maps rather than using large computer programmes to draw the boundaries as in case of Ashby's maps.

Ashby's maps give a very good overall picture of the deformation mechanisms of materials on the basis of their original crystal structure, or the bond type, and provide a superb reference point for further research work into any particular deformation mechanism. There has been talk of producing Ashby type maps from a series of maps derived on the basis of Langdon type maps at various temperatures[124]. However, both types of maps have their own advantages according to the needs of the user, and both have not incorporated the less understood deformation mechanisms such as superplasticity.

2.6.3 High Temperature Tensile Properties

The most reliable method for studying high temperature properties would be to apply the inservice conditions, where the variables inherent in the application (rate of straining, nature of stress system, temperature) are simultaneously tested. However, such a method is expensive and the obvious advantage of a laboratory test, such as the ease of checking different casts, ease of determining optimum conditions for new materials, close control of variables, and the possibility of relating structure and properties, have led to the development of high temperature tensile testing as a means of assessing the high temperature behaviour of a material. Although there is a considerable difference of opinion concerning the way materials behave, both in tests and in use, because of the loading system to which the material is subjected, yet it has been shown that a knowledge of the stress-strain curve, stress-strain analysis, plasticity theory, and fracture mechanics provide the key to a number of common problems.

In the conventional engineering tensile test, stress and strain are defined by[126]:-

$$\text{stress } \sigma = \text{load/area} = L/A \quad \text{and}$$

$$\text{engineering strain} = \frac{L-L_o}{L_o} = \frac{\Delta L}{L_o}$$

In the elastic regions of stress-strain curves, stress is linearly related to strain $\sigma = Ee$, where E is the elastic modulus. The conventional measures of ductility that are obtained from the tensile test are the engineering strain at fracture, e_f,

$$e_f = \frac{l_f - l_o}{l_o}$$

and the reduction of area at fracture,

$$q = \frac{A_o - A_f}{A_o}$$

With large plastic strains it is more useful to define true strain, ϵ, as the change in linear dimension divided by the instantaneous value of the dimension and given by $\epsilon = \ln(1+e)$. The flow curve in the region of uniform deformation can be expressed by $\sigma = K\epsilon^n$, where K is the value of the flow stress at $\epsilon = 1$, and n is the strain hardening exponent.

2.6.3.1 Effect of Temperature and Strain Rate on the Strength of Austentic Steels

The strength of high temperature materials is markedly dependent on both temperature and rate of straining. Generally pure metals and simple alloys increase in strength with increasing rate of straining for a fixed temperature and decrease in strength with increasing temperature at a fixed rate of strain[127]. Investigations on various alloy steels have correlated strength with strain rate and temperature by using a power law equation:-[127]

$$\sigma_{\epsilon} = \sigma_{o}(T)\ \dot{\epsilon}^{N(T)} \qquad \ldots\ldots\ldots (44)$$

where σ_{ϵ} is the flow stress developed at some strain ϵ, $\dot{\epsilon}$ is the applied strain rate, $\sigma_{o}(T)$ and $N(T)$ are temperature dependent constants. At low strains these constants are also strain dependent, but once the steady state condition is established, the values appear to remain constant for a given temperature. $N(T)$ increases with temperature from ~ 0.02 at $0.5\ T_m$ to 0.2 near T_m.

In austenitic steels the maximum load increases with increasing strain rate and the effect has been generally attributed to the occurrence of the time dependent softening processes during high temperature testing, especially at slow strain rates[128]. The decrease in strength with increasing testing temperature is also thought to occur because of similar reasons. On the other hand at very high strain rates exceptionally high strengths can be obtained and such an effect was recently studied by Prus[129] on nickel-base heat resistant alloys and an explanation was given on the basis of softening and embrittlement processes, which do not have time to occur to the same extent as during slow deformation, because of the reduction in the time to failure. The strength of grain-boundaries is considerably higher than that of the grains, with the result that substantial deformation takes place within the grains. Also the stresses in the grains do not reach the yield strength of the boundaries and failure occurs only at substantially larger stresses.

In more complex systemsthe strength can increase with increasing temperature because of the precipitation effects involved, e.g. carbide or intermetallic precipitation within the grains or grain-boundaries during testing.[128,130,131] Furthermore, the increase in strength also depends upon the size and distribution of the precipitates, and above all the volume fraction[130-132]. The mechanisms of such effects have already been dealt in more detail in Section 2.2 of this literature survey.

2.6.3.2 Serrated Yielding

Serrated yielding (also commonly referred to as jerky flow) has been found to occur over a range of temperatures and strain rates in both austenitic stainless steels and nickel-iron base super alloys.[133-137] General mechanisms proposed have been briefly summarised by Bilsby.[138] However, the effect has been widely attributed to dynamic strain ageing of dislocations by either substitutional or interstitial solutes in a large number of alloy systems[135,136]. It is thought that diffusing solute atoms exert a drag effect on moving dislocations, thereby causing an increase in the stress required for dislocation movement. But once the dislocation tears itself away from the diffusing solute, the overall stress required for dislocation movement is reduced and this process is thought to continue over a length of time thereby giving a serrated flow curve.

There is a considerable amount of doubt over the effect of interstital and substitutional solutes exerting the drag effect on moving dislocations. Sukharov and Popov[133] working on commercially pure Ni reported that this material between test temperatures of 20°C and 650°C showed irregular yielding beyond a certain extension, which decreased with temperature. They attributed the observation to carbon drag, and the serrated yielding was not observed in material free from carbon. Boothby[137] in his recent work on PE16 suggests the interstitial atoms are too mobile to exert a drag on dislocations and holds molybdenum to be predominantly responsible for such effects i.e. substitutional solutes. The mechanism proposed by Bilsby[138] also suggests interstitials (carbon or nitrogen) to be most likely responsible for locking and unlocking of dislocations. However, no one seems to have thought of an additive effect exerted by both interstitials and substitutional alloying additions in a complex alloy system.

2.6.3.3 Effect of Microstructural Features On High Temperature Tensile Strength

Austenitic steels for high temperature application usually

contain precipitating elements such as Al, Ti, Mo, B, N etc. which form second phase particles. During high temperature applications these phases can transform or precipitation accelerated so that the strength alters during use or testing, and the resultant structure can be markedly different from the initial structure. The strength is markedly influenced by the distribution and morphology of the phases in the structure (127,132,139).

In austenite , carbides at grain-boundaries markedly increase the high temperature strength, which increases with increasing carbon content in the alloy.(140) The effect is more pronounced at slower strain rates because of the inhibition of the grain-boundary sliding.(128) The size and shape, including the distribution of carbides is directly related to the tensile strength for a number of materials and has been explained on the basis of void initiation due to decohesion at the carbide/matrix interface, or by fracture of the carbide itself.(132) In PE16, carbide precipitation at the grain-boundaries was also found to cause an appreciable increase in tensile strength at high temperatures.(141) The precipitation of γ' in austenitic steels again improves high temperature strength by hindering dislocation motion, and the strength increases with increasing volume fraction of the precipitate. Particle size of the γ' is very important, for it can change the deformation mechanism from one type to another.(130,131,139, 141). The effect is attributed to the glide dislocations shearing through the particles of smaller sizes, whereas larger particles are bypassed by such dislocations, leaving loops around the precipitate particles.(141)

2.6.3.4 Effect of Strain Rate and Temperature on Tensile Ductility

Generally metals become more ductile as the temperature is increased. Increased temperature may permit the introduction of new slip systems, a diminution in strain hardening, and the operation of deformation mechanisms such as grain-boundary sliding, etc. At temperatures around $0.7T_m$, recrystallization occurs concurrently with deformation.

For f.c.c. systems, increased ductility is observed above ambient temperature[40]. In Ni-base alloys below the recrystallization temperature, there is an intermediate temperature range of minimum ductility. Rhines and Wray[142] studied the phenomenon in Cu-Ni alloys and showed that it was due to grain-boundary sliding and associated intergranular rupture. When the temperature is raised so that recrystallization occurs, the new grains isolate the grain-boundary cracks, and the overall ductility is increased. In the case of precipitation hardened austenite , an increased testing temperature has been shown to precipitate different types of carbides at various sites, thereby promoting the deformation within the grains which improves the overall ductility of such steels.[128] In these steels the effects were much more pronounced at slower strain rates, and increased ductility was attributed to longer testing times whichpromoted the preferential growth of certain particles, in effect giving rise to fewer and large precipitates, thereby easing the process of softening and recovery. On the other hand, at extremely high strain rates in heat-resisting nickel-base alloys, exceptionally high ductilities have been observed and the effect has been attributed to higher strengths of grain-boundaries compared to grain-interiors, because the softening and embrittlement processes do not have time to occur.[129] In general, the ductility of austenite during high temperature tensile testing is governed by the balance between work-hardening and dynamic softening processes.

Attempts have been made to relate ductility to temperature and strain rate, and Tegart et. al[56] have proposed a relation for a torsion test in the form of:-

$$P = S\, D^{\frac{1}{2}}\, f(x) \qquad \text{..... (45)}$$

where P is the ductility (revolution to failure), S is a constant roughly equivalent to the number of active slip systems, D is the self diffusion co-efficient, and f(x) is a function of factors such as purity, amount of grain-boundary sliding etc. Available literature does not show many attempts of correlating ductility to strain-rate and temperature for

tensile tests; perhaps the problem becomes more complex due to varying deformation mechanisms for varying strain rates and temperatures, particularly for complex microstructures.

2.6.3.5 Effect of Microstructural Features on High Temperature Tensile Ductility in Austenitic Steels

Different structural variables which affect ductility in any alloy system are void nucleation by dislocation interactions, the effect of holes and precipitated particles and the embrittling effect of a certain distribution of a second phase in a two-phase system. Any system containing second phase particles shows that true strain at fracture is a strong function of the volume fraction of the second phase particles, but the nature of the particles (hard non-deformable or deformable), the shape and size of the particles play an important role[56]. Although it has been shown that only a fraction of particles present in the alloy are contributing to the final fracture, yet their sites are important with regard to high temperature ductility.[4]

Most of the austenitic steels for high temperature application contain $M_{23}C_6$ or MC type carbides at grain-boundaries or at intragranular sites. Opinions on the role of these carbides differ appreciably, yet certain common generalizations can be drawn from the available literature. Detrimental effects of carbides on the grain-boundaries have been noted, but reducing the carbon in the alloy to a very low level reduces the high temperature ductility e.g. Nimonic 80A (0.03%C) and Alloy 800 (0.05%C)[4,143]. The beneficial effects of a certain amount of carbides at the grain-boundaries have been attributed to the precipitate free zone or grain-boundary denuded zone which is less strong in comparison with the matrix, thus accommodating much of the deformation. In cobalt base super alloys it has been noted that if the excess carbon present in the alloy remains in solution and is precipitated in the matrix as secondary $M_{23}C_6$ during service, these interact with dislocations thus giving rise to lower overall ductility.[4]

In PE16, a ductility minimum (or a trough) was observed when tested over a range of strain rates at high temperature[141]. The effect was attributed to the general effect of diffusion creep strain on the cracking behaviour, especially due to cavity nucleation at carbides in the grain-boundaries. However, the variation of ductility with strain rate showed no ductility trough when the grain-boundary carbides were removed by means of a heat-treatment sequence. Nevertheless, the authors do not consider the change in the morphology of γ' within the matrix due to the new heat-treatment sequence, which may or may not have an influence on the overall ductility. Therefore, the explanation given should be treated with an element of doubt unless thoroughly investigated.

Most Ni-Fe base super alloys are strengthened through the formation of spherical semi-coherent γ' in the matrix, which maintains overall ductility.[24] It is the inherent ductility of γ' itself which makes it a contributory factor towards high-temperature ductility in a strong alloy.[144] If the γ' is in the overaged state, or completely incoherent with the matrix, the dislocations will not be able to cut through the particle, but develop a dislocation-particle interaction, leading to voids and to premature failure.[56] However, such a mechanism can only operate if the deformation is governed by dislocation movement, for if the deformation mechanism is predominantly diffusional type flow, such interactions will hardly be of any significance.

Another contribution to better high temperature tensile ductility has been attributed to a fine grain size in nimonic PE16.[141] The fine grain-size was achieved by cold-work prior to ageing. The increase in ductility was attributed to the Nabarro-Herring strain. Again, no consideration has been given to the effect of cold-work on the precipitation of γ'.

2.6.4 Creep Properties in Precipitation Hardened Austenite

Usually creep and creep rupture behaviour are determined under conditions of constant load, and in many commercial alloys, various types of solid state reactions occur that influence

the properties being determined. Since time dependent tensile deformation during creep is represented graphically by a creep rupture curve, the total strain can be represented by:[126]

$$\epsilon_r = \epsilon_o + \epsilon_p + \epsilon_s + \epsilon_t$$

ϵ_o is the instantaneous strain on loading, ϵ_p is the primary creep where creep rate decreases with time because of initial work hardening, ϵ_s is the secondary creep strain where creep rate remains reasonably constant because of a balance between work-hardening and recovery and finally ϵ_t is the tertiary creep strain where creep rate increases rapidly because of void coalescence or crack propagation leading to fracture.[56]. There have been various creep theories for total strain put forward, briefly summarised by Adamson[69], and an expression due to Lacombe is:-

$$\epsilon = a + bt^m + ct^n \qquad \ldots\ldots\ldots\ldots\ldots (46)$$

where m is an exponent whose value is between zero and unity, whereas n is an exponent with a value just slightly greater than unity. It has been found that equation (46) gives a good fit for the variation of creep strain with time for single phase polycrystalline materials.

2.6.4.1 Stress Dependence of Minimum Creep Rate/Rupture Life

For both metals and alloys tested at constant temperature, the stress dependence of the secondary creep rate, $\dot{\epsilon}_s$, at low stresses, is given by the power law.[113] :-

$$\dot{\epsilon}_s = A\sigma^n \qquad \ldots\ldots\ldots\ldots\ldots (47)$$

where σ is the constant applied stress, and A and n are independent of stress. The significance of the value of n will be discussed in detail later in this section. At high stress levels the stress dependence of the secondary creep rate is given by:-

$$\dot{\epsilon}_s = A' \exp(\beta\sigma) \qquad \ldots\ldots\ldots\ldots\ldots (48)$$

Where β and A' are constants.

The existence of equations (47) and (48) has led for sometime to the belief that different mechanisms control secondary creep at low and high stresses. But it is unlikely that an abrupt change in mechanism occurs, and it has been shown that equations (47) and (48) are satisfied by a single stress function, given by:-[113]

$$\dot{\epsilon}_s = A''(\sinh \alpha \sigma)^n \quad \ldots\ldots\ldots\ldots (49)$$

where A'' and α are constant at constant temperatures.

Grant et al[109] produced an empirical relationship between rupture life and secondary creep rate in creep-rupture tests for various alloys:-

$$\log t_r + m \log \dot{\epsilon}_s = c \quad \ldots\ldots\ldots\ldots (50)$$

where t_r is the rupture life, m and c are constants. For all practical purposes equation (50) has been found to be independent of testing temperature and stress. Assuming t_r varies inversely as $\dot{\epsilon}_s$, i.e. $t_r = \frac{K'}{\dot{\epsilon}_s}$, then equation (47) takes the form

$$t_r = K \sigma^{-n} \quad \ldots\ldots\ldots\ldots (51)$$

Also the more generalised form of stress dependence as shown in equation (49) becomes:-

$$t_r = \frac{\alpha_o (\sinh \alpha \sigma)^{-n}}{A''} \quad \ldots\ldots\ldots\ldots (52)$$

Where α_o is a constant.

2.6.4.2 On the Value of Stress Exponent n

Generally n is taken as a negative valued constant, independent of stress and temperature, in accordance with the fact that the time to failure decreases as the stress increases[109]. Higher values of n give greater stress dependence of rupture life. The parameter n is said to be independent of crystal structure, but there is a question on what exactly n depends[113].

In most cases, for high temperature creep, n lies between 3-7 for both pure metals and alloys.[122] In the case of nickel n = 5.6 but drops rapidly from this value upon alloying, reaching a minimum value of approximately 3.[113] Materials

hardened by finely dispersed second phase particles typically show a much stronger stress sensitivity and furthermore the variation of the exponent from one material to another is much larger.[145] It has been noted that in precipitation hardened steels containing niobium, stress dependencies with n values as high as 9-16 were obtained.[146] In steels containing controlled niobium carbide dispersions, the value of n changed from 9.5 to 10.3 when the coarse distribution of precipitates was replaced by a fine distribution.[147] The increased stress dependence was attributed to the increased hinderance of dislocation movement by the presence of finer particles than that caused by coarse precipitates. Gladman et al[122] also noticed a change in the value of n from 6.2 to 8.2 by increasing the carbon content from 0.015% to 0.056% in the same austenitic stainless steel, but did not regard this change as being of any particular significance. Alloys strengthened by γ' precipitation give values of n as high as 13 above a certain stress, and the value was shown to depend upon the magnitude and the stress dependence of the friction stress.[148] It has been suggested that the dislocation structure, developed in a given material during creep under a stress σ, is characterised by a friction stress σ_o. A decrease in σ_o raises n, and an increase in σ_o decreases the value of n. Whatever the reason for these varying values of stress-dependence (at least in the dislocation creep range) the evidence certainly seems to point towards the varying microstructural features as a strong factor for such a change.

Studies of creep in γ' - hardened nickel and iron-base alloys suggest that a pronounced break in the stress-creep rate relationship occurs in precipitation hardened alloys.[145,148] Below a certain stress the value of n decreases to a very small value i.e. from 13 to 4.5.[148] The behaviour is often called creep yield, and the decreasing stress-dependence of creep rate at low stresses and at about 0.6 T_m and even below, has been attributed to grain-boundary diffusion creep, and at somewhat higher temperatures volume diffusion creep has been said to account for such a dependency for n.[148, 150] The microstructural evidence in support of diffusional creep has been given in the form of denuded zones of precipitates

normal to the stress axis. But it is disputed that diffusional flow control should give a linear stress dependence of strain rate i.e. n should be equal to 1, which is in contradiction with the observed values.[145] Also the concept of friction stress, σ_o, has been said to show the stress dependence of creep rate over a wide range of stresses in the form:-[148]

$$\dot{\epsilon}_s \propto (\sigma - \sigma_o)^4 \qquad \ldots\ldots\ldots\ldots (53)$$

However, the possibility of diffusional creep at such stresses cannot be completely ignored, and the role and understanding of various microstructural features might give a better picture of the whole concept of the stress dependence of creep rate.

2.6.4.3 Tertiary Creep

The tertiary creep strain depends on the deformation throughout the creep history and there can be many factors responsible for the onset of tertiary creep.[56] The factors usually considered include increasing stress, under constant load or during necking, and the re-solution of one or more phases. At higher stresses, tertiary creep is associated with necking and at intermediate stresses, tertiary creep is associated with the formation of intergranular cavities throughout the test section. One of the factors that strongly influences the onset of tertiary creep is void formation, and except at high stresses or when extensive microstructural changes occur, void formation can start well before the onset of tertiary creep or even well before the initiation of secondary creep.[56] The increase in creep rate during tertiary creep has been associated with void formation at grain-boundaries, to an increasing vacancy flow to grain-boundaries, and to the rate of climb of edge dislocations.

2.6.4.4 Influence of Second Phase Particles on Creep Properties

Second phase particles are added to a matrix to enhance its creep strength[152] by:-

(a) Increasing the high temperature flow stress and/or rate of work hardening

(b) Decreasing the rate of recovery due to an intragranular dispersion of second phase particles.

Refractory particles such as carbides are dispersed in the matrix, using a relatively small volume fraction, and the effect of this dispersion is to markedly reduce the scale of the dislocation cell structure which is formed at a given creep rate. In Ni-base superalloys the cell structure is observed near the grain-boundaries, and therefore grain-boundary carbide precipitation is thought to have a beneficial effect on creep strength. In most of the Ni-Fe base superalloys the particles are usually intermetallics, e.g. Ni_3 (Al Ti), and the required volume fraction is quite often larger, so that the particles are dispersed on a much finer scale than are carbides.[4] The effect of these particles is to increase the high temperature flow stress and reduce the rate of recovery of the alloy. The conventional dislocation cell structure resulting from recovery is therefore greatly suppressed.[152]

In general, creep ductility is related to the presence and dispersion of second phase particles as well as to grain size. In many alloys, particles are deliberately produced at grain-boundaries in order to inhibit grain-boundary sliding with the consequent inhibition of nucleation of wedge cracks or cavitation failure. Conversely, grain-boundary carbides are often thought to be the nucleation sites for cavities and hence to initiate rupture in a creep test.[153-155] Another effect of grain-boundary particles is the grain refinement which is said to have a beneficial effect on high temperature creep ductility.[152] These generalizations are quite consistent with mathematical models (section 2.6.1) where high creep strength is favoured by solute additions which raise the modulus or lower the stacking fault energy, and which lower diffusivity.

2.6.4.4.1 Effect of $M_{23}C_6$ Precipitates on Creep Properties

Sadao, Otha, and Ken-ichi[155] studied the effect of $M_{23}C_6$ precipitates in 20%Cr - 20% Ni austenitic steel and observed that when there was no precipiation of carbides at grain-boundaries, wedge type cracks appeared in the early stages of creep, and the specimens fractured in a very short time. In the steel having a continuous film of carbides at grain-boundaries, the creep life was greatly improved and wedge type cracking was prevented. The beneficial effect was attributed to a decrease in grain-boundary sliding and reduction of interfacial energy. Similar effects were observed on a 18.6% Cr, 12%Ni, 2.7%Mo steel because of $M_{23}C_6$ precipitation at grain-boundaries.[156] The presence of $M_{23}C_6$ within the grains, particularly on dislocations, has been known to decrease the creep rate because of a decrease in dislocation mobility within the grains.[122] This reduction in dislocation mobility within the grains reduces the sub-grain-boundary density, thereby strengthening the alloy.

In a situation where appreciable carbon is left in solution, even after a heat-treatment sequence, the precipitation of $M_{23}C_6$ may improve the creep strength.[122,157] The sequence of $M_{23}C_6$ precipitation at various microstructural sites has been shown to vary with the creep process itself, e.g. during primary creep grain-boundary precipitation of $M_{23}C_6$ occurs, and secondary creep is strongly controlled by the precipitation of $M_{23}C_6$ particles on dislocations. Tertiary creep is associated with the coarsening of $M_{23}C_6$ precipitates with no fresh nucleation of precipitates.[157] Perhaps the process becomes more complex when carbides have already been precipitated at various microstructural sites before testing and there is still some carbon in solution which is to come out as $M_{23}C_6$ during testing.

The precipitation of $M_{23}C_6$ at grain-boundaries improves the ductility by hindering nucleation and growth of cavities by inactivating nucleation sites, increasing the intercavity distance and also by reducing the rate of diffusion along

grain-boundaries.[155,156] Heslop[153] found similar results on Nimonic 80A and 90, where $M_{23}C_6$ precipitates produced a zone softer than the matrix near grain-boundaries, which deformed more readily and relaxed stress concentration at the grain-boundary triple point junctions. It has been suggested that if zones are wide and very much weaker than the matrix, the deformation will be concentrated in these regions, resulting in early failure at low overall ductility. The role of the presence of precipitate free zones on creep ductility is but imperfectly understood.

2.6.4.4.2 Effect of TiC Precipitates on Creep Properties

The replacement of $M_{23}C_6$ at the grain-boundaries of PE16 by TiC has been observed to double the ductility and fracture life and the effect was independent of the dispersion of the carbide.[138] The improvement in properties has been ascribed to retardation of the viscous creep controlled growth of the triple point cracks by the high surface energy of TiC. In viscous creep crack growth, the crack is assumed to grow by the migration of atoms by surface diffusion from the ends of the sides of the crack. The volume of the crack this will remain constant apart from the volume change arising from elastic deformation. Such a phenomenon is hindered by the presence of TiC at grain-boundaries. Some other work[158] on Ti-bearing austenitic steel suggests that creep of such alloys is not dependent on the precipitate concentrations and distributions, but is controlled by solute drag due to excess titanium solute atoms which interact strongly with dislocations, thereby strengthening the alloy. It has also been suggested that at very high Ti contents the creep rate is predominantly controlled by the volume fraction of TiC precipitates. Although the presence of Ti in austenite seems to improve the creep properties, the actual mechanism is still in dispute.

2.6.4.4.3 Effect of γ' Precipitates on Creep Properties

Hopkins[159] showed that in Ni-Cr base alloys hardened with γ' precipitates, the mechanism of deformation was similar to that at room-temperature. Also in the alloys having lower

$\gamma'-\gamma$ mismatch, the minimum creep rate was found to be proportional to the volume fraction, f, of the precipitate. The minimum creep rate was found to vary as the cube root of the volume fraction of the precipitate. Also the rate of recovery in such alloys was found to be proportional to the minimum creep rate, or in other words the volume fraction of the precipitate. Gamma-prime is usually coherent with the matrix and is a very stable phase at high temperatures because of the low diffusion coefficient of Ti and Al, yet coarsening occurs at significant rates at normal service temperatures.(4,155).

In a recent study on Fe-Ni-Cr alloys(160) it was shown that when the matrix was strengthened by γ' zones, the ductility was reduced. The effect was attributed to difficult dislocation movement, causing plastic deformation to occur preferentially at grain-boundaries and leading to localization of plastic strains at the grain-boundaries junctions, thereby enhancing void formation and hence fracture. Some workers suggest that the ductility of Nimonic alloys is very dependent on the tertiary creep behaviour.(161) In other words the control of tertiary creep can control the overall ductility e.g. sintering out of cavities by annealing at creep temperatures, etc. There is very little work on the actual property relationships although it has been said that creep rate continuously decreases with increasing particle diameter, and above a certain particle size the creep rate is independent of such a variable.(148) In PE16 it has been noticed that when γ' is present in the form of zones, dislocation pairing does not operate, whereas dislocation climb mechanisms dominate, giving an overall decreased creep rate. An Orowan looping mechanism operates at bigger particle size resulting in increased creep rate.(138)

2.7 HIGH TEMPERATURE FRACTURE

Polycrystalline metals and alloys fracture by various mechanisms, but in this review we will be mainly concerned with different types of fractures occuring at temperatures above 0.3 T_m, i.e. high temperatures fracture mechanisms.

At temperatures below $0.3T_m$, plastic flow does not strongly depend upon temperature, or time, but above this range materials creep, with the result leading to different modes of fracture. Apart from temperature variables such as strain-rate and microstructural features also control the modes of fracture, and strong correlations have been observed between microstructural parameters and the type of fracture.(162) High temperature fracture mechanisms can be broadly classified into three major groups(163), Fig. 7 :-

a) Transgranular growth of voids by creep
b) Intergranular creep fracture - by growth of grain boundar voids
c) Rupture

2.7.1 Transgranular Creep Fracture

The presence of pre-existing holes or non-deformable particles (i.e. carbides/nitrides) which concentrate stress during deformation, causes the stress to build up as the plastic strain increases, until the particle either parts from the matrix or fractures. At high temperatures the nucleation of the particle-matrix holes can be postponed where diffusion is possible.(163) At such temperatures matter can flow from regions on the particle surface which are in compression to those which are in tension, reducing the incompatibility which needs to be accommodated by the local plastic flow. However, once such holes are nucleated, they grow as the matrix containing them continues to creep, and start to link up leading to ultimate fracture. In general, lower temperatures and faster strain rates favour this type of fracture, but if the strain rate is low enough the holes are stabilized thus postponing coalescence.(113,163) A complete transgranular fracture was observed in PE16 at a test temperature of 450°C, the effect was attributed to cavity formation at cracked Ti(CN) particles which led to the plastic instability of the matrix around these particles, thereby leading to a transgranular fracture mode.(137) Generally it is felt that transgranular void formation does not depend upon the volume fraction of the particles but is a strong function of the size of the particle, and larger particles are said to form voids

at smaller strains than smaller particles.[164] But there is evidence that some systems do not show a marked particle size-dependence of void formation.

2.7.2 Intergranular Creep Fracture

With increasing time to fracture, a transition from transgranular to intergranular fracture is observed.[163] The cracking has been found to occur at grain-boundary triple point junctions or by the formation of cavities (or voids) on grain-boundaries which are approximately normal to the applied stress.[165] This change of fracture mode is said to depend upon many factors, such as temperature, strain-rate composition and above all the effect of microstructural features on grain-boundary sliding and migration.[113,162-165] The change from transgranular to intergranular rupture is often said to be more abrupt in complex alloys than in metals, and a pronounced drop in ductility is found at the temperature where the change occurs.[113] However, with increasing temperature, grain-boundary migration becomes more prominent leading to an increased ductility.

Experimental observations of intergranular ruptures show the occurrence of two types of fracture.[113] These include wedge, or w-type cracks and r-type voids which by metallographic techniques are revealed as elliptical, round or even polyhedral in shape. Triple-point cracking (w-type) is generally a preferred mode at higher stresses whereas r-type cavitation is favoured by lower stresses.[165] The transition is not distinct; both types are frequently found together and the detailed microstructure is also significant[113,162].

2.7.2.1 Nucleation and Growth of w-type Cracks

A mechanism for the nucleation of w-type cracks at triple points was proposed initially by Zener,[160] on the basis that a crack is nucleated as a result of stress concentration set up at a triple point by a sliding grain-boundary Fig. 8 . This model predicts that the crack will be transverse to the direction of the applied stress, which rarely corresponds

with observations.[138] However, another form of crack nucleation Fig 7 predicted by this model is nucleation along the inclined boundaries; and the crack grows along these under the normal component of the applied stress. McLean estimated the minimum stress necessary to form a crack at the head of a sliding boundary on the basis of a calculation by Stroh for the formation of a stable crack by the stress concentration at the tip of the slip band.[107] The computed values were lower than the actual values and the discrepancy was said to be because experiments were on fracture at grain-boundaries of complex alloys and not of pure metals.[113,167] In general, the nucleation of wedge cracks has been treated as analogous to cleavage crack formation in brittle solids by considering the stress concentrations at triple points by grain-boundary sliding[167]. However, the application of such theories to wedge crack nucleation during creep is dubious, because the theories do not account for stress relaxation mechanisms occurring during deformation.[168] In 316 stainless steel, the conditions for nucleation have been explained on the basis of the Stroh criterion for cleavage crack nucleation, with very little stress relaxation occurring during high temperature creep. Although such a criterion may apply to stainless steel (type 316) it becomes unacceptable to suggest that no relaxation mechanisms operate at such temperatures.

The factors that govern the growth of w-type cracks are not clear, but generally it is felt that continuation of grain-boundary sliding increases the crack length.[113] Such an indication of extensive plastic deformation has also been observed in type 316 austenitic stainless steel, with the crack propagating across grain-boundary facets.[168] Heald and Williams[169] proposed a model for the growth of wedge cracks under creep conditions, which enables the creep fracture of a polycrystalline material to be calculated. It considers the energy balance in the growth of wedge cracks which form at triple points due to grain-boundary sliding. A wedge crack of length, c, is nucleated at a triple point junction due to grain-boundary sliding, plastic relaxation occurring ahead of the crack over the region $c < x < a$ where x is the crack length

and a is the length of the crack and the plastic zone. The analysis gives the equation:-

$$\sigma \dot{\epsilon}_{gbs} t_f = \theta_c \frac{\sigma_1}{k\,d} \qquad \ldots\ldots\ldots\ldots\ldots (54)$$

where $\dot{\epsilon}_{gbs}$ is the creep strain rate due to grain-boundary sliding, t is the time to fracture, θ_c is the critical value of displacement at the crack tip for growth to occur, σ_1 is the yield stress of the material in the region of the crack, and d is the grain size, and k a constant.

The essential conditions of the model are that the crack growth is stable and that the cracks are nucleated during steady state creep; this condition being true in many material.(5

The growth of w-type cracks by vacancy condensation or other thermally aided crack-propagation mechanisms has not been examined extensively.(113)

2.7.2.1.1 Effect of Microstructures on w-type Cracks

It is well established that grain-size is an important factor in controlling high temperature fracture and thereby the ductility.(169) Relatively coarse grain sizes tend to promote fracture by the propagation of a crack of critical size which in effect might lead to low overall ductility.(137) Growth of a crack to the critical length becomes more difficult as the grain-diameter is reduced due to the larger number of triple points encountered, resulting in an increased ductility.(1 Grain shape is also said to influence the crack nucleation, for any elongation of the grains along the stress axis tends to reduce the area of grain-boundary suitably oriented for sliding, thereby decreasing crack nucleation.

The morphology of grain-boundary carbides is also known to affect the crack nucleation and growth.(4,165) Discrete globular particles are generally considered the most beneficial to ductility, since they reduce the extent of the grain-boundary sliding, and therefore the stress concentration at grain-boundary triple points, thus delaying the formation of w-type

cracks.[4,138,165] The presence of γ' depleted zones which are generally observed to form adjacent to grain-boundaries containing Cr-rich $M_{23}C_6$ allows the relaxation of stresses which otherwise could initiate early w-type cracking, and such an effect has been observed in PE16.[137]

2.7.2.2 Nucleation and Growth of r-type Cracks

The nucleation of r-type voids has been studied for many materials and the various theories put forward have been discussed in detail by Perry in a recent review.[165] The most popular mechanism for pure metals and alloys containing grain-boundaries free from particles involves the formation of cavities at grain-boundary ledges by grain-boundary sliding, and the ledges are said to be produced during creep by edge dislocations penetrating a grain-boundary.[113] Grain-boundary sliding can produce a cavity of volume(xyz)as shown in Fig. 9 . The stability of the void formed after sliding is said to depend on several factors including the original ledge height. If the ledge height is too small, the cavity may collapse.[165] Although there are certain arguments over ledge formation by slip, in any case local normal stresses are generated by sliding and are necessary for crack formation.[113] Generally, in alloys with second phase particles at grain-boundaries, heterogeneous nucleation of voids occurs.[165] It is said that stress is concentrated at particles in the boundaries which slide, and concentration of stress can cause the nucleation of these voids near such particles.[163] The mechanisms proposed for nucleation of both w-type and r-type fractures depend on the same criterion of grain-boundary sliding and concentration of normal stresses at line or planar obstacles. None of the proposed mechanisms are able to explain directly the finding that w-type cracks occur predominantly at high stresses and low temperatures and that r-type cavities occur at low stresses and high temperatures.

Generally, the volume of the cavities increases monotonically with increasing deformation, thereby indicating sliding is a factor in void growth.[113] However, if this were the only mechanism of growth, the cavities would be expected to maintain

a platelike shape, but generally the shape has been found to be nearly spherical.[109,113] Therefore, alternative mechanisms based on vacancy/atom diffusion have been proposed, all based on a single concept that a tensile traction acting across a grain-boundary lowers the chemical potential of the atoms, and vacancies migrate to the void by diffusion, thus causing it to grow.[165,171] There are still many disagreements on the comparative role of sliding and vacancy diffusion contributing to the void growth, but evidence suggests that both might be operative at the same time.[113,169,171]

2.7.2.2.1 Effect of Microstructure on r-type Cracks

The occurrence of cavitation in Nimonic 80A was shown by Weaver[162] to depend on grain-boundary structure and the presence of carbide particles. The voids were reported to form preferentially on the transverse boundaries between carbide particles and did not form on the particles which stopped crack propagation. The size of the carbide particles is important because a fine dispersion leads to low creep ductility. The significance of coarse carbides has been questioned by Gibbons and Hopkins[172] who studied carbon free alloys. These alloys had poor ductility but it was found possible to correct this by adding niobium. The presence of γ' is again said to be beneficial for similar reasons to those discussed for w-type cracks.

2.7.3 Rupture

If no other fracture mechanism intervenes, a material pulled in tension becomes mechanically unstable. Deformation becomes localised in a neck or a shear band and continues until the cross-sectional area has decreased to zero, when the material is said to rupture.[163]

Rupture obviously involves large reductions in area and it is thought of as the tensile failure mode which appears when all other modes are suppressed. Perhaps the suppression of all other modes of deformation would be unrealistic

considering the complex alloy systems, such as precipitation hardened austenites.

2.7.4 Fracture Maps

Similar to deformation mechanism maps, Ashby in his recent work on constructing fracture maps, has tried to quantify fracture by calculating the strain to fracture/time to fracture, as a function of stress and temperature[163]. The mechanisms are compared on the basis of their effect on strain/time to fracture and the one with the smallest value is selected as the dominant one, i.e. the mechanism which will lead most quickly to failure.

The maps are plotted simply by tabulating the homologous temperature, T/T_m and the normalised tensile stress, σ_n/E, where σ_n is the normal stress in a creep or tensile test, and E is Young's modulus, adjusted to the temperature of the test, together with the time to fracture, and strain to fracture. Then each datum is assigned a mode of failure, generally based on fractographic observations. All this information is fed into a computer programme and a map of this type is shown in Fig. 10 for copper, which is said to be broadly typical of f.c.c. metals and alloys.[163] Finally, boundaries are drawn separating blocks of data with a given mode of failure, based upon fractographic evidence.

2.7.4.1 Effect of Microstructure on Fracture Maps

Strictly, one fracture map applies to only one composition of alloy, with one grain-size and in one state of heat-treatment.

Alloying moves the entire pattern to higher stresses, and causes certain fields to shrink or grow. Solid solution strengthening expands the intergranular creep fracture field at the expense of the transgranular one. Precipitation hardening does this more strongly, and because precipitates suppress recrystallization, it may eliminate or shrink the rupture field as well.

2.7.4.2 Applications

The map gives a broad and self-consistent picture of the way a material fails in tension. Each mechanism is dominant over a range of normalised stress and temperature; and the fields for similar materials have a similar extent. The emphasis is that final fracture reflects the competition between a number of alternative mechanisms; suppressing one simply means that the material will fail by another. Therefore such maps are a great help to alloy designers.

3. EXPERIMENTAL METHODS

3.1 MANUFACTURE OF ALLOYS

The alloys were made in a high frequency induction furnace, vacuum melted as 10 kgs melts and cast in two ingots weighing 5 kgs each. The furnace lining was magnesite and the analysis of all the alloys is listed in table 1.

The following materials were used to make the alloys:-

(a) Japanese Iron
(b) Nickel Pellets
(c) Chromium Metal
(d) Carbon (as graphite)

and/or additions of

(i) Molybdenum
(ii) Titanium
(iii) Aluminium
(iv) High Nitrogen Iron
(v) Ferro-boron

Alloying additions were calculated on the basis of 100% yield, using a charge weight of 10 kg. The melting procedure was carried out under argon at a reduced pressure, and all the additions were made during this period; with the exception of titanium, aluminium and high nitrogen iron, to reduce vapourisation losses to a minimum. Some considerable difficulty was experienced in obtaining alloys of correct composition due to variable carbon losses in the furnace, however this was overcome by changing the sequence of alloying additions. The melts were cast at a temperature of $\sim 1550^{\circ}C$.

3.2 PROCESSING, HOT ROLLING AND HEAT-TREATMENTS

The surfaces of all the ingots were planed to reduce the incidence of surface defects during further processing, and also ingot 'pipes' were removed. Nearly two thirds of each ingot was rolled at a starting temperature of $1150^{\circ}C$ to bars approximating 12.5 mm diameter, taking into account the specimens sizes required for mechanical testing. The

remaining one third of each ingot was hot rolled at 1150°C to 3 mm thick strip, in order to study the effect of cold work prior to ageing. Hot rolling was carried out using a 2 high 1×10^6 Newton rolling mill with 250 mm diameter rolls. A constant strip thickness is of particular importance in determining grain-coarsening characteristics, for the specimen thickness is known to affect such results.(62)

3.2.1 Solution Treatments

The effect of solution treatment temperature and time was studied on all the alloys listed in Table 1, using both bar and strip material. Small discs 6 mm thick were cut from the 12.5 mm diameter bars, and 12 mm square pieces were used from the 3 mm thick strip. The solution treatments were carried out in muffle furnaces, the specimens resting on alumina pallets. Temperatures in the range 1000-1250°C were used with soaking times of 0.25h, 0.50h, 1h, 2h and 4h. After the appropriate solution treatment, specimens were rapidly quenched in water to minimise precipitation during cooling. Metallographic examination carried out on these specimens will be discussed later.

3.2.2 Ageing Treatments

Small discs, ~6 mm thick, were cut from 12.5 mm diameter bars and solution treated using the conditions shown in Table IV. Specimens were water quenched after solution-treatment and ageing was carried out at temperatures of 500-900°C, using intervals of 50°C, and for times of 0.25h, 0.50h, 1h, 2h, 6h, 10h, 30h, 70h, and 100h. Ageing times upto 1000 hours were used at the lower ageing temperatures where ageing was less rapid i.e. 500-550°C. Ageing treatments were carried out in a muffle furnace in which there was a limited access of air, the specimens resting on small alumina pallets. Excessive scaling was not observed, even at the highest temperatures. The temperature control of the furnaces was ±5°C.

Immediately after ageing, the specimens were water quenched, mounted, polished, hardness tested and then metallographically examinated, the details of which will be given in the later part of this chapter.

3.3 COLD ROLLING AND AGEING

The 3 mm thick strip for Alloys 2,3,4,5,7 and 8 (Table 1) was solution treated for appropriate times and temperatures (Table IV), and cold rolling was carried out on these alloys using a SOAG mill, with 75 mm diameter rolls, without lubrication, in incremental reduction of ~ 0.1 mm. The 3mm strip was cold rolled to 1.9 mm, 1.27 mm and 0.63 mm thick strips to study the effect of 40%, 60% and 80% cold reduction prior to ageing respectively. The cold rolled strips were cut into 25 mm squares for subsequent ageing treatments. Ageing treatments from 0.25h to 100 hours were carried out in sodium chloride/sodium-carbonate salt baths, for all reductions, at temperatures of 650°C, 700°C and 750°C. The temperature variability in the salt bath was ~ ± 3°C. The specimens were water quenched, mounted, hardness tested and metallographically examined.

3.4 SPECIMEN PREPARATION

The specimens from the solution treatment, age-hardening and coldworking/ageing work, were all sectioned longitudinally and mounted in cold setting resin. Similar sections were taken from the cold rolled strip for various reductions. The mounted specimens were prepared for metallographic examination in the usual way, except that a considerable difficulty was experienced in obtaining a fine polish on the specimen surface, the material being too soft for 1 micron diamond wheels. An additional step of polishing on vibrators containing 0.05 micron alumina paste produced better results.

Metallographic examination of solution treated specimens was carried out using a modified Schaftmeister's etchant containing 25 c.c. concentrated HCl, 15-20 c.c. concentrated

HNO_3 and 65 c.c. water. This etchant clearly revealed the grain-boundaries, which were free from precipitates, more distinctly than the conventional electrolytic etching in glyceregia.[68] Polished specimens after age-hardening and cold-working/ageing were electrolytically etched in 10% oxalic acid at 6v for about 10-15 seconds, using a stainless-steel anode and a platinium cathode. This particular etchant was observed to furnish detailed information of the microstructure within the grains i.e. twin boundaries, undissolved precipitates and precipitation during ageing.

3.5 EXPERIMENTAL TECHNIQUES

This section deals with the details of experimental techniques employed in the present investigation, which were fairly conventional yet specific to high nickel austenites.

3.5.1 Grain Size Measurements

Grain size measurements were made, using the mean linear intercept method, often termed the Heyn, or Jeffries method. The method measures the chord length defined by the intersection of a random straight line, by the grain-boundaries on the plane of the polish. The mean linear intercept, m.l.i, is defined as $\bar{d}$ where:-

$$\bar{d} = \frac{l}{n}$$

where l is the length of the random line on the planar surface, and n is the number of grain-boundary intersections on this line. The mean linear intercept is obviously less than the true grain size, for it includes sectioning effects. The true mean diameter $\bar{D}$ is defined as

$$\bar{D} \simeq 1.75 \ \bar{d}$$

3.5.1.1 The Accuracy of the Mean Linear Intercept

Statistically the standard deviation of the mean is defined as:-

$$\sigma_{\bar{d}} = \frac{\sigma_d}{\sqrt{N}} \qquad \ldots\ldots\ldots\ldots (55)$$

where N is the number of observations made, and σ_d is the standard deviation of the individual measurements. Therefore, the relative error, α, is given by:-

$$\alpha = \frac{\sigma_{\bar{d}}}{\bar{d}} \qquad \ldots\ldots\ldots\ldots\ldots (56)$$

It has been found empirically that the error of the individual intercept is given by:-(173)

$$\frac{\sigma_d}{\bar{d}} = 0.7 \qquad \ldots\ldots\ldots\ldots\ldots (57)$$

Thus the relative error is:-

$$\alpha = \frac{0.7}{\sqrt{n}} \qquad \ldots\ldots\ldots\ldots (58)$$

3.5.1.2 Measurement of Grain Size

Generally, austenitic stainless steels exhibit a fairly equiaxed and uniform grain size, but to improve the accuracy of the results, measurements were made in three different directions on the polished surface of the specimen, each direction being at an angle of 120° to one another, The average grain sizes were calculated using relationship:-

$$\text{Average grain diameter} = \frac{\bar{D}_1 + \bar{D}_2 + \bar{D}_3}{3} \qquad \ldots\ldots\ldots (59)$$

where $\bar{D}_1$, $\bar{D}_2$ and $\bar{D}_3$ are the average true grain-diameters in the three directions of measurement. It was assessed that the 95% confidence limits for the determination of the mean linear intercept of grain-size are $\pm$ 15% of the reported value, with rather larger error in coarser grain material for which fewer grains were able to be measured.

3.5.2 Hardness Testing

Hardness measurements were carried out using a Vicker's pyramid indenter, at a load of 30 kg, on the solution

treated and aged bar material. Measurements were carried out on the longitudinally sectioned and mounted specimens. The surface of the specimens was prepared to a 600 grit finish and hardness results were calculated by taking the average of at least five impressions. The calibration of the hardness machine was checked at intervals using standard calibration blocks. From time to time, check hardness values were made using a 5 kg load to ensure that the specimens did not bed down into the resin mount under the 30 kg standard load and thus give incorrect hardness results.

In the case of cold-worked material the selection of the load for hardness testing was done by observing the hardness change at varying loads on the soft material i.e. Alloy No. 1. A load of 5 kg was selected on the basis of zero recovery effects and minimum edge distortion effects on the indentation.

3.5.3 High Temperature Tensile Testing

High temperature tensile tests were carried out on the INSTRON TT-CM-L machine, provided with an automatic curve recording facility and changeable cross-head speed arrangement. Although a constant cross-head speed does not represent a constant strain-rate, yet it was assumed to approximate to a certain degree of constancy in terms of minimum strain rate, i.e. a particular cross-head speed corresponds to a given strain rate.

3.5.3.1 Specimen Preparation and Heat-Treatment

All the alloys, in the form of 12.5 mm diameter and 300 mm long bars, were solution treated and aged at various temperatures in muffle furnaces, as listed in table IV and table VI respectively. The heat-treated bars were quenched in water and threaded tensile specimens were machined to dimensions given in Fig. 11.

3.5.3.2 The High Temperature Tensile Test

High temperature tensile tests at 700°C were carried out

in air in a vertical tube type furnace designed for the INSTRON, with a 254 mm long heating zone. Special testing grips were made from Nimonic 105 to suit the selected specimen sizes. Three thermocouples were wired to various places on the gauge length, covered with heat-resisting wool to avoid any radiation effects on the thermocouples giving incorrect temperature readings. Generally, the specimens were given an hour's time to reach the desired temperature, although the heating rate of the furnace was 25°C/minute, in order to maintain the correct test temperature. The temperature readings were checked by means of a potentiometer.

Tensile specimens in each heat-treated condition (Table IV and Table VI) were strained to failure using five different strain rates ranging from 3.2×10^{-1} /sec to 3.2×10^{-5}/sec, varying by 10^{-1}/sec. In all cases a 5000 kg load cell was used and the load cell was recalibrated between each test using a 50 kg load. The load-extension curve in each case was recorded with the help of the automatic chart recorder. The curve was used to give an engineering stress - engineering strain curve.

The fractured specimens were then allowed to cool in air for further investigations.

3.5.4 Creep Testing

The heat-treatment conditions and specimen preparation were similar to those described for high-temperature tensile testing, except that Alloy No. 5, heat-treatment condition 2 (Table VI), was not tested because of shortage of time. The size and shape of the specimen is described in Fig. 11 and both creep rupture and interrupted tests were performed at a temperature of 700°C.

The tests were carried out in Denison T47E constant load type creep machines, fitted with an automatic strain/time recorder and a dial gauge extensometer. The strain/time recorder utilises the fall of the lever arm to mark the strain

on a rotating drum, and the magnification factor between the graph and actual specimen extension is 30:1. The readings from both the drum and the dial guage were taken to compare the results and to improve the accuracy of extension measurements. All the specimens were tested in air, in a furnace wound in three zones, the temperature in each of which could be separately adjusted.

The procedure was to bring the furnace to temperature, to screw the specimens into the Nimonic 80 A grips, and attach three thermocouples to it, shielded with heat-resisting wool. The furnace was lowered into the position round the specimen, and a load of 10 kg (exerting a small stress of about 6,3 MN/m^2) was applied while the assembly reached the desired temperature of 700°C. Generally, 2 hours was allowed for the temperature to stabilise. The load was then applied by placing the weights separately on the loading pan. The creep curves were obtained by replotting the automatically recorded curves, with the elastic strain subtracted. In the case of 1000 hour tests, the temperature and the assembly was checked regularly and the temperature zones of the furnace adjusted.

3.5.5 Electron Microscopy

Electron microscopy was carried out on the material in the solution-treated, solution treated and aged, coldworked and aged, heat-treated and tensile tested and heat-treated and creep tested conditions, using thin foil techniques. Limited investigations were carried out on the volume fraction measurements of undissolved carbo-nitrides in various solution-treatment conditions, and on the distribution of the precipitates.

Thin foils in solution treated and solution treated - age hardened materials were made by spark cutting 3 mm diameter cylinders out of heat-treated discs. Small discs were cut out of 3mm diameter bars and reduced to 0.25 mm thickness by grinding both faces on a 400 grit grinding paper. Polishing and thinning of these foils was carried out using a Struer's unit, in a solution of 94 parts acetic acid to 6 parts perchloric acid at a potential of 70 volts and keeping the flow

rate as low as possible. In the case of cold-worked material, small 3 mm diameter discs were stamped out of the coldworked - heat treated sheets and the preparation was as described above. In the case of high temperature tested specimens the gauge length was machined to 3mm diameter after testing, and the procedure was as above.

The thin foils were examined using transmission electron microscopy at accelerating voltages of 100 and 1000 KV. The advantages of using the 1000 KV instrument over 100 KV were that:-

(1) The increased penetration allowed thicker specimens to be examined, which are more representative of bulk materials.

(2) The improved penetration also allowed studies to be made of larger precipitated particles by electron diffraction.

3.5.6 Scanning Electron Microscopy

Most of the fractured specimens were examined by scanning electron microscopy in order to elucidate the changes in fracture characteristics with varying microstructures. This was performed on both high temperature tensile tested and creep tested specimens. Immediately after testing the specimens were mounted on aluminium studs and coated with gold-palladium alloy, in order to improve the conductivity of the fractured surfaces, for oxidation of such surfaces during high temperature testing is inevitable.

Selected fractured surfaces, containing chromium rich $M_{23}C_6$ and/or titanium rich TiC particles at grain boundaries and twin boundaries were examined for titanium and chromium distribution, using the mapping technique with the help of the EDAX facility attached to the scanning electron microscope. This proved to be very helpful in examining cavity formation around such particles and thereby the ultimate fracture mechanism of a particular microstructure. Ideally the mapping surface should be flat, but by tilting the specimen, such a

condition can be approximately achieved when looking at a particular area of the fractured surface. Also, in the case of fractured surfaces, absorption effects occur due to the surface roughness . Therefore the relative heights of various peaks were not taken to be a measure of the amount of metal segregated at a particular site.

3.5.7 Chemical Analysis of Carbides

This procedure was followed only in the case of alloy 4 (table 1) because even after solution treating for longer times at very high temperatures (> 1100°C), many undissolved carbides were observed within the matrix. It was found very difficult to determine the nature of the carbide by electron diffraction techniques.

After solution treating the bar at the selected temperature (table IV), the carbides were extracted in an electrolytic cell containing aqueous 10% HCl as electrolyte and using an electrolytic potentiostat. These extracted carbides were fused with Lithium - tetra-borate and a small amount of lanthium oxide to make them into a glass bead. This was further analysed by the x-ray fluoresence technique.

3.5.8 Quantitative Metallography

3.5.8.1 Volume Fraction Measurement

Thin foil techniques and transmission electron microscopy was used to measure the volume fraction of second phase particles both in the solution treatment and age hardening work. An estimation of the volume fraction of undissolved carbides during the solution treatment of the alloys was carried out, to verify various mathematical models of grain-growth. In the case of age-hardening, the volume fraction measurements of gamma-prime particles was determined on alloys 7 and 8 (table 1) at various stages of the age-hardening treatment , in order to obtain a constant volume fraction of γ' for further high-temperature testing.

The technique involved taking the photographs of certain

areas of thin foils representing reasonably general areas of the heat-treated material, and measuring the radius and number of undissolved or precipitated second phase particles at a given magnification. The usual calculations were carried out to determine the volume fraction, by extending the two dimensional data for three dimensional specimens.

Although this technique overcomes the resolution errors introduced by using the optical point counting method, the method is generally regarded to overestimate the volume fraction because only a slice of the material is viewed through the microscope. Also, the method assumes the shape of all the undissolved particles to be spherical, which may or may not be true in practice, e.g. Ti(CN) particles.

3.5.8.2 Crack Counting

Crack counting was carried out on all the specimens which wer tensile tested at 700°C. Sections of fractured specimens were cut as close to the diameter as possible, polished and etched in the usual way. The crack densities and average crack lengths were determined by counting the number of cracks per unit area at a constant magnification. Several such areas were examined in each specimen across the fractured cross-section. Crack counting was limited to areas within about 2mm of the fracture as the crack density was generally lower in the regions more remote from the fracture. The length of each crack was determined by estimating the number of grain facets (to the nearest one-quarter of a facet) covered by the crack.

4. EXPERIMENTAL RESULTS

4.1 THE EFFECT OF SOLUTION TREATMENT ON GRAIN COARSENING CHARACTERISTICS

The effect of time and temperature of solution treatment on the grain size of a series of alloys (table 1), building up in composition towards commercial PE16 analysis, for both bar and strip material are shown in Figs 12-27. In all the alloys, using a constant solution treatment time, the grain size remained fairly constant upto a particular solution treatment temperature at which grain coarsening commenced. This temperature varied from alloy to alloy. Below this grain coarsening temperature, the alloys which contained few undissolved particles showed a progressive increase in grain size with increasing solution treatment time, but there was less effect of time in alloys which contained second phase particles or higher solute concentrations. Above the grain coarsening temperature, the grain size continued to increase with increasing solution treatment temperature, but at a slower rate, and at these temperatures there was frequently a greater time dependence of grain size due to more rapid grain boundary migration.[174] The initial grainsize was usually finer in the strip material than in bar material due to the greater amount of deformation during the preparation of the material.[175,176] This was particularly the case where there were few second phase pinning particles, but the effect was virtually absent when the alloy contained appreciable numbers of particles, or solute capable of restricting grain-boundary migration.

4.1.1 Low Carbon Fe-Ni-Cr, Alloy No. 1 (Figs. 12 and 13)

This alloy contained very low carbon content $\sim$ 0.01%, and thus no undissolved carbides. In the bar the grain-coarsening temperature was $\sim$1100°C, and did not vary with solution treatment time. In the strip however, the initial grain size was rather finer and did not increase so markedly as for the bar with increasing solution treatment time below the grain coarsening temperature. The actual grain coarsening

temperature of the strip after short times was rather higher than that of bar, i.e. ~ 1150°C, but decreased rapidly to ~1050°C as the solution treatment time increased from ¼h to 4h. The increase in grain size with increasing time above the grain coarsening temperature was rather greater for the strip than for the bar, but the maximum grain size obtained was the same for both, i.e. ~0.4 mm.

4.1.2 Medium Carbon Fe-Ni-Cr, Alloy No. 2 (Figs. 14 and 15)

The only difference between alloys 1 and 2 was the higher carbon content of 0.05% in alloy 2. This carbon was largely in solution even at the lowest solution treatment temperature of 1000°C, and the initial grain size below the grain coarsening temperature was similar to that in alloy 1. The grain coarsening temperature in both bar and strip was at about 1100°C and did not vary with increasing solution treatment time. The maximum grain size above the grain coarsening temperature was ~ 0.4 mm. In general, the grain coarsening characteristics were rather similar to those of alloy 1.

4.1.3 High Carbon Fe-Ni-Cr, Alloy No. 3 (Figs. 16 and 17)

This alloy had the same base composition as alloys 1 and 2, but contained a rather higher carbon content of 0.10%. The grain coarsening characteristics were considerably different however, in that the initial grain size below the grain-coarsening temperature was much finer and moreover did not increase greatly with increasing time. The grain-coarsening temperature was sharply defined, and occurred at 1150°C, which was ~50°C higher than for the lower carbon alloys.

Grain growth above the grain coarsening temperature was not so pronounced as for the lower carbon alloys, particularly in the case of the strip material, although the grain coarsening temperatures for both strip and bar were virtually identical. The maximum grain size obtained above the grain coarsening temperature was considerably smaller than for the lower carbon alloys, at about 0.25/0.30 mm diameter.

4.1.4 High Carbon Molybdenum Alloy, Alloy No. 4 (Figs 18 and 19)

The alloy was identical with alloy 3 but contained an additio of ~3.5% Mo. The initial grain size below the grain coarsening temperature was similar to that observed for alloy 3, and was the same for both bar and strip. A reasonably sharp grain-coarsening temperature was observed at ~1100°C for solution treatment times up to ½ h, and this temperature was about 50°C lower than in the molybdenum free alloy, alloy 3. The grain size below the grain coarsening temperature increased progressively with increasing temperature and the grain coarsening temperature tended to decrease slightly with increasing solution treatment time. In general there was little difference between the grain coarsening temperature of strip and bar material. Above the grain coarsening temperature the strip had a finer grain size than the bar but the maximum observed grain size was in the range 0.16 mm - 0.24 mm diameter for both.

4.1.5 High Carbon Mo - Ti Alloy, Alloy No. 5 (Figs 20 and 21)

This alloy contained a slightly higher carbon content of 0.14% compared with alloy 4, and an addition of 1.18% Ti. Both alloys 4 and 5 contained ~3.5% Mo. The initial grain size below the grain coarsening temperature was similar to that of alloy 4, but grain coarsening occured at rather low temperatures, below 1100°C, and for the longer solution treatment time of 4 h the grain size coarsened progressively with increasing temperature above 1000°C. In fact, in this alloy there was a distinct effect in both strip and bar material for the grain coarsening temperature to decrease with increasing solution treatment time. The maximum grain size observed was however only about 0.12 mm diameter, which was very much less than that observed in the alloys free from titanium.

4.1.6 Extra High Carbon Mo - Ti Steel, Alloy No. 6 (figs. 22 and 23)

Alloy 6 was identical in composition to alloy 5 but contained a much higher carbon content of 0.35%. The initial grain size below the grain coarsening temperature was 0.01-0.02 mm diameter, which was the smallest for any of the alloys. This fine grain size was maintained upto the very sharp grain coarsening temperature which occurred at 1150°C for solution treatment times greater than 1h, and at ~1200°C for shorter solution treatment times. The grain coarsening temperature decreased progressively with increasing solution treatment time. Above the grain coarsening temperature the maximum grain size increased negligibly with increasing solution treatment time, but was by far the smallest of any of the alloys studied, being in the range 0.02/0.10 mm diameter.

4.1.7 Low Carbon PE16 Composition, Alloy No. 7 (Figs 24 and 25)

This alloy had an addition of 1.20% Al, compared with alloy 6, together with 0.002%B and 0.009% N_2 and was typical of the commercial PE16 composition except for a very low carbon content of 0.012%. The initial grain size below the grain coarsening temperature increased both with increasing temperature and with increasing solution treatment time. In fact, at any given temperature below the grain coarsening temperature the grainsize could vary by a factor of ~3 with increasing time from ¼h to 4h. This grain size was in the range 0.03/0.14 mm diameter, which was similar to that for the two low carbon alloys (1 and 2), and much coarser than was observed for the alloys containing 0.10%C with molybdenum and/or titanium. The grain coarsening temperature was quite sharply defined and occurred at 1100°C for all solution treatment times, the same for both strip and bar materials. However, the grain-size at which grain coarsening occurred, increased with increasing solution treatment time. Above the grain coarsening temperature the grain size increased markedly with both solution treatment temperature and time, and the maximum grain size observed was ~0.28 mm diameter which was similar to that for the alloys free from either molybdenum

and/or titanium.

4.1.8 High Carbon PE16 Composition, Alloy No. 8 (Figs 26 and 27)

This alloy is virtually identical in composition with alloy 7, but contained 0.12%C. It had the general composition of commercial PE16. Below the grain coarsening temperature, the time dependence of the grain size was much less than in alloy 7, and the grain size initially was of the order of 0.02/0.03 mm diameter, i.e. much finer than in the low carbon alloy. The grain coarsening temperature was at 1100°C for both strip and bar material increased with shorter solution treatment times, particularly in the strip material. Above the grain coarsening temperature the grain size increased with both increasing time and temperature, the time dependence being particularly marked in the bar material. The maximum grain size observed was in the range 0.08/0.12 mm diameter.

4.1.9 General Comparison of All Alloys (Figs 28, 29 and 30)

A general comparison was made of the grain coarsening characteristics, by showing the temperature dependence of the grain size for all the alloys after 1 hour solution treatment, Fig. 28. These curves will be discussed later. The time dependence of grain size below and above grain coarsening temperature for all alloys is shown in Table IL and Figs. 29 and 30, and activation energies were calculated, Table III. This information will be discussed later. The solution treatment temperatures selected for each alloy are shown in, Table IV and will be discussed further in section 4.4.4.

4.2 AGE HARDENING CHARACTERISTICS

Typical isothermal hardness curves are shown for each of the alloys in Figs. 31-38.

4.2.1 Low Carbon Base Composition, Alloy No. 1 (Fig. 31)

The ageing curves, showed that at all temperatures the hardness decreased below that of the solution treated condition.

The rate of decrease in hardness increased progressively as the ageing temperature increased from 500°C to 650°C, but at 700°C, the rate of decrease in hardness was less than at 550°C. This possibly indicates slight precipitation offsetting the annealing of the structure. Further increasing the ageing temperature from 750°C to 900°C caused the rate of decrease in hardness to accelerate. Ageing for longer times at 900°C could also contribute towards the grain growth, thereby further decreasing the hardness.

4.2.2. Medium Carbon Base Composition, Alloy No. 2(Fig. 32)

The lower initial solution treated hardness of this alloy which contained 0.049%C indicates that alloy 1 was probably strained during quenching so as to generate the dislocations. The intensity of age hardening was small, the maximum increase in hardness being ~20HV. In general the rate of age-hardening increased with increasing ageing temperature, and the maximum hardness decreased.

4.2.3 High Carbon Base Composition, Alloy No. 3 (Fig. 33)

Due to the increased carbon content of 0.101% much more intense age-hardening was observed, the maximum increase in hardness being~40 HV. The age hardening followed the well known trend for the rate of ageing to increase and the maximum hardnes to decrease with increasing ageing temperature. There was an indication that a two stage age hardening process occurred, as also indicated by the results from alloy 2, and this will be discussed later.

4.2.4 High Carbon Molybdenum Steel,Alloy No. 4 (Fig. 34)

The ageing curves show some unusual features. The solution treated hardness was higher than that of the alloy 3 despite the same carbon content. The reason for this is believed to be the dislocations introduced into the structure due to stresses produced by differential thermal expansion effects between the undissolved carbides and the matrix. Such a

feature has frequently been observed in other austenitic alloys containing undissolved carbides.(177) These dislocations are annealed but during the ageing treatment, the extent to which this occurs depending on competition between the annealing process and the precipitation process because carbides can precipitate on dislocations and prevent them annealing out. The presence of undissolved carbides resulted in less precipitation during ageing, Table V, which accounts for the smaller increment in hardnes, i.e. ~20HV, compared with alloy 3. Also, the annealing out of the dislocations can explain the fact that the hardness levels in the early stages of ageing and in the heavily overaged condition was often lower than the initial solution treated hardness. The competition between the ageing and annealing effects may also explain the unusual agei characteristics, which show a fairly rapid reaction at 500-600°C, but an apparently different and slower reaction at 650-900°C. This will be discussed in detail later in the thesis.

4.2.5 High Carbon Molybdenum, Titanium Steel, Alloy No. 5 (Fig. 35)

The composition of this alloy was similar to that of alloy 4 plus an addition of 1.18% Ti at the slightly higher carbon content of 0.14%. It was expected that Ti would result in a considerable amount of undissolved TiC, and being in excess of the stoichiometric ratio had probably removed most the carbon from solution and at the same time decreased the titanium in the solution down to ~ 0.65%. The solution treated hardnes was 171 HV due mainly to dislocations generated by the undissolved TiC, together with slight dispersion strengthening and solid solution strengthening by the dissolved Ti. The most noticeable effect was the rapid initial age hardening, which could probably be due to the formation of zones of γ' - Ni_3 Ti, for the titanium remaining in the solution may have been just sufficient for some γ' - Ni_3 Ti to be precipitated

The maximum hardness increment observed was ~40HV, which suggests that age hardening may only be due to carbide precipitation. This also will be discussed later.

4.2.6 Extra High Carbon Molybdenum, Titanium Steel, Alloy No. 6 (Fig. 36)

This alloy was similar to alloy 5 but with an increased carbon content of 0.35%. This will have, providing all the titanium has combined with the carbon, virtually removed both carbon and titanium from solution, but the use of 1150°C as a solution treatment temperature and the fact that the alloy contains less than the stoichiometric Ti:C ratio, will have resulted in there being a small amount of carbon remaining in solution prior to ageing. The Ti remaining in solution however was not sufficient to cause the precipitation of γ'- Ni_3 Ti. The ageing curves were similar to those for alloy 5, but the ageing was rather slower and much less intense. A hardness increment of ~ 25 HV was observed compared with ~40HV for alloy 5. These features may be explained by a smaller amount of carbon, and particularly of titanium, in solution and available for precipitation during ageing. The evidence therefore suggests that in both alloys 5 and 6, the ageing observed was mainly due to carbide precipitation.

4.2.7 Low Carbon PE16 Composition, Alloy No. 7 (Fig. 37)

This alloy was of the commercial PE16, composition but contained only 0.012%C. The solution treated hardness was very low, due to the absence of carbon in solution and any dispersed phases apart from a very small amount of TiC and TiN. It can be seen that a very much increased age-hardening effect was observed compared with all the previous alloys. The maximum increase in hardness was ~140HV. Ageing was slow at 500°C but increased rapidly as the ageing temperature increased. The major age hardening could not have been due to carbide, and will be shown later to be the result of γ'-Ni_3 (Al, Ti) precipitation. The aluminium and titanium combined to give a reasonable volume fraction of γ' and thus much increased age hardening.

The ageing curves indicated a two stage age hardening process and such effects have been observed in other alloys containing nickel, titanium and aluminium.[40,41] The interpretation of this two stage ageing will be discussed later.

4.2.8 High Carbon PE16 Composition, Alloy No. 8 (Fig. 38)

This alloy of commercial PE16 composition contained 0.12%C. Because of the higher carbon content, the amount of undissolved TiC and TiN increased, which in effect lowered the amount of Ti in solution to below the level in alloy 7. This was shown by the slightly smaller increase in hardness of ~ 120HV compared with ~ 140HV in alloy 7, due to the smaller volume fraction of γ' which had precipitated. In general however, the ageing characteristics were very similar to those observed for the low carbon PE16, alloy 7, a two stage age hardening process being clearly visible.

The effect of the lower titanium in solution compared with alloy 7, was most evident in the decreased maximum hardness increment during ageing at 850°C and 900°C, when γ' probably precipitated directly from the matrix without intermediate zone formation.

4.2.9 General Comparison of Ageing Characteristics

The precipitation curves for the various carbide forming alloys a shown in Fig. 39, and also the effect of varying carbon content on the maximum intensity of age hardening in the same base composition (Alloy 1,2, and 3) is shown in Fig. 40. There appears to be a linear increase in hardness with increasing carbon content at all ageing temperatures. The intensity of age hardening as a function of temperature is shown in Fig. 41, where the titanium bearing alloys are compared with the molybdenum and the molybdenum free alloys. These results will be discussed in detail in a later section of this thesis. A general comparison is made between alloys precipitating carbides alone and those precipitating γ', and the effect of temperature on the maximum increase in hardness during ageing, in Fig. 42. Two very different ageing reactions are involved. The selected ageing treatments are shown in Table VI and will be considered in detail in section 4.4.4.

4.3 COMBINED EFFECT OF COLD WORK AND AGEING ON PRECIPITATION AND RECRYSTALLIZATION CHARACTERISTICS

To investigate the effect of 40%, 60% and 80% cold rolling

reduction on the ageing characteristics, a selection of alloys (table 1) was used, ommitting alloys 1 and 6. Hardness tests were carried out on both cold worked and aged material. The effect of cold rolling on the hardness of unaged material is shown in Fig. 43, from which the work hardening rate may be assessed, Table VII. Also graphs of hardness after various times at ageing temperatures of 650°C, 700°C and 750°C were used to establish precipitation/recrystallization characteristics. Only selected graphs of such nature have been shown to emphasise certain special effects exerted by the alloying additions, Figs 44-58. In general, the results clearly indicated a pattern of effects with respect to cold reduction, ageing temperature and alloy composition. The effect of alloying additions and precipitation on recrystallization were clearly apparent. These effects will be categorized and discussed in detail.

In addition, the hardness data was used to derive a percentage change in hardness for various times at any given temperature, assuming that the matrix was fully recrystallized at the longest ageing time. The percentage was calculated as:-

$$\% \Delta H = \frac{H_o - H}{H_o - H_f} \times 100$$

where H_f is the hardness of fully recrystallised matrix, H the hardness at any stage of ageing and H_o the initial hardness. Activation energies at 50% recrystallization were calculated by plotting $\% \Delta H$ against ageing time at various temperatures for each cold worked condition, Table VIII. In general, the normalised hardness curves showed an eventual softening when recovery, and recrystallisation were completed, but in the case of PE16 compositions, there was a continuous increase in hardness on ageing, even after 80% cold reduction. An attempt was made to obtain the effects of recovery and recrystallization for these alloys by assuming that cold working did not influence the kinetics of gamma-prime precipitation, and subtracting the corresponding hardness values for 0% cold work. Such normalised hardness curves will be referred to as "softening curves". An account of special features observed with varying alloy composition are described in the following subsections.

4.3.1 Medium Carbon Base Composition, Alloy No. 2

The hardness increased with increasing cold reduction, but the increment of hardness was smallest in comparison with other alloys, Fig. 43. The effect of ageing on the hardness at various cold reductions is shown in Figs. 44 to 46. There was an increasing rate of softening both with increasing reduction and ageing time, and also the hardness in the fully recrystallized state was always higher than that of 0% cold worked material. The final hardness values of the recrystallized specimens increased with increasing amount of cold work at any ageing temperature, Fig. 45, and decreased with increasing ageing temperature for a given cold reduction, Fig. 46. A slightly enhanced ageing, Fig. 44, perhaps due to carbide precipitation was observed after the intermediate amounts of cold working. Indirect evidence for this effect was also available in softening curves for 40% cold reduction, Fig. 47, where the hardness maxima were much more marked, showing negative softening, i.e. precipitation effects. It seems clear that precipitation preceded any recrystallization processes.

4.3.2 High Carbon Base Composition, Alloy No. 3

The increase in hardness during cold rolling was similar to that of alloy 2, but the actual level of hardness was higher than for alloy 2, Fig. 43. This effect could be due to a combination of the finer grain size and higher carbon content giving more undissolved carbides in the matrix after solution treatment. Both these effects are known to increase the overall dislocation density of the matrix after cold working.(95) Ageing did not seem to have altered the recrystallization characteristics to any significant extent, Figs 44 and 48, but no pronounced age-hardening peak was observed in the case of alloy 3, Fig. 48. However, the softening curves showed slight precipitation at shorter ageing times and at lower ageing temperatures, Fig. 49. The overall softening effect was probably due to the increased dislocation density in the cold worked matrix, whereas the precipitation of carbides was insufficient to produce an increase in hardness to offset the annealing out of dislocations on ageing.

4.3.3 High Carbon Molybdenum Steel, Alloy No. 4

The effect of molybdenum on the level of hardness during cold working was evident, Fig. 43, and this alloy showed the highest cold worked hardness at 60% and 80% cold reduction. This was probably due to the effect of undissolved carbides and also due to Mo decreasing the stacking fault energy so that the work hardening rate actually increased, see Fig. 43. The ageing of the cold worked structure showed certain interacting features, presented in Figs. 50 and 51. First the temperature dependence of recrystallization was clearly portrayed, Fig. 50. At 650°C the decrease in hardness was small compared with 700°C and 750°C ageing temperatures. This showed an inhibition of dislocation movement caused by slow diffusion rates of molybdenum at lower temperatures. The immediate decrease of hardness on ageing for shorter times, Fig. 50, followed by a gradual increase, suggested localised softening at high dislocation density sites near to undissolved carbides. Such temperature effects and delayed precipitation are clearly shown in Fig. 51, where even after 80% cold-work there are clearly defined hardness maxima. It is suggested that recrystallization and precipitation mechanisms occur together in competition in this particular alloy, at least at lower ageing temperatures, Fig. 50.

4.3.4 High Carbon Molybdenum, Titanium, Steel, Alloy No. 5

The work hardening characteristics were very similar to those of alloy 4, but the general level of the hardness was lower than in alloy 5 at 60% and 80% cold work, probably due to fewer undissolved carbides, Fig. 43. The precipitation and recrystallization characteristics however were very similar to those of alloy 4, Figs. 52 and 53, despite the addition of titanium. The slow diffusion of Mo and Ti was clearly evident at lower temperatures, Fig. 52, where there was hardly any decrease in the hardness at 650°C, even after 100 hours of ageing. Surprisingly, there seemed to be two hardness maxima at all temperatures, the first during the initial stages of ageing and the second towards longer ageing times, Fig. 52. These results indicate the possibility of two ageing reactions occurring i.e. two types of precipitates. Whilst the validity

of the second ageing peak may be questioned, its significance will be discussed later with the help of electron microscopical evidence.

4.3.5 PE16 Compositions, Alloy Nos. 7 and 8

Both these alloys were of PE16 composition with varying carbon-contents. The variation of hardness with cold reduction was very similar in both, Fig. 43. The effect of ageing after cold working is shown for both alloys in Figs. 54 and 55 respectively. There was a consistent increase of hardness for both alloys at all cold reductions, even during ageing at 750°C. The rate of age-hardening increased with increased cold work for both alloys, although it seemed to be higher in the case of low carbon PE16 than in the higher carbon alloy. Also, the final hardness was higher than the initial cold worked hardness for both alloys, even after the longest ageing times at 750°C. The softening curves for both alloys are shown in Figs. 56 and 57. Both alloys showed negative softening after all cold reductions, and the magnitude of the negative softening, or age-hardening, increased with increasing cold work. Perhaps the negative softening is an indication of the enhanced rate of gamma-prime precipitation due to cold working. However, the effect seemed to be more pronounced in the low carbon PE16 than in the higher carbon alloy.

4.3.6 General Comparison of All Alloys

A general comparison of all the alloys aged at 700°C, and after 40% cold work, is shown in Fig. 58. The alloys each show the features mentioned earlier, and a definite difference can be detected between carbide forming and gamma prime forming alloys.

The various carbide forming alloys were further compared on the basis of their activation energy values for 50% softening and the results are shown in Table VIII and Fig. 59. It is evident that in all cases, the activation energy for recrystallization decreases with increasing cold reduction, and the effects could be related to the increased dislocation

density induced by increased cold working, thereby accelerating diffusion. The magnitude of the activation energy in alloy 2 at 40% cold reduction is the same as for its grain growth below th grain coarsening temperature. Surprisingly, the activation energy for the 0.1%C alloy, was lower than that for the 0.049%C alloy, at all cold reductions. This effect might be related to the increased dislocation density in the higher carbon steel due to the finer grain size and undissolved carbides. However, in the alloys containing Mo and Ti, the magnitude of the activation energy compared well with that for grain-boundary migration in austenite. Also, for high and low carbon PE16 alloys, the magnitude of the activation energy was very low, table VIII. These results will be discussed in detail later.

4.4 MICROSTRUCTURAL FEATURES

The cast structure, a typical example being shown in Plate 1(a), revealed coring which was removed by hot rolling to produce a fine grained structure with a few undissolved carbides present in an austenite matrix, Plate 1(b). The further details of microstructural features produced on further treatments will be discussed in the following sections.

4.4.1 Solution Treated Structures

The base composition (Alloy No. 1) contained virtually no second phase particles, the carbon content being ~0.01%. However a few chromite particles were present . The electron microscopy of the solution treated structures revealed the presence of a fairly high dislocation density, Plate 1(c). This feature has often been observed in quenched stainless steels and is due to the quenching strains. The medium carbon steel (alloy No. 2) also did not contain any undissolved particles and the solution treated structure was similar to that of the base composition. The high carbon alloy (alloy No. 3) showed many undissolved carbides even after solution treating at 1100°C for 4 hours. This indicates that the high nickel content appreciably reduces the solubility of carbon in austenite, for such undissolved $M_{23}C_6$ would not be present

in a lower nickel austenitic stainless steel solution treated at 1100°C.

The molybdenum containing alloy (alloy No. 4), showed a large amount of undissolved carbides, plate 1(d), after solution treating at 1100°C for 2 hours. The carbides were in the form of stringers, resulting from rolling. Electron microscopy of the solution treated condition showed a randomly distributed and high volume fraction of carbides, plate 1(e). Electron diffraction patterns identified these as $M_{23}C_6$ or M_6C type carbides, suggesting that Mo stabilised the carbides, thereby reducing their solubility in austenite. However, the extraction of the carbides and further identification by x-ray flourescent analysis revealed the composition to be $(Cr_{15}\ Fe_4\ Ni_2\ Mo_2)C_6$, suggesting a combined stabilizing effect exerted by both nickel and molybdenum.

The high carbon titanium bearing alloy (alloy No. 5) contained a considerable amount of undissolved TiC, Plate 1(f) distributed randomly with varying particle sizes. Most of the grain-boundaries were free from precipitates, Plate 2(a). On the contrary, the extra-high carbon titanium bearing alloy (alloy No. 6) contained a much larger volume fraction of undissolved TiC after solution treatment, and precipitates were present at grain-boundaries, Plate 2(b). The overall effect of varying carbon contents was very evident on the volume fraction of undissolved TiC even after very high solution treatment temperatures and longer heating times.

Both the low and high carbon PE16 compositions were observed to contain both TiC and TiN particles after solution treatment. As expected, the nitrides were a direct result of the intentional addition of nitrogen during alloy preparation, Table 1, perhaps formed during the casting of the alloys. However, there was a smaller amount of TiC/TiN in low carbon PE16 than was observed in the high carbon alloy. In the case of alloys containing second phase particles, the volume fractions of these were calculated and various mathematical models for grain-coarsening characteristics compared, Table IX. These results will be discussed later.

4.4.2 Aged Microstructures

4.4.2.1 Low Carbon Base Composition (Alloy No. 1)

Ageing at 700°C caused a smaller decrease in hardness than expected, Fig. 31, which may have been due to some $M_{23}C_6$ precipitation. Whilst no clear signs of $M_{23}C_6$ precipitation were observed optically, confirmation of this suggestion was obtained from electron microscopical examination, which showed fine precipitates of $M_{23}C_6$, predominantly at triple junctions and occasionally on grain boundaries. There were no signs of precipitation within the grains or at non-coherent twin-boundaries. At higher ageing temperatures of 900°C some grain-growth was clearly observed, especially at the longer ageing times.

4.4.2.2 Medium Carbon Base Composition (Alloy No. 2)

Some precipitation of $M_{23}C_6$ was observed by optical microscopy, occurring mainly at the austenite grain boundaries, Plate 2 (c) and (d). At higher ageing temperatures the carbides spheroidised. However, electron microscopical examination revealed the precipitation occurring at both triple point junctions and at grain boundaries, at temperatures as low as 550°C. The precipitates were identified as $M_{23}C_6$ by electron diffraction, and the general orientation relationship with one of the contiguous grains found to be $\{111\}\langle 110\rangle M_{23}C_6 // \{111\}\langle 110\rangle$ austenite. At higher ageing temperatures the $M_{23}C_6$ was observed on non-coherent twin boundaries, and also the non-coherent ledges associated with coherent twin boundaries. The orientation relationship of these precipitates with the matrix was the same as that given above. Very little precipitation was observed within the grains, although dislocations showed a 'dot' contrast effect. It was not possible to obtain a clear diffraction pattern to establish whether precipitates were present on the dislocations. All the precipitates coarsened with increasing ageing temperatures. However, at higher ageing temperatures (800°C and above) there was a much more limited amount of $M_{23}C_6$ present.

4.4.2.3 High Carbon Base Composition (Alloy No. 3)

Typical optical microstructures are shown in Plates (e) and (f) Ageing at 650°C produced a grain boundary network of $M_{23}C_6$ after 30 minutes, but longer ageing times or higher temperatures, i.e. 700°C - 16 hours, produced very heavy $M_{23}C_6$ precipitation locally near the grain boundary and a general carbide precipitation within the grains. These two stages of precipitation seem to be related to the two stage age-hardening reaction which was observed. These structures, showing marked precipitation, were very different from a 0.10%C conventional stainless steel containing 10-12% Ni, and indeed were more typical of higher carbon stainless steels, thus confirming that Ni decreases the solubility of carbon in austenite.

Electron microscopical examination revealed grain-boundary and non-coherent twin boundary precipitation at temperatures as low as 550°C. A typical micrograph revealing grain boundary precipitates in the shape of continuous chain of gobules is shown in Plate 3(a). There was a cube-on-cube orientation relationship between the grain-boundary $M_{23}C_6$ and one of the contiguous grains. The first signs of matrix precipitation were observed after longer ageing times at 600°C, Plate 3(b), clearly revealing a Widmanstatten morphology, with an orientation relationship of $M_{23}C_6$ $\{111\}$ $\langle 110\rangle$ // to $\{111\}$ $\langle 110\rangle$ of austenite. At higher ageing temperatures the matrix Widmanstatten $M_{23}C_6$ occurred at very short ageing times (700°C at 1 hour), and the orientation relationships were again cube-on-cube. Also, at longer ageing times the amount of precipitation increased greatly, Plate 3(c), and there were signs of coherent twin boundary precipitation of $M_{23}C_6$, Plate 3(d). A further increase in ageing temperature caused precipitates to coarsen, Plate 3 (e). However, increasing the ageing temperature from 750°C to 800°C decreased the amount of precipitation, Plate 3(f), no matrix $M_{23}C_6$ being observed. This effect was due to the increased solubility at the higher ageing temperature.

4.4.2.4 High Carbon, Molybdenum Alloy (Alloy No. 4)

At lower ageing temperatures accelerated precipitation of

$M_{23}C_6$ carbides was observed on dislocations, Plate 4(a), with a cube-on-cube orientation relationship with the matrix. At these temperatures very little grain-boundary precipitation was observed, and this could be the reason for the rapidity of ageing at low temperatures, Fig. 34. However, at higher ageing temperatures only triple point and grain-boundary precipitates were visible, Plates 4 (b) and (c), corresponding to the slower ageing reaction. It is possible that the dislocations annealed out rapidly at higher ageing temperatures thus only allowing relatively slow grain boundary precipitation of carbide. The orientation relationship of these carbides was found to be $M_{23}C_6$ {111} <110>// to {111} <110> with one of the contiguous austenite grains. Only grain-boundary precipitation was observed by optical microscopy when the slower ageing reaction had occurred, Plate 4(e), and it is also significant that the general kinetics of this slower process are of a general order of magnitude similar to those in the molybdenum free alloy 3. However, with longer ageing times and higher temperatures (750°C/100 hours) there were very fine precipitates along coherent twin boundaries, Plate 4(f). A further increase in ageing temperature caused precipitate coarsening, particularly within the matrix and at non-coherent twin boundaries, Plates 5 (a) and (b). The matrix precipitate resembled a more Widmanstatten morphology, Plate 5(a), suggesting that these had nucleated on vacancies.

4.4.2.5 High Carbon, Molybdenum and Titanium Alloy (No. 5)

Electron microcopy showed that γ' precipitation did not occur in this alloy, despite possible indications of a two stage ageing reaction from the hardness measurements. Electron diffraction gave no superlattice reflections.

The optical microstructures, Plates 5(c),(d) and (e), showed that grain boundary precipitation occurred, which could be either $M_{23}C_6$ or TiC depending on the amount of carbon in solution at the solution treatment temperature and the relative kinetics of $M_{23}C_6$ and TiC precipitation. First, signs of grain-boundary $M_{23}C_6$ precipitation were visible at 500°C at the longer ageing times, but discrete particles of $M_{23}C_6$

were only seen at ageing temperature above 600°C, Plate 5(f). At these ageing temperatures there was some non-coherent twin boundary precipitation, and the orientation relationship of carbides at both sites was that of a cube-on-cube. No major change occurred in the morphology of the grain-boundary $M_{23}C_6$ precipitates on increasing the ageing temperature to 750°C, Plates 6(a) and (b), but the first signs of TiC precipitation were clearly visible at this temperature, particularly on dislocations within the matrix, Plate 6(c). Increasing the ageing temperature to 800°C caused some grain-boundary TiC precipitation together with $M_{23}C_6$, Plate 6(d). Generally, $M_{23}C_6$ particles at grain-boundaries were observed to be larger in size than TiC precipitates on the same boundary, but the particle size increased with increasing ageing time for both phases.

4.4.2.6 Extra High Carbon, Molybdenum and Titanium Alloy No 6

The first signs of precipitation in this alloy were observed at 650°C, when precipitates were predominantly seen at grain boundaries and identified as $M_{23}C_6$ with a cube-on-cube orientation relationship with one of the contiguous grains. However, at higher ageing temperatures some non-coherent twin-boundary precipitation was also observed having an orientation relationship of $\{111\} / \langle 110 \rangle$ of $M_{23}C_6$ // to $\{111\} \langle 110 \rangle$ of austenite. Such precipitation was clearly visible even optically, Plate 6(e), but there was no evidence of any TiC precipitation either at grain-boundaries or within the grains.

4.4.2.7 Low Carbon PE16 Composition (Alloy No. 7)

At lower ageing temperatures there was evidence for a small amount of carbide precipitation, Plate 6(f), but this was not detectable by optical microscopy until the highest ageing temperature of 900°C, Plate 7(a).

However, a detailed electron microscopical examination revealed grain-boundary precipitation of $M_{23}C_6$ on ageing at 500°C, but no γ' zones were seen even at the longer ageing times at 500°C. Nevertheless, the matrix did reveal a few

super dislocations, Plate 7(b), which suggests the existence of an ordered structure. Clear signs of a mottling effect due to γ' zone formation were observed after ageing at 550°C, Plate 7(c), and this was confirmed by obtaining superlattice reflections on diffraction patterns from the matrix area. With increasing ageing time and temperature the density of zones increased, Plate 7(d), and also there was also an increase in $M_{23}C_6$ precipitation at grain-boundaries, Plate 7(e). Not until longer ageing times at 750°C were the γ' precipitates starting to lose coherency with the matrix and appeared as semi-coherent particles uniformly distributed throughout the matrix, Plate 7(f). A further increase in the ageing temperature caused an overall increase in the semicoherent γ' particle diameter, Plate 8(a), which clearly revealed the spherical shape of the particles. However, at higher ageing temperatures grain-boundary $M_{23}C_6$ precipitation was observed to be limited to relatively few grain-boundaries, and the overall volume fraction of such precipitates was greatly reduced. At 850°C and above, γ' was observed to precipitate directly from the matrix without intermediate zone formation, even after very short ageing times.

4.4.2.8 High Carbon PE16 Composition (Alloy 8)

The optical microstructures were very similar to those observed for alloy 7, Plate 8(b), except for an increased amount of carbide precipitation at grain-boundaries due to the higher carbon content.

The electron microstructures showed $M_{23}C_6$ precipitation at ageing temperatures as low as 500°C, particularly at triple points and grain boundaries, whereas γ' zone formation was not observed until longer ageing times at 600°C. The delayed zone formation could be an effect of less titanium in solution due to increased amounts of undissolved TiC in this alloy. The intensity of zone formation increased with increasing ageing temperatures, Plate 8(c), and carbide precipitation was observed to occur on non-coherent twin boundaries. Most of these carbides were uniformly distributed along grain-boundaries, Plates 8(d)and(e). After longer ageing times at

750°C the γ' zones had grown appreciably and some showed strained regions around them, Plate 8(f). Also, at 750°C $M_{23}C_6$ was observed to precipitate on the undissolved TiC/matrix interface , plates 9(a) and(b) with a cube-on-cube orientation relationship with the matrix, perhaps nucleating on the interface dislocations. At longer ageing times at 750°C the growing γ' zones were observed partially to loose coherency, Plate 9(c), although some of the zones were still completely coherent with the matrix. Particle growth was observed at 800°C where nearly all the precipitates were semi-coherent after longer ageing times, Plate 9(d). This was accompanied by growth of the grain-boundary $M_{23}C_6$, Plates 9(e) and(f). There were no signs of TiC precipitation at any ageing temperature, and the microstructural features at 850°C and above were very similar to those described for alloy 7.

4.4.3 Cold Worked and Aged Structures

Optical microstructures of strip samples cold rolled by 40%, 60% and 80% reduction showed similar features for the various alloys. At 40% reduction, parallel groups of deformation bands, mostly aligned along the rolling direction of the elongated austenite grains were observed. At 60% reduction the number of deformation bands had increased, and they were observed in several directions within the same grain. With 80% reduction, however, no detail could be resolved in polished and etched samples, particularly in the finer grained alloys.

Electron microscopy did not reveal individual dislocations readily even after 40% reduction, although occasional diffuse cell structures were found. In the regions of deformation bands, high dislocation densities were observed. Increasing the reduction from 40 to 60% resulted in an increase in the number of deformation bands and pronounced arcing of diffraction patterns. At very heavy deformations (80%) the structure was considerably more diffuse, and the diffraction patterns obtained from these areas approximated to ring patterns.

The following sections describe the microstructure of the deformed and aged specimens for each alloy with respect to precipitation and recrystallization effects.

4.4.3.1 Medium Carbon Base Composition (Alloy 2)

Optical microstructures clearly revealed the formation of carbides on the elongated grain-boundaries, even after the shortest ageing times at the lowest ageing temperature, Plate 10(a). The precipitates also had occurred on the deformation bands, formed during cold working. The amount of such precipitation was observed to increase both with increasing cold working and increasing ageing temperature and time, Plate 10(b). There was very strong evidence that precipitation occurred prior to recrystallization. At longer ageing times and moderate (40%) deformation, areas of recrystallization were observed, having nucleated at prior grain-boundaries and growing within the elongated grain, Plate 10(b). Plate 10(c) illustrates the formation of subgrains at grain-boundaries, even after shorter ageing times at lower temperatures. Nucleatio and growth of these subgrains occurred at both sides of the boundary and such effects were not visible optically, particularl at lower ageing temperatures. Growing recrystallized nuclei within the grains were also observed, occurring in or near to the deformation bands due to higher energy associated with such sites. These regions revealed a cell structure, with a great decrease in dislocation density within the cells, whilst the cell walls were sharp and clearly defined.

Optical microscopy of heavily (80%) deformed and aged strip showed heavy carbide precipitation and a few recrystallized grains, even after the shortest ageing times at lower ageing temperatures, Plate 10(d). However, such structures were seen to be almost fully recrystallized by electron microscopy, Plate 10(e), and some cold-worked regions were being consumed by the growing recrystallised grains. The micrograph also showed bands of $M_{23}C_6$ carbides precipitated along the deformation bands. The carbides had a cube-on-cube orientation relationship with the matrix. The unrecrystallized parts of the structure indicated a general rearrangement of the dislocations on a fine scale, when seen at higher magnifications, Plate 10(f), i.e. recovery had occurred. Selected area diffraction of these deformed regions showed that the rings and streaks in the cold worked condition had broken up into discrete spots, indicative of recovery and subgrain

formation.

4.4.3.2 High Carbon Base Composition (Alloy No. 3)

Optical microstructures showed very similar precipitation and recrystallization structures to those in the lower carbon alloy (alloy No. 2), Plate 11(a), except that more intense precipitation was observed along deformation bands in the higher carbon composition. Electron microscopy confirmed the precipitation of $M_{23}C_6$ on deformed grain-boundaries prior to any recrystallization in moderately deformed material, Plate 11(b), the orientation relationship again being cube-on-cube with one of the contiguous grains. However, areas around undissolved $M_{23}C_6$ particles in this alloy were observed to show enhanced recovery and recrystallization effects, Plate 11(c), suggesting that the carbide interfaces acted as a nucleation site for recrystallization. Also, there were regions where recrystallized grain boundaries were observed to have been pinned by precipitated $M_{23}C_6$ particles, Plate 11(d). This behaviour suggests that nucleation of these $M_{23}C_6$ precipitates occurred initially on dislocations, as such pinning particles were more evident after heavy deformation.

4.4.3.3 High Carbon Molybdenum Alloy, (Alloy No. 4)

Together with the carbide precipitation on deformed grain-boundaries, the recovered regions around undissolved $M_{23}C_6$ particles were very clearly observed even after shortest ageing times at the lowest ageing temperatures. However, regions around the deformed grain boundaries showed some rearrangement of dislocation structure, Plate 11(e), suggesting an incipient subgrain formation. However, the dislocation rearrangement was not enhanced by increasing the ageing time, particularly at lower ageing temperatures, which indicated retardation of dislocation movement due to the molybdenum. Such effects were not evident in the molybdenum free alloys. Increasing ageing temperature enhanced dislocation movement, resulting in marked subgrain formation near the deformed grain-boundaries. Some very fine precipitation was also observed on certain dislocations, but it was extremely difficult to obtain the diffraction patterns

to identify the carbides because of their small size. Increasing cold work resulted in enhanced recrystallization, Plate 11(f), and the pinning effects due to $M_{23}C_6$ precipitation were also evident.

4.4.3.4 High Carbon Molybdenum, Titanium Alloy (No. 5)

The precipitation and recrystallization characteristics were very similar to those of alloy No. 4, showing a poorly developed cell structure at lower ageing times and lower cold reductions. Optical microscopy revealed the precipitation of carbides along deformed grain-boundaries and deformation bands prior to any recrystallization, and these precipitates were identified as $M_{23}C_6$. The temperature dependence of recrystallization was very obvious, particularly at very high cold-reductions, Plate 12(a), which shows complete recrystallization at intermediate ageing temperatures. Some grain-boundary pinning effects due to precipitated carbides were observed. Nevertheless, at ageing temperatures of 700°C there were regions showing partial recrystallization, Plate 12(b). This type of structure was not frequently observed in the molybdenum containing alloy (No. 4), thereby suggesting that even slower diffusion rates were prevalent in the titanium bearing composition However, at very high ageing temperatures $\sim$ 750°C, the matrix was fully recrystallized even after intermediate ageing times, Plate 12(c), with $M_{23}C_6$ carbides dispersed throughout the structure. At this ageing temperature, TiC was observed to precipitate on dislocations within the recrystallized grains, Plate 12(d), having an orientation of $\{110\}\langle 111\rangle_{TiC}$ // to $\{110\}\langle 111\rangle_{\gamma}$. An increase in the ageing time caused the growth of recrystallized grains, Plate 12(e), and to a limited extent coarsening of carbides. Also, Plate 12(e) clearly reveals the precipitated $M_{23}C_6$ particles on dislocations, and some pinning effect of the growing grains.

4.4.3.5 Low and High Carbon PE16 Compositions (No. 7 and 8)

Low carbon PE16 composition did not show any substantial amount of carbide precipitation during ageing after cold working, apart from occasional $M_{23}C_6$ particles present on

deformed grain-boundaries. Cold working prior to the ageing treatment was however found to enhance the rate of γ' zone formation, Plate 12(f), which shows intense zone formation within the cold worked structure even after ageing temperatures as low as 650°C. Also, the rate of growth of the zones increased, Plate 13(a), which shows semi-coherent γ' particles within the deformed structure after ageing 750°C/30 hours. Such effects were not observed in the solution treated and aged condition. These observations suggest that the precipitation of γ' may occur on dislocations, and the rate of growth of γ' precipitates so nucleated would be expected to increase due to enhanced diffusion along dislocations. However the increased vacancy concentration due to cold working will also enhance γ' growth. These observations are further supported by the fact that the matrix only revealed a slightly modified dislocation structure even after ageing at temperature as high as 750°C, Plate 13(b). However, at very long ageing times at 750°C and 80% cold reduction, recrystallized nuclei were observed within the deformed structure, Plate 13(c). Whilst all the subgrain boundaries were not clearly defined, Plate 13(d), selected area diffraction revealed discrete spots, indicating that a general rearrangement of the dislocations during recovery was occurring. Nevertheless, the overall recrystallization rate was greatly reduced at all cold working reductions in this alloy.

High carbon PE16 showed a considerable amount of $M_{23}C_6$ precipitation along deformed grain boundaries compared with the low carbon composition. The effect of coldworking on γ' precipitation was very similar to that in the low carbon alloy, showing an increase in the rate of nucleation and growth of these precipitates at all cold-working reductions. The recrystallization mechanisms were also similar to those in the low carbon alloy, Plate 13(e). The rate of recrystallization was slightly faster in the higher carbon alloy, Plate 13(f), compared with the lower carbon composition, and the effect was observed to be more pronounced with increasing cold working, Plates 13(e) and(f). Such effects may be attributed to a larger amount of TiC in the high carbon alloy, thereby leaving less titanium for γ' precipitation. Also, the undissolved TiC helped

recrystallization, and this was evident at all ageing temperatures.

4.4.4 Selection of Heat Treatments For Producing Various Microstructural Features

(a) Solution Treatment Selection

In order to achieve as much solution of precipitate particles as possible, so as to obtain a maximum ageing response, as high a solution treatment as possible was required. This allowed not only the kinetics of the ageing process, but also major microstructural changes to be introduced for subsequent investigation by high temperature testing. However, during high temperature creep and rupture testing, intergranular fracture has been a frequently observed phenomenon in alloys of the PE16 type, and this could lead to anomolously low ductility. Consequently it might be expected that changes in high temperature ductility could be obscured if too coarse an initial grain-size was used. It was necessary therefore to achieve as much solution as possible consistent with as fine an initial grain size as possible.

From the results obtained, solution treatment conditions were selected using the above criterion, and applied prior to the study of ageing characteristics. This was done for the bar material in the case of the ageing characteristics, but solution treatments were selected for the strip materials which were to be used to investigate the effect of cold rolling prior to ageing so that comparable grain sizes were achieved for both bar and strip material. These solution treatment conditions, together with the associated grain size and hardness values are shown in Table IV. In the case of alloys 3, 5 and 8, the solution treatment temperatures were identical for both bar and strip material, and varied only very slightly in the cases of the other alloys. In every case, the grain size in strip and bar after these selected solution treatment conditions were very similar for a given alloy. Because of the presence of large volume fractions of grain-boundary pinning particles in some of the alloys, it was not

possible to achieve the same initial grain size in all of them. It can be seen from Table IV that the maximum variation in grain size was from 25 to 80μm diameter, which corresponds to an ASTM grain size range of 4-7.

(b) Ageing Treatment Selection

To study grain-boundaries during high temperature deformation and fracture, particularly with regard to the effect of various grain boundary precipitates, was one of the objectives of the work. Ageing treatments were selected on the basis of optical and electron microscopical examination for all of the alloys, using electron diffraction as the major technique for the identification of precipitates at various microstructural sites. The base composition, Alloy 1, was used in the solution treated condition and having no grain boundary precipitates, in order to have a base microstructure for comparison purposes. The medium carbon base composition, alloy 2 was heat treated to produce grain-boundary $M_{23}C_6$, with the matrix free from any precipitates. The high carbon composition, alloy 3, was aged to produce $M_{23}C_6$ at grain-boundaries, non-coherent twin boundaries and within the matrix. In order to study the separate effects of molybdenum, which is present in the commercial age-hardening alloy, alloy 4 was heat-treated to produce molybdenum rich $M_{23}C_6$ at grain boundaries. However, the solution treatment conditions left much molybdenum rich $M_{23}C_6$ undissolved, and these carbides were therefore present in the aged condition. Two ageing conditions were selected in the case of alloy 6, one with TiC/$M_{23}C_6$ at grain-boundaries aged at 800°C, and the other using a lower ageing temperature to produce only $M_{23}C_6$ at the grain-boundaries. This was done to investigate the effects of grain-boundary TiC on the high temperature properties. In the case of the PE16 compositions two heat-treatment conditions for each alloy were used to study the effects of two dispersions of γ' within the matrix, both with and without any grain-boundary $M_{23}C_6$.

Particularly in PE16 compositions, it was not possible to select a suitable heat-treatment condition to obtain TiC/

$M_{23}C_6$ at grain boundaries together with or within the matrix. All these heat-treatment conditions are outlined in Table VI.

4.5 HIGH TEMPERATURE PROPERTIES

The high temperature properties described in this section include both the results of tensile testing and creep testing.

4.5.1 Tensile Properties

All the alloys comprising varying microstructural features, were tested at a fixed temperature of 700°C, over a range of strain rates. The effect of the different microstructural changes will be considered separately in terms of the proof stress, tensile strength and high temperature tensile ductility.

4.5.1.1 Base Composition With No Grain Boundary Precipitates (Alloy 1)

The stress-strain curves obtained at various strain rates are presented in Fig. 60, and the tensile properties from these tests are given in, Table X. It is evident that both the 0.2% proof stress and tensile strength decreased with decreasing strain rate and the overall ductility also followed the same trend. However, the total elongation at a strain rate of 3.28×10^{-2} sec^{-1} was much higher compared to other ductility values, and perhaps indicates a different deformation mechanism. As shown in Fig. 60, the stress-strain behaviour at 3.28×10^{-2} sec^{-1} and 3.28×10^{-3} sec^{-1} was slightly different to that of lower strain rates in that the specimens exhibited serrated flow curves. At the faster strain rate of the two, i.e. 3.28×10^{-2} sec^{-1}, the serrated flow commenced after 2.6% strain and continued nearly until fracture. On the other hand at 3.28×10^{-3} sec^{-1} the serrated flow commenced after 4% strain and followed right until fracture. However, the amplitude of the serration at 3.28×10^{-2} sec^{-1} was 1.31 MN/m^2 compared to 0.66 MN/m^2 at a lower strain rate of 3.28×10^{-3}, sec Table XI. Both the commencement strain and serration stress amplitude values suggest that serrated flow was more apparent at faster strain rates than the slower ones.

4.5.1.2 Base Composition With $M_{23}C_6$ at Grain Boundaries (Alloy 2)

The stress-strain behaviour with carbides at grain-boundaries was very similar to that of the base composition without any carbides present, Fig. 61, particularly when taking into account the effect of decreasing strain rate on the tensile properties. As expected, the introduction of carbides at grain-boundaries increased the 0.2% proof stress and tensile strength at all strain rates, compared with the base composition. The ductility values were also higher in this alloy and this trend was observed at all strain rates. This observation is contradictory to normal strength-ductility relationships and emphasises the role of grain-boundary $M_{23}C_6$ in suppressing certain modes of deformation, as will be discussed later. However, serrated flow was observed at similar strain rates as for alloy 1, although it commenced at an earlier strain of 1.2% at both strain rates and continued nearly until fracture. The stress amplitude of the serrated flow was of the order of 3-4 MN/m^2, Table XI, which is nearly three times that of alloy 1, perhaps indicating the influence of increased carbon in this alloy. Also, a higher value of serration amplitude at the lower strain rate indicates the influence of increased dislocation density introduced by the presence of carbides at grain-boundaries, and this also will be discussed later.

4.5.1.3 $M_{23}C_6$ at Grain Boundaries and Within the Matrix (Alloy 3)

The general effects of the influence of decreasing strain-rate on the strength characteristics were very similar to those previously described, Fig. 62. By introducing carbide precipitates within the matrix, the 0.2% proof stress as well as the tensile strength was increased compared with alloys 1 and 2. The higher temperature ductility values were very similar to those for Alloy 1, except at the fastest strain rate where 15% decrease in elongation was observed, Table X. It is evident that the ductility at faster strain rates was greater compared to the slowest strain rate test,

Fig. 62, perhaps indicating a change in deformation mechanism with decreasing strain rate. The serrated flow was observed at similar strain rates of 3.28×10^{-2} sec^{-1} and 3.28×10^{-3} sec^{-1}, to those in the previous alloys. Serrated flow commenced at 2% strain at both strain rates but only continued until 20% strain at the higher strain rate compared to 26.5% strain at the lower strain rate. The serration stress amplitude was similar for both strain rates and was lower compared to Alloy 2, thereby making serrated flow more apparent at lower strain rates.

4.5.1.4 Comparison of $M_{23}C_6$ Precipitating Alloys

A brief comparison of three different microstructures is presented in Figs. 63, 64 and 65, showing the influence of $M_{23}C_6$ morphology and precipitation sites on the tensile properties. It is evident that with increasing volume fraction of carbides in the steels, both the 0.2% proof stress and the tensile strength increased at all strain rates Figs. 63 and 64. The high temperature ductility was observed to increase with $M_{23}C_6$ at the grain-boundaries, Fig. 65, but precipitating $M_{23}C_6$ carbides both at grain-boundaries and within the grains appeared to be detrimental to the high temperature ductility. This indicates the importance of the relative strength of grain boundary and the matrix during high temperature deformation.

4.5.1.5 Molybdenum Rich $M_{23}C_6$ at Grain Boundaries (Alloy 4)

The effect of molybdenum rich grain boundary $M_{23}C_6$ precipitates on stress-strain behaviour is shown in Fig. 66, which illustrates the expected decrease in 0.2% proof stress and tensile strength with decreasing strain rate. However, both strength parameters showed a higher value at all strain rates, compared with alloy 3, Table X. This indicates an increased strengthening effect due to the presence of molybdenum within the matrix and due to carbides at the grain-boundaries. The ductility values were very comparable to those of alloy 3, if anything being slightly inferior at the lower strain rates. This poor ductility at lower strain rates could be attributed

to the presence of a considerable amount of undissolved $M_{23}C_6$ within the matrix, thereby facilitating void nucleation. Although serrated flow was observed at similar strain rates as for alloy 3, the serration stress amplitude was more pronounced at a lower strain rate of 3.28×10^{-3} sec^{-1}, Table XI. At the higher strain rate of 3.28×10^{-2} sec^{-1} the stress amplitude of the serrations was comparable to that in Alloy 1, suggesting that carbon was responsible for the serrated flow. On the other hand, a higher serration stress amplitude and its early commencement at the lower strain rate of 3.28×10^{-2} sec^{-1} could be due to the presence of molybdenum or combined Mo and C in the alloy.

4.5.1.6 Combined Effect of Molybdenum and Titanium (Alloy 5)

Two heat-treatment conditions employed in this composition will be described individually in relation to the microstructural features which were introduced.

a) Mo - rich $M_{23}C_6$ at Grain Boundaries, Heat Treatment No. 2

The presence of titanium within the matrix and molybdenum rich $M_{23}C_6$ at grain-boundaries did not greatly alter the strength parameters, compared with Alloy 4, Fig. 67. However, the ductility values were considerably higher than any of the other structures containing carbides which have been discussed previously, particularly at the lower strain rates of 3.28×10^{-4} sec^{-1} and 3.28×10^{-5} sec^{-1}, Table X. This seemed to be associated with the presence of titanium in this alloy and perhaps was related to the slow diffusion rate of titanium which thereby exerted a pinning effect on grain-boundary dislocatio movement and increased matrix deformation. The serrated flow characteristics were very similar to those of, Alloy 4, and can be explained on the basis of the slow diffusivity of both molybdenum and titanium.

b) $M_{23}C_6$/TiC at Grain Boundaries and in Matrix (H.T. No. 1)

The strength and ductility values were similar to those

for heat-treatment condition No. 2, in this alloy, Table X. Also, the strain rate sensitivity of the stress-strain behaviour was comparable in both heat-treatment conditions, Fig. 68. The serrated flow characteristics were also very similar in both cases, except that the serration stress amplitude was higher in this heat-treatment condition, Table XI. This is perhaps a reflection of using a higher ageing temperature of 800°C, where the amount of $M_{23}C_6$ precipitated was decreased thereby resulting in increased molybdenum in the matrix, which hindered dislocation movement.

4.5.1.7 Low Carbon PE16 (Alloy No. 7)

With the introduction of γ' zones within the grains the tensile strength and 0.2% proof stress values were markedly increased compared with the carbide forming alloys, Fig. 69, and proof stress values as high as 559 MN/m^2 were obtained at the slowest strain rate. Also, as expected, the ductility was considerably lower and a continuous decrease in ductility was observed with decreasing strain rate, Table X. This could be attributed to the presence of weaker grain boundaries compared with the matrix, and an increasing time dependence of the grain-boundary contribution to the overall deformation with decreasing strain rate. Serrated flow was predominant at a strain rate of 3.28×10^{-3} sec^{-1} and could be attributed to the presence of molybdenum as a substitutional solid solution component within the grains. Most of the titanium was precipitated as γ' zones, thus leaving negligible titanium within the matrix to contribute towards serrated flow.

Replacing the γ' zones by semi-coherent γ' particles within the grains did not reduce the strength levels by any significant amount, but the ductility was greatly improved, Fig. 70. In particular, a large increase in tensile ductility was observed at a strain rate of 3.28×10^{-5} sec^{-1}, thereby illustrating the importance of the morphology of the micro-structural features within the grains and their subsequent influence on the deformation mechanisms.

The improved ductility may be attributed to the ease with which dislocations can move between semi-coherent particles compared with cutting through the zone, and this will be considered later. However, the serrated flow characteristics were very similar to those of previous heat-treatment condition. This again emphasises the fact that serrated flow is a strong function of the diffusion of substitutional alloying additions rather than the precipitate type or morphology.

4.5.1.8 High Carbon PE16 (Alloy8)

Introducing $M_{23}C_6$ carbides at grain and twinboundaries, and γ' zones within the grains,did not materially alter the strength and ductility profiles at varying strain rates as compared with the low carbon PE16 composition, Fig. 71. However, the very slight decrease in ductility in the high carbon composition was perhaps due to an increased amount of undissolved TiC/TiN particles which facilitated void nucleation and therefore more early fracture, Table X. Replacement of zones by semicoherent γ' particles and maintaining the $M_{23}C_6$ precipitates distribution at the grain boundaries,did not reduce strength levels by any significant amount, whereas ductility was greatly improved at all strain rates, Fig. 72. The serrated flow characteristics were very similar to those of the low carbon PE16 composition, Table XI.

4.5.1.9 General Comparison of All Alloys

A general comparison, carried out on the basis of the 0.2% proof stress, tensile strength and ductility, is briefly presented in, Figs. 73, 74 and 75 respectively. Figure 73, clearly shows three groups of microstructural features separated by large differences in 0.2% P.S. values. It is evident that by introducing carbides at grain boundaries, the proof stress was not significantly improved whereas precipitating $M_{23}C_6$ within the grains, gave an increase in proof stress similar to that of introducing substitional alloying additions. This could be attributed to the restricted dislocation movement as a result of both substitional alloying elements and carbide precipitates within the grains. However, introducing γ' type

precipitates into the matrix significantly increased the 0.2% proof stress, Fig. 73, and γ' zones appeared to be more effective than the semicoherent γ' form. A comparison on the basis of the tensile strength values at varying strain rates, showed that in all carbide forming alloys the strength was greatly dependent on such microstructural features as grain size, types of precipitate and its morphology, Fig. 74. The effect of a coarse grain size is clearly revealed in the case of the molybdenum steel, whereas the importance of precipitates, e.g. TiC on dislocations, is illustrated by the two heat-treatment conditions in the titanium bearing alloy. However, steels containing gamma-prime precipitates within the matrix possess a much higher strength at any strain rate, Fig. 74. Also, high carbon PE16 showed lower strength than the low carbon composition in both heat-treated conditions. This effect could be attributed to the lower volume fraction of gamma-prime present in the high carbon steel due to increased undissolved TiC, which in effect resulted in less titanium available for γ' precipitation on ageing.

The general strength-ductility concept of increasing ductility with decreasing strength is obeyed by most of the alloys, Fig. 75, except for the medium carbon base composition, the titanium bearing alloys, and both PE16 compositions containing semicoherent gamma-prime mithin the grains. These effects could be best described by considering the influence of various microstructural features on deformation and fracture maps and this will be discussed in detail later.

Serrated flow was observed in all the alloys at strain rates of 3.28×10^{-2} sec^{-1} and 3.28×10^{-3} sec^{-1}, Table XI. However, on the basis of the commencing strain and the stress amplitude of the serrations, all the alloys containing carbon as major alloying addition, showed much more pronounced serrations at the faster strain rates of the order of 3.28×10^{-2} sec^{-1}. On the other hand, alloys containing substitutional alloying additions revealed predominant serrations at a slower strain rate of 3.28×10^{-3} sec^{-1}, Table XI. This effect could be perhaps explained on the basis of the influence of the diffusion rates of carbon, and other substitional solutes

such as molybdenum and titanium on their drift velocities. These values may then be compared to the dislocation velocities at the appropriate strain at a testing temperature of 700°C. This will be dealt in the discussion.

4.5.2 Creep Properties

The creep rupture properties of all the alloys tested at 700°C have been summarised in Table XII, and will be considered in detail on the basis of the microstructural features introduced prior to any testing. The properties will be described in terms of the influence of microstructure on the creep strength and ductility, and also their effect on the stress dependence of the minimum creep rate. An attempt will be made to correlate the constant strain rate tensile ductility values with that of creep ductility, to emphasize the importance of changing deformation mechanisms.

4.5.2.1 Base Composition (Alloy No. 1)

Typical creep curves obtained at 700°C are shown in, Fig. 76. The expected trend of decreasing strain rate and increasing rupture life, with decreasing creep stress was observed. This alloy showed the lowest creep strength of 49 MN/m^2 for a 1000 hour rupture life, compared to any other alloy, Table XIII. Also it was observed to have the highest minimum strain rate of 3.2×10^{-6}/sec at a constant applied stress of 100 MN/m^2, compared with any other carbide forming composition, Table XIV and Fig. 77.

The stress dependence of the rupture life, is shown in Fig. 78, the value of the stress exponent, $n \simeq 4.4$, being comparable to that for most austenitic stainless steels.(113) However, incorporating the observed minimum strain rate data with tensile testing results, the ductility values followed a definite pattern, Figs 79(a) and (b)and the commonly observed ductility trough was observed. Generally, the ductility profile indicated a decrease with decreasing strain rate and a ductility minimum of 9.5% was observed at a strain rate of 10^{-7} sec^{-1}. Decreasing the strain rate further showed an

increase in overall ductility, i.e. a change in deformation mechanism. Nevertheless, it was interesting to note that a large amount of creep strain had been accommodated during the tertiary stages of creep, particularly at the higher rupture times, Table XII.

4.5.2.2 Base Composition With $M_{23}C_6$ at Grain Boundaries (Alloy 2)

The creep behaviour of an alloy with carbides at the grain boundaries is presented in, Fig. 80, showing similar features to those of alloy 1. Both the creep strength and the rupture life was increased compared with the base composition, Tables XIII and XIV. Also, the minimum creep rate was decreased to 4.4×10^{-7} sec^{-1} compared with Alloy 1 at a constant applied stress of 100 MN/m^2, Table XIV. The evidence was further supported by the considerably higher stress exponent value of 6.75, Table XIII, which indicates the beneficial effects exerted by grain-boundary $M_{23}C_6$. The tensile ductility, in conjunction with creep results at varying strain rates, again showed a pattern similar to that described for alloy 1, Figs 79(a) and (b). However, the presence of grain boundary $M_{23}C_6$ shifted the ductility trough towards higher strain rates, and in general the creep ductility was also improved by a significant amount. Also, most of the creep strain was accommodated during the secondary stages of testing, Table XII, which partly explains the improved creep ductility results.

4.5.2.3 $M_{23}C_6$ at Grain Boundaries and Within the Grains (Alloy 3)

The general effects were very similar to those for the two previous alloys, Fig. 81. However, the 100 hour rupture strength showed the expected increase compared to alloy 2, Table XIII. On the other hand the 1000 hour rupture strength was comparable to that for alloy 2, Fig. 78, which indicates the structure sensitivity of the fracture mechanisms which lead to early failure. Also, the magnitude of the stress exponent, n, decreased to, 4.4, indicating that when grain-boundaries and

grains were similar in strength, the stress dependence of the rupture life was low, but when grain-boundaries were stronger than grains, the stress dependence of the rupture life was higher.

The creep ductility and the minimum strain rates fitted in with the tensile testing results, Figs. 79 (a) and (b), showing a decreasing elongation with decreasing strain rates or increasing rupture life. Although there was every indication of a ductility trough, no minima was observed in the range of creep stress used. However, it is envisaged that the trough would be clearly apparent on testing at slower strain rates than could be achieved during the present investigation. By introducing carbides into the matrix, the ductility trough had been shifted to lower strain rates, and generally the creep ductility was inferior to alloys 1 and 2.

4.5.2.4 Molybdenum Rich $M_{23}C_6$ at Grain Boundaries (Alloy 4)

The effect of molybdenum rich grain-boundary $M_{23}C_6$ precipitate on creep rupture behaviour is presented in Fig. 82, showing the expected increase of creep strength compared with Alloy 3, perhaps due to substitional solute strengthening of the matrix. However, it was interesting to note that the rupture life at a constant stress of $100MN/m^2$ was significantly increased compared with previously described alloys, Table XIV. Also, a major fraction of the creep ductility occurred during the tertiary stages of the test, Table XII, which may indicate the effect of slow diffusion rates of molybdenum, in delaying fracture. The evidence of grain-boundary strengthening due to $M_{23}C_6$ carbides and a lower minimum creep strain rate at 100MN compared with other alloys was further supported by the higher stress exponent value of, 5.3, Tables XIII and XIV.

The tensile ductility profiles fitted reasonably well with observed creep elongations, Figs 83(a) and (b) showing a ductility trough towards lower strain rates with a ductility minimum at a strain rate of 1.3×10^{-8} sec^{-1}. This observation suggests that the presence of Cr_{21} Mo_2 C_6 only at grain-boundaries moves the ductility trough towards lower strain rates.

4.5.2.5 $M_{23}C_6$/TiC in Grain Boundaries and Matrix (Alloy 5)

The titanium bearing steel showed improved creep strength compared with alloy 5, but an unusually large amount of the creep strain occurred during the tertiary stages of the tests, Fig. 84. This suggests a different deformation mechanism and will be dealt with in detail later. However, overall rupture life at a constant creep stress of 100 MN/m^2 was significantly improved compared with other carbide forming alloys, Table XIV. The stress dependence of the minimum creep rate, i.e. the magnitude of stress exponent n, was very similar to that of alloy 2, Table XIII, indicating the importance of the strength of the grain-boundaries to that of the matrix.

The creep ductility values were the highest for any alloy under investigation, Table XII, and formed a definite and a continuous profile with the constant strain rate tensile ductility results, Figs 83(a) and (b). Although there was no pronounced ductility trough, the tendency for one at lower strain rates was quite apparent Figs 83(a) and (b). At least two different deformation mechanisms appeared to be operative at different strain rates.

4.5.2.6 Low Carbon PE16 Composition (Alloy No. 7)

A microstructure containing γ' zones within the matrix markedly increased the rupture strength compared with carbide forming alloys, and a major proportion of the creep strain was accommodated during the second stages of the tests, Fig. 85 and Table XII. However, very low minimum strain rates and extremely high values of the stress exponent, $n \sim 13$, Tables XIII and XIV, suggested that grain boundary sliding was hindered. This effect may be attributed to γ' zone formation near the boundaries, and will be discussed later. Nevertheless, the ductility profile showed a definite pattern, Figs. 86(a) and (b) showing a marked

ductility trough at the lower strain rates, with a ductility minimum at a strain rate of 5×10^{-7} sec^{-1}.

Replacing γ' zones by semi-coherent γ' particles markedly reduced the rupture strength and increased the minimum strain rate, Tables XIII and XIV. These effects were also associated with a significant decrease in the stress exponent of the strain rate, $\sim$ 3.14, Table XIII. The majority of the strain during creep occurred in the tertiary stages, Fig. 87, emphasising the change of deformation mechanism due to a change in the microstructure. The creep ductility values fitted in reasonably well with constant strain rate tensile results and a tendency for a ductility trough was evident, Figs 86(a) and (b). It is envisaged that a true minima would be observed by further lowering the strain rate. In general, the high temperature creep ductility was markedly improved by introducing semicoherent γ' particles compared with the presence of zones within the matrix, Table XII.

4.5.2.7 High Carbon PE16 (alloy 8)

Introducing $M_{23}C_6$ at grain and twin boundaries and γ' zones within the grains gave rise to the lowest minimum strain rates and highest stress exponent values of $\sim$ 15, compared with any other alloy under investigation, Tables XIII and XIV. However, the creep rupture life was inferior to that for the low carbon PE16 composition, which suggests the grain-boundary sensitivity of the fracture mechanism, leading to earlier failure, Tables XIII and XIV. Also, this microstructure showed the lowest creep ductility values compared with any other alloy, which further supports the structure sensitivity of fracture, Table XII and Fig. 88. The ductility trough was observed at a lower strain rate of 2×10^{-8} sec^{-1}, compared with low carbon PE16, Figs 86 (a) and (b).

Maintaining the $M_{23}C_6$ dispersion at grain-boundaries and replacing γ' zones by semi-coherent γ' precipitates improved the ductility by a significant amount without any marked detriment to the creep strength, Fig. 89. However, the stress exponent was decreased, $n \sim 5.5$, which is slightly higher than for low carbon PE16 composition containing semi-coherent γ' precipitates. This indicates the beneficial effects exerted by grain-boundary $M_{23}C_6$ on the creep properties in general.

The ductility profile was very similar to that for low carbon PE16, Figs 86(a) and (b).

4.6 MICROSTRUCTURAL FEATURES OF TESTED MATERIALS

4.6.1 Transmission Electron Microscopy After Creep Testing

Transmission electron microscopy was carried out on both interrupted creep tested specimens and whereever possible on ruptured specimens. Difficulty was encountered in making thin foils from ruptured gauge lengths due to the presence of intergranular cracking, because of preferential attack by the electrolyte at these sites during polishing/etching of the disc. A brief account of certain special features observed is presented as follows:-

4.6.1.1 $M_{23}C_6$ Carbide Forming Alloys

The low carbon base composition, ruptured at 50 MN/m^2 at 700°C, resulted in occasional precipitation of $M_{23}C_6$ carbides, both on grain-boundaries and twin boundary ledges. However, no precipitation was observed on dislocations within the matrix, and the overall dislocation density was very low, Plate 14(a), with no evidence of either cell formation or subgrain boundaries. The dislocation density near to or at the grain-boundaries was considerably higher, Plate 14(a), with some dislocation pile ups within the matrix. Higher dislocation densities were also observed near twin boundary ledges, Plate 14(b). After testing at a higher stress of 70 MN/m^2 at 700°C, some form of substructure was clearly evident. In the medium base composition, ruptured at 63 MN/m^2, the general structure showed tangles of dislocations associated with occasional $M_{23}C_6$ precipitates on dislocations, and the overall dislocation density was higher than in the low carbon base composition. However, the initial $M_{23}C_6$ particle size precipitated at grain-boundaries during ageing had considerably grown during testing and grain boundary migration was not clearly observed. The high carbon base composition revealed many dislocation tangles between the Widmanstatten $M_{23}C_6$ plates, and the overall dislocation density at and near the grain-boundaries was

considerably higher compared with alloy 2.

4.6.1.2. Effect of Molybdenum and Titanium

The high carbon molybdenum steel, tested at 85 MN/m^2 at 700°C and interrupted after 400 hours revealed a considerable amount of Widmanstatten $M_{23}C_6$ precipitates within the matrix and many dislocation tangles associated with such precipitates. Although, a few regions showing grainboundary migration were identified, there was no evidence of any well developed cell structure within the matrix.

In the high carbon molybdenum/titanium containing alloy, tested at 114 MN/m^2 at 700°C, the general structure showed considerable deformation within the grains, Plate 14(c). The dislocations formed a poorly developed cell structures and there was some evidence of grain boundary migration, Plate 14(d). There were many low angle sub-boundaries within the grains, Plate 14(e), but no precipitation had occurred on such boundaries during creep testing. However, Plate 14(e), also showed a number of dislocation tangles formed between three of such low angle boundaries.

4.6.1.3 PE16 Compositions

The low carbon PE16 composition containing γ' zones after the initial ageing treatment, creep tested at 316 MN/m^2 and interrupted after 400 hours, revealed a high dislocation density within the grains, Plate 14(f). However, the γ' zones had lost coherency and particle-dislocation interaction was clearly identified. The bowing of dislocations around such semi-coherent particles was clearly visible, together with some particle cutting, Plate 15(a). The high carbon composition after a similar ageing treatment, revealed very similar microstructural features. But the $M_{23}C_6$ carbides had coarsened both at grain-boundaries and twin boundaries, during testing in the high carbon alloy. In both alloys there was very little, grain boundary migration and super dislications were also visible within the grains.

The low carbon PE16 composition containing semi-coherent

γ' particles after ageing, creep tested at 253 MN/m^2 at 700°C and interrupted after 150 hours, revealed a large number of loops around the γ' precipitates, Plate 15 (b). In some cases there were even double loops around these precipitates, perhaps not co-planar but arranged one above the other, Plate 15(c). The paired super-dislocations were no longer a distinct feature of the microstructure. Regions showing grain boundary migration were distinctly visible, Plate 15(d), and such migration had occurred near the smaller $M_{23}C_6$ precipitates. On the other hand the grain-boundary associated with the larger precipitates was straight and showed no apparent migration, Plate 15(e). Also, Plate 15(d) shows the formation of low angle boundary associated with larger numbers of dislocations present at such sites. Such a feature was not observed in the case of the specimen containing zones. However, the microstructural features of the high carbon PE16 containing a semi coherent γ' dispersion within the grains, were very similar to those of low carbon PE16, except for the grain-boundary migration which was not clearly apparent, perhaps due to a very coarse and uniform distribution of $M_{23}C_6$ particles at such boundaries.

4.6.2 Fracture Characteristics

The effect of varying microstructural features on the fracture characteristics was assessed on the basis of the cracking behaviour of the specimens. Also a detailed metallographic examination of fractured surfaces was carried out. The parameters governing the cracking characteristics include, N_A, (number of intergranular cracks per unit area) and crack length $\bar{c}$, (average number of grain facets per intergranular crack), Table XV. Also, the influence of varying strain rates and microstructures on the nature of cracking was assessed in terms of the percentage of a particular type of crack present under given test conditions, Table XVI. All these factors will be considered individually for each microstructural variatio

4.6.2.1 Base Composition (Alloy No. 1)

The number of intergranular cracks per unit area (N_A)

remained fairly constant with decreasing strain rate, indicating the importance of the number of nucleation sites for intergranular cracking, Table XV. However, the crack length, $\bar{c}$, was observed to increase with decreasing strain rate, thereby indicating the importance of rupture time on crack propagation. The cracks were predominantly w and r-type, at all strain rates, but there was an overall increase in the percentage of w-type cracks and a decrease in r-type cracks with decreasing strain rates, Fig. 90.

Metallographic examination of fractured surfaces revealed large cavities formed around undissolved chromite particles, Plate 16(a), and small voids formed along grain-boundaries, when tested at very high strain rates. However, decreasing the strain rate to 10^{-2}/sec gave areas of intergranular fracture, Plate 16(b), but fracture was still predominantly of the transgranular ductile type. At a strain rate of 10^{-3}/sec the fractured surface, Plate 16(c), showed many intergranular facets with many ductile dimples present on the facets. Lowering the strain rate to 10^{-4}/sec gave intergranular facets coupled with ductile areas, Plate 16(d). However, oxides covered the whole fractured surface on long term creep testing, Plate 16(e).

4.6.2.2 Base Composition With $M_{23}C_6$ at Grain Boundaries (Alloy 2)

The introduction of $M_{23}C_6$ at grain boundaries resulted in very low N_A values (about half the value of alloy 1), Table XV, which emphasised the decrease in crack nucleation sites for this microstructure. However, the crack length was very similar to that of Alloy 1 and followed a similar pattern with decreasing strain rate, Table XV. Also, an increased tendency for w-type cracks and an overall decrease of r-type cracks was clearly visible at all strain rates, Fig. 90. This indicates the beneficial effects exerted by grain boundary $M_{23}C_6$ precipitates in suppressing cavity formation.

The suppression of cavities by grain boundary $M_{23}C_6$ was further evident in fractographs, which showed a large amount of transgranular fracture and very fine void formation around the carbides at grain boundaries, Plate 16(f). Also, the areas showing intergranular fracture were greatly reduced in

number compared with alloy 1, indicating that delayed grain boundary deformation had occurred. A truely ductile intergranular fracture behaviour was observed only on long time creep tested specimens, Plate 17(a), where cracks had nucleated on triple points, Plate 17(b). Such cracks were observed to have propagated along grain boundaries containing $M_{23}C_6$ particles, Plates 17(c)and(d).

4.6.2.3 $M_{23}C_6$ at Grain Boundaries and Within the Grains (Alloy 3)

With the introduction of $M_{23}C_6$ precipitates within the grains, the number of intergranular cracks per unit area was greater than in alloy 2 and comparable to that in alloy 1, Table XV. This suggested an overall increase in crack nucleation sites in this particular microstructure. Surprisingly unlike the previous two alloys the overall percentage of w-type cracks remained fairly constant with decreasing strain rate but the r-type cracks showed a definite decrease with decreasing strain rate, Fig. 90. Twin boundary cracking was observed at all strain rates and the extent of such cracking was enhanced with decreasing strain rate, Table XVI. This perhaps contributes towards the increased number of crack nucleation sites compared with alloy 2.

The metallographic evidence for twin boundary cracking is shown in Plates 17(e)and(f), where such cracks seem to be associated with the presence of $M_{23}C_6$ precipitates. However, the fractures were generally ductile in appearance and the areas of ductile intergranular facets showed a clear strain rate dependence, similar to that in Alloy 1. This again points out the effect of $M_{23}C_6$ precipitates within the grains, thereby rendering grain boundaries more suceptible to void formation due to strengthening of the grain interiors.

4.6.2.4 Molybdenum Rich $M_{23}C_6$ at Grain Boundaries (Alloy 4)

The number of intergranular cracks per unit areas was similar in magnitude to that of alloy 3 and also crack length values followed a similar pattern with decreasing strain rate, Table XV. However, the extent of w-type cracking was enhanced

with decreasing strain rate whilst r-type cracks decreased, Fig. 91. Despite the presence of $Cr_{21}Mo_2C_6$ particles on some non-coherent twin boundaries in the heat-treated microstructure, there was no indication of any twin-boundary cracking, Table XVI.

The fractures were of the generally transgranular-ductile type, but intergranular facets were more distinct with decreasing strain rate, with the intergranular facets showing many ductile dimples, Plate 18(a). The very low strain rate creep fractures showed much oxidation, therefore making the fractures more difficult to interpret, but the general appearance of such surfaces was ductile in nature.

4.6.2.5 Combined Effect of Molybdenum and Titanium (Alloy 5)

Precipitating $M_{23}C_6$/TiC at the grain boundaries produced a considerable reduction in intergranular cracking compared with alloy 4, Table XV. The N_A values were quite comparable to those in alloy 2. The cracks were generally of the w-type and the percentage of such cracks was higher at all strain rates compared with alloy 4, Fig. 91. Precipitating only $M_{23}C_6$ at the grain boundaries (H-T No. 2) gave N_A values slightly higher than for the high temperature heat-treated microstructure (H-T No.1), which correlates with the observed ductility values, Table XV. In this microstructure also, the cracks were predominantly w-type but the percentage of such cracks was slightly lower than for H-T No. 1, Fig. 91 and Table XVI. However, both heat-treatment conditions showed similar crack length characteristics compared with alloy 4, Table XV.

The fractographic characteristics were very similar in both heat-treated conditions and will be described together. At very high strain rates the cup and cone nature of the fracture surface was quite apparent, Plate 18(b), and specimen necking was also observed. However, lower strain rate tests showed ductile fractures with marked necking tendencies, Plate 18(c). With a further reduction in strain rate, the necking behaviour was clearly predominant, Plate 18(d), and an extremely ductile fracture was apparent. Unlike other

carbide forming alloys, intergranularly fractured grains were not clearly visible, Plate 18(e), and a large number of ductile dimples was observed all over the fractured surface. All these features suggest that fracture was very different compared with the other carbide forming alloys. Nevertheless, long time creep tested specimens revealed some grain boundary carbides with undeformed regions around them, Plate 18(f), but it was difficult to comment on these fractures with any degree of certainty due to intense oxidation.

4.6.2.6 Low Carbon PE16 Composition (Alloy 7)

Introducing γ' zones within the matrix in conjunction with occasional $M_{23}C_6$ grain boundary precipitates resulted in a N_A value very comparable with alloy No. 5 (H.T.No.2) Table XV. Also, the crack length variations with decreasing strain rate were very similar. A comparison between two such extremes of microstructures would be of very little meaning, because the relative strength of the matrix to that of the grain boundaries is too different. Therefore, alloys containing γ' precipitates formed a class of their own. Replacing the γ' zones with semi-coherent γ' particles markedly reduced the number of inter-granular cracks per unit area, although the crack lengths were very similar to those in γ' zone bearing microstructures, Table XV. Also, the type of cracking in the latter was predominantly w-type and at lower strain rate tests the cracks were 100% w-type, Fig. 92.

An examination of the fractured specimens (initially heat-treated to form γ' zones) revealed an intergranular ductile failure at all strain rates with segregated areas containing many ductile dimples, Plate 19(a). Some areas showed clearly defined facets. However, the microstructure containing semi-coherent γ' particles revealed a fully ductile failure, Plate 19(b). Such an effect was more apparent at slower strain rate tests.

4.6.2.7 High Carbon PE16 Composition (Alloy 8).

Precipitating $M_{23}C_6$ particles at the grain boundaries and γ' zones within the matrix resulted in a considerable increase in the number of intergranular cracks per unit area, Table XV. However, replacing γ' zones by semi-coherent γ' particles revealed a lower number of cracks, i.e. fewer crack nucleation sites. The nature of these cracks in both heat-treatment conditions is clearly revealed in Fig. 92 and Table XVI. It was interesting to note the extent of twin boundary cracking in both these microstructures, which showed an increase with decreasing strain rate, Fig. 92. This might be associated with non-wetting $M_{23}C_6$ at such microstructural sites and will be discussed later.

At very high strain rates, the microstructure containing γ' zones showed clear ductile failure, Plate 19(d), with some intergranular fracture in the centre of the specimen. However, this intergranular appearance had extended across the whole cross-section of the specimen at lower strain rate tests, Plate 19(e). At higher magnification, these facets were sharply visible together with a few areas of ductile failure, Plate 19(f). These facets however contained ductile dimples on their surfaces, perhaps due to the presence of carbides at grain-boundaries. Replacing the zones by semi-coherent γ' particles and maintaining a $M_{23}C_6$ dispersion on the grain-boundaries resulted in predominantly ductile fracture, Plate 20(a). At higher magnification some intergranular appearance of the fractured surface was distinctly visible, but a large area of the specimen had fractured in a ductile manner, Plate 20(b). The intergranular facets may be attributed to the presence of carbides at grain boundaries.

5. DISCUSSION OF RESULTS

5.1 GRAIN COARSENING CHARACTERISTICS

The grain coarsening characteristics of an alloy can be described in terms of the magnitude, time dependence and temperature dependence of:-

(a) The grain size below the grain coarsening temperature

(b) The grain size above the grain coarsening temperature

(c) The grain coarsening temperature itself.

Beck et al[58-61] have shown that the grain size, D, at any given temperature, T, varies with time, t, according to equation (20). In equation (20), K and n are constants, and K varies with temperature according to an Arrhenius relationship. Equation (20) can thus be written:-

$$D = a.\ e^{-Q/RT}.t^{n} \qquad \ldots\ldots\ldots (60)$$

where a is a constant.

A graph of lnD v/s lnt at constant temperature thus gives the value of 'n', which will indicate by its magnitude whether there is any restriction of grain growth by pinning particles or solute segregation to grain boundaries[179]. Similarly a graph of lnD V/S $\frac{1}{T}$ at constant time will give a value of Q, the activation energy for grain growth, which also by its magnitude will indicate whether grain-boundary pinning occurs.

5.1.1 The Grain Size Below the Grain Coarsening Temperature

It can be seen that the grain size below the grain-coarsening temperature decreased as the carbon content increased from ~0.01% to ~0.10%, see Fig. 28 and Table II. This effect is related to undissolved carbides, and was especially pronounced on increasing the carbon content from ~0.05% to ~0.10%. The addition of ~3.5% Mo caused only a slight further decrease in the grain size below the grain coarsening temperature, and an addition of ~1.2% Ti with the 3.5% Mo

produced little further decrease in this grain size despite the undissolved particles of TiC, Plates 1(f) and 2(a). This indicates that the fine grain size in alloy 3 (0.10%C) at 1000°C must be due to undissolved $M_{23}C_6$. Similarly the 3.5% Mo alloy, also contained undissolved carbides, but in this case they were a different type of $M_{23}C_6$ carbides, Plates 1(d) and (e), as will be discussed later. Increasing the carbon content to 0.35% in the presence of 3.5% Mo and 1.2% Ti, alloy 6, produced the finest grain size below the grain coarsening temperature due to the very large volume fraction of undissolved TiC, Plate 2(b) and Table IX. In the PE16 alloy containing a very low carbon content of 0.012%, alloy 7, the grain-size below the grain coarsening temperature was only slightly finer than that of the 0.049%C unalloyed material, Alloy 2, presumably due to the absence of carbide pinning particles. The slightly finer grain size of alloy 7 compared with alloy 2 could be due to the presence of TiN particles. Increasing the carbon content of PE16 to 0.12%, alloy 8, produced a considerable refinement of the grain size below the grain coarsening temperature, due to the increased volume fraction of TiC particles, Table IX.

Graphs showing the time dependence of grain size at 1000°C, which was clearly below the grain coarsening temperature for all the alloys, are given in Fig. 29. Despite some scatter, the results for any given alloy showed a straight line relationship between the logarithms of time and grain-size, thus confirming the relationship[58-61] in equation (20). The slopes of these lines can be helpful in indicating the presence of grain-boundary pinning, a very small slope indicating very effective pinning and restriction of grain growth. Such a smaller slope, approximating to zero, was observed for alloys 3, and 6. This very effective pinning was expected for alloy 6, which contained a large volume fraction of TiC, but was not expected for alloys 3 and 4. However, metallographic examination of alloy 4 which contained 0.10%C, 3.5% Mo showed that there was much undissolved carbide at 1000°C, which persisted up to 1100°C, Plates 1(d) and (e). With the help of carbide extraction techniques, the carbide was found to be $Cr_{15}Fe_4Ni_2Mo_2C_6$. It is widely accepted that if Fe, Ni or Mo enter

the $M_{23}C_6$ unit cell, they tend to have a stabilising effect [4]. Particularly, the presence of nickel in the $M_{23}C_6$ unit cell can le to very high solution treatment temperatures for dissolution. The absence of grain growth with increasing time at 1000°C in alloy 3 can only be attributed to $M_{23}C_6$ at this temperature, and both optical and electron microstructure indicated that a large volume fraction of $M_{23}C_6$ carbides, Table IX, was in fact undissolved.

The time dependence of grain size at 1000°C in alloys 5 and 8 was greater than that for alloys 3, 4 and 6, and the slopes of the lines for alloys 5 and 8 were very similar. This similarity might be expected as both contained the same carbon, molybdenum and titanium contents, but the fact that the grain size of these alloys below the grain coarsening temperature increased slowly with time indicates that TiC progressively dissolved and coarsened, as expected from the slow solution rate of TiC[4].

The time dependence of grain size at 1000°C in alloys 1, 2 and 7 was very marked, and similar for all three alloys. These alloys all contained less than 0.05%C, alloy 1 and 7 only containing 0.01%C. There were thus very few pinning particles, Plate 1(c), so that the grain size was able rapidly to coarsen progressively with time.

In general, the magnitude of the grain size below the grain coarsening temperature could be related to the volume fraction of undissolved carbide/nitride particles, Table IX.

The temperature dependence of grain size below the grain coarsening temperature can be seen from Fig. 28. Alloys 1, 2 and 7 which contained few if any pinning particles coarsened more rapidly with increasing temperature. The other alloys showed little grain coarsening with increasing temperature below the grain coarsening temperature, and of these the extra-high carbon-titanium alloy showed virtually no grain growth with increasing temperature due to the very large volume fraction of undissolved TiC. Graphs of the logarithm of the grain size against the reciprocal of the absolute temperature, after one hour solution treatment, gave linear relationships. Assuming that the grain size prior to grain growth (D_o) was

vanishingly small so that $(D-D_o) \simeq D$, and that the time exponent in equation (20) is constant with varying temperature, then it is possible to obtain the activation energy for grain-growth. The linear graphs of log D $^{v}/_{s}$ 1/T indicated a constant activation energy for each alloy over the temperature range 1000°C to 1150°C, but the values of the activation energy were very variable, as shown in Table III. Whilst the validity of these activation energies may be questioned, it is significant that:-

(a) the values for alloys 1 and 2, which have no grain-boundary pinning were similar to those for other f.c.c. alloys in which there are no pinning particles[52].

(b) The alloys containing no pinning particles had low activation energies ~70 KJ/mol, whilst those with effective pinning particles had much higher activation energies of 150-210 KJ/mol. In alloy 6, the activation energy was extremely high, probably because there was always more than enough undissolved TiC, irrespective of any coarsening or solution of that phase, to ensure that no grain growth occurred with increasing temperatures below the grain-coarsening temperatures.

5.1.2 The Grain Size Above the Grain Coarsening Temperature

The grain size above the grain-coarsening temperature is largely dependent on the presence of any undissolved particles which may be present and thus retard grain growth[57,63]. Using a typical solution treatment time of 1 hour, it can be seen that there was a wide variation of this grain size from alloy to alloy, Fig. 28. The two low carbon alloys containing only nickel and chromium, alloys 1 and 2, had similar very coarse grain sizes which seemed to have reached a limiting value. Increasing the carbon content to 0.10%, alloy 3, markedly reduced the grain size above the grain coarsening temperature although most of the carbide was in solution. The reason for this is not clear, but may be associated with the higher grain coarsening temperature in this alloy or solute drag effects. Introducing ~3.5% Mo into the 0.10%C alloy, alloy 4, produced a grain

size above the grain coarsening temperature, intermediate between that of alloys 2 and 3. This could be associated with the faster diffusion rate of molybdenum in austenite above 1100°C compared with that of chromium[180]. At lower temperatures, molybdenum has been regarded as an inhibitor of grain boundary migration[57], possibly due to grain boundary segregation, but at the high temperatures of 1200/1250°C involved in the present work, this effect probably seems not to be operative.

Introducing ~ 1.2% Ti into the 3.5% Mo alloy, alloy 5, produced a marked refinement in the grain size above the grain coarsening temperature, as expected due to remnant undissolved TiC/TiN. Increasing the carbon content of the 3.5% Mo - 1.2%Ti to 0.35%, alloy 6, produced even further substantial refinement of the grain size due to the greatly increased volume fraction of undissolved TiC particles, Table IX. The low carbon PE16 alloy, alloy 7, had a similar grain size to the 0.1%C- 3.5% Mo alloy despite the presence of ~ 1.2%Ti. This was due to the virtual absence of any TiC particles in such a low carbon material. However, increasing the carbon content of PE16 to 0.12% caused a refinement of grain size above the grain coarsening temperature, but not to the extent shown by the 0.14%C - Mo - Ti alloy, alloy 5. The reason for this is no doubt related to the rather greater carbon content in alloy 5 compared with alloy 8. In general, the variation in the level of grain size above the grain coarsening temperature can be correlated with the chemical composition and overall constitution of the alloy.

The time dependence of the grain size above the grain coarsening temperature was investigated at the highest temperature studied for each alloy, Fig. 30. The grain size did not vary greatly with time for alloy 4 which contained 0.10%C, 3.50% Mo because of a very duplex grain size. This was due to some boundaries becoming unpinned and allowing grain growth whilst other boundaries were still heavily pinned by particles. Metallographic evidence, Plate 1(e), indicates that many precipitates, identified as $(Cr_{15}\ Fe_4\ Ni_2\ Mo_2)\ C_6$ were present at 1100°C, and only partially dissolved at higher temperatures.

Alloys 1, 2 and 7 showed only a small change in grain size with time at temperatures above the grain coarsening temperatures,

and these alloys all contained less than 0.05%C so that there were virtually no undissolved particles. The grain size was therefore established mainly by the temperature, and increasing time had little effect. On the other hand, alloys 4 and 5 contained much precipitate, and did not vary in grain size with time because there were sufficient precipitates to pin the grain boundaries even though with increasing time these precipitates coarsened and dissolved to some extent. Alloys 3 and 8 however, showed a marked time dependence of the grain size above the grain coarsening temperature. The increased time dependence in alloy 3 was due to progressive coarsening and solution of $M_{23}C_6$ precipitates with increasing solution treatment time. The marked time dependence of the grain size in alloy 8 was unexpected as this 0.12%C - 3.5%Mo - 1.2%Ti - 1.2% Al alloy contains many undissolved TiC/TiN particles. A possible explanation of this could be that, there being a large volume fraction of TiC/TiN, the particle size was large, Table IX, particularly due to the presence of TiN precipitates. In effect any particle coarsening with increasing time allows some grain coarsening to occur. This effect is shown by the Zener[63] and Gladman[57], equations (22) and (29) respectively. From these equations it can be seen that $R \propto r/f$. For a given volume fraction of particles any increase in r by Ostwald Ripening will allow grain growth, and likewise any decrease in f by solution will also allow grain growth. A simultaneous particle coarsening and solution will thus allow fairly rapid grain growth with time above the grain coarsening temperature. The effect of a larger particle size is clearly seen for alloy 4, Table IX.

The negligible time dependence of grain size in alloy 6 was expected as this 0.35%C - 3.5%Mo - 1.2%Ti alloy contains very many undissolved TiC particles, Plate 2(a). A possible reason for this effect is that the grain coarsening temperature for this alloy was very high and at the temperature of 1250°C, which was the highest studied, grain coarsening had not yet been fully effected.

Because of the variations in grain coarsening temperature between the different alloys, which varied from $<$ 1100°C to $>$ 1200°C, there was insufficient data to establish the temperature dependence, and therefore the activation energy for grain growth at temperatures above the grain coarsening temperature.

5.1.3 The Grain Coarsening Temperature

The grain coarsening temperature of alloys 1, 2 and 7 which all contained less than 0.05%C and a minimum of undissolve particles, were at ~1100°C and did not vary systematically with increasing solution treatment time. Alloy 3, which contained 0.10%C, but no molybdenum or titanium, coarsened at a rather higher temperature of ~1150°C, due to undissolved $M_{23}C_6$, but this temperature was not markedly influenced by solution treatment time. The high nickel in these alloys compared with conventional austenitic stainless steels decreased the solubility of carbon, but a contributory effect could be due to solute drag. Despite the fact that alloy 4, which contained 3.50%Mo, exhibited a large volume fraction of undissolved carbides, Plate 1(d) and (e), the grain coarsening temperature was still only at ~1100°C. This temperature did however tend to decrease slightly as the solution treatment time increased, possibly due to a combination of Ostwald Ripening and solution, Table II.

Alloy 5, which contained 0.14%C, 3.5%Mo and 1.2%Ti surprisingly showed the lowest grain coarsening temperature of ~1050°C, and this decreased to as low as ~1000°C with a solution treatment time of 4 hours. It is suggested that this indicates progressive solution and particle coarsening of TiC with time so that grain growth can occur due to the effects illustrated by equations (22) and (29). Increasing the carbon content of this type of alloy to 0.35%, alloy 6, so increased the volume fraction of TiC that despite particle coarsening and solution, a very fine grain size was retained, giving the highest grain coarsening temperature of any of the alloys studied, ~1200°C. However, at these higher temperatures particle coarsening and solution were much more time dependent so that the grain coarsening temperature decreased appreciably as the solution treatment time increased from $\frac{1}{4}$ hours to 4 hours. Finally, the commercial PE16 composition, alloy 8, coarsened at a slightly higher temperature than the low carbon alloys, i.e. 1100/1150°C, and again there was little effect of solution treatment time, possibly due to the increased volume fraction of TiC/TiN, Table IX compared with low carbon PE16,

alloy 7.

5.1.4 Comparison of Various Mathematical Models On the Effect of Second Phase Particles On Grain Coarsening

The comparison of various mathematical models[57,63,65] with the actual observed data is briefly presented in, Table IX. The strong influence of r/f on the actual grain size is clearly apparent and in agreement with results of other workers.[57,63]. Substituting observed precipitate particle sizes and volume fractions into Zener's equation (22), indicates a much larger grain size than was actually observed. These observations confirm that the driving force in Zener's mod is overestimated, as suggested by other workers[66].

The modified version of Zener's model[65], and taking into account the appropriate value of the correction factor, β, in equation (30), Fig. 1, still indicates a somewhat larger grain size than actually observed, Table IX. This suggests that the original Zener model based upon initial spherical grain shapes plays an important role in the overestimation of the driving force.

On the other hand, Gladman's model[57] fits well with the observed data, Table IX[67]. One of the interesting features is that the corrected observed grain size using $\bar{D}=1.75$ is slightly higher than that predicted by Gladman's equation whi represents a slight overestimation of the pinning effects. Hellman and Hillert[65] argue that Gladman's model neglects the local variation in the shape of the grain boundary due to the presence of second phase particles, suggesting an underestimation of the overall driving force due to a larger available grain-boundary area. This is in agreement with the observed data, Table IX, but it is suggested that an overall underestimation of the driving force may also be due to an overestimation of the volume fraction of the second phase particles. Gladman's equation takes into account the whole volume fraction of the precipitates present in the steel prior to any growth. However, the second phase particles are generally heterogeneously distributed within the matrix. Therefore, the second phase particles present within the growing grains take no part in the pinning effects.

Perhaps, an ideal grain-growth model should take both these points into account in Gladman's equation[57].

5.2 AGE HARDENING AND PRECIPITATION MECHANISMS

5.2.1 Low Carbon Base Composition (Alloy No. 1)

This alloy shows no age hardening, Fig. 31, although the softening curves previously discussed in section 4.2.1 indicate some precipitation in the temperature range 550°-750°C, which is confirmed by electron microscopical evidence. Due to the very low carbon content in this alloy, growth of $M_{23}C_6$ precipitates did not occur and neither did the precipitation occur to any significant extent on grain boundaries or twin boundaries.

However, it seems that even at this low carbon content, there was still some supersaturation with respect to $M_{23}C_6$ and this supports the evidence of the undissolved $M_{23}C_6$ in the 0.10%C alloy at 1100°C, which indicates that the high nickel content has decreased the solubility of carbon in austenite. The overall decrease in hardness at lower ageing temperatures was due to the annealing-out of quenched in dislocations, Plate 1(c) and the precipitation of $M_{23}C_6$ was not enough to compensate for this. At higher ageing temperatures grain growth also produced some softening.

5.2.2 Medium Carbon Base Composition (Alloy 2)

Age-hardening was clearly observed due to the increased carbon content of 0.05%, Fig. 32. An analysis of the temperature dependence of the time for achieving a given hardness leve during ageing gave an Arrhenius relationship in which the activation energy was 140 KJ/mol (33 k cal/mol). This activation energy was very similar to that for carbon diffusion in austenite, but it is strange that diffusion of carbon should be the rate controlling mechanism because it would be expected that substitutional chromium atoms would also need to diffuse. Such chromium diffusion would require an activation energy at least twice that observed[180]. However, as $M_{23}C_6$ mainly occurred at grain boundaries, Plates 2(c) and

(d), it is probable that more ready diffusion along grain boundaries lowered the activation energy.

The sequence of $M_{23}C_6$ precipitation was in agreement with that observed by other workers[21,69,74]. $M_{23}C_6$ precipitation at grain boundaries was probably on dislocations lying in the grain boundary plane. This was confirmed by the fact that the $M_{23}C_6$ precipitates had cube-on-cube orientation relationships with the matrix which was in agreement with Adamson's work[69]. Although, electron metallography revealed the nucleation of new dislocations at the interface between the matrix and grain/twin boundary $M_{23}C_6$ precipitates, no further precipitation of any significance occurred on such defects. The reason is thought to be associated with the low carbon content of this alloy compared to those used by other workers[74]. However, on ageing at lower temperatures the grain boundary $M_{23}C_6$ was more closely spaced than after ageing at higher temperatures, due to a greater supersaturation, more copious nucleation and less particle growth.[69]

5.2.3 High Carbon Base Composition (Alloy 3)

Increased age-hardening compared with alloy 2, Fig. 33, resulted in an increased activation energy of the order of 166 KJ/mol (40 k cal/mol) for $M_{23}C_6$ precipitation. This was slightly higher than that required for chromium diffusion along grain boundaries.[180] The $M_{23}C_6$ initially occurred on grain boundaries and then within the grains, Plates 2(e) and (f). Thus bulk diffusion of chromium was necessary and the combined grain boundary and bulk diffusion of chromium may explain the observed activation energy.

Apart from more closely spaced grain boundary $M_{23}C_6$ precipitates at lower ageing temperatures, Plate 3(a), the orientation relationship of these precipitates in the high carbon alloy was different.[69] This would largely depend upon the initial orientation of the dislocation lying in the grain-boundary plane. As long as the carbide has a parallel orientation relationship with the parent austenite, precipitation is generally energetically favourable.[21] This alloy also showed both stringer and Widmannstatten type $M_{23}C_6$ precipitates

within the grains, Plate 3(b), with an orientation relationship similar to that reported by other workers.[48, 74]. The mechanism of Widmanstatten type $M_{23}C_6$ formation is believed to be the same as that proposed by Singhal and Martin,[48] because these precipitates were mainly in the grain interiors rather than near the grain boundaries. Although, some Widmanstatten $M_{23}C_6$ precipitation was observed near the non-coherent edge of the twins, Plates 3(a) and (b), these are thought to be less efficient vacancy sinks than grain boundaries The stringer type $M_{23}C_6$ carbides must be associated with the dislocations[74] for such precipitates were also observed nearer twin boundary precipitates which are known to generate dislocations during growth, Plate 3(d).

The morphology and orientation relationship of $M_{23}C_6$ precipitated at non-coherent twin boundaries, Plates 3(c) and (d), were similar to that observed by Lewis and Hattersley.[74] However, the coherent twin boundary $M_{23}C_6$ precipitation was observed after ageing at longer times at higher ageing temperatures, and this observation is in agreement with that of Adamson, Plate 3(e).[69] However, the growth of such precipitates was slow and occurred parallel to the twin plane, rather than fanning out into the matrix. This is possible because coherent twin interfaces are poorer vacancy sinks than grain or non-coherent twin boundaries. Nevertheless, at high ageing temperatures, the less precipitation can be attributed to a smaller supersaturation of solute, and to the rapid annealing out of the defects which act as nucleation sites.

5.2.4 Comparison of the Effect of Carbon Content

The ageing curves, Figs. 32 and 33 , indicated that even in these low carbon steels a two stage ageing process was operative. The microstructures of both the medium and high carbon alloys showed that precipitation first occurred on the grain boundaries but later at higher ageing temperature or longer ageing times, spreads into the matrix. This is thought to be the cause of a two stage age-hardening process.

5.2.5 Effect of Molybdenum (Alloy 4)

dissolved (Cr Fe Ni Mo) C

carbides considerably lowered the amount of carbon available for precipitation, and thus the intensity of age hardening, Table V. This agrees with the microstructures which showed only grain boundary precipitation and very little matrix precipitation, Plates 4(b), (c) and (e). It is also significant that the age-hardening did not show a two stage process. The occurrence of a rapid reaction at lower ageing temperatures of 500-600°C but a slower reaction at higher temperatures has already been discussed in terms of the annealing out of the dislocations generated by the undissolved carbides, section 4.2.4. This is further supported by electron microscopy, Plate 4(a), in that at low temperatures precipitation occurred on dislocations but at higher temperatures the dislocations annealed out before precipitation occurred and so precipitatio was mainly on grain boundaries, Plate 4(c). The temperature dependence of these two reactions supports this suggestion in that the high temperature reaction had an activation energy of 106 KJ/mol (25 K cals/mol) typical of grain boundary $M_{23}C_6$ precipitation in the molybdenum - free alloy. On the other hand, the low temperature reaction had a much higher activation energy of 720 KJ/mol (171 K cals/mol), which is high even for precipitation on dislocations which would require bulk solute diffusion.(180)

A tentative 'C-curve' for the start of carbide precipitatior is shown in comparison with the molybdenum free alloys in Fig. 39. The rate of the reaction seems to be about the same as for the same carbon content in the molybdenum free steel, but the nose of the steel has been depressed by about 100°C. It is possible that the C-curve for the molybdenum steels is a combination of the two ageing reactions already discussed, but the precise mechanism for the depression in the nose of the C-curve is at present very uncertain.

However, on comparing Plates 3(d), and 4(d), it is evident that the molybdenum bearing steel contained many fewer but coarser precipitates along non-coherent twin boundaries. This is perhaps a direct reflection of the amount of carbon available for precipitate nucleation and growth.

5.2.6 Effect of Titanium (Alloy Nos 5 and 6)

The two alloys which contained 1.2%Ti with ~3.5%Mo, contained very different carbon contents of 0.14% (Alloy 5) and 0.35% (Alloy 6). The presence of the higher carbon content resulted in a greater volume fraction of undissolved TiC, Table IX, and whilst in the low carbon steel there may be just sufficient titanium available for a small amount of γ' precipitation, this is certainly not the case in the higher carbon alloy. No γ' precipitation was however detected by electron nicroscopy. It is believed therefore that the age-hardening was entirely due to carbide precipitation, and this was confirmed by the similar age-hardening curves for both steels, Figs. 35 and 36, and also by the same activation energy for the process, namely 94-125 KJ/mol (23-30 k cal/mol). A comparison of the age-hardening intensity against other carbide forming alloys, Fig. 41, indicates that the increase in hardness during ageing was less for the high carbon alloy than for the low carbon alloy, as might be expected due to a smaller amount of titanium in solution. The temperature dependence of this maximum increase in hardness during ageing was very different for the two alloys. It can be seen that the maximum increase in hardness of the 0.14%C steel, which contains much more titanium in solid solution than the 0.35%C steel, did not vary appreciably with temperature until the higher ageing temperatures. This indicates that at the higher ageing temperatures some TiC precipitation occurred which was confirmed by electron microscopy, Plates 5 and 6.

The sequence of precipitation in this alloy, was entirely related to the relative diffusion rates of chromium, molybdenum and titanium and also dependent upon the amount of titanium dissolved in the matrix after solution treatment.[31,69,75,76] The early nucleation of $M_{23}C_6$ at grain boundaries at lower ageing temperatures was due to the rapid rate of diffusion of chromium compared with titanium, Plate 5(f).[69] At higher ageing temperatures the dislocation precipitation of TiC was preferred due to a high Ti:C ratio and the smaller TiC unit cell, which required less surface energy to form a stable nucleus, Plates 6(a) - (c)[31,75]. However, at very

high ageing temperatures, due to the increased diffusion rate of titanium, combined grain boundary TiC and $M_{23}C_6$ precipitation was observed, Plate 6(d)[69]. In all cases the orientation relationships were in agreement with those observed by previous workers.[69,75,76]

5.2.7 The Effect of Combined Aluminium and Titanium Additions (Alloy No. 7 and 8)

Alloys 7 and 8 had identical compositions of the PE16 type, but with carbon contents of 0.012% and 0.12% respectively. The ageing characteristics of both alloys were very similar but the 0.12%C alloy showed a slightly lower increase in hardness during ageing, because the titanium level was reduced by combination with the carbon to form undissolved TiC. The ageing characteristics were very different from the other alloys studied, the increase in hardness being very much greater and the intense ageing reaction extending to higher ageing temperatures, Figure 42. The age hardening was due to γ' - Ni_3 (Al, Ti) since the Ni/(Al+Ti) ratio was quite high[39]. A feature of the ageing of both the PE16 alloys was the two stage ageing process, for which there are several possible explanations:-

(a) The first stage was due to zone or γ' formation followed by the formation of Ni_2Al Ti. This is not believed to be the reason as no evidence of large plate-like Ni_2Al Ti precipitates were observed in the heavily overaged condition, Plates 7-9.[178] A similar reason eliminates the possibility of Ni(Al Ti) being responsible for the second stage of ageing. In addition the Al/Ti ratio was so low in both alloys as to eliminate any such possibility.

(b) Following zone or γ' formation, sigma phase or chi phase may be responsible for the second stage of ageing. This is not likely because no larger intermetallic compounds were observed in the overaged condition, Plates 7-9. Moreover the composition did not contain sufficient

titanium and aluminium for these phases to precipitate[33] In addition a Phacomp[40,182] analysis of the constitution indicated that the composition of PE16 was not within the range of electron hole vacancy numbers in which intermetallic compounds of the laves, sigma or chi type are formed.

(c) The most likely explanation for the two stage ageing is that the first stage is due to the formation of zones rich in nickel, aluminium and titanium, which grow is the second stage, with partial loss of coherency, into γ' precipitates, Plates 7-9. At temperatures above 850°C, the zone solvus was exceeded so that γ' formed direct without the prior formation of zones, and only a single stage ageing reaction was observed. Also, the high activation energy for the ageing process of 297-308 KJ/mol (71-74 k cal/mol) indicated that bulk substitional solute diffusion, as would be required by zone and γ' formation, was the rate controlling mechanism[77].

The nucleation sites for γ' are believed to be pre-existing lattice defects, i.e. both quenched in vacancies and matrix dislocations.[41, 82] The nucleation of zones on dislocation cores is hard to visualise, but zones could form near to the dislocation line due to the enhanced core diffusion.[83]

Electron microscopy, Plate 7(e) and Plate 8(c), revealed the presence of dislocations in association with γ' zones, but the density of the zones was too great for nucleation to have occurred solely on or near dislocations. The relative concentration of quenched in vacancies and dislocations control the dominating mechanism, and in this case the quenched in vacancies have a dominant role.[82] The loss of coherency of these precipitates is probably associated with the absorption of matrix dislocations at their interface, perhaps due to an interaction between the strain field of the dislocations and the elastic strain field of the precipitat[79] This is further supported by the fact that there were few dislocations present in the microstructures showing semi-coherent γ' precipitates, Plate 7(f).

The enhanced nucleation and growth of $M_{23}C_6$ precipitates at the grain boundaries compared with γ' precipitates within the grains, Plates 7 and 8, is due to the lower driving force required for grain boundary diffusion compared with the bulk diffusion[52]. However, there was no significant evidence of γ' depleted regions adjacent to the grain boundaries even during the initial stages of ageing. A possible explanation for this could be the generation of dislocations near the grain boundaries due to $M_{23}C_6$ precipitate growth, which act as nucleation sites for γ' zone formation.[69,82] Also, a contributory factor could be the migration of quenched in dislocations towards grain boundaries during ageing, thus increasing the number of nucleation sites for γ' precipitation. Although, due to the presence of $M_{23}C_6$ at grain boundaries, the chromium concentration will be lower in the adjacent areas,[30,38] this decrease is not perhaps enough to cause γ' depletion in these regions.

The precipitation of $M_{23}C_6$ particles on undissolved TiC particles, Plates 9(a) and (b), can be attributed largely to a simple nucleation effect at an interface, particularly as the orientation relationships are favourable. In addition, dislocations generated at the TiC/matrix interface will also contribute to the nucleation of $M_{23}C_6$[69].

5.3 COLD WORK, RECRYSTALLIZATION AND PRECIPITATION

5.3.1 Medium Carbon Base Composition (Alloy No. 2)

The higher hardness values observed after recrystallisation compared with the un-cold worked material, Figs. 44 and 45, can be explained in terms of the finer overall grain size.[32,90] Similarly the increase in the recrystallised hardness with increasing prior cold work reflected the decrease in grain size.[95] The temperature dependence of the rate of recrystallization after moderate (40%) deformation was comparable to that of grain growth, Tables III and VIII, indicating that the matrix was fully recrystallized and that growth of these recrystallized grains was occurring, Plate 10. The temperature dependence of the recrystallization rate

decreased with increasing cold work, Table XIII, perhaps due to a decrease in the overall activation energy for the nucleation and growth of recrystallization nuclei.[95]

On the basis of hardness data and electron microscopical observations, Plate 10, precipitation was observed to occur prior to significant recrystallisation. In an attempt to compare these observations with the theoretical models,[104,105] equation (32) and (33), it is evident that the annealing time until the start of precipitation (tp) was far less than the incubation time (t_R) for the start of recrystallization. This could be attributed to the lower activation energy for diffusion of solute atoms (chromium) along grain boundaries, compared with the activation energy for the start of recrystallization, which is generally of the order for self diffusio Although, the activation energy for recrystallization decreased with increasing cold work, resulting in an increased driving force and a decrease in t_R; the activation energy for the nucleation of the second phase $\Delta G(T,C)$, also decreased, resulting in an overall reduction of tp[104]. Therefore, increasing cold work did not alter the situation, as both parameters were decreased at the same time.[104,105]

The enhanced nucleation of $M_{23}C_6$ along deformed grain boundaries and deformation bands, Plate 10, is believed to result from a large number of linear defects, i.e. dislocations and ledges known to be present at such sites after cold-working[103]. Although, some workers[90,106] have reported more intense precipitation within the grains compared with that in the grain boundaries, it is likely that such precipitates had occurred along deformation bands and were observed as uniformly distributed carbides within a fully recrystallized matrix. On ageing at higher temperatures, the average size of the precipitates increased with increasing holding time.[106] $M_{23}C_6$ particles were observed to grow more rapidly at deformed grain boundaries and deformation bands, compared with those nucleated on dislocations. This could be attributed to the faster diffusion at grain boundaries, and within deformation bands where there is a heavy dislocation density.

In moderately (40%) cold worked material the formation of recrystallization nuclei occurred at pre-existing grain boundaries and on deformation bands, Plate 10(c), not by grain boundary migration[99] but by the formation of distinct sub-grains due to dislocation rearrangement[95,98]. Although it is believed that the grain boundary bulge, mechanism is operative at low deformations,[100,101] such a mechanism would be impossible in this alloy, since the deformed grain boundaries were pinned by the precipitated $M_{23}C_6$ particles, prior to any recrystallization, Plate 10. The reasons for preferential recrystallization at deformed grain boundaries and deformation bands can thus be attributed to their ability to act as vacancy sources, which is required for dislocation climb to occur in the formation of low angle boundaries.[103] Also, the heavier local deformation at such sites results in a higher stored energy and hence a greater driving force for recrystallization.[104,105] However, with increasing deformation, nucleation within the deformed grains occurred by recovery to form dislocation cell structures, and once a new grain had nucleated this grows rapidly by grain-boundary migration into the adjacent regions.

5.3.2 High Carbon Base Composition (Alloy No. 3)

The hardness characteristics in the fully recrystallized state compared with those not subjected to cold work and recrystallization, were very similar at all deformation levels to those of alloy 2, Fig. 48. The presence of a finer grain size and a larger volume fraction of undissolved $M_{23}C_6$ after solution treatment resulted in an overall increase in dislocation density in the cold worked condition th with alloy 2,[53,95] i.e. a higher work-hardening rate, Fig. 43. The increased dislocation density in a fine grained material is generally attributed to a decreased average slip path length[95] and the undissolved $M_{23}C_6$ particles are not readily mechanically deformed, thus generating dislocations near the particle/matrix interface.[53,54] This also explains the lower temperature dependence of the rate of recrystallization compared with alloy 2, Table VIII, due to increased stored energy, creating an increased driving force

for recrystallization.(95)

On the basis of theoretical models(104,105), the driving force for the precipitation of $M_{23}C_6$ at grain boundaries and in deformation bands, Plate 11(a-d), should increase due to an increased carbon concentration, resulting in an overall decrease in the pre-exponential term in equation (32),i.e. a shorter annealing time for the start of precipitation. On the other hand, due to an increased dislocation density compared with the medium carbon alloy, the driving force for recrystallization also increased, resulting in a shorter incubation time for the start of recrystallization in equation (33). These mechanisms have opposing effects and are likely to cancel out. Also, comparing, Figs. 3(b) and (39), the nose of the C-curve for this alloy was $\sim 800^{o}C$, whereas the maximum ageing temperature employed was $750^{o}C$, which indicates that precipitati preceded recrystallization. It might be expected that cold working would move the precipitation C-curve, Fig. 39, to shorter times and that the temperature of the nose of this curve would be largely unaffected.

The recrystallization mechanisms were similar to those proposed for alloy 2, except that the finer recrystallised grai size resulted from the finer solution treated grain size and the pinning effects on the migrating boundaries of the intense $M_{23}C_6$ precipitation.(95,98)

5.3.3 Effect of Molybdenum (Alloy No. 4)

The increased work-hardening rate was typical of a combination of a fine grain size and undissolved $(Cr_{15}Fe_4Ni_2Mo_2)C_6$ particles, resulting in an increased dislocation density.(53,95) The increased work-hardening rate could also be due to the presence of molybdenum, giving a decreased stacking fault energy of the matrix, thereby making cross-slip more difficult.(9,17) Despite the presence of a high dislocation density prior to ageing, the increased temperature dependence of the rate of recrystallization, Table VIII, was a direct result of dislocation locking and the retardation of recovery processes, due to the slow diffusion of molybdenum (103,180).

The slower diffusion of molybdenum atoms caused a delay

in the start of the precipitation,[104,105] and on the other hand the higher dislocation density increased the driving force for recrystallization. Also, the nose of the C-curve was ~700°C in this alloy, Fig. 39, and it seems likely that both the precipitation of $M_{23}C_6$ and the recrystallization processes are competing. This is confirmed by electron microscopy, Plate 11(e), and is why at 650°C precipitation occurs prior to any recrystallization. At 700°C however both processes seem to influence each other, but at 750°C the sudden decrease in hardness was due to recrystallization preceding any precipitation.

The mechanisms of recrystallization and precipitation were similar to those observed in the previous alloys. With increased ageing time the recrystallized grains showed restricted growth due to the pinning effects exerted by the precipitated $M_{23}C_6$ particles, Plate 11(f).

5.3.4 Effect of Titanium (Alloy No. 5)

The temperature dependence of the recrystallization rate was higher than in the molybdenum bearing steel, at all deformation levels, Fig. 59. This was due to the slow diffusion rates brought about by the presence of molybdenum and titanium, which resulted in an overall retardation of the recovery processes.[75,103,180]

In this alloy also, the presence of molybdenum and titanium increased the time for the start of precipitation, tp. A contributory factor towards the lower driving force for precipitation was the lower supersaturation of carbon due to the presence of undissolved TiC, after solution treatment, Table IX. On the other hand, a higher dislocation density due to the presence of a finer solution treated grain size, a large volume fraction of TiC in the matrix, and also a lower stacking fault energy of the matrix, increased the driving force for the recrystallization reaction, i.e. there was a decrease in the incubation period for the start of recrystallization (t_R). However, the decrease in t_R in this alloy was more dominant than a decrease in tp, compared to other carbide forming alloys, due to the lower supersaturation for carbon. As both alloys 3 and 4 also contain a large amount of undissolved

$M_{23}C_6$, a similar effect might be expected in those alloys but the solubility of TiC is less than that of $M_{23}C_6$ and so there would be a much lower supersaturation for carbon in the TiC bearing alloy.

The time-temperature-precipitation characteristics for this alloy should show two C-curves for $M_{23}C_6$ and for TiC precipitation.[31,69] Because TiC precipitates at higher temperatures than $M_{23}C_6$, there is always the possibility that, as t_R decreases rapidly with increasing temperature, recrystallization always precedes TiC precipitation. However, there will be situations developed, due to the overlap of the TiC, $M_{23}C_6$ and t_R curves, where particularly at lower ageing temperatures ($\sim 750^{\circ}C$) recrystallization occurs prior to $M_{23}C_6$ precipitation and then the TiC is formed much later in the ageing sequence, Plates 12(c) and 12(d). Any further increase in the ageing time gave more precipitation, and precipitate coarsening, within the fully recrystallized matrix, Plate 12(e).

The mechanisms of recrystallization were however similar to those discussed for previous alloys.

5.3.5 PE16 Compositions (Alloy No. 7 and 8)

Despite the smaller solution treated grain size, Table IV, and a larger volume fraction of undissolved carbides in the high carbon PE16 composition, Table IX, similar work-hardening characteristics for the two PE16 compositions were observed possibly due to the lower stacking fault energy and the suppression of cross slip in the low carbon composition, Fig. 43 [9,17]

The increased rate of γ' zone formation in both low and high carbon PE16 compositions, Plate 12(f), can be explained in terms of Dollins' [83] treatment of nucleation in the vicinity of a dislocation. Although, other workers[184] have concluded that only with large particle-matrix misfits of $> \sim 0.05\%$, is γ' preferencially nucleated within the stress field of an edge dislocation, the low value of the misfit in PE16,[43,44] eliminates this possibility. It has been argued that nucleation of γ' at dislocations should be favoured

even in the absence of particle-matrix misfit, since the concentration of solute at the core of the dislocation will be higher than that elsewhere[183]. This theory, would predict that the rate of growth of γ' precipitates so nucleated would increase due to the enhanced diffusion along dislocations. This is in agreement with the present observations, Plate 13(a) [83]. Boothby[183] rejects this possibility due to the lack of any correlation between the observed γ' strings and the dislocation structure and also, on the basis of a similar γ' particle size in both worked and unworked material. However, the average γ' particle size would also depend upon the number of nucleation sites, i.e. a larger number of γ' precipitates could result in a smaller overall particle size. Furthermore, this suggestion is supported by the hardness data and the softening curves, Figs. 54-57. Such considerations were not taken into account in Boothby's work.

Due to the continuous precipitation of γ' and the increased rate due to cold working prior to ageing, the recrystallization incubation period t_R was far greater than the time for precipitation t_p, at all temperatures. Thus a greater driving force was required for the start of recrystallization in both the PE16 compositions. Hence recrystallization occurred progressively due to a fine intra-granular precipitation of γ', which exerted pinning effects on the moving sub-boundaries.[104] This may be why the softening curves, Figs. 56-57, indicated a low temperature dependence of the recrystallization rate, which was still in the nucleation stage even at the highest ageing temperature, Table VIII and Plates 13(b)-(f). It is well known that the activation energy for recrystallization nucleation is far less than the activation energy for the growth of such nuclei.[95] The general recrystallization mechanisms were, however associated with the formation of sub-grains and their growth, Plates 13(b)-(f).[98]

5.4 HIGH TEMPERATURE PROPERTIES

5.4.1 Expected Effects of Various Microstructural Features on the Deformation and Fracture Mechanism Maps

Considering the deformation mechanism map for type

304L austenitic stainless steel, Fig. 5, as a base for austenitic matrices, certain generalizations can be drawn of the effect of various microstructural features on different deformation regimes of the map. Similarly, taking the fracture mechanism map presented in, Fig. 10, as a base for f.c.c. structures, the effects of various microstructural features can also be deduced on different fracture fields of the map. Although a brief account of these features has already been presented in sections 2.6.2.2 and 2.7.4 respectively, a detailed examination of the microstructural features under investigation will be useful in explaining the observed results during high temperature tensile and creep testing.

The deformation mechanism map presented in, Fig. 5, applies only to one grain size, whereas the alloys under investigation cover a wide range of grain sizes, Table IV. Since diffusional creep rate is proportional to the square or the cube of the grain size[115-117], such a flow field will show a slight decrease with a coarser grain size compared with 304L steel (e.g. alloys 1 and 7) and vice versa (e.g. alloys 3,4,5 and 8). An increasing grain size also expands the glide field at the expense of a slight contraction in the high-temperature creep field.[29,121,122] This enhanced glide will also result in an increase in the transgranular fracture field of the fracture mechanism map,[163] Fig. 10.

The presence of grain-boundary precipitates such as $M_{23}C_6$ and TiC will lead to a decrease in the diffusional flow field and also, deformation will not be strictly controlled by Herring - Nabarro or Coble type creep, instead being controlled by an interface reaction due to the limited grain boundary mobility as described in section 2.6.1.3. Also, due to grain boundary strengthening, the deformation will be confined within the grains rather than near the grain-boundaries, with an expansion of the transgranular fracture field of the fracture mechanism map, Fig. 10, at the expense of the intergranular fracture field. However, the type of carbide can also play an important role, in that the higher the surface energy the more would be the retardation of the overall diffusional flow. On the other hand, the

size of TiC is generally smaller than $M_{23}C_6$ carbides, thus facilitating the dislocation climb necessary for interface reaction control. Also, alloys precipitating TiC at grain-boundaries will have a Ti-rich matrix, resulting in a slower overall diffusivity, thus decreasing the diffusional flow field even further.

Precipitating $M_{23}C_6$ or TiC carbides within the grain interiors, e.g. Alloy Nos. 3 and 5, will cause a decrease in both the glide and high-temperature creep fields of the deformation mechanism map, due to the pinning of the dislocations. The effect of such precipitation on the fracture mechanism map, Fig. 10, would be to expand the intergranular creep fracture field at the expense of the transgranular field,[163] by making grain boundaries relatively weaker.

The presence of coherent or semicoherent particles within the grains, e.g. γ' (alloys 7 and 8) will considerably decrease the dislocation glide field and the high-temperature creep field by hindering dislocation movement, Fig. 5[29,121] This will result in a significant expansion of the diffusional flow field and also shift the whole pattern of the deformation map to higher stress levels. However, even within the diffusional flow field the deformation will be strictly interface reaction controlled rather than by virtue of conventional Herring-Nabarro or Coble type creep. A smaller particles size, i.e. a decreased interparticle spacing will render these mechanisms more effective than with larger precipitates. The effect of such precipitates will also be to expand significantly the creep fracture field at the expense of transgranular fracture, Fig. 10.[163] However, it must be emphasized that a continuous change of microstructure during creep, will significantly change the deformation and fracture fields of the deformation and fracture mechanism maps, in a continuous manner. Some of the simplest examples are that of increasing dislocation density acting as a strengthening mechanism for dislocation glide and climb, thereby contracting these fields, and also γ' zones loosing coherency, grain boundary interparticle spacing increasing due to coarsening of carbides etc. Finally, it must be realized that one particular deformation or

fracture mechanism will not be completely suppressed but its total contribution towards the overall deformation can vary considerably with changing microstructure.

5.4.2 Alloys Forming $M_{23}C_6$

In order to assess the influence of varying dispersions of $M_{23}C_6$ and their precipitation sites, on the high temperature properties, each microstructural feature will be dealt with individually.

5.4.2.1 Base composition with no grain boundary precipitates (Alloy No. 1 solution treated)

An increase in both the 0.2% P.S. and tensile strength with increasing strain rate at 700°C, Table X, was quite consistent with equation (44)[127], and can be attributed to the suppression of time dependent softening processes during high temperature testing.[128] At very high strain rates of 10^{-2} and 10^{-3}/s, higher strengths were observed because softening processes did not have time to occur to the same extent as during slower deformation.[129] The creep strength, as indicated by the stress required for the minimum strain rate and the time to rupture, was considerably lower in this alloy, Table XII, due to an increased rate of recovery and a lower work-hardening rate, which resulted in a high minimum strain rate and a decreased time to rupture.[152] The higher rate of recovery is because there was nothing within the matrix to hinder dislocation movement, Plates 14(a) and (b). However, compared with other austenitic steels, this alloy shows higher creep strength due to increased substitutional strengthening effects by Cr and Ni. Therefore, the rate controlling factor for the lower creep strength is the increased value of the minimum creep rate, leading to a very low rupture life, Table XIV.

The high temperature ductility values at 700°C over a range of strain rates, Fig. 79(a) and (b), can be explained on the basis of changing deformation mechanisms in terms of

Ashby's deformation maps, Fig. 5, [29,121,122] The net effect of a coarser grain size and an increased nickel content compared with 304L austenitic steel will be a slight shrinkage in glide field and an expansion in the diffusional flow field at the expense of the dislocation creep field, Fig. 5. Considering a homologous temperature T/T_M of 0.5, the deformation at strain rates of 10^{-2} and 10^{-3}/s occurs by a dislocation glide mechanism and this is further supported by fractographic evidence which revealed the intragranular mode of deformation and fracture, Plates 16(a) and (b). Strain rates of 10^{-4}/s were near the boundary between the glide and high-temperature creep fields, Fig. 5, and all other tests up to a strain rate of 10^{-7}/s were within the high-temperature creep field. The predominence of the high-temperature creep deformation mechanism is further supported by the observation of intergranular ductile failure at lower strain rates, Plates 16(c) and (d). This provides a tentative explanation for the general decrease in high-temperature ductility with decreasing strain rate, since the strain due to glide is more than the strain due to high-temperature creep. Also, with increasing rupture time the grain boundary strain contribution to the overall strain increased.[128,129]

The creep test which showed a minimum strain rate of 10^{-8}/s was near the boundary between the high-temperature creep and diffusional flow fields. Both these mechanisms would therefore be expected to contribute towards the overall deformation, i.e. result in a higher strain than would be expected from any one deformation mechanism. This is supported by the observed ductility values, Figs. 79(a) and (b), which showed a 10% increase in ductility, over the general level of creep ductility of $\sim$20% elongation. Although, it might be questioned whether increased strain would be expected at the boundary between the glide and high-temperature creep fields, the glide mechanism results in more intense deformation than high-temperature creep mechanisms,[129] and a higher contribution to strain of the high-temperature creep mechanisms.[129] Therefore, the contribution to strain by high-temperature creep is over-

shadowed by the decrease in ductility, since the glide mechanism is not operating to a high efficiency.

The fracture mechanisms expected from the concepts used in Ashby's fracture maps were in agreement with the results obtained from the fractured surfaces, Fig. 10 and Plate 16.[163] The transgranular mode of fracture at very high strain rates, Plates 16(a) and (b), was associated with crack nucleation around non-deformable chromite particles due to stress concentration during deformation. This caused the stress to build up as the plastic strain increased, until the particle decohesed from the matrix, Plate 16(a). However, once such voids are nucleated, they grow as the matrix continues to deform, start to link up, and then lead to ultimate fracture. It seems to be the linking up of voids which accommodates a considerable amount of strain prior to ultimate fracture. In fact, this is why tests carried out within the glide region of the deformation maps showed a much larger high-temperature ductility. A transition from transgranular to intergranular fracture was associated with the lower strain rate of 10^{-4}/s, resulting in a gradual decrease in ductility, since the grain boundary weaknesses were emphasised with decreasing strain rate.[113,163]

The constant number of intergranular cracks per unit area (N_A) or per 1000 grains (N_G), Table XV, indicated that up to a strain rate of 10^{-5}/s, there was a constant number of intergranular crack nucleation sites. Although, the number of intergranular cracks would be expected to decrease with decreasing strain rate due to an interlinkage of the cracks, it is believed that owing to the very low rupture time, the cracks were not able to link up even at a strain rate as low as 10^{-5}/s. However, the cracks did increase in length ($\bar{c}$) with a decrease in strain rate, Table XV, showing the increased participation of a grain boundary sliding mechanism with decreasing strain rate. An overall decrease in the number of intergranular cracks and an increase in the average crack length ($\bar{c}$) should result from testing at very low strain rates or due to an increased rupture life. Therefore, on tensile testing at the strain rates of 10^{-4} and 10^{-5}/s, the mechanism of final intergranular fracture

seems to be associated with a crack of critical length (or a critical crack opening displacement) which extends rapidly along the grain boundaries to cause failure[137]. This suggestion is supported by the fact that in the specimens tested at 10^{-4} and 10^{-5}/s, wedge cracks were observed to extend over several grain facets, thereby making them energetically unstable. The alternative mechanism which requires linkage of intergranular cracks via internal necking with ductile rupture between the cracks, is not operative since the fractured surfaces did not reveal the propogation of intergranular cracks over the complete specimen width.[137]

The nature of the cracking at various strain rates was contradictory to the accepted mechanisms for both w and r-type cavity formation.[113,163,165] It is generally reported that w-type cracks occur predominantly at high stresses and low temperatures, whereas the r-type cavities occur at low stresses and high temperatures.[163] Thus, at a constant testing temperature, the w-type cavities, would be expected to form at higher creep strain rates and r-type cavities at lower strain rates. This is in contradiction to the present results, in that there was an increased percentage of r-type intergranular cavities and a decreased occurrence of w-type cracks with increased strain rate, Fig. 90 and Table XVI. The immediate question that arises is whether the round cavities observed in the present investigation were in reality true r-type cracks, considering the high magnitude of the applied strain rates employed during tensile testing. Some of the strain rates involved in the present studies range midway between hot-working and true creep tests[56,127], therefore the r-type cavity formation mechanisms proposed for creep testing may not strictly apply. Hence, at very high strain rates of 10^{-2} and 10^{-3}/s, the voids may arise from extensive deformation of the whole matrix, resulting in the stress relief in the form of grain boundary decohesion, owing to the defect structur of the grain boundary.[50] However, at lower strain rates of 10^{-4} and 10^{-5}/s this stress relief may be accommodated

by grain boundary sliding mechanisms, resulting in an increased tendency for w-type crack formation, and a diminution of such grain boundary cavities.

5.4.2.2 Base composition with $M_{23}C_6$ at grain boundaries (ALLOY 2)

The higher tensile strength and 0.2% P.S. compared with the precipitate free microstructure (alloy 1), Figs. 63 and 64, can be attributed to an overall increase in grain boundary strength[140]. The effect was more pronounced at slower strain rates because of the inhibition of grain boundary sliding by the grain boundary carbides.[128] The variation of the strength with decreasing strain rate was very similar to that of the base microstructure (alloy 1), and can be explained on the basis of the time dependence of the softening processes.[128,129] Also, the improved creep strength, Tables XIII and XIV, of this microstructure was due to the inhibition of grain boundary sliding, resulting in a decreased creep rate and an increased rupture life.[155,156]

The deformation mechanism map for this microstructure should show larger dislocation glide and high-temperature creep fields, Fig. 5, at the expense of a decrease in the diffusional flow field, compared with the base microstructure, section 5.4.1.[29,121] In accordance with the deformation map, the deformation mechanism up to an applied strain rate of 10^{-4}/s would be dominated by dislocation glide. In fact, this is quite consistent with the observations, Plate 16(f), where transgranular fracture dominated at strain rates faster than 10^{-4}/s, presumably due to the strengthening effects of the grain boundaries.[53,54] However, at a strain rate of 10^{-5}/s the deformation mechanism changed into the high-temperature creep field, which remained the dominant deformation mechanism even at the slowest strain rate, Figs 5 and 79(a). Unlike the base microstructure, there was no definite change in the deformation mechanism on creep testing, but the ductility minimum was very prominent, Figs. 79(a) and (b). The gradual increase of creep ductility at lower strain rates was associated with the time dependent microstructural changes occuring during the tests. Two

major microstructural changes occurred.[4,52,165] First, there was the continuous coarsening of grain boundary $M_{23}C_6$ particles, and second the formation of a cell structure near the grain boundary regions. The discrete, large $M_{23}C_6$ particles are often believed to be beneficial to ductility, since they reduce the extent of grain boundary sliding, and therefore the stress concentration at grain boundary triple points, thus delaying the formation of w-type cracks.[138,165] Also, such carbides inhibit the linking of r-type cavities, i.e. the initial sub-critical propagation of cracks.[162] It is proposed that this mechanism was operative in this microstructure and evidence for this is presented in Table XII, where there was a continuous increase in tertiary creep strain with decreasing strain rate or increasing rupture time. The onset of tertiary creep is generally regarded to be a function of intergranular cavity formation.[56] Also, the formation of the cell structure near to the grainboundaries would contribute to the strengthening of these regions, thereby promoting deformation within the grain interiors and contributing to an overall increase in ductility. This is because the presence of subgrains adjacent to the original grain-boundaries inhibits further dislocation movement near to the grainboundaries, and such strengthening effects would be more pronounced at lower strain rates due to an increased rupture life. Combining the effects of the changing deformatio mechanism and the microstructural variations, accounts for the observed minimum ductility with varying strain rate. One of the contributing factors towards the improved high temperature ductility compared with the base microstructure was also the presence of solute depleted zones adjacent to the grain boundaries, resulting from the $M_{23}C_6$ precipitation, which were less strong than the matrix, thus accommodating more deformation.[4]

The net effect of grain boundary $M_{23}C_6$ precipitation on the fracture map is to expand both the transgranular and the intergranular creep fracture fields, Fig. 10, at the expense of diffusion controlled fracture mechanisms, section 5.4.1.[163]

Therefore at higher strain rates the transgranular fracture mechanism was operative, through the nucleation of voids and their linking causing ultimate failure, Plate 16(f).[163] However, at lower strain rates the intergranular fracture mechanisms were similar to those proposed for the base microstructure (alloy 1), Plate 17(a).[137] However, the cracks nucleated at triple point junctions, Plate 17(b), propagated more readily along grain boundaries due to the presence of $M_{23}C_6$ carbides, once the critical size has been attained.

The decreased number of crack nucleation sites compared with the base microstructure, Table XV, and the smaller extent of w-type cracking, Fig. 90, showed that the grain boundaries were strengthened due to the precipitation of $M_{23}C_6$ particles, thus considerably reducing the stress concentration at triple points.

5.4.2.3 $M_{23}C_6$ at grain boundaries and within the grains (ALLOY 3)

The increase in 0.2% proof stress and tensile strength, Figs 63 and 64, compared with the alloy containing only grain-boundary $M_{23}C_6$, was due to the presence of $M_{23}C_6$ precipitates within the grains, which obstructed dislocation glide at the higher strain rates and inhibited dislocation climb at the lower strain rates.[127,132,139] Despite, the large volume fraction of $M_{23}C_6$ in this microstructure, the creep strength was only comparable to that of the microstructure containing no $M_{23}C_6$ precipitates, Tables XIII and XIV, both in terms of the stress dependence of the rupture life and the minimum creep rate at a constant creep stress. One of the factors responsible for the less than expected creep strength is probably the effect of the $M_{23}C_6$ dispersion in markedly reducing the scale of the dislocation cell structure at a given creep rate.[152] Also, cell structure formation was not observed near the grain boundaries, since $M_{23}C_6$ precipitates were present throughout the matrix, with the result that the rate of recovery was markedly reduced, and deformation was confined to a narrow zone near the grain boundaries; these zones being so narrow that cells did not form. This resulted in an increased creep rate at a lower

applied stress, and ultimately to early failure. Therefore, the factor controlling the creep strength was the dispersion and morphology of the $M_{23}C_6$ precipitates within the grain interiors.

The net effect of a decreased grain size and the presence of grain boundary and matrix $M_{23}C_6$ precipitates, section 5.4.1, should lead to a slight decrease in the glide field and a small increase of the diffusional flow field, at the expense of a decrease in the high-temperature flow field, compared with the base microstructure. At a homologous temperature of 0.5, the deformation mechanisms at higher strain rates were very similar to those proposed for the base microstructure, and this was supported by fractographic evidence. However, one of the striking features was the observation of a constant high-temperature tensile ductility up to a strain rate of 10^{-4}/s, Figs 79(a) and (b), when normally there would be expected to be a continuous decrease in ductility with decreasing tensile strain rate.[128,129] It is suggested that at the higher strain rates of 10^{-2} and 10^{-3}/s, voids nucleated rapidly at the undissolved $M_{23}C_6$/matrix interface, and probably propogated rapidly due to the fracture of widmannstatten $M_{23}C_6$ platelets. This, it is suggested, led to premature failure. However, in the high temperature creep region, (i.e. at the lower strain rates slower than 10^{-4} and 10^{-5}/s) these voids may be stabilized since deformation is confined more to the grain boundary regions, thus postponing void coalescence; the material therefore exibited its true ductility.[113,163] At strain rates lower than 10^{-4}/s the ductility continued to fall, Figs 79(a) and (b), up to a strain rate of 10^{-8}/s. The 10^{-8}/s strain rate contour line on the deformation map must be close to the boundary between the high-temperature creep and diffusional flow fields, Fig. 5. Therefore, both these mechanisms would be expected to contribute towards the overall deformation, with the result that there would be an improved creep ductility. However, it must be pointed out that due to the presence of $M_{23}C_6$ carbides at grain boundaries, and in the matrix, the process of diffusional flow will be controlled by the interface reaction, i.e. the dislocations present in the

grain boundary/precipitate interface[115,119]. Such a flow mechanism would not be expected to contribute significantly to increased creep strain, particularly when both the grain-boundary dislocation density and the applied stress are very low, equation (43). Nevertheless, it is envisaged that at the slower strain rates, a coarsening of both transgranular and intergranular $M_{23}C_6$ precipitates resulting from an increased time of testing at 700°C, would occur. This will enhance recovery and increase the interparticle spacing of the grain boundary carbides, which would give improved creep ductility. This indicates the formation of a ductility trough at decreased creep rates and longer rupture times, Figs 79(a) and (b).

The increased number of intergranular cracks per unit area compared with the microstructure containing only grain-boundary $M_{23}C_6$, was due to the finer grain size giving rise to more triple points, and also due to the strengthening of the matrix leading to greater stress concentration at such junctions, Table XV. A contributory effect was also associated with the presence of $M_{23}C_6$ on non-coherent twinboundaries, which therefore act as crack nucleation sites during creep testing, Plates 17(e) and (f).[137] An increase in the percentage of twin boundary cracks, Fig 90, with decreasing strain rate emphasises the time dependence of the boundary deformation at such sites and could be explained in a similar manner to that of grain boundary sliding. However, the lower overall ductility of this microstructure compared with the microstructure containing only grain boundary $M_{23}C_6$ (alloy 2), Fig. 79(a), is reflected by the increased crack length, Table XV, which indicates the ease of crack propagation. Although, the number of intergranular cracks per 1000 grains (N_G), Table XV, was lower in this structure compared with the microstructure containing only grain boundary $M_{23}C_6$, the validity of such a parameter is questionable,[137] because it compensates for the grain size variation, but totally ignores the stress sensitivity of crack nucleation and growth[137]. Therefore, it is suggested that the parameter (N_A) in Table XV is more useful in comparing the effect of varying microstructures at a constant applied stress.

Intragranular and grain boundary $M_{23}C_6$ precipitation have opposing effects on the fracture mechanism maps, section 5.4.1[163]. Depending upon the volume fraction of $M_{23}C_6$ precipitates within the grains, the grain boundary $M_{23}C_6$ effects may be overshadowed, which is indicated by the fractographic evidence and the observed ductility values. In general, the fracture mechanisms were very similar to those proposed for microstructures containing only grain boundary $M_{23}C_6$.

5.4.3 Effect of Molybdenum and Titanium Additions

The effect of these alloying additions will be discussed individually in terms of their influence on microstructures.

5.4.3.1 Molybdenum rich $M_{23}C_6$ at grain boundaries (Alloy 4)

The effect of these precipitates on the 0.2% proof stress and tensile strength at varying strain rates was very similar to that described for the microstructure containing chromium rich grain boundary $M_{23}C_6$ precipitates (alloy 2). The improved strength compared with the structure containing grain boundary and matrix $M_{23}C_6$ precipitates, Table X, may be due to the finer grain size and to substitutional strengthening by molybdenum.[30,31] The improved creep strength compared with the microstructure containing only chromium rich grain boundary $M_{23}C_6$, Tables XIII and XIV, was due to the additive effects of these factors, itemised as follows:-

(i) Owing to the finer initial grain size of the microstructure, the growth of a crack to a critical length was more difficult due to the larger number of triple points encountered. This resulted in delayed fracture.[169,170]

(ii) The presence of slow diffusing molybdenum considerably hindered dislocation climb, leading to a lower overall strain rate.[30,180]

(iii) An appreciable amount of carbon was left in solution even after heat-treating at 700°C/6 hours, with the

result that Widmanstatten $M_{23}C_6$ precipitates formed within the matrix, and decreased dislocation mobility still further.[122,157]

Despite the more slowly diffusing molybdenum, there should be an overall increase in the glide and diffusional flow fields of the deformation map, at the expense of a decrease in the high-temperature creep field, compared with the microstructure containing chromium rich grain boundary $M_{23}C_6$ precipitates (alloy 2), due to the finer grain size (29,121). Therefore, the decrease in ductility up to a strain rate of 5.0×10^{-8}/s can be ascribed to the same mechanisms as those suggested for the structure containing chromium rich grain boundary $M_{23}C_6$ precipitates. A contributory factor towards the decreased ductility at the slower strain rates was the precipitation of the Widmanstatten $M_{23}C_6$ within the grains during the test, leading to strengthening of the alloy and promoting grain boundary deformation. However, in accordance with the deformation map, the test at 10^{-8}/s strain rate was near the boundary of both the high-temperature and diffusional flow fields. Therefore, both mechanisms contribute towards the creep strain at this strain rate, resulting in an overall increase in ductility, Figs. 83(a) and (b). Since the diffusional flow is controlled by an interface reaction, it would not be expected to contribute significantly to the creep strain.[115,119] Nevertheless, owing to the grain-boundary migration through the interface reaction, an increase in the creep strain is possible. This suggestion is supported by the evidence of a large amount of creep strain during the tertiary stages of the test, Table XII, which was a reflection of the slower void coalescence due to grain boundary migration.[119] The improved ductility could also be attributed to the coarsening of the grain boundary and matrix $M_{23}C_6$ precipitates, thereby allowing a rapid recovery of the deformed structure and more easy dislocation movement.[122,157]

The comparable number of crack nucleation sites in the

structures containing no precipitates (alloy 1) and grain-boundary as well as matrix $M_{23}C_6$ precipitates (alloy 3), Table XV, is probably due to the fine grain size of the material and also to the substitutional strengthening by molybdenum. The net effect of molybdenum rich $M_{23}C_6$ at grain-boundaries, substitutional strengthening by molybdenum and a finer grain size of this alloy would be to expand both the transgranular and diffusional fracture fields at the expense of intergranular fracture,and this is consistent with the observations. In general, the nature of the fracture mechanisms with varying strain rate was very similar to that described for the base microstructure and the microstructure containing grain boundary $M_{23}C_6$ precipitates.

5.4.3.2 $M_{23}C_6$ at grain boundaries in a titanium rich matrix (Alloy 5 - H.T.No.2)

The improved high temperature strength of this micro-structure compared with other carbide forming alloys can be attributed to its finer grain size and substitional strength-ening by titanium. Although, no creep tests were carried out on this microstructure, it is most probable that the creep strength will also improve due to the hindrance of dislocation movement by titanium atom clusters.[30,31]

Despite the presence of a finer grain size compared with the structure containing molybdenum rich $M_{23}C_6$ at grain boundaries (alloy 4), Table IV, the net effect of grain-boundary $M_{23}C_6$ and the slow diffusivity of titanium, should be to decrease the diffusional flow field and increase the high-temperature creep field, with very little change in the glide field compared with the Mo rich microstructure. There-fore, in accordance with the 304L deformation map, the transitio from dislocation glide to high-temperature creep mechanisms should occur below a strain rate of 10^{-4}/s, Fig. 5. Such a change in deformation mechanism does not explain the initial increase of ductility with decreasing strain rate; the expected trend would be quite the opposite.[128,129] Also, this change of deformation mechanism still does not explain the extremely high ductility values, Table X and Fig. 75, compared with other carbide containing microstructures. Nevertheless,

the shape of the stress/strain curves, Fig. 67, and the fractographic evidence, suggests that ductile fracture occurs. The initial increase in ductility with decreasing strain rate, Fig. 75, may be due to the strain rate sensitivity of this fracture.(185) The decrease in overall ductility at a strain rate of 10^{-5}/s was due to the increasing contribution of the grain boundary deformation to the overall strain during rupture, rather than the predominance of transgranular deformation, Fig. 67. Crack nucleation is associated with the undissolved TiC particles, voids being nucleated at the TiC/matrix interface, and leading to localised deformation in a shear band. This gave rise to very high ductility.(163) Why such a mechanism should not be operative in the previous alloys containing undissolved $M_{23}C_6$ may be due to differences in the bonding between $M_{23}C_6$ and TiC and the matrix.(163)

The decreased extent of intergranular cracking, Table XV, compared with other microstructures, confirmed that the deformation was confined to the matrix rather than occurring at the grain boundaries. However, at a strain rate of 10^{-5}/s, the increased crack length ($\bar{c}$) and the nature of the cracking, Fig. 90, did suggest that some grain boundary deformation was also associated with a very ductile fracture.

5.4.3.3 $M_{23}C_6$ and TiC at the grain boundaries and within the matrix (Alloy 5 - H.T.No. 1)

The presence of TiC precipitates at grain boundaries and on dislocations improved the creep strength compared with the microstructure containing molybdenum rich grain boundary $M_{23}C_6$ precipitates, Tables XIII and XIV, both in terms of the creep stress for a given rupture life and the minimum creep rate at a given stress. The effect is associated with the grain boundary strengthening mechanism, where the overall number of crack nucleation sites was noticeably reduced, Table XV. Also, a contributory factor towards the improved creep strength was the pinning of dislocations by TiC.(150,178) It is, however, difficult to define the behaviour of TiC precipitates on the strengthening mechanism, when

present at the grain boundaries, and to differentiate their effects from grain boundary $M_{23}C_6$ carbides. One possibility is the segregation of titanium atoms to the grain boundaries, pinning the dislocations within the grainboundary plane. Thus would also slow down the diffusion of vacancies necessary for r-type void nucleation and growth, thereby delaying fracture.[109,113,165]

Owing to the presence of TiC precipitates within the matrix, the deformation mechanism map for this microstructure should show an increase in the high-temperature creep field at the expense of a slight decrease in the glide field, compared with the microstructure containing only grain boundary $M_{23}C_6$ precipitates in a titanium rich matrix.[29,121] The effect of varying strain rate on the high temperature tensile ductility was, however, similar to that of the grain boundary $M_{23}C_6$ containing microstructure in a titanium rich matrix, Fig. 15. Due to the strain rate sensitivity of the ductile fracture, the creep ductility decreased with decreasing strain rate, Figs 83(a) and (b).[185] Although, there was a small contribution of ductile fracture strain towards the overall creep ductility, (since much deformation was accommodated during the final stages of the tertiary creep, Fig. 84,) most of the improvement in creep ductility compared with the microstructure containing grain boundary $M_{23}C_6$ in a titanium rich matrix, was associated with the presence of TiC at grain boundaries and dislocations.[138,158] Previous workers[138] have ascribed the ductility improvements to the restricted growth of w-type cracks because of the grain-boundary TiC. It is thought however, that the ductility improvements are primarily associated with a decrease in the nucleation rate of w-type cracks (N_A) due to a smaller lattice parameter of TiC, Table XV, compared with other carbides. The number of cracks per unit area was similar to that of the microstructure containing chromium rich $M_{23}C_6$ at grain boundaries (alloy 2), Table XV, despite the presence of matrix TiC. This emphasises that the grain boundaries are much stronger in this microstructure, and these effects are connected with the presence of titanium in the steel. The details of the actual mechanism still remain

uncertain, but it can be deduced that titanium imparts a beneficial effect to creep ductility. One of the factors responsible for improved creep ductility at the lower strain rates is the recovery of the deformed structure, and the onset of recrystallization, Plates 14(c),(d) and (e). The grain boundary migration is also associated with recrystallization, Plate 14(d), thereby delaying the coalescence of r-type voids and thus the ultimate fracture.[119] At lower creep rates of 10^{-9}/s, both the high-temperature creep and diffusional flow mechanisms are controlled by an interface reaction, and will contribute towards the overall creep deformation, because such a strain rate might lie near the boundary of these two fields in the deformation mechanism map.[29,121] This will result in an increased creep ductility and a profound ductility trough on extrapolating the strain rate v/s ductility curve to lower strain rates, Fig. 83(a). It is evident that very ductile transgranular fracture can be operative at temperatures of 0.5 Tm in more complex alloys, particularly at relatively higher strain rates. The ductile fracture is perhaps more dominant, only when there were many nucleation sites such as undissolved TiC particles within the matrix.

5.4.4 Gamma-Prime (γ') Forming Alloys

The results will be discussed on the basis of varying dispersions of γ' within the matrix, in both the low and high carbon alloys.

5.4.4.1 γ' zones and with virtually no $M_{23}C_6$ at grain boundaries (alloy 7, H.T.No.1)

The considerable increase in the proof and tensile strength, Table X, compared with simple carbide containing structures, was due to the presence of the γ' zones.[30,32,34] The coherency strains hindered dislocation movement, thereby strengthening the structure. However, the rate of decrease in strength with decreasing strain rate was similar to that of the simple carbide containing structures, Figs 73 and 74. Generally, the rate of decreasing strength with decreasing

strain rate would be expected to be very small at the higher strain rates, since recovery of the deformed structure containing γ' zones within the matrix would be minimal, owing to very short testing times. One of the recovery processes operative in such a microstructure would be the piling up of dislocations around the more highly strained regions, thus requiring vacancy diffusion for dislocation climb to operate in order to surmount these barriers.[30] Such a mechanism would be slow, and considering the short testing time at the higher strain rates it is hard to visualise this effect alone controlling the variation in strength with strain rate. The decrease in strength with decreasing strain rate may be possibly due to the occurrence of cross-slip by dislocations between the zones. The increased creep strength of this microstructure compared with simple carbide containing structures is clearly shown by the rupture life, creep stress and minimum creep rate, Tables XIII and XIV. The mechanism of improvement is very similar to that described for the proof and tensile strengths, provided that the zones remain coherent with the matrix. However, once this coherency is partially lost, as evident in creep tested microstructures Plate 15(a), other processes of strengthening such as antiphase boundary energy and Orowan looping play a more dominant role.[30,48,49]. Ideally, such a change in microstructure during testing, should result in an increased creep rate, due to an increased freedom of movement of dislocations between the more widely spread semicoherent γ' particles, but this would require very sensitive strain measurements to be detected.

The presence of γ' zones within the matrix will be to decrease the glide and high-temperature creep fields, and to significantly expand the diffusional flow field, section 5.4.1 [29,121]. The evidence to the effect that the glide field decreases is presented in Plates 19(a) and (b), where at a strain rate of 10^{-3}/s the fracture was of a mixed trans/inter-granular type, suggesting that this strain rate was near the boundary between the glide and dislocation creep fields. However, tests between strain-rates of 10^{-4}/s and 10^{-6}/s should lie well within the dislocation creep field, and the

ductility decrease, Figs 86(a) and (b), is due to the increasing participation of grain boundary sliding mechanisms (112,113,115).

Minimum creep rates of 10^{-7} and 10^{-8}/s respectively were observed and were presumably due to diffusional flow. Therefore, the overall strain would be expected to decrease, which is consistent with the observations, Figs 86(a) and (b). One of the factors responsible for the decreased creep strain is the pinning effect of the γ' zones on the migrating boundaries. However, the interrupted creep tests revealed that during the test the γ' zones partially lost coherency and their growth resulted in an increased interparticle spacing, Plate 15(a). Because of this the deformation mechanism changed and was controlled by both dislocation creep and diffusional flow, leading to an increased tertiary creep strain, Fig. 85.(121,161) Therefore, at lower creep stresses, i.e. longer rupture times and lower creep rates, the contribution of such deformation to the tertiary stages of creep would increase, resulting in an overall increase in creep ductility and the formation of a profound ductility trough, Figs 86(a) and (b). Hence the suggestion that the creep rate continuously decreases with increasing γ' particle size, and that above a certain particle size the creep rate is independent of particle size, seems invalid.(140) The experimental results can be interpreted in terms of a larger particle size and consequent larger interparticle spacing, allowing Orowan looping to occur more readily, i.e. the creep rate increasing with increasing particle size.

The smaller number of crack nucleation sites, Table XV, was a direct reflection of the coarse grain size of this microstructure. The higher percentage of the grain boundary voids at higher strain rates of 10^{-2} and 10^{-3}/s, Fig. 92, can be attributed to stress concentration at grain boundaries due to the strengthening by γ' zones within the matrix, resulting in stress relief in the form of grain boundary decohesion, as described in section 5.4.2.1.

The effect of γ' zones within the matrix, will be to significantly expand the creep fracture field at the expense the transgranular fracture and to suppress rupture.(163)

This is consistent with the observed fractographic evidence. Therefore, at higher strain rates, transgranular cracks can nucleate at undissolved TiC/TiN particle-matrix interfaces, the cracks gradually linking up to cause ultimate failure.[163] However, at intermediate strain rates in the intergranular fracture field, fracture is associated with w-type crack nucleation. These cracks reach a critical length and rapidly extend along grain-boundaries to cause ultimate failure.[137] This extension of energetically unstable cracks takes place readily, since the grain interiors in this microstructure are far stronger than in simple carbide containing structures, which results in an overall lower ductility. At slower strain rates in the diffusional flow regime, void coalescence is delayed due to grain boundary migration, thereby also delaying fracture.[165,169,171] Such a mechanism would improve the rupture life as shown in, Table XIV, and also would improve creep ductility, particularly during tertiary creep. Although the creep strain during tertiary creep was improved, this improvement was not large enough to cause an overall increase in ductility, since the migrating boundaries were pinned by the γ' precipitates within the adjacent grains.

5.4.4.2 Semicoherent γ' and virtually no $M_{23}C_6$ at grain boundaries (alloy 7, H.T.No. 2)

The lower 0.2% proof stress and tensile strength of this microstructure compared with the microstructure containing γ' zones, Figs. 73 and 74, was due to the change in strengthening mechanism[130,131,139,141]. This was because strengthening mechanisms such as antiphase boundary energy and Orowan looping played a dominant role, rather than the interactions between the strain fields of γ' zones and dislocations.[30,44,47] It is believed that the antiphase boundary energy strengthening will be dominant at the higher strain rates, whereas Orowan looping will be operative at the lower strain rates, because the former needs particle cutting whilst Orowan looping requires dislocation climb. The rate of decrease in strength with decreasing strain rate,

Figs 73 and 74, was comparable to that of the microstructure containing γ' zones, up to a strain rate of 10^{-4}/s. This can be attributed to the processes of dislocation climb and cross-slip between the particles. However, an increased rate of strength decrease in this microstructure at a strain rate of 10^{-5}/s is due to the occurrence of softening processes, owing to an increased γ' interparticle spacing compared to the microstructure containing γ' zones.[128,129] The decreased creep strength, as indicated by the minimum creep rate and rupture time at a constant creep stress, compared with the microstructure containing γ' zones, Tables XIII and XIV, was due to an increased γ' interparticle spacing which resulted in an increased creep rate, i.e. earlier failure at lower stresses, since Orowan looping becomes easier as Λ increases.[138]

The effect of a semicoherent γ' dispersion on the deformation mechanisms will be very similar to that described for the microstructure containing γ' zones (H.T.No. 1), except that the changes in the different flow fields will not be as prominent.[29,121] However, a deformation mechanism map does not explain the initial increase in ductility with decreasing strain rate, as the expected trend would be the reverse, Figs 86(a) and (b).[128,129] The shape of the stress-strain curves, Fig 87, and the extremely ductile fractures at the lower tensile strain rates, Plate 19(c), suggests that there was much intragranular ductile fracture together with intergranular and transgranular deformation processes. Void nucleation is associated with undissolved TiC/TiN particles,[163] and the mechanism is very similar to that discussed previously. It might be questioned whether a similar ductile fracture should be operative in the microstructure containing γ' zones, since the number of nucleation sites, i.e. undissolved TiC/TiN particles, is the same for both microstructures. However, the dislocations were able to cut through the γ' zones, whereas dislocations will not be able to do so in the microstructure containing large semicoherent γ' particles, but will tend to loop around γ' particle. This leads to an increased stress concentration near undissolved TiC/TiN particles, thus

resulting in an increased tendency to reach the critical stress level necessary to nucleate a very ductile fracture.[163] Such a condition is not satisfied in the microstructure containing γ' zones, since dislocations are able to cut through the zones.

On decreasing the strain rate during creep testing, the grain boundary deformation mechanisms play a more dominant role, resulting in a lower overall ductility. Nevertheless, the improved creep ductility of this microstructure compared with the microstructure containing γ' zones, is due to the increased interparticle spacing of γ' resulting in an enhanced dislocation movement which allows deformation to occur more readily, Plates 15(b) and (c).[160] The recovery of the deformed structure will be easier, compared with the microstructure containing γ' zones, thereby further improving the ductility. At a creep rate of 2.0×10^{-8}/s where the dominating deformation mechanism might be diffusional flow, Plate 15(d), the creep strain will increase compared with the microstructure containing γ' zones, Figs 86(a) and (b). This is due to the increased γ' interparticle spacing allowing an increased rate of migration of the grainboundaries. Decreasing the strain rate further will cause an increase in the γ' interparticle spacing because of the increased testing time at 700°C, thereby improving the overall ductility, i.e. a ductility trough will be formed.

The effect of a semicoherent γ' dispersion on the fracture mechanism maps, Fig. 10, will be very similar to that described for the microstructure containing γ' zones except that transgranular ductile fracture will be suppressed. Indirect indications of the higher overall ductility compared with the microstructure containing γ' zones, is presented in Table XV, where the number of intergranular cracks was much reduced due to a lower matrix strength. Also, the number of voids formed by grainboundary decohesion was reduced, Table XVI and Fig. 92, thus confirming that grainboundary deformation was less marked.

5.4.4.3 Matrix γ' zones and grain boundary $M_{23}C_6$ (Alloy No. 8 H.T.No.1)

The decreased tensile strength of this microstructure compared with the microstructure containing γ' zones but no grain boundary $M_{23}C_6$, Figs 73 and 74, was due to a lower volume fraction of the γ' zones, since a larger amount of titanium was tied up as TiC/TiN, thereby leaving less titanium in solution for γ' precipitation on ageing.(140) Although, the strengthening mechanisms at various strain rates were similar to those proposed for the microstructure containing γ' zones but no grain boundary $M_{23}C_6$, the contribution of such mechanisms largely depends upon the volume fraction of the precipitates, equations (7) to equation (10).(43,47) This microstructure also showed a decreased creep strength on the basis of rupture life, Tables XIII and XIV, compared with the microstructure containing γ' zones but no grain boundary $M_{23}C_6$ precipitates. On the other hand the observed minimum creep rate was lower than for the microstructure containing γ' zones but no grain boundary $M_{23}C_6$, Table XIV, suggesting an increase in the creep strength. The decreased rupture life for a constant stress was possibly due to the presence of a continuous film of $M_{23}C_6$ particles at grain and twin-boundaries, which facilitated crack propagation. The lower creep rate was also due to the presence of grain boundary $M_{23}C_6$ precipitates inhibiting grain boundary sliding.(155,156) These results indicate that the general inverse relationship between rupture life and minimum creep rate does not hold if fracture is facilitated by some microstructural feature.

Despite its finer grain size, Table IV, the deformation mechanism map will be similar to that for the microstructure containing γ' zones but no grain boundary $M_{23}C_6$, since the presence of $M_{23}C_6$ precipitates will counteract any grain-size effects.(29,121) Therefore, the variation of ductility at varying strain rates, Figs 86(a) and (b), can be discussed in a similar manner to that described in section 5.4.4.1. A similar effect will also be observed on fracture maps, and the observed fractures can also be explained in

a similar manner.[163] However, the lower overall ductility for this microstructure compared with the microstructure containing γ' zones but no grain boundary $M_{23}C_6$, was a function of various microstructural features playing a dominant role at different strain rates. At the higher strain rates the presence of a larger volume fraction of undissolved TiC/TiN led to an increased number of intragranular voids, the result of which was earlier failure and a lower overall ductility. At relatively lower strain rates, the increased number of intergranular cracks and their easier propogation due to grain boundary $M_{23}C_6$, Table XV, led to poor ductility. Twin boundary cracking also probably contributed to the lower ductility, Table XVI and Fig. 92. At very low creep rates, where the diffusional flow mechanism is dominant, the accumulation of creep strain is very low since grain boundary migration is greatly hindered due to the presence of grain boundary $M_{23}C_6$ and γ' zones, Plate 15(e).[115,119]

5.4.4.4 Matrix semicoherent γ' and large grain boundary $M_{23}C_6$ precipitates (Alloy No. 8 H.T.No.2)

The decrease in the tensile strength compared with the microstructure containing semicoherent γ' particles but no grain boundary $M_{23}C_6$ precipitates, Figs 73 and 74, was due to a decreased volume fraction of γ' precipitates,[43,47,141] and the strain rate dependence of the strength and proof stress is as explained in section 5.4.3.2. Despite, the presence of a smaller volume fraction of γ' precipitates, the improved creep strength of this microstructure, on the basis of rupture life and observed minimum creep rate, Tables XIII and XIV, may be due to the presence of a continuous chain of large grain boundary $M_{23}C_6$ precipitates. These precipitates are well known to impede grain boundary sliding more effectively than small $M_{23}C_6$ particles, thereby increasing the rupture life and decreasing the creep rate.

The deformation and fracture mechanism maps for this microstructure should be very similar to those for the microstructure containing semicoherent γ' precipitates with

no grain boundary $M_{23}C_6$ particles, due to the reasons outlined in section 5.4.4.3[29,121]. Therefore, the ductility profile with varying strain rates, Figs. 86 (a) and (b), can be explained in terms of similar mechanisms. However, the increased ductility of this microstructure at most strain rates, Figs. 86(a) and (b), compared with the microstructure containing semicoherent γ' precipitates with no grain boundary $M_{23}C_6$ particles can be attributed to a number of factors, such as:-

(1) At higher strain rates there will be a clearly developed ductile fracture due to the larger volume fraction of undissolved TiC/TiN particles, compared with the microstructure containing semicoherent γ' precipitates but no grain boundary $M_{23}C_6$ precipitates. Therefore, an increased number of transgranular particle/matrix cavities will result in an increased rupture strain.

(2) At relatively low strain rates, the larger grain-boundary $M_{23}C_6$ precipitates inhibit grain boundary sliding. Despite, the presence of a large number of intergranular cavities, the growth of these cavities is inhibited due to a larger interparticle spacing of $M_{23}C_6$, thus delaying failure. Both these mechanisms result in an increased ductility.

(3) On the other hand, at very low strain rates where deformation is governed by diffusion controlled mechanisms, the lower ductility of this microstructure compared with the microstructure containing semi-coherent γ' precipitates but no grain boundary $M_{23}C_6$ precipitates, can be attributed to a marked interface reaction control mechanism, Plate 15(e), due to the presence of grain boundary $M_{23}C_6$ precipitates, Figs 86 (a) and (b)[115,119].

5.4.5. Serrated Yielding

Serrated yielding is generally regarded as a direct reflection of the drag effect exerted by the solute atoms on moving dislocations[133-138]. For this to occur the

solute atoms must be capable of diffusing at a rate approaching the dislocation velocity. The type of solute responsible for serrated flow may therefore be deduced from their diffusion velocities, in comparison with the dislocation velocities. The solute diffusion velocity (V_S) is given by (138):-

$$V_S = \frac{D_S W}{kTb} \qquad \ldots\ldots\ldots\ldots (61)$$

where D_S is the solute diffusion coefficient, W the solute-dislocation binding energy, k Boltzmann's constant, T the testing temperature in ^{o}K, b the burgers vector $\sim(2.5A^{o})$ and V_S in the solute drift velocity. On the other hand, the average dislocation velocity, V, can be related to the tensile strain rate by(138):-

$$\dot{\epsilon} = {}^{1}/_{m} \rho b V$$

or

$$V = \frac{m \dot{\epsilon}}{\rho b} \qquad \ldots\ldots\ldots\ldots (62)$$

where m is the Schmid factor (~ 3 for polycrystalline f.c.c. metals), $\dot{\epsilon}$ is the applied strain rate, and ρ is the quenched in mobile dislocation density ($\sim 10^{10}$ lines/cm^2). Therefore, the dislocation velocity is independent of any compositional variations and solely depends upon the dislocation density of the structure and the applied strain rate, Table XVII.

On the basis of this analysis, i.e. equations (61) and (62), for carbon in austenite the drift velocity is far greater than the dislocation velocity, Table XVII. Therefore, carbon is most probably too mobile to exert a drag on dislocations in this alloy system. On the other hand, the solute-dislocation binding energy, W, can be calculated for various substitional atom species(138), from the following equation:-

$$W = \frac{\mu a^{3}}{2\pi} \cdot \frac{r_s - r_m}{r_m} \qquad \ldots\ldots\ldots\ldots (63)$$

where r_m is the matrix atomic radius of 1.27 A^{o}, r_s the solute atomic radius, 'a' the lattice parameter (3.59 A^{o}), and

$\mathcal{N}$ is Avagadro's No. Substituting calculated values of W in equation (61), the drift velocity of the solutes such as Cr, Mo and Ti, are much lower than the dislocation velocity, Table XVII. However, as pointed out by Boothby[138], such values are based on the assumption that a thermal equilibrium vacancy concentration is maintained throughout tensile testing, whereas the vacancy concentration changes due to the creation of vacancies during straining, prior to the onset of the serrations. This increased vacancy concentration could lead to increased substitutional solute diffusivity, and the modified substitutional diffusivity can be represented by:-[135]

$$\bar{D}_S \sim 0.12 \; C_v \; \exp\left(-Em/_{RT}\right) \quad \ldots\ldots\ldots\ldots (64)$$

where C_v is the vacancy concentration, assumed to be similar to that in nickel ($\sim 4 \times 10^{-6}$ per 1% strain), Em is the activation energy for vacancy migration ~ 30 kcal mole^{-1} (about half of the activation energy for thermal diffusion). Using this modified value of $\bar{D}_S$ in equation (61) gives a substitutional solute drift velocities, V_s, very near the order of the dislocation velocities, Table XVII. This indicates that substitutional solutes are more likely to be responsible for serrated flow, but does not explain the observation of serrations at higher strain rates of 3.28×10^{-2}/ sec, Tables XI and XVII. There may be a chemical interaction between the mobile carbon atoms at a dislocation and strong carbide forming elements, such as chromium, molybdenum and titanium, which increases the binding energy and to an increased value of solute drift velocity in equation (61)[138]. But, such an increase is only going to change the solute drift velocity by a factor of 2-3, which still does not account for the difference of nearly an order of magnitude in the drift velocity and the dislocation velocity at a strain rate of 3.28×10^{-2}/sec, Table XVII. However, such a chemical interaction does explain the increased serration amplitude, when substitutional solutes such as Mo and Ti are present in the matrix, Table XI. Perhaps, the strain rate sensitivity of the serrated flow

is dependent on the dislocation participation in the tensile deformation at varying strain rates. Also, mechanisms such as recovery and the generation of dislocations on straining prior to the onset of serration can greatly affect the dislocation density parameter, ρ , in equation (62).

Therefore, many details still remain to be resolved, but serrated yielding seems clearly to be associated with the presence of substitutional alloying additions in this alloy system.

5.4.5 Microstructural Dependence of the Stress Exponent, n

For all the alloys tested at 700°C, both the stress dependence of the strain rate and the rupture life equations (47) and (51), were reasonably obeyed,[109,113] Figs 77 and 78. This shows that the stress exponent 'n' is a direct reflection of the observed strain rate or the rupture life, in a given microstructure. Although, both these parameters will be influenced by the constants A and K in equations (47) and (51) respectively, the value of n should also play a dominant role in controlling the creep strain rate. In particular, as long as the observed minimum creep strain rates lies within the limits of one deformation mechanism, Fig. 5, certain correlation can be made with the initial microstructure and the chemical composition of an alloy, Table XIII.

The value of n for the base composition, Table XIII, was well within the limits specified by other workers for alloyed austenite .[113,122] Such a low value of n also corresponds with the highest minimum strain rate in this alloy, Table XIV, compared with other compositions. Introducing $M_{23}C_6$ carbides at the grain boundaries showed an increased value of n from 4.4 to 6.7, and corresponded with the decreased creep rate and an improved rupture life, compared with the base composition (alloy 1), Table XIV.[145] This indicates that due to the strengthening of the grain-boundaries, the deformation takes place within the grain interiors, thus reducing the rate of creep straining. This may be why Gladman et al[122] noticed a change in the value

of n from 6.2 to 8.2 by increasing the carbon content from 0.015% to 0.056% in the same austenitic stainless steel, because in the low carbon alloy, the supersaturation was not enough to cause grain boundary strengthening by $M_{23}C_6$ precipitation. However, on introducing intensive $M_{23}C_6$ precipitation within the grain interiors, alloy No. 3, the deformation was transferred to a narrow zone near the grain-boundaries, resulting in a relatively higher creep rate than expected, Table XIV, and ultimately leading to early failure, i.e. a decreased value of $n \sim 4.4$.

In accordance with the above hypothesis, the presence of molybdenum rich grain boundary $M_{23}C_6$ precipitates should result in a value of n, similar to that observed for alloy 2. But, the value of n ($\sim$ 5.30) was less by 1.4 compared with alloy 2. However, plotting the results on the basis of the logarithms of the creep rate v/s applied stress, equation (47), there was a definite change in the slope of the straight line at the lower creep rates, Fig. 77, and also the value of n at higher creep rates was $\sim$ 7, i.e very similar to that of alloy 2. Therefore, the empirical relationship between rupture life and secondary creep rate, equation 50,[109] is only true, so long as the deformation mechanism does not change drastically, i.e. from the high-temperature creep region to interface reaction control, Fig. 5. With the introduction of $M_{23}C_6$/TiC at the grain boundaries, similar factors contribute to an increased value of $n \sim 6.4$, since there were only high temperature creep deformation mechanism operative within the creep rate ranges studied.

The gamma prime forming alloys in various heat-treatment conditions showed that the stress dependence of the strain rate or rupture life, was a strong function of the morphology of the precipitate distribution, Table XIII. In accordance with the deformation mechanism maps, Fig. 5, the deformation at the lower strain rates was interface reaction controlled,[29,121] and a linear relationship between the observed creep rate and the applied stress should have been followed, equation (42).[29,115,119] However, such a linear relationship was not shown by the present data, and previous workers

(145,148,149,150) have also reported similar observations. There may be several factors affecting this non-linearity which contribute equally to a higher value of the stress exponent, n. Due to a homogenous γ' dispersion within the grains, a moving grain boundary is subjected to a continuous diffusional interface reaction control during deformation. In other words, a diffusing grain boundary after bypassing one set of γ' particles, will be pinned by another array of γ' precipitates, and this will continue throughout the deformation process, resulting in an increasingly small value of grain boundary mobility M, in equation (42). Also, due to a continuous grain boundary-particle interaction, the dislocation density will be continuously increasing in equation (42), thus contributing to a loss of linearity.(115,119) Both these factors are thought to be responsible for a higher stress dependence of the strain rate in these alloys. Also, a finer dispersion of γ', (i.e. zones), will do this more effectively than a semicoherent γ' dispersion, since the interparticle spacing is significantly reduced. It is interesting to note that power law creep and interface reaction controlled creep are both governed by dislocation climb.

6. CONCLUSIONS

6.1 GRAIN COARSENING CHARACTERISTICS

1. The grain size at all stages of grain coarsening was dependent on the undissolved carbide particle size and the volume fraction, i.e. r/f.

2. The grain size below the grain coarsening temperature decreased with increasing amount of carbon and other carbide forming elements, due to an increased volume fraction of undissolved particles. The time and temperature dependence of the grain size below the grain-coarsening temperature was clearly seen in the lower carbon alloys.

3. The temperature dependence of the grain size above the grain coarsening temperature was evident in low carbon alloys, whereas there was little time dependence due to the absence of pinning precipitates. On the other hand, the time dependence of the grain size in alloys containing a large volume fraction of particles was related to the nature of the undissolved carbides, since the coarsening and solution characteristics varied with increasing solution treatment time.

4. The grain coarsening temperature varied markedly with the composition and the overall constitution of the alloys, i.e. with the presence of different types of carbides in the system.

5. The results verified Gladman's equation[57] for predicting the grain size. Other models were less successful in predicting the grain size, but it is concluded that the Gladman model slightly overestimated the pinning force exerted by undissolved precipitates.

6.2 AGE HARDENING AND PRECIPITATION KINETICS

1. A high nickel content significantly decreased the solubility of carbon in austenite, and $M_{23}C_6$ precipitation was observed even at carbon levels as low as 0.01 wt.%. However, the age-hardening increased markedly with the

amount of carbon in solution, and the hardness increment showed a linear relationship with increasing carbon in the Fe-Ni-Cr alloys. In these, a two stage ageing process was operative and possibly associated with the separate occurrence of $M_{23}C_6$ precipitation at grain boundaries, and later within the grains. Chromium diffusion was the rate controlling mechanism for $M_{23}C_6$ precipitation at all stages of ageing.

2. In the high carbon base composition, both stringer and Widmanstatten $M_{23}C_6$ was observed within the grains, associated with quenched in dislocations and vacancies. The general sequence of $M_{23}C_6$ precipitation was first at triple point junctions, then grain-boundary surfaces and non-coherent twin boundaries, and finally within the grains. The general orientation relationship of the precipitates at all nucleation sites was cube-on-cube with the appropriate matrix grain.

3. A Molybdenum addition resulted in undissolved $(Cr_{15}\ Fe_4\ Ni_2\ Mo_2)\ C_6$ carbides after solution treatment, and the intensity of age-hardening was lower than in the high carbon base composition, due to a smaller amount of carbon available for precipitation. This alloy also showed two separate ageing reactions associated with precipitation on dislocations and on grain-boundaries.

4. Combined molybdenum and titanium additions resulted in ageing reactions which were related to the relative diffusion rates of chromium, molybdenum and titanium, and also to the titanium in solution. Thus at lower ageing temperatures, $M_{23}C_6$ precipitated on grain boundaries, but at higher ageing temperatures TiC precipitated on dislocations. At very high ageing temperatures, grain-boundary TiC and $M_{23}C_6$ was observed. The age-hardening was a result of carbide precipitation only, and the Ti in solution was not sufficient to cause γ' precipitation.

5. Combined titanium and aluminium additions resulted in a two stage ageing process below the zone solvus temperature of $\sim 850^{\circ}C$. The ageing reactions were controlled by the bulk substitutional solute diffusion.

The first stage was due to the formation of zones, which grew in the second stage, with a partial loss of coherency, into γ' precipitates. Above the zone solvus temperature, γ' formed directly without the prior formation of zones and only a single stage ageing reaction was observed.

6. γ' nucleated predominantly on defects such as vacancies and dislocations. Vacancy nucleation was dominant within the grains and dislocation nucleation mainly observed near to grain boundaries. No γ' depleted regions were observed.

6.3. COLD-WORK, RECRYSTALLIZATION AND PRECIPITATION

1. The work-hardening rate of Fe-Ni-Cr alloys depended on the initial solution treated grain size, the volume fraction of undissolved particles and their size, and also on effects of the various alloying additions on the stacking fault energy. The contribution of the lower stacking fault energy became more prominent at higher cold-working reductions.

2. In all the alloys, recrystallization occurred by subgrain formation at the original grain/twin boundaries and deformation bands. After heavy deformations, nucleation from dislocation cells and deformation bands became more prominent. Recrystallization by a grain-boundary bulge mechanism was not observed. Only in the carbide forming alloys did the recrystallized grains grow rapidly into the surrounding matrix by grain-boundary migration. The migration rates after low deformations in the carbide forming alloys were comparable to those observed during grain growth. However, at higher deformations, boundary migration rates were significantly increased.

3. Undissolved carbides accelerated the rate of recrystallization and acted as nucleation sites.

4. The results can be interpreted in terms of the competition between precipitation and recovery/recrystallization reactions, and were clearly influenced by the initial structure of the alloy.

5. In plain carbon Fe-Ni-Cr alloys, precipitation preceded recrystallization and $M_{23}C_6$ carbides precipitated mainly at deformed grain-boundaries and on deformation bands. Both molybdenum and titanium additions significantly retarded precipitation at 700°C and 750°C. Late carbide precipitation inhibited the growth of recrystallized grains.

6. In γ' forming compositions, cold working prior to ageing significantly increased the rate of zone formation and their growth. Nucleation occurred near to dislocations and growth was assisted by dislocation core diffusion.

7. γ' precipitation within the deformed grains preceded any recrystallization, with the result that γ' particle-dislocation interactions retarded the recrystallization processes.

6.4. HIGH TEMPERATURE PROPERTIES

1. Both the 0.2% proof stress and tensile strength increased with increasing volume fraction of precipitated second phase particles. Substitutional solutes such as Mo and Ti also contributed towards this strength increase by solid solution hardening. The strain rate sensitivity of the decreasing strength with decreasing strain rate, was similar for all microstructures tested at 700°C.

2. Generally, in the carbide forming alloys, the minimum creep rate and rupture life increased with increasing volume fraction of carbides. The overall creep strength also, depended upon the relative strength of the grain boundaries to the matrix. Heavy Widmanstatten $M_{23}C_6$ precipitation confined the deformation to a narrow zone near the grain boundaries, resulting in a shorter rupture life. Substitutional solutes also improved the creep strength, provided the carbide precipitates were predominantly at the grain boundaries. Copious

grain boundary carbides were beneficial to creep strength and ductility.

3. The microstructures containing varying dispersions of γ' showed a major increase in creep strength. However, the microstructures containing γ' zones were significantly stronger than those containing semicoherent γ' dispersions.

4. There was no simple effect of strain rate on the high temperature ductility, because both deformation and fracture mechanisms were continuously changing with strain rate. The possibility of a relationship between these two variables only exists as long as there is one deformation mechanism operative over a range of strain rates, and providing there are no microstructural changes during testing. The ductility results were explained by considering the effect of varying microstructural and compositional features on the deformation and fracture mechanism maps, and also on the microstructural changes occurring during testing.

5. Grain boundary $M_{23}C_6$ improved the high-temperature ductility by inhibiting intergranular cracking and suppressing the growth of r-type voids. Larger grain-boundary $M_{23}C_6$ particles, however, were even more beneficial to high temperature ductility.

6. The titanium steel (alloy 5) showed the highest creep ductility. This may have been due to either the presence of TiC or titanium segregation at the grain boundaries.

7. Microstructures containing semicoherent γ' dispersions showed better high temperature ductility than those containing γ' zones, due to a larger interparticle spacing and decreased coherency strains at the particle/matrix interface. Large $M_{23}C_6$ particles at grain boundaries, in conjunction with semicoherent γ' dispersion, further improved the ductility by inhibiting grain boundary sliding. However, when the deformation was diffusion controlled, the ductility was slightly reduced due to a marke interface reaction control of the deformation process.

8. Nucleation of transgranular fracture at very high strain rates commenced with cracks around undissolved non-deformable particles, which grew as the matrix deformed, and started to link up to cause ultimate failure. At lower strain rates the intergranular fracture was associated with the nucleation of energetically unstable w-type cracks which grew rapidly to cause failure.

9. In the microstructures containing a large volume fraction of undissolved TiC/TiN particles, a very ductile transgranular fracture was observed. Undissolved $M_{23}C_6$ suppressed void nucleation due to their high degree of bonding with the matrix. Also, the presence of larger semicoherent γ' precipitates facilitated this type of fracture at relatively high strain rates, by increasing the stress concentration near TiC/TiN particles due to the increased matrix deformation.

10. The presence of a heavy dispersion of $M_{23}C_6$ particles along twin boundaries, initiated twin boundary cracking.

11. In all the microstructures, specimens tested at a strain rate of 10^{-2} and 10^{-3}/s, showed serrated yielding. Substitutional solutes were responsible for this effect. The chemical interaction between the carbon atoms and strong carbide forming elements, such as chromium, molybdenum and titanium, was observed to increase the yield serration amplitude.

12. The stress dependence of the creep rate was related to the different microstructural features in Fe-Ni-Cr alloys, as long as there was only one deformation mechanism operative within a given range of creep rates. Therefore, the empirical relationship between the rupture time and observed minimum creep rate was not found to hold in carbide forming alloys, if the deformation mechanism changed, i.e. from high temperature creep to diffusional creep. Such an empirical relationship still holds true if the deformation mechanism changed from the high temperature creep to diffusional creep which is controlled by a marked interface reaction, such as occurred in the γ' forming alloys.

6.5 SUGGESTIONS FOR FURTHER WORK

1. In order to present an accurate account of the effect of second phase particles on grain coarsening characteristics, Gladman's model may be corrected to allow for the underestimation of the driving force arising due to:-
   a) the local variations in the shape of the boundary because of the presence of second phase particles, thus providing a larger grain boundary area.
   b) the part of the total volume fraction of second phase particles present within the growing grains, which do not necessarily participate in the pinning of a moving grain boundary.
2. The effect of molybdenum additions on the kinetics of $M_{23}C_6$ precipitation in Fe-Ni-Cr alloys should be thoroughly investigated, because:-
   a) the reason why molybdenum additions stabilize the formation of undissolved $M_{23}C_6$ carbides during solution treatment, is not clear.
   b) the reason for the depression of the nose of the 'C' curve in the molybdenum bearing steel is not understood.
3. Work should be undertaken to explore the possibility of precipitating only TiC at the grain boundaries, and also to investigate the probability of titanium segregation on ageing at various temperatures and times.
4. Having established the general effects of various alloying additions on the relative incubation times for the start of precipitation and recrystallization in Fe-Ni-Cr alloys, the immediate need to quantify these parameters with varying alloy composition, in the form of a regression analysis or a mathematical model, would be advantageous.
5. The relative effects of quenched in vacancies and dislocations on the nucleation of γ', at different cold

working reductions, should be further investigated.

6. Although the high temperature ductility results at varying strain rates have been interpreted on the basis of deformation mechanism maps, there is a need to quantify these effects. Also ductility - strain rate relationships for different microstructures should be developed, for a regime of strain rates operative in a single flow field.

7. The diffusional flow controlled by an interface reaction has only been considered for situations where precipitates are mainly present at the grain boundaries. However, in alloys containing γ' dispersions, flow is controlled by a marked interface reaction. The relationship between creep rate and the applied stress may be usefully investigated, as the results obtained indicated a power law relationship.

8. Further investigations of the quantitative effects of microstructure on fracture maps are required.

9. The microstructural dependence of the stress exponent 'n' of the minimum creep strain rate, should be further investigated.

7. REFERENCES

1. E. V. Bennett, Low nickel austenitic stainless steels, Div. of Eng. and Industrial Research, National Research Council, Washington, June 10, 1955.

2. M. G. Fontana and N.D. Greene, "Corrosion Eng.", McGraw Hill Inc., 1967, p. 319.

3. F.B. Pickering, Review 211, International Metals Reviews, p. 227, Dec. 1976.

4. C.T. Sims, "SUPERALLOYS," Vol. 1, Chapter 4, p. 114, 1972

5. C.P. Sullivan and M.J. Donachie, Jr. Met. Eng. Q., 11, pp. 1-11, 1971.

6. R. Fawley et al, Trans AIME, Vol. 242, p. 77, May 1968.

7. United Steel Cos. Ltd., Research Report, Ref. No. PM/4617/25/67.

8. E.J. Dulis, ISI Special Report 86, p. 162, 1964.

9. R.F. Decker and S. Floreen, Tech. Paper 380, The International Nickel Co. Inc., Bayonne, N.J., April 8, 1964.

10. H.J. Beattie and W.C. Hagel, Trans. AIME, 221, 28, 1961.

11. P.G. Stone and J. Orr, A Conference on "Nickel and its Specific Role in Certain Types of Alloys," 18th Colloque de Metallurgie, France, June 1975.

12. D.M. Haddrill et. al, Acta. Met., Vol.9, No. 10, pp. 982-984, 1961.

13. D.R. Muzyka and G.N. Maniar, Met. Eng. Q., 9, pp. 23-27, 1969.

14. W.C. Hagel and H.J. Beattie Jr, "Precipitation Processes in Steels", ISI Special Report, London, pp. 98-107, 1959.

15. O.F. Paulonis et. al, Trans. ASM, 62, pp. 611-622, 1969.

16. F.H. Keating, "Chromium-nickel Austenitic Steels", London, Butterworths, 1956.

17. D. Dulieu and J. Nutting, ISI Special Report 86, p. 140, 1964.

18. A.J. Lena, "Precipitation from Solid Solutions", ASM, Cleveland, p.244, 1958.

19. T. Angel, JISI, 171, 345, 1951.

20. D. L. Douglas et. al, Corrosion, 20, 15, 1964.

21. Ursula E. Wolff, Trans. AIME, Vol. 236, p. 19, Jan. 1966.

22. J. R. Mihalisin and R.F. Decker, Trans. AIME, 218, 507, 1960.

23. B.S. Natapov et.al., Met. Sci. Heat Treat., 1-2, ppll-14, 1966.

24. F. B. Pickering et. al, JISI, 199, pp. 153-175, 1961.

25. P. G. Stone and J. Orr, "A review of Properties and Metallurgy of alloy 800", B.S.C Special Steels Division. Ref. No. PROD/MT/7342/-/74/D.

26. J.F. Baker, Metal Progress, 81, pp, 72-76, May 1962.

27. A.S.M Handbook Vol. 1, p. 543, 1961.

28. J.O. Edstrom and B. Skold, "New Steels for chemical Industry", ISI Publication 117, Proc. Conf., 10-12 Sept. 1968, p. 135.

29. M. F. Ashby, "Strengthening methods in metals and alloys", Third International Conference on the strength of metals and alloys, Keynote address, Vol. 1, Cambridge, England, 20-25th August.

30. C. H. Lund, DMIC Report 153, May 5, 1961.

31. R.W.K. Honeycombe, ISI Special Report 86, p.1, 1964.

32. A. Kelly and R. B. Nicholson, Prog. Mat. Sci., Vol. 10, p.144, 1963.

33. F.G. Wilson and F. B. Pickering, JISI, 204, p. 288, 1966.

34. H. Brooks, "Metal Interfaces", p. 20, ASM, 1952.

35. W. Betteridge and J. Heslop, "The Nimonic Alloys", Arnold, London, 1974.

36. A. Kelly and R. B. Nicholson, "Strengthening Methods in Crystals", Elesevier Publishing Co., 1971.

37. B.R. Clark and F.B. Pickering, JISI, Vol. 205, p. 70, 1967.

38. W.I. Mitchell et. al., "Structural Processes in Creep", ISI and Inst. Met. Special Report, London, p. 136, 1961.

39. F.B. Pickering, Proc. Conference, "Heat Treatment '73", ISI, International Hotel, London 12-13 December, 1973.

40. R.F. Decker, "Steel Strenghening Mechanisms", Climax Moly. Co., Symposium, Zurich, p. 147, 1969.

41. F.G. Wilson and F.B. Pickering, Acta. Met., 16, p. 115, 1968.

42. J. M. Silcock, and D. Raynor, Metal Sci. J., Vol. 4, p. 121, 1970.

43. V. Martens and E. Newbach, Acta. Met., Vol. 23, Feb. 1975.

44. E. Newbach, Scripta Met., Vol. 8, pp. 1067-1072, 1974.

45. I. Kirman and D. H. Warrington, Met. Trans., 1, pp. 2667-2675, 1970.

46. D. J. Mitchell et. al., Mats. Sci. Eng., 11, p.97, 1973.

47. H. Gleiter and E. Hornbogen, Phys. Status Solidi, 12, 235, 251, 1965.

48. L. K. Singhal and J. W. Martin, Acta. Met., 16, p. 447, 1968.

49. R.J. White et. al., J. Nuclear Mat., 55, pp. 273-278, 1968.

50. C.M. Sellars, "Spring residential conference on grain-boundaries", Inst. of Metals, p. 22, April 1976.

51. K. C. Russell, "Nucleation III", (ed. Zettlemoyer, A.C.), Marcell Decker, New York, p.1.

52. R. W. Cahn, "Physical Metallurgy", p. 1973, 1965.

53. J.L. Brimhall et. al., Acta. Met., Vol. 14, April 1976.

54. A.R. Jones and B. Ralph, Acta. Met., Vol. 23, March 1975

55. K.C. Russell and H.I. Aaronson, Scripta Met., Vol. 10, pp. 463-470, 1976.

56. W.J. McG. Tegart, "Ductility" Seminar A.S.M., Oct. 4-15th, pp. 20, 46, 119-121, 1967.

57. T. Gladman, Proc. Roy. Soc., 294, p. 298, 1966.

58. P. A. Beck, "Advances in Physics", 3, p. 245, 1954.

59. P. A. Beck et. al, Trans. Met. Soc., AIME, 175, p. 362, 1948.

60. P. A. Beck et. al., ibid, p. 162.

61. P. A. Beck et. al., ibid, 180, p. 147, 1949

62. W.W. Mullins, Acta. Met., 6, p. 414, 1958.

63. C. Zener, Private Communication to C.S. Smith, AIMME, 175, p. 15, 1949.

64. M. Hillert, Acta. Met., Vol. 13, p. 227, March 1965.

65. P. Hellman and M. Hillert, Scand. J. Met., 4, p. 211-219, 1975.

66. T. Gladman and F.B. Pickering, JISI, p. 653, 1967.

67. R.M. Boothby, AERE Report R9136, July 1978

68. Nimonic, "Structures of Nimonic alloys", Henry Wiggin & Co.

69. J.P. Adamson, Thesis for D. Phil., Oxford, 1972.

70. N.F. Mott, Proc. Phys. Soc., Vol. 60, p. 391, 1948.

71. A.B. Kinzel, Trans. AIME, Vol. 149, pp, 469-488, 1952.

72. R.L. Cowan and C. S. Tedman Jr., Advances in Corrosion Science and Tech., 3, 293, 1973.

73. C.S. Pande et. al., Scripta Met., Vol. 11 , pp. 681-684, 1977.

74. M.H. Lewis and B. Hattersley, Acta. Met., Vol. 13, p.1159, 1965.

75. B. Young, D.Phil., Thesis, Univ. of Sheffield, 1962.

76. F.H. Froes et. al., Acta. Met., Vol. 18, p. 1209, 1970.

77. F.G. Faulkner and B. Ralph, Acta. Met., Vol. 20, p. 703, May 1972.

78. C. Laird and H.I. Aaronson, Trans. Metal Soc. AIME, 242, 1393, 1968.

79. G.C. Weatherley, D.Phil., Thesis, Cambridge Univ., 1966.

80. R.G. Ramirez and G.M. Pound, Met. Trans., Vol. 4, p. 1563, June 1973.

81. K. Saito and R. Watanabe, Jap. J. Appl. Phys., 8, p. 14, 1969.

82. K.C. Russell and H.I. Aaronson, J. Mat.Sci, 10, p. 991, 1975.

83. C.C. Dollins, Acta. Met., Vol. 18, p. 1209, 1970.

84. C.M. Hammond et.al. Trans. ASM, Vol. 57, p. 727, 1964.

85. N.J. Grant et. al., Trans. AIME, P.210, Feb. 1954.

86. H. Hughes, JISI, 203, pp. 1019-1023, 1965.

87. J. Jordan, Personal Correspondence.

88. J. B. Clark, Acta. Met., Vol. 12, p. 1197, 1964.

89. P. B. Hirsch et. al., Phil Mag. 3, 897, 1958.

90. V. Lupnic et.al., Z. Metallk., 65, p. 63, 1974.

91. Ram Kossowsky and D. Moon, Trans. JIM, Vol. 9, p. 398, 1968.

92. E. Orowan,"Dislocations in Metals", AIME, 181, 1954.

93. R.A. Oriani, Acta. Met., 8, 134, 1960.

94. J. E. Bailey, Phil. Mag., 5, 833, 1960.

95. P. Cotterill and P. R. Mould, "Recrystallization and Grain-Growth in Metals", p. 60-93, 1976.

96. R. W. Cahn, Proc. Phys. Soc., A(63), 323, 1950.

97. P. A. Beck, J. Appl. Phys., 20, 633, 1949.

98. R. D. Doherty, Met. Sci. J., 8, 132, 1974.

99. P. A. Beck and P.R. Sperry, J. Appl. Phys., 21, p. 150, 1950.

100. J. E. Bailey and P.B. Hirsch, Phil. Mag., 5, p. 485, 1960.

101. J.E. Bailey and P. B. Hirsch, Proc. Roy. Soc., A267, p. 11, 1962.

102. V. Ramaswamy and D.R.F. West, JISI, 208, p. 395, 1970.

103. R. Schofield and A.J. Baker, "In Recrystallization in the Control of Microstructure", I.S.I/I.O.M. Meeting, London, 1973.

104. H. Kreye et. al., Phys. Stat. Sol. (a), 1, 97, 1970.

105. U. Koster, Metal Sci., Vol. 8, p. 151, 1974.

106. A.A. Popov et. al, Fiz. Met., Metalloved, 38, No. 2, pp. 337-342, 1974.

107. K. Koster, J. Mat. Sci., Vol. 8, p. 15, 1974.

108. T. Gladman et.al., JISI, London, 209, 380, 1971

109. N.J. Grant, "Deformation and fracture at elevated temperatures", Cambridge (Mass), M.I.T. Press, pp. 91-105 165, 1965.

110. R.W. Balluffi, Phys. Stat. Sol. 42, 11, 1970.

111. S.L. Robinson and O.D. Sherby, Acta. Met., 17, 109,1969.

112. A.K. Mukherjee et.al., Trans ASM 62, 155, 1969.

113. F. Garofalo, "Fundamentals of creep and creep rupture in metals", Macmillan, pp. 46-241, 1965.

114. M.V. Speight and J.R. Harris, Met. Sci.J., Vol. 1, p. 83, 1967.

115. M.F. Ashby, Surface Science, 31, 498-542, 1972.

116. F.R.N. Nabarro, Report on a Conference on the strength of solids (Phys. Soc.), London, p. 75, 1948.

117. C. Herring, J. Appl. Phys., 21, 437, 1950.

118. R. L. Coble, J. Appl. Phys., 34, 1679, 1963

119. M.F. Ashby, Scripta Met., Vol. 3, pp. 837-842, 1969.

120. J.W. Weertman, Trans ASM, Vol. 61, pp. 681-694, 1968.

121. M. F. Ashby, Acta. Met., Vol. 20, p. 887, July 1972.

122. T. Gladman et.al., "Creep strength in steels and high temperature alloys", organised by ISI, p. 71, 20-22 Sept. 1972.

123. F. A. Mohamed and T.G. Langdon, Met. Trans., Vol. 5, p. 2339, Nov. 1974.

124. F.A. Mohamed and T.G. Langdon, J. of Eng . Mat. Tech., p. 125, April 1976.

125. H. Ford, J.I.M., Vol. 95, p. 65, 1968.

126. G. Dieter, Mechanical Metallurgy, McGraw Hill Book Co. Inc., Chapter 2, p. 17, 1961.

127. J.J. Jones et. al., Met. Rev., Rev. - 130, Metals and Metallurgy Trust, 1969.

128. J. Myers, Welding Technology, Spring Meeting, P. 106, 1962.

129. A.A. Prus, Metallovedenic Termicheskaya Obrabotka Metalloved, No. 1, pp. 7-9, Jan. 1976.

130. N.T. Travina and A.A. Nikitin, Fiz. Met. Metalloved, 39, No. 6, 1257-1262, 1975.

131. I.L. Svetlov and V.N. Tolo Raiya, ibid, 40, No. 3, 409-414, 1975.

132. N.W. Lui and I. Le. May J. Eng. Mat. and Tech., p. 173, April 1976.

133. N.F. Sukharov et. al., Phys. of Metals and Metallography, 11, 3, p. 100, 1964.

134. R. Summerling and J. Nutting, JISI, 203, 398, 1965.

135. E. J. Brindley and J.P. Worthington, Met. Rev., 15, 101, 1970.

136. J. D. Baird, Met. Rev., 16, 1, 1971.

137. R.M. Boothby, Private Communication, 1977.

138. C. F. Bilsby, D.Phil., Thesis, Univ. of Cambridge, 1966.

139. M.C. Chaturvedi et. al., Met. Sci., p. 373, Nov. 1976.

140. J. Guest, A. "Status review of alloy 800," Proceedings of British Nuclear Energy Society, Conference at Univ.

of Reading, Paper No. 22, p. 25, 25 and 26 Sept. 1974.

141. G. H. Broomfield, Spec. Tech. Rep., 147, ASTM, p. 38, 1969.

142. F.H. Rhines and P. J. Wray, Trans ASM, 54, p. 117, June 1961.

143. J. Kurdman, Kovove Materially, 11(5), pp. 491-501, 1973.

144. J. Orr,"A Status review of alloy 800", Proceedings of British Nuclear Energy Society, Conference at Univ. of Reading, paper No. 30, p. 267, 25 and 26 Sept. 1974.

145. R. Lagneborg, J. Mat. Sci., 4, 195, 1969.

146. B. Russell et. al., Metal Sci. J., 2, 201, 1968.

147. G. Knowles, Metal Sci. J., p.117, April 1977.

148. P. L. Threadgill and B. Wilshire, "Creep Strength in steels and high temp. alloys", organised by ISI, p. 8, 20-22 Sept. 1972.

149. I.M. Bernstein, Trans. Met. Soc., AIME, 239, 1518, 1967.

150. J. E. Harris and R. B. Jones, J. Nucl. Mat., 10, 360, 1963.

151. D. Hull and R.E. Rimmer, Phil. Mag., 4 , p. 673, 1959.

152. C.I. Smith et.al., "Creep strength in steels and high temp. alloys," organised by ISI, p. 15, 20-22 Sept. 1972.

153. J. Heslop, Jap. I. Metals, Vol. 91, p. 28, 1961-63.

154. R. Lagneborg and B. Bergman, Proceedings of the third International Conference on "Strength of Metals and Alloys", Vol. 1, Cambridge, England, paper No. 64, 20-25 August 1973.

155. Sadao Otha and Ken-ichi-Aota, ibid, paper No. 40, 1973.

156. L.G. Liljestard and A. Omsen, Met. Trans., Vol. 6A, p. 279, Feb. 1975.

157. S. R. Keown, "Creep strength in steels and high temp. alloys", organised by ISI, p. 78, 20-22 Sept. 1972.

158. T.M. Williams and D.R. Harries, ibid, p. 152.

159. B.E. Hopkins and T.B. Gibbons, ibid, p. 165.

160. A. Plumtree and N.G. Persson, Met. Trans., Vol. 7A, p. 1743, 1976.

161. P.W. Davies and H.E. Evans, J. Inst. of Metals, Vol. 96, p. 245, 1968.

162. C.W. Weaver, J. Inst. of Metals, Vol. 80, p. 296, 1959-60.

163. M. F. Ashby, A report on fracture maps, Cambridge University, 1978.

164. L.M. Brown and J. D. Embury, Proc. of the third International Conf. on,"Strength of Metals and Alloys", Vol. 1, Cambridge, paper 33, 20-25, August, 1973.

165. A. J. Perry, J. of Mat. Sci., 9, pp. 1016-1039, 1974.

166. C. Zener,"Fracturing of Metals", Cleveland, ASM, p1, 1948.

167. G. W. Greenwood, Proceedings of the Int. Conf. on "Interfaces," Melbourne, p. 223, 1969.

168. D. G. Morris and D. R. Harries, J. Mat. Sci., 12, pp. 1587-1597, 1977.

169. F. Garafalo, 'Ductility', ASM, p. 87, 1968.

170. R. G. Fleck et. al., Met. Trans., 1, 3415, 1970.

171. R. Raj and M.F. Ashby, Acta. Met., 23, p. 653, 1975.

172. T.B. Gibbons and B.E. Hopkins, Met. Sci. J., 5, 233, 1971.

173. J.K. Tien and R.P. Gamble, Met. Trans., Vol. 2, June 1971, pp. 1663-1667.

174. B.B. Argent, Proc. Int. Conf. "Chemical Metallurgy of Iron and Steel", Sheffield, 301, Metal Society, 1971.

175. J. Wulff, "The structure and properties of materials", Vol. III, p. 84.

176. S. Bjorkland and M. Hillerts, Met. Sci. J., 9, 127, 1975.

177. F.B. Pickering, N.P.L. Symposium "The relationship between structure and mechanical properties of metals", H.M.S.O., 398, 1963.

178. G. Engberg and R. Lagneborg, Scand. J. Met., 7, pp 282-286, 1978.

179. O.O. Miller, Trans A.S.M., 43, 260, 1951.

180. P. J. Alberry and C.W. Haworth, Met. Sci. J., 8, 407, 1974.

181. B. Weiss and R. Stickler, Met. Trans., Vol. 3, p. 851, 1972.

182. L. R. Woodyatt, C.T. Sims and J. H. Beattie, Trans. AIME, 36, 519, 1966.

183. R. M. Boothby, Private Communication, 1976.

184. H. Gleiter and E. Hornbogen, Mats. Sci. Eng., 2, 285, 1967-68.

185. E. W. Hart, Acta. Met., 15, 351, 1967.

TABLE 1 - Analyses of Experimental Materials

ALLOY NO.	Chemical Analysis wt %							
	C	Ni	Cr	Mo	Ti	Al	B	N_2
1	0.0096	44.82	20.01	-	-	-	-	-
2	0.049	43.80	20.50	-	-	-	-	-
3	0.101	44.02	20.45	-	-	-	-	-
4	0.104	43.60	18.08	3.50	-	-	-	-
5	0.14	42.60	17.76	3.57	1.18	-	-	-
6	0.35	42.00	17.60	3.67	1.11	-	-	-
7	0.012	43.19	17.06	3.67	1.20	1.20	0.0024	0.0096
8	0.12	42.80	16.95	3.54	1.20	1.23	0.0018	0.0086

TABLE II - Grain Size Values below Grain Coarsening Temperature
Average Grain Diameters at 1000°C (Bar)

ALLOY NO.	Alloy Additions (wt %)						Grain size after time of (mm):-				
	C	Mo	Ti	Al	B	N	¼h	½h	1h	2h	4h
1	0.0096	-	-	-	-	-	0.077	0.093	0.112	0.135	0.195
2	0.049	-	-	-	-	-	0.052	0.073	0.089	0.090	0.124
3	0.101	-	-	-	-	-	0.022	0.024	0.024	0.022	0.024
4	0.104	3.50	-	-	-	-	0.016	0.019	0.015	0.018	0.018
5	0.14	3.57	1.18	-	-	-	0.016	0.020	0.020	0.027	0.026
6	0.35	3.67	1.11	-	-	-	0.009	0.010	0.014	0.017	0.012
7	0.012	3.67	1.20	1.20	0.0024	0.0096	0.032	0.035	0.050	0.110	0.100
8	0.12	3.54	1.20	1.23	0.0018	0.0086	0.018	0.019	0.018	0.024	0.028

TABLE III - Activation Energies for Grain Growth below the Grain Coarsening Temperature

Alloy No.	Activation Energy KJ/mol.
1	67
2	75
3	150
4	210
5	188
6	∞
7	125
8	205

TABLE IV - Solution Treatment Conditions Selected for Age Hardening and High Temperature Testing

Alloy No.	Alloy Additions (wt %)						Bar Material			Strip Material			Solut. Treat Hardn HV.
	C	Mo	Ti	Al	B	N	Temp. (°C)	Time (h)	Av. Grain Dia. (mm)	Temp. (°C)	Time (h)	Av. Grain Dia. (mm)	
1	0.0096	-	-	-	-	-	1000	¼	0.077	1050	¼	0.079	147
2	0.049	-	-	-	-	-	1050	¼	0.073	1050	½	0.080	119
3	0.101	-	-	-	-	-	1100	4	0.050	1100	4	0.050	154
4	0.104	3.50	-	-	-	-	1100	2	0.038	1100	2	0.040	165
5	0.14	3.57	1.18	-	-	-	1050	2	0.029	1050	2	0.032	171
6	0.35	3.67	1.11	-	-	-	1150	4	0.025	1150	4	0.029	188
7	0.012	3.67	1.20	1.20	0.0024	0.0096	1000	1	0.050	1050	½	0.059	146
8	0.12	3.54	1.20	1.23	0.0018	0.0086	1100	4	0.037	1100	4	0.042	171

TABLE V - EFFECT OF MOLYBDENUM ON INTENSITY OF AGE HARDENING

Ageing Temp. °C	Maximum increase in hardness HV	
	0.101%C	0.104%C-3.50%Mo
700	40	17
750	29	17
800	30	10
850	24	8
900	18	6

TABLE VI

Ageing Treatment Conditions Selected For High Temperature Testing

Alloy No.	Ageing Temp. in °C	Ageing Time in hours	Microstructural Features Present
1	Left in solution treatment condition		Base composition with no precipitates either on grain boundaries or twin boundaries. A few undissolved chromites in the matrix.
2	700°C	10 hours	$M_{23}C_6$ precipitates at grain boundaries with little or no carbides o twin boundaries.
3	700°C	16 hours	$M_{23}C_6$ precipitates at grain boundaries and within the grains
4	700°C	6 hours	Molybdenum rich $M_{23}C_6$ at grain boundaries with little or no precipi on twin boundaries.
5	800°C	6 hours	Combined $M_{23}C_6$/TiC precipitates at grain boundaries. Some TiC prec tes on dislocations within the grains too.
	650°C	30 hours	$M_{23}C_6$ at grain boundaries and no precipitation within the grains.
7	700°C	30 hours	γ' zones present within the grain with a little $M_{23}C_6$ present on occasional grain boundary.
	800°C	70 hours	Semi-coherent γ' present within the grains and little or no $M_{23}C_6$ at grain boundaries
8	700°C	30 hours	$M_{23}C_6$ precipitates at grain/twin boundaries with γ'zones within the grains
	800°C	70 hours	Massive $M_{23}C_6$ precipitates at grain/twin boundaries with semi-coher γ'particles within the grains.

TABLE VII - WORK HARDENING DATA

Alloy No.	Increase in hardness (HV) with cold working		
	40%	60%	80%
2	131	168	186
3	148	175	196
4	160	196	215
5	158	186	212
7	151	190	209
8	174	186	211

TABLE VIII - ACTIVATION ENERGIES OF VARIOUS ALLOYS FOR 50% SOFTENING

Alloy No.	Activation Energy at various cold-working reduction in KJ/mol/ok.		
	40%	60%	80%
2	77.0	72.0	52.0
3	58.0	52.0	45.0
4	88.0	71.0	68.0
5	103.0	80.0	72.0
7	42.0	36.0	33.0
8	47.0	52.0	37.0

TABLE IX

COMPARISON OF GRAIN GROWTH MODELS

Alloy No.	Solution treatment	Particle radius (r) μm	Volume fraction (f)	Observed grain dia. μm	Corrected Observed grain size using $\bar{D} = 1.75\bar{d}$ μm	Calculated Grain Size		
						Zener's model grain dia. ($\bar{d}$) μm	Gladman's model at Z = 2 ($\bar{D}$) in μm	He Hi Cor ($\bar{d}$)
3	1100°C/4 hrs	0.332	0.00396	50.0	87.5	223.5	43.87	6
4	1100°C/2 hrs	0.372	0.00494	38.0	66.5	201.0	39.4	5
5	1050°C/2 hrs	0.250	0.00367	29.0	50.7	181.6	35.65	5
6	1150°C/4 hrs	0.336	0.00780	25.0	37.5	115.00	22.54	3
8	1100°C/4 hrs	0.394	0.00502	37.0	64.7	209.24	41.07	6

ALLOY	HEAT TREATMENT & MICROSTRUCTURE	MN/m^2 σ_F				U.T.S. MN/m^2				0.2 P.S. MN/m^2				% Elongation			
		10^{-2}	10^{-3}	10^{-4}	10^{-5}	10^{-2}	10^{-3}	10^{-4}	10^{-5}	10^{-2}	10^{-3}	10^{-4}	10^{-5}	10^{-2}	10^{-3}	10^{-4}	10
No.1	Solution treated Base composition	271	221	196	133	295	246	221	178	222	216	206	180	40.5	24.8	22.8	17
No.2	Aged 700°C/10 hrs $M_{23}C_6$ at g.b.	265	271	221	145	340	322	262	199	232	222	235	201	41.5	34.4	26.5	21
No. 3	Aged 700°C/16 hours $M_{23}C_6$ at g.b.+ T.B. + matrix	316	316	253	183	385	385	322	253	363	353	314	250	25.6	26.5	25.6	19
No. 4	Aged at 700°C/6 hrs Mo rich $M_{23}C_6$ at g.b.	360	315	265	221	436	404	369	294	387	363	329	289	31.5	26.0	20.8	16
No.5 H.T.No.1	Aged 800°C/6 hours $M_{23}C_6$ and TiC at g.b.	328	303	151	63	477	493	398	312	363	333	314	304	34.4	40.5	52.1	49
No.5 H.T.No.2	Aged 650°C/30 hours $M_{23}C_6$ at g.b.	321	278	133	69	493	453	366	275	368	382	343	280	39.2	39.0	62.6	40
No.8 H.T.No.1	Aged 700°C/30 hours $M_{23}C_6$ at g.b. + γ' zones	556	530	455	442	790	726	638	518	726	696	598	510	26.9	24.8	21.6	11
No.8 H.T.No.2	Aged 800°C/70 hours $M_{23}C_6$ at g.b. + γ' semicoherent	448	376	265	234	641	597	490	428	608	584	486	432	23.5	36.0	48.4	27
No.7 H.T.No.1	Aged 700°C/30 hours very little $M_{23}C_6$ at g.b. + γ' zones	569	600	543	486	704	758	666	568	598	657	598	559	28.1	27.6	24.8	14
No.7 H.T.No.2	Aged 800°C/70 hours very little $M_{23}C_6$ at g.b. + γ' semicoherent	569	354	341	208	701	635	540	404	647	598	539	412	25.6	35.4	33.0	46

Table X

Tensile Properties at 700°C

TABLE XI

SERRATION CHARACTERISTICS AT 700°C

ALLOY	HEAT TREATMENT AND MICROSTRUCTURE	SERRATION STRAIN LIMIT AT		SERRATION AMPLITUDE MN/m^2 AT	
		Strain Rate 3.28×10^{-2}	$3.28 \times 10^{-3}\ s^{-1}$	$3.28 \times 10^{-2}\ s^{-1}$	$3.28 \times 10^{-3}\ s^{-1}$
A1	Solution treated Base composition	0.026-0.372	0.04-0.248	1.31	0.66
A2	Aged 700°C/10 hours $M_{23}C_6$ at g.b.	0.012-0.352	0.013-0.309	3.30	3.95
A3	Aged 700°C/16 hours $M_{23}C_6$ at g.b + T.B. + matrix	0.02 - 0.197	0.018-0.265	2.63	2.63
A4	Aged 700°C/6 hours Mo rich $M_{23}C_6$ at g.b.	0.039 - 0.236	0.023-0.114	1.32	5.27
A5 H.T.No.1	Aged 800°C/6 hours $M_{23}C_6$ and TiC at g.b.	0.019-0.197	0.015-0.367	1.97	6.60
A5 H.T.No.2	Aged 650°C/30 hours $M_{23}C_6$ at g.b.	0.0196-0.268	0.078-0.39	1.32	3.96
A7 H.T.No.1	Aged 700°C/30 hours Very little $M_{23}C_6$ at g.b. + η' zones	0.026-0.229	0.022-0.276	0.92	3.96
A7 H.T.No.2	Aged 800°C/70 hours Very little $M_{23}C_6$ at g.b. + η' semi-coherent	0.02 - 0.16	0.018-0.354	0.66	3.95

continued ...

TABLE XI (Continued ...)

SERRATION CHARACTERISTICS AT 700°C

ALLOY	HEAT TREATMENT AND MICROSTRUCTURE	SERRATION STRAIN LIMIT AT		SERRATION AMPLITUDE MN/m^2 AT	
		Strain Rate $3.28 \times 10^{-2} s^{-1}$	$3.28 \times 10^{-3} s^{-1}$	$3.28 \times 10^{-2} s^{-1}$	$3.28 \times 10^{-3} s^{-1}$
A8 H.T.No.1	Aged 700°C/30 hours $M_{23}C_6$ at g.b. + γ' zones	0.059-0.242	0.022-0.248	0.66	3.96
A8 H.T.No.2	Aged 800°C/70 hours $M_{23}C_6$ at g.b. + γ' semi-coherent	0.052-0.206	0.022-0.360	0.66	3.96

ALLOY NO.	MICROSTRUCTURAL FEATURES	APPLIED STRESS IN MN/m^2	RUPTURE LIFE IN HOURS	MINIMUM STRAIN RATE OBSERVED IN SEC^{-1}	TOTAL % CREEP ELONG.	INDIVIDUAL CREEP ELONGAT OF VARIOUS STAGES DURIN		
						% PRIMARY CREEP ELONG.	% SECONDARY CREEP ELONG.	%T ( ]
1	Base composition	85.0 70.0 50.6	75 135.5 1043.0	8.8×10^{-7} 2.07×10^{-7} 2.5×10^{-8}	11.512 9.64 13.97	0.79 1.472 1.083	7.11 6.024 5.905	
2	$M_{23}C_6$ at g.b.	126.5 95.0 63.0	17 82 1042	1.64×10^{-6} 3.55×10^{-7} 3.8×10^{-8}	9.24 12.18 19.37	0.134 0.803 2.24	7.36 8.03 11.91	
3	$M_{23}C_6$ at g.b. + T.B + matrix	139.0 111.0 63.0	30.25 124.6 934.0	1.1×10^{-6} 1.75×10^{-7} 1.82×10^{-8}	14.36 12.59 8.66	3.15 1.77 0.59	9.64 4.035 4.96	
4	M_o rich $M_{23}C_6$ at g.b.	158 126.5 63.0	129.6 496.0 1512.0	1.82×10^{-7} 2.73×10^{-8} 1.82×10^{-8}	11.02 9.84 17.12	2.26 2.66 6.10	0.98 2.36 6.50	
5 H.T.No.1	$M_{23}C_6$ and TiC at g.b.	190.0 166.0 114.0	35.30 70.00 569.0	1.16×10^{-6} 8.2×10^{-8} 9.5×10^{-8}	46.95 38.20 33.65	2.75 1.28 1.57	10.43 11.81 17.32	3 2 1
7 H.T.No.1	Very little $M_{23}C_6$ at g.b. + γ' zones	379.0 332.0 316.0	67 342 760	2.81×10^{-7} 6.8×10^{-8} 2.04×10^{-8}	10.82 11.02 11.22	0.78 1.18 1.18	6.10 6.49 5.51	
7 H.T.No.2	Very little $M_{23}C_6$ at g.b. + γ' semicoherent	379.0 316.0 253.0	63.0 162 432	6.56×10^{-7} 3.50×10^{-7} 1.1×10^{-7}	21.2 17.5 17.0	0.78 1.37 1.40	8.66 4.13 5.80	1 1
8 H.TNo.1	$M_{23}C_6$ at g.b. + γ' zones	348.0 316.0 300.0	116 362 1500	8.2×10^{-8} 2.18×10^{-8} 1.1×10^{-9}	6.69 5.12 8.10	0.59 0.98 1.35	1.77 1.38 2.85	
8 H.T.No.2	$M_{23}C_6$ at g.b. + γ' semicoherent	379 348 253.0	127.0 190.0 880.0	4.1×10^{-7} 3.5×10^{-7} 2.8×10^{-8}	27 26 15	1.20 1.28 1.90	19.83 17.92 8.78	

CREEP DATA AT 700 °C

Table XII

TABLE XIII

ALL ALLOYS AT 700°C

STRESS DEPENDENCE AND CREEP STRENGTH

ALLOY NO.	MICRO-STRUCTURAL FEATURES	STRESS EXPONENT 'n' in $tr = K\sigma^{-n}$	STRESS REQUIRED TO PRODUCE CONSTANT RUPTURE LIFE MN/m^2	
			1000 hr. Life	100 hr. Life
1	Base composition	-4.436	49.0	70
2	$M_{23}C_6$ at g.b.	-6.75	66.0	94
3	$M_{23}C_6$ at g.b. + T.B. + matrix	-4.39	64.0	105
4	Mo rich $M_{23}C_6$ at g.b.	-5.30	97.0	152
5 H.T. No.1	$M_{23}C_6$ and TiC at g.b.	-6.27	102.0	158
7 H.T. No.1	Very little $M_{23}C_6$ at g.b. + γ' zones	-12.71	390.0	650
7 H.T. No.2	Very little $M_{23}C_6$ at g.b. + γ' semicoherent	-3.14	205.0	475
8 H.T. No.1	$M_{23}C_6$ at g.b. + γ' zones	-14.85	305.0	355
8 H.T. No.2	$M_{23}C_6$ at g.b. + γ' semicoherent	-5.5	245.0	400

TABLE XIV

EFFECT OF MICROSTRUCTURAL FEATURES ON STRAIN RATE AT 700°C

ALLOY NO.	MICRO-STRUCTURAL FEATURES	RUPTURE LIVES AT CONSTANT STRESS IN MN/m^2 (Hrs)		CORRESPONDING STRAIN RAT IN SEC^{-1}	
		AT 100 MN/m^2	AT 300 MN/m^2	AT 100 MN/m^2	AT 300 MN/m^2
1	Base composit-ion	37	-	3.2×10^{-6}	-
2	$M_{23}C_6$ at g.b.	66	-	44×10^{-7}	-
3	$M_{23}C_6$ at g.b. + T.B.+ matrix	125	-	1.1×10^{-7}	-
4	Mo rich $M_{23}C_6$ at g.b.	880	-	2.1×10^{-8}	-
5 H.T.1	$M_{23}C_6$ and TiC at g.b.	1050	-	5.5×10^{-8}	-
7 H.T.1	Very little $M_{23}C_6$ at g.b. + γ' zones	-	3350	-	1.25×10^{-8}
7 H.T.2	Very little $M_{23}C_6$ at g.b. + γ' semi-coherent	-	365	-	1.1×10^{-7}
8 H.T.1	$M_{23}C_6$ at g.b. + γ' zones	-	1250	-	1.2×10^{-8}
8 H.T.2	$M_{23}C_6$ at g.b + γ' semi-coherent	-	400	-	0.98×10^{-8}

ALLOY	MICROSTRUCTURE	GRAIN SIZE, d, μm	N_A/mm^2 [No. of intergranular cracks/unit area]				N_G [No. of intergranular cracks/ 10^3 grains $= 10^3 N_A d^2$]				$\bar{C}$ = Average no. of grain facets/intergranular crack			
			10^{-2}	10^{-3}	10^{-4}	10^{-5}	10^{-2}	10^{-3}	10^{-4}	10^{-5}	10^{-2}	10^{-3}	10^{-4}	10^{-5}
1	Grains free from any precipitates	77	62	60	65	65	370	355	383	383	0.70	0.85	1.40	1.70
2	Only $M_{23}C_6$ at grain boundaries	73	35	34	35	36	185	180	185	190	0.70	0.87	1.50	1.80
3	$M_{23}C_6$ at grain/twin boundaries & within the grains	50	63	61	64	65	157	152	158	162	0.43	1.05	1.70	2.01
4	M_o rich $M_{23}C_6$ at grain boundaries and twin boundaries	38	57	57	63	65	82	82	88	93	0.61	0.93	1.27	2.20
5 H.T.No.1	$M_{23}C_6$ + TiC at grain/ twin boundaries	29	-	34	37	32	-	28	29	25	-	0.87	0.94	1.92
5 H.T.No.2	Only $M_{23}C_6$ at grain boundaries in M_o + Ti alloy	29	-	46	48	50	-	37	39	40	-	0.74	1.35	1.94
7 H.T.No.1	γ' zones within the grains + very little at g.b.	50	-	41	42	38	-	102	105	95	-	0.71	1.13	1.56
7 H.T.No.2	Semicoherent γ' within the grain + very little at g.b.	50	-	28	27	30	-	70	67	75	-	0.72	1.19	1.65
8 H.T.No.1	γ' zones within the grains + $M_{23}C_6$ at (g.b. + T.B)	37	-	62	70	68	-	80	91	88	-	0.56	1.11	1.28
8 H.T.No.2	semicoherent γ' within the grains + $M_{23}C_6$ (massive) at (g.b. + T.B.)	37	-	51	47	44	-	66	61	57	-	0.78	1.30	1.96

EXTENT OF INTERGRANULAR CRACKING IN VARIOUS MICROSTRUCTURES TESTED AT 700°C

ALLOY NO.	MICROSTRUCTURAL FEATURES	GRAIN SIZE IN μm	STRAIN RATE 10^{-2}/s				STRAIN RATE 10^{-3}/s				STRAIN RATE 10^{-4}/s				STRAIN RATE 10^{-5}/s			
			CRACK NATURE				CRACK NATURE				CRACK NATURE				CRACK NATURE			
			TYPE	% AMOUNT			TYPE	% AMOUNT			TYPE	% AMOUNT			TYPE	% AMOUNT		
				w	r	t		w	r	t		w	r	t		w	r	t
1	No precipitates	77	w, r	52	48	0	w, r	66	34	0	w, r	85	15	0	w, r	97	3	0
2	$M_{23}C_6$ at g.b.	73	w, r	64	36	0	w, r	75	25	0	w, r	90	10	0	W	100	0	0
3	$M_{23}C_6$ at g.b/T.B. + matrix	50	w, r, t	63	30	7	w, r, t	78	15	7	w, r, t	77	11	12	w, r, t	74	7	19
4	Mo rich $M_{23}C_6$ at g.b./T.B.	38	w, r	68	32	0	w, r	67	33	0	w, r	76	24	0	w, r	86	14	0
5 H.T.No.1	$M_{23}C_6$ + TiC at g.b./T.B.	29	-	-	-	-	w, r	72	28	0	w, r	89	11	0	W	100	0	0
5 H.T.No.2	$M_{23}C_6$ at g.b. in Mo + Ti alloy	29	-	-	-	-	w, r	55	45	0	w, r	80	20	0	w, r	94	6	0
7 H.T.No.1	γ' zones + no g.b. ppt.	50	-	-	-	-	w, r	64	36	0	w, r	95	5	0	W	100	0	0
7 H.T.No.2	γ' semicoherent + no g.b. ppt.	50	-	-	-	-	w, r	78	22	0	W	100	0	0	W	100	0	0
8 H.T.No.2	γ' zones + $M_{23}C_6$ at g.b.	37	-	-	-	-	w, r, t	54	36	10	w, t	87	0	13	w, t	86	0	14
8 H.T.NO.2	γ' semicoherent + $M_{23}C_6$ at g.b.	37	-	-	-	-	w, r, t	69	25	6	w, r, t	80	13	7	w, r, t	79	7	14

TABLE XVI

NATURE OF CRACKING IN VARIOUS MICROSTRUCTURES AT VARYING STRAIN RATES, TESTED AT 700°C

ALLOYING ADDITION	SOLUTE DISLOCATION BINDING ENERGY (W) IN ev	SOLUTE DIFFUSION COEFFICIENT (D_s) AT 700°C IN cm^2/sec	SOLUTE DRIFT VELOCITY (V_s) IN cm/sec	QUENCHED IN DISLOCATION DENSITY (ρ) lines/cm^2	DISLOCATION VELOCITY (V) AT VARYING STRAIN RATES IN cm/sec		VACANCY MODIFIELD DIFFUSION COEFFICIENT OF THE SOLUTE ($\bar{D}_s$) IN cm^2/sec	MODIFIELD SOLUTE DRIFT VELOCITY ($\bar{V}_s$) IN cm^2/sec.
					3.28×10^{-2}/sec	3.28×10^{-3}/sec		
C	0.50 (assumed)	7.0×10^{-9}	1.67	10^{10}	3.93×10^{-4}	3.93×10^{-5}	even higher than D_s	even higher than V_s
Cr	0.19	1.0×10^{-4}	9.05×10^{-7}	10^{10}	3.93×10^{-4}	3.93×10^{-5}	2.16×10^{-13}	1.9×10^{-5}
M_o	0.28	3.45×10^{-15}	4.6×10^{-7}	10^{10}	3.93×10^{-4}	3.93×10^{-5}	2.10×10^{-13}	2.8×10^{-5}
T_i	0.32	4.47×10^{-16}	8.9×10^{-8}	10^{10}	3.93×10^{-4}	3.93×10^{-5}	1.24×10^{-13}	2.48×10^{-5}

TABLE XVII

SERRATED YIELDING CRITERION AT 700°C

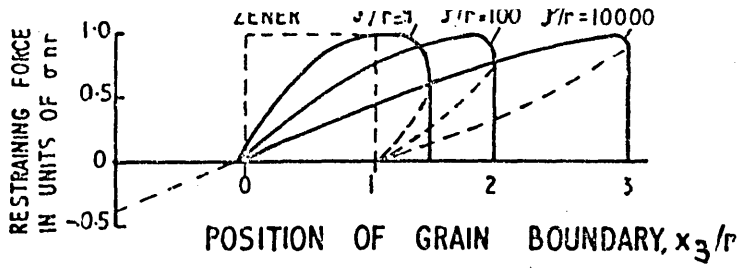

FIG.1. THE FORCE BETWEEN A SPHERICAL BOUNDARY AND A PARTICLE AS A FUNCTION OF THEIR RELATIVE POSITION. CURVES ARE GIVEN FOR THREE DIFFERENT VALUES OF ρ/r, WHERE ρ IS THE RADIUS OF THE UNDISTURBED BOUNDARY, AND r THE RADIUS OF THE PARTICLE. AFTER HELLMAN AND HILLERT (65)

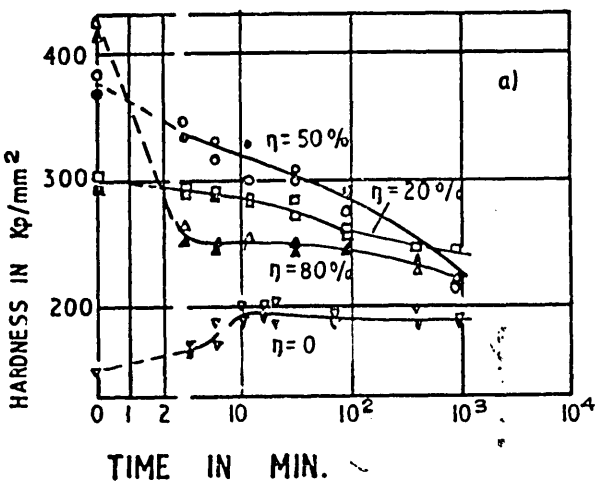

FIG. 2 COMBINED EFFECT OF COLD WORKING AND AGEING ON THE HARDNESS PROFILE OF γ' FORMING ALLOYS. AFTER LUPNIC (90)

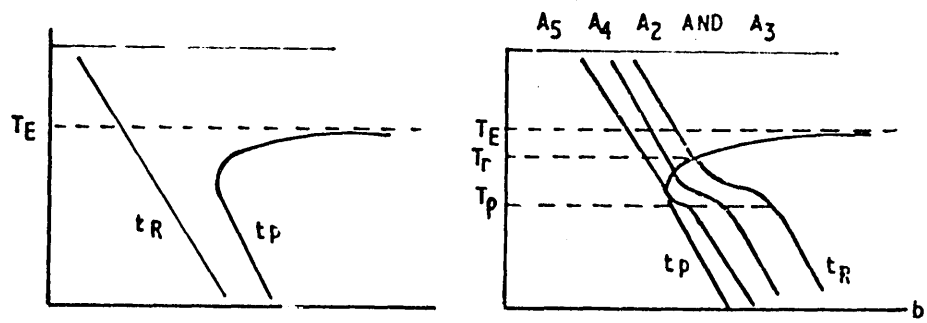

FIG. 3 TEMPERATURE DEPENDENCE OF THE START OF PRECIPITATION. t_P AND RECRYSTALLIZATION. t_R (a) BOTH PROCESSES DO NOT INFLUENCE EACH OTHER. (b) THE MUTUAL INFLUENCE DURING AGEING OF A SUPERSATURATED DEFORMED SOLID SOLUTION LEADS TO TEMPERATURE RANGES WITH DIFFERENT RECRYSTALLIZATION BEHAVIOUR. $T > T_{II}$: DISCONTINUOUS RECRYSTALLIZATION : $T < T_{II}$: CONTINUOUS RECRYSTALLIZATION. AFTER KREYE (104)

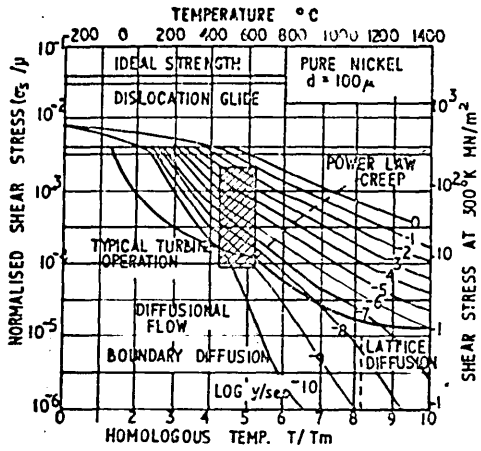

FIG. 4 A MAP OF NICKEL WITH A GRAIN SIZE OF 100 μm. THE SHADED BOX SHOWS THE RANGE OF OPERATION OF A TYPICAL TURBIN BLADE AFTER ASHBY (29)

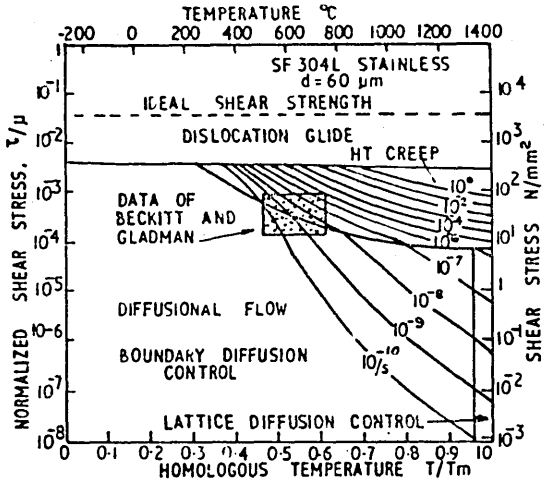

FIG.5 DEFORMATION MECHANISM MAP FOR SF 304L AUSTENITIC STAINLESS STEEL AFTER ASHBY (122)

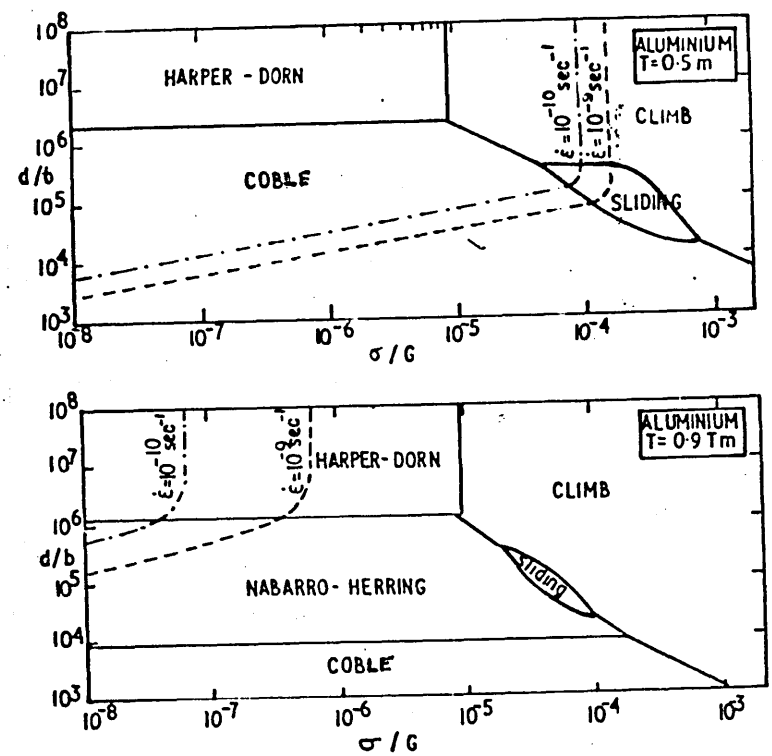

FIG. 6 DEFORMATION MECHANISM MAPS FOR PURE ALUMINIUM INCLUDING GRAIN BOUNDARY SLIDING AS A SEQUENTIAL PROCESS, HOMOLOGOUS TEMPERATURES OF (a) 0·5 Tm (b) 0·5 Tm, AFTER LANGDON. (124)

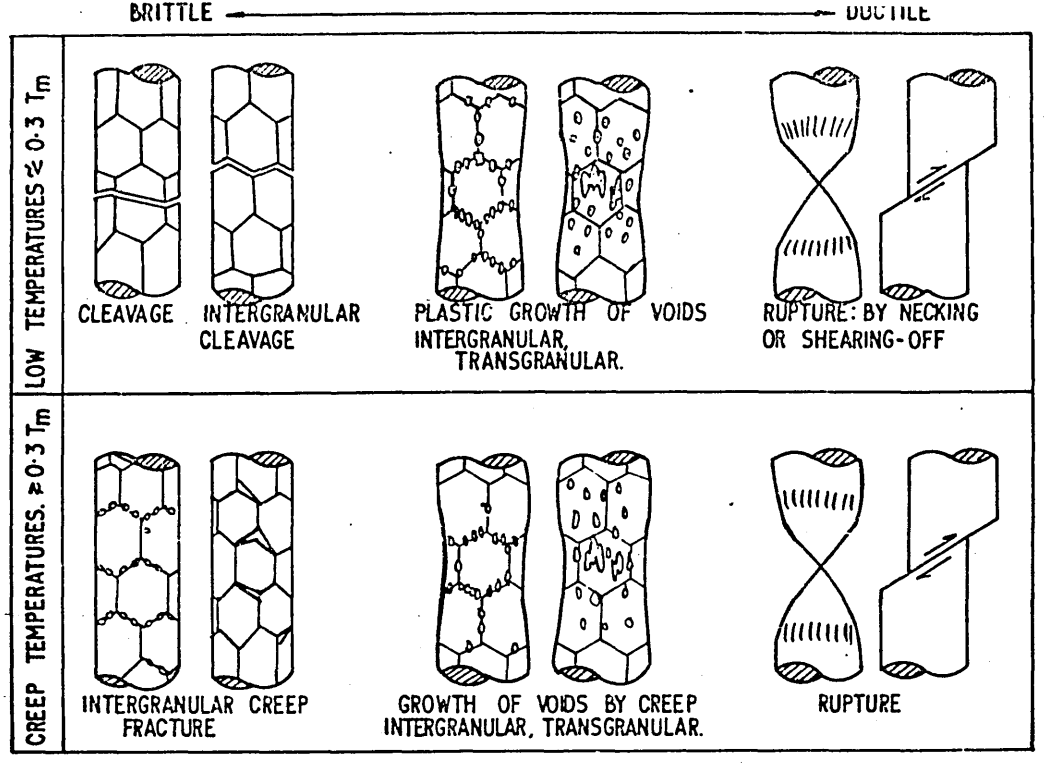

FIG. 7 THE SIMPLEST CLASSIFICATION OF FRACTURE MECHANISMS. THE UPPER ROW REFERS TO LOW TEMPERATURES ($< 0{\cdot}3\ T_m$) WHERE PLASTIC FLOW DOES NOT DEPEND STRONGLY ON TEMPERATURE OR TIME; THE LOWER ROW REFERS TO THE TEMPERATURE RANGE ($< 0{\cdot}3\ T_m$) IN WHICH MATERIALS CREEP. AFTER ASHBY (163)

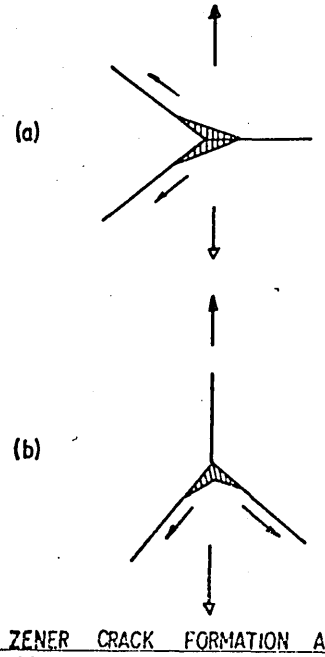

FIG. 8 ZENER CRACK FORMATION AT TWO TRIPLE POINT ORIENTATIONS. AFTER BILSBY (138)

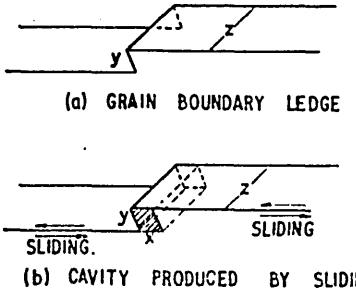

FIG. 9 SCHEMATIC REPRESENTATION OF CAVITY FORMATION AT A GRAIN BOUNDARY LEDGE. AFTER GAROFALO. (113)

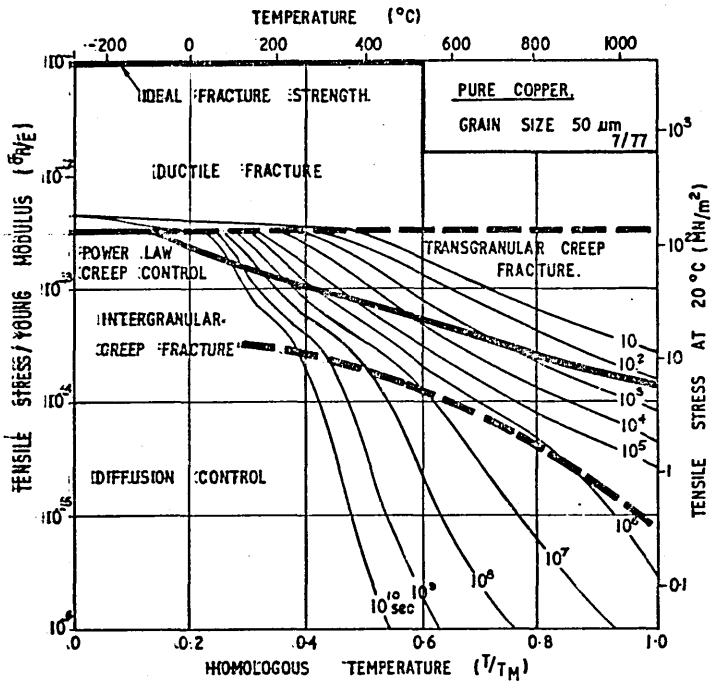

FIG. 10. A MODEL-BASED FRACTURE MAP FOR COPPER. AFTER ASHBY (163)

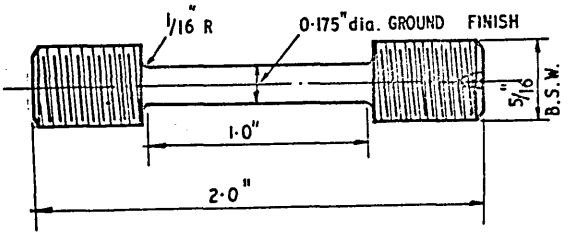

FIG. 11 DIMENSIONS OF HIGH TEMPERATURE TENSILE/CREEP TESTING SPECIMEN.

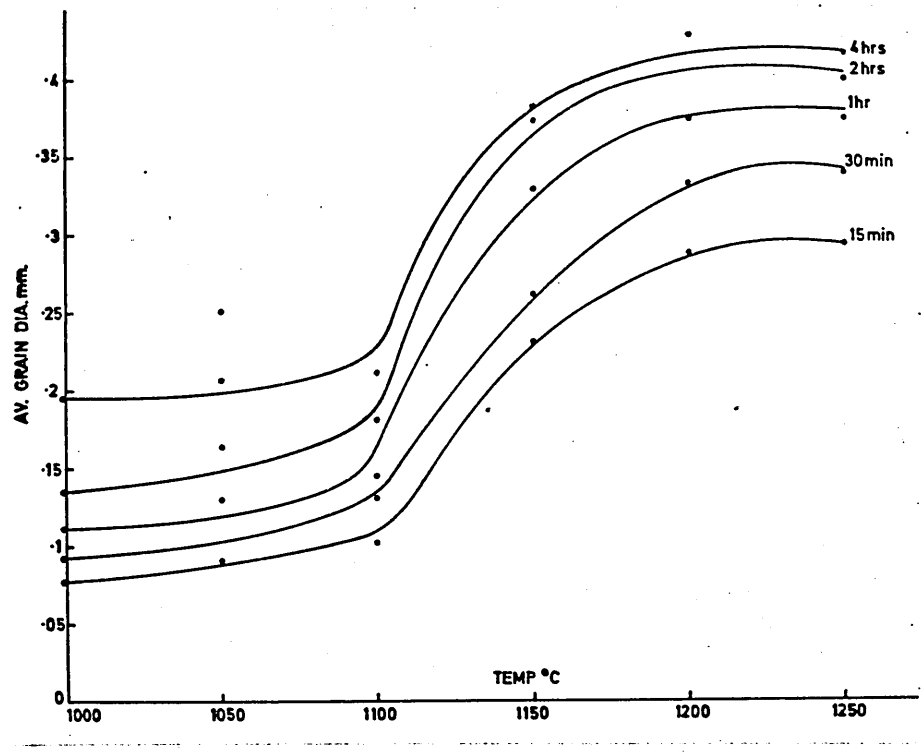

Grain coarsening characteristics of Alloy 1 (Bar)

Fig 12

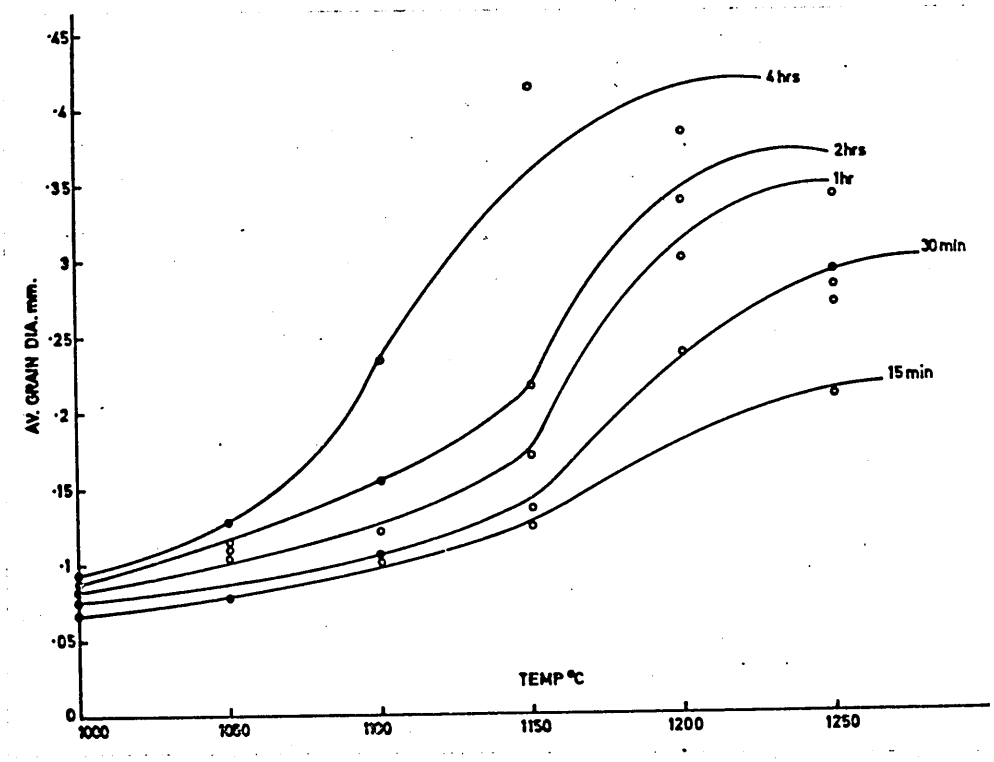

Grain coarsening characteristics of Alloy I (Strip)

Fig 13

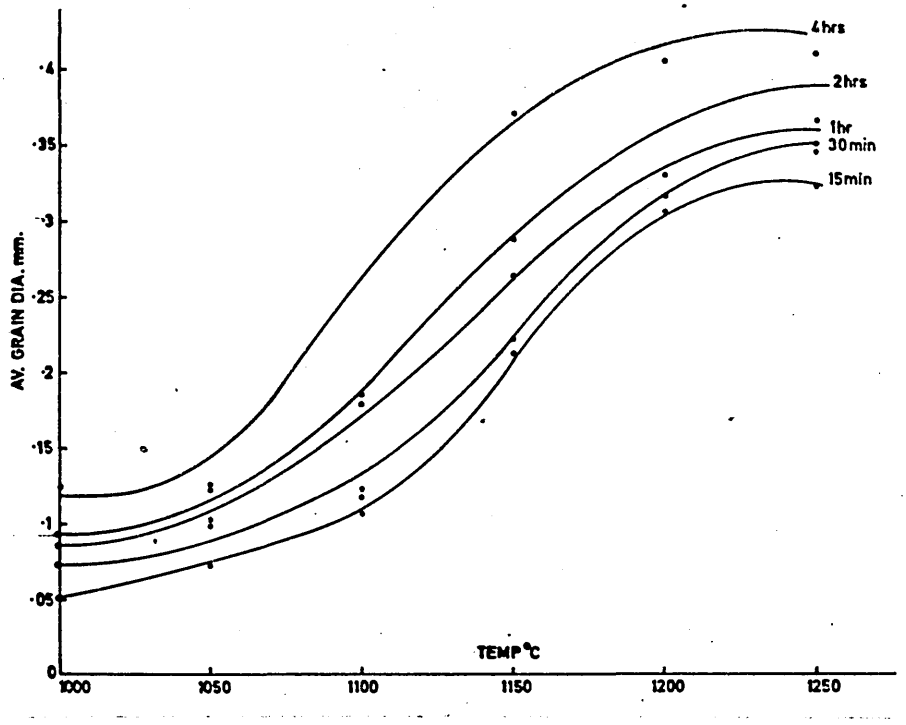

Fig 14

Grain coarsening characteristics of Alloy 2 (Bar)

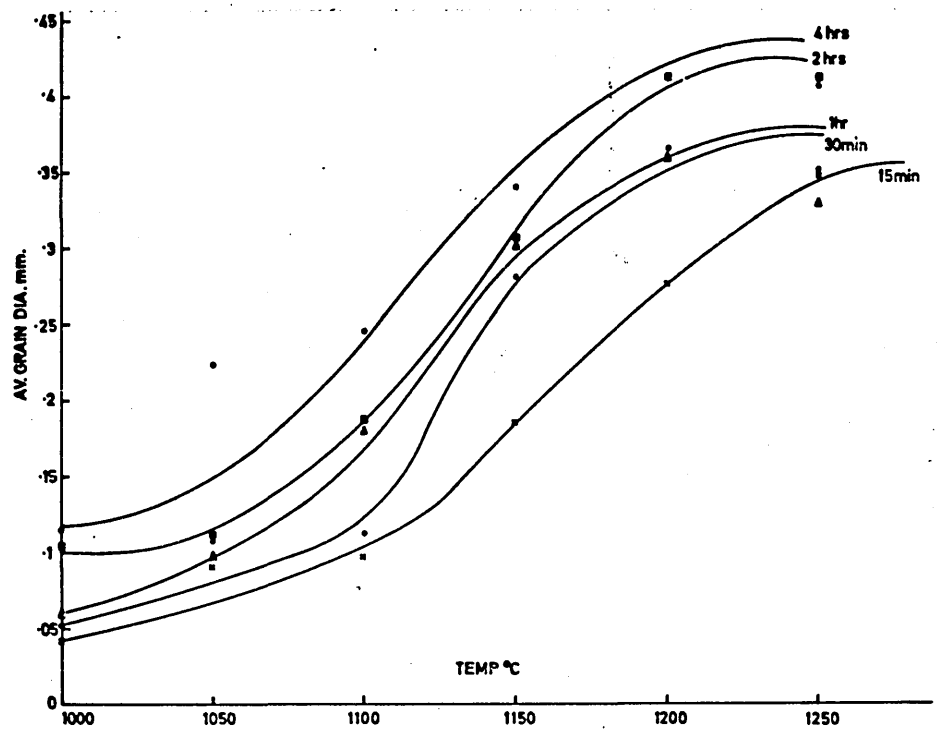

Fig 15

Grain coarsening characteristics of Alloy 2 (Strip)

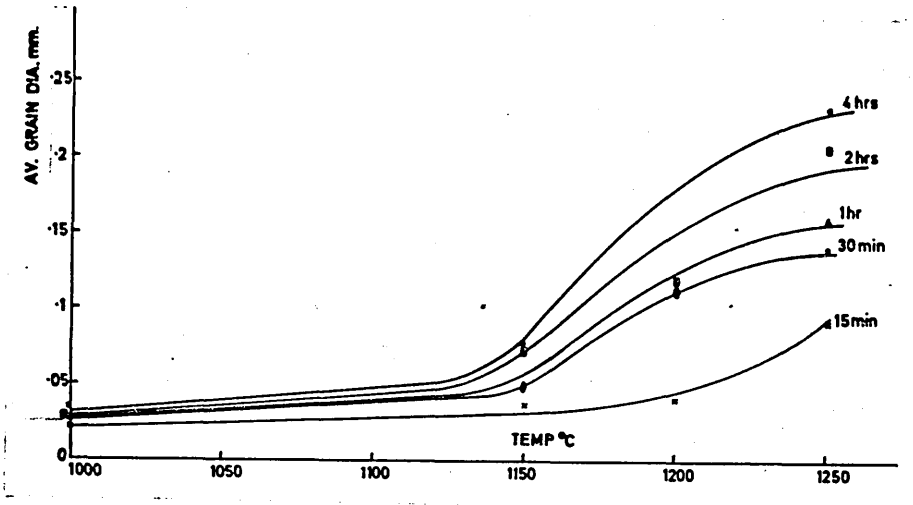

Fig 16

Grain coarsening characteristics of Alloy 3 (Bar)

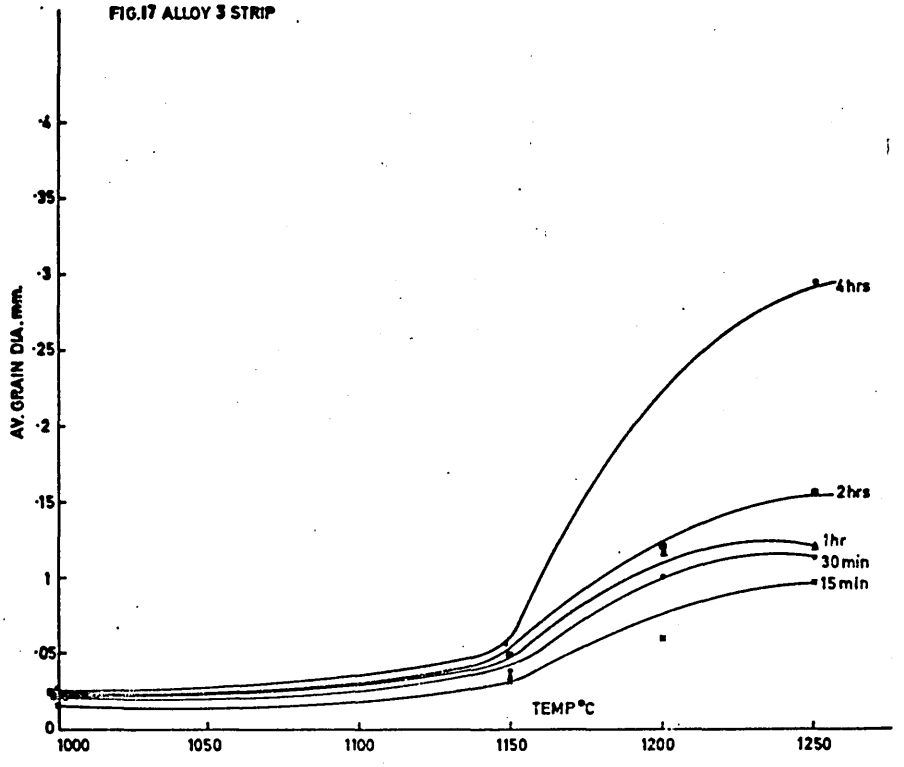

Fig 17

Grain coarsening characteristics of Alloy 3 (Strip)

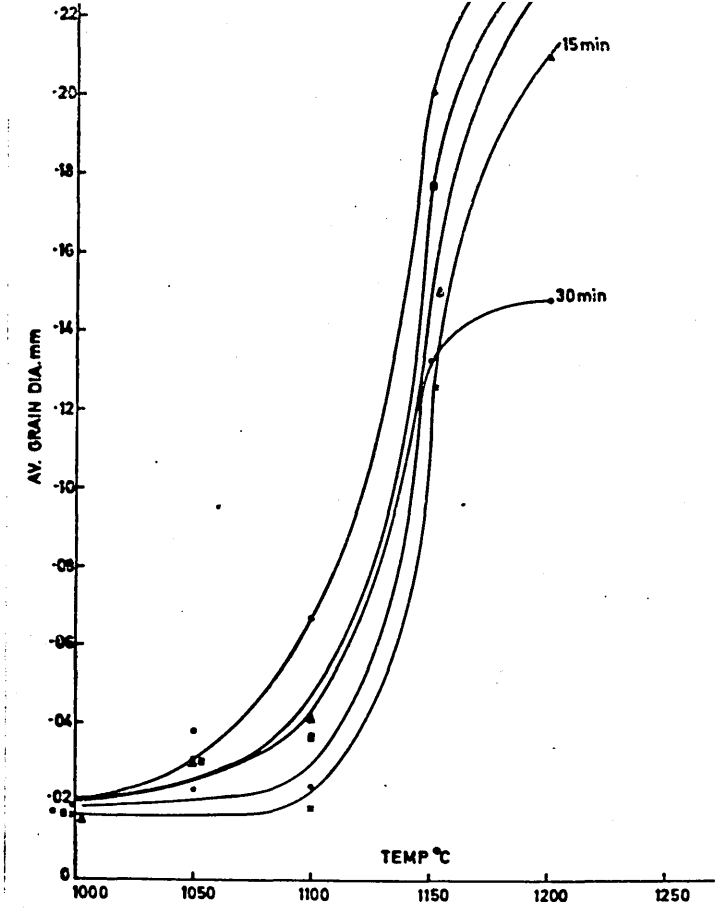

Fig 18

Grain coarsening characteristics of Alloy 4 (Bar)

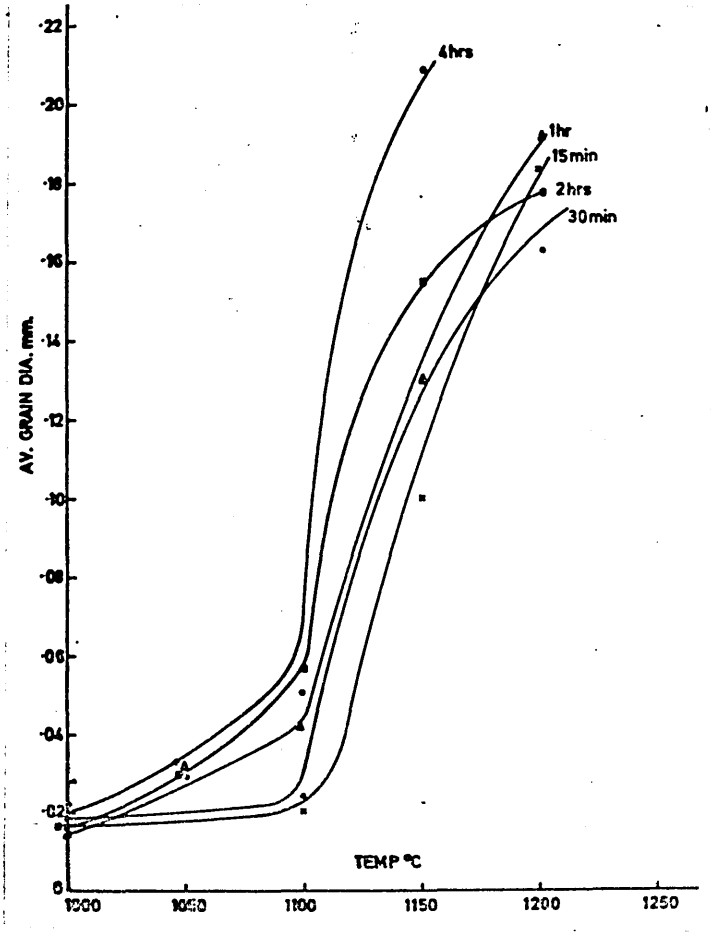

Fig 19

Grain coarsening characteristics of Alloy 4 (Strip)

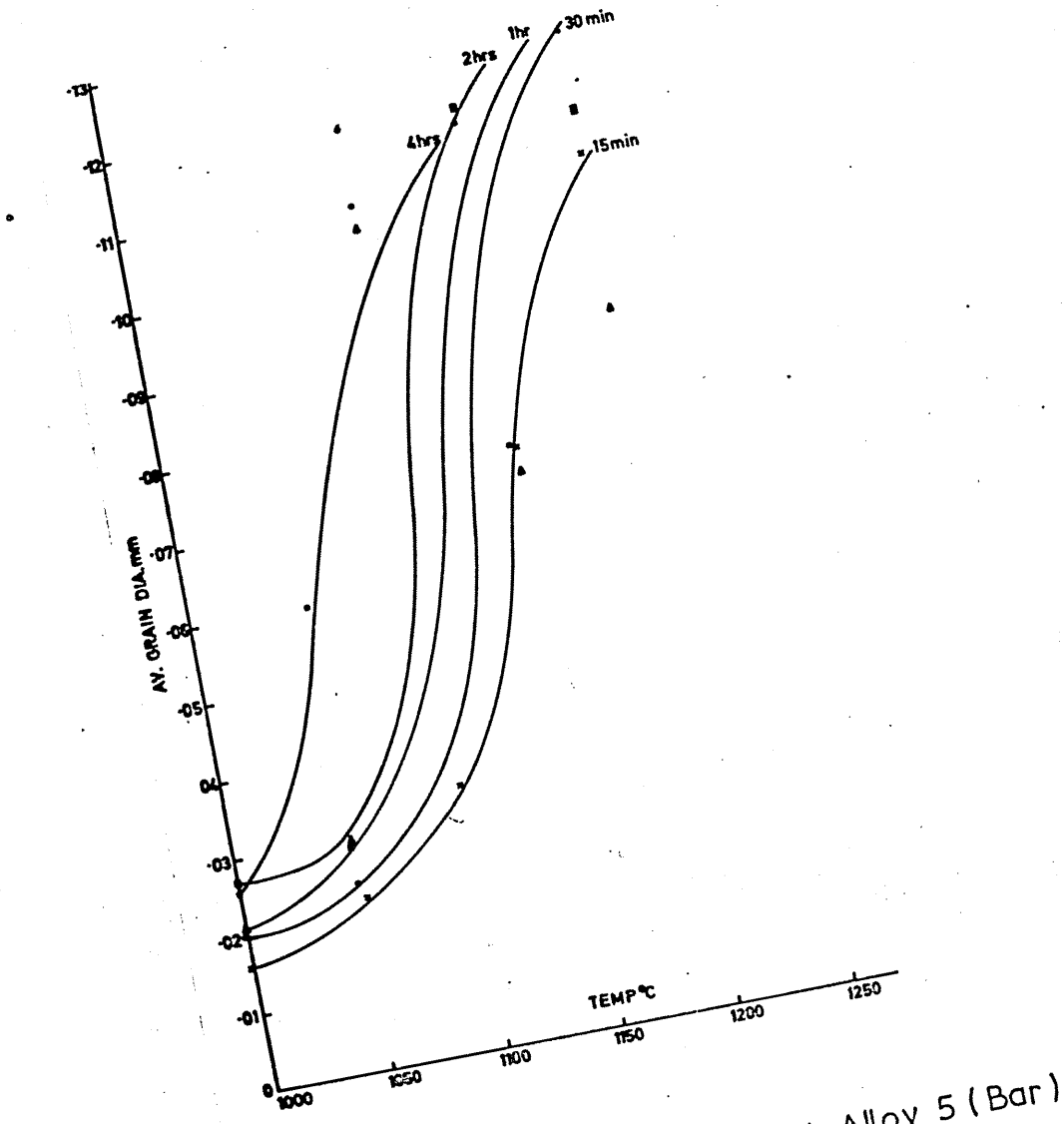

Fig 20

Grain coarsening characteristics of Alloy 5 (Bar)

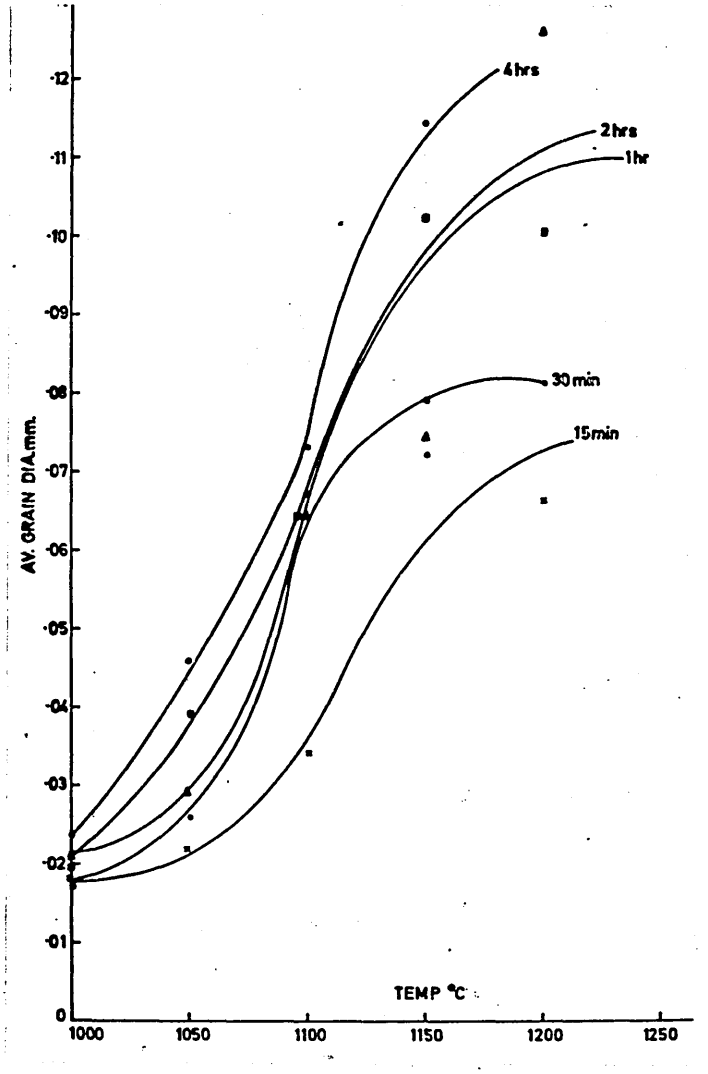

Fig 21

Grain coarsening characteristics of Alloy 5 (Strip)

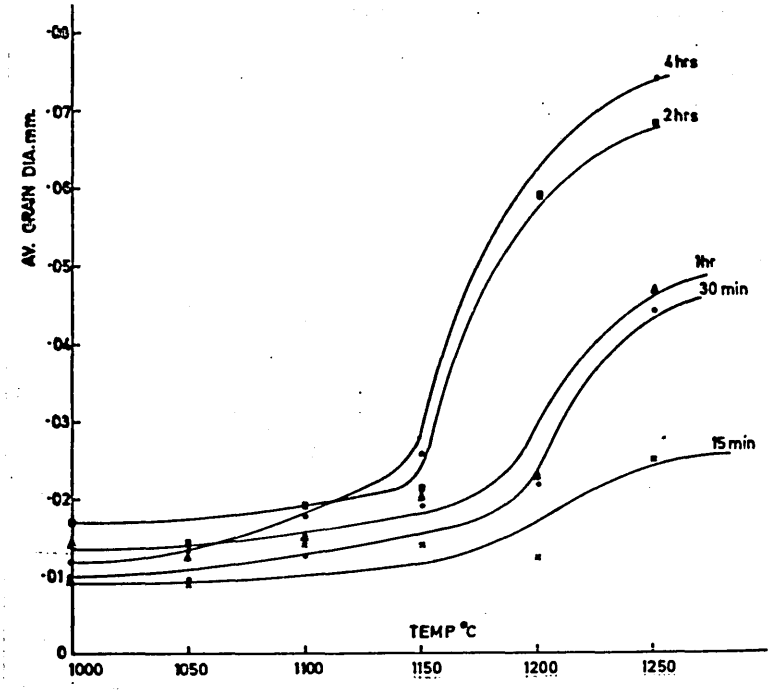

Fig 22

Grain coarsening characteristics of Alloy 6 (Bar)

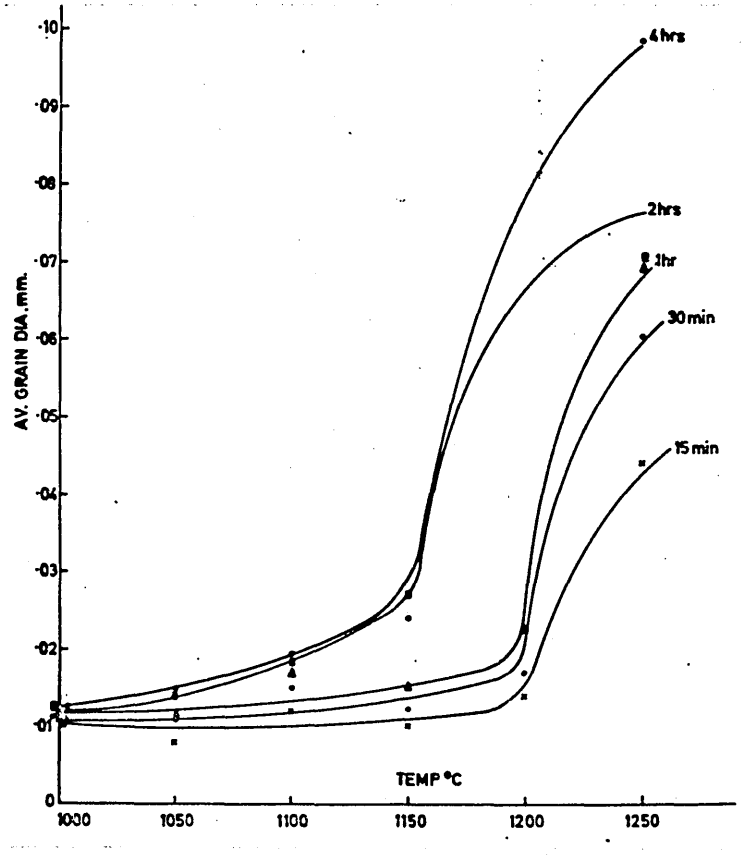

Fig 23

Grain coarsening characteristics of Alloy 6 (Strip)

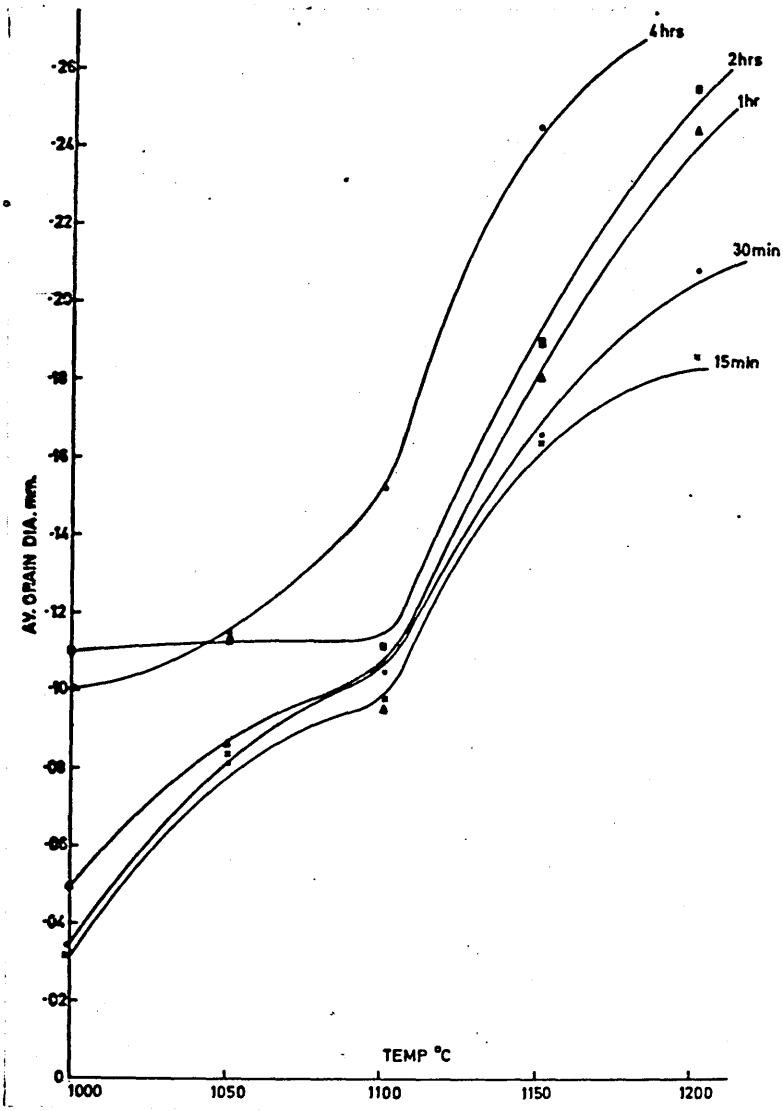

Fig 24

Grain coarsening characteristics of Alloy 7 (Bar)

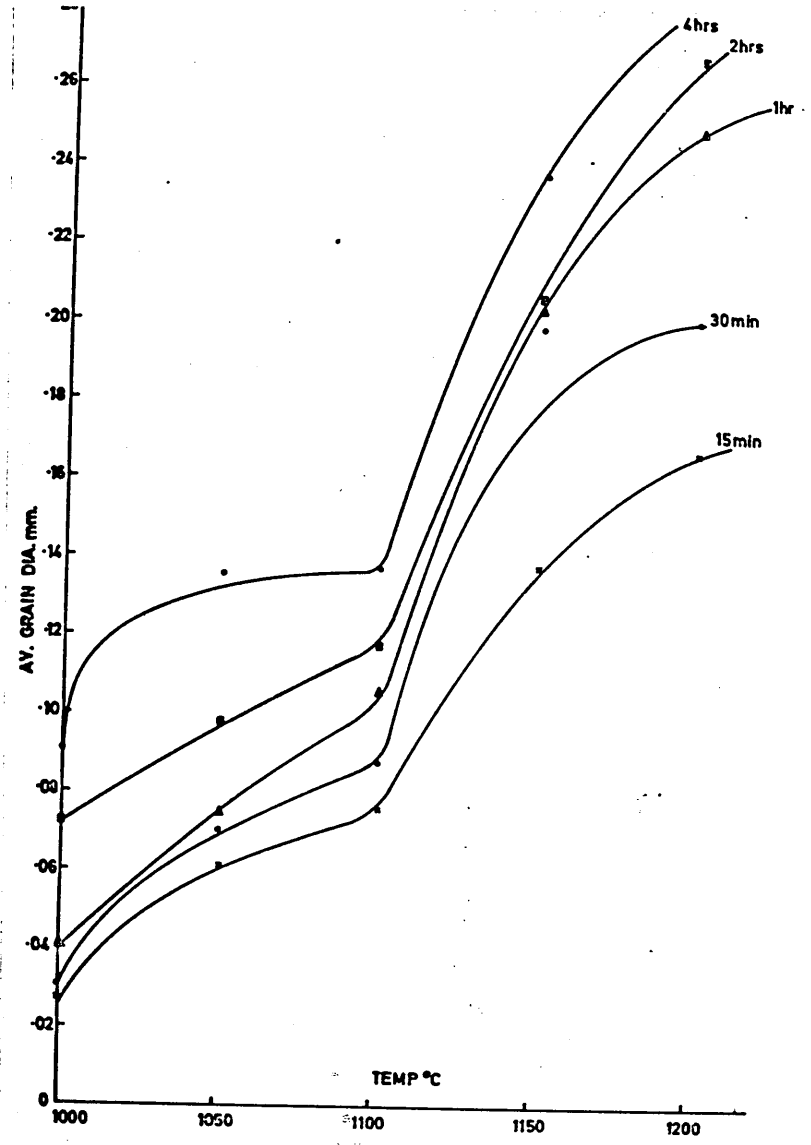

Fig 25

Grain coarsening characteristics of Alloy 7 (Strip)

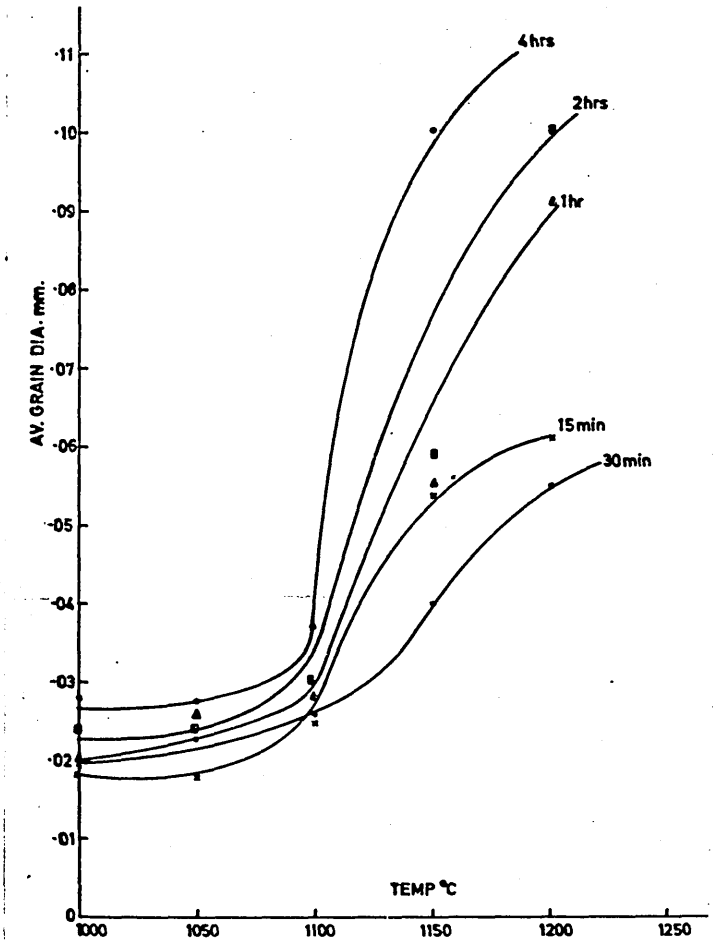

Fig 26
Grain coarsening characteristics of Alloy 8 (Bar)

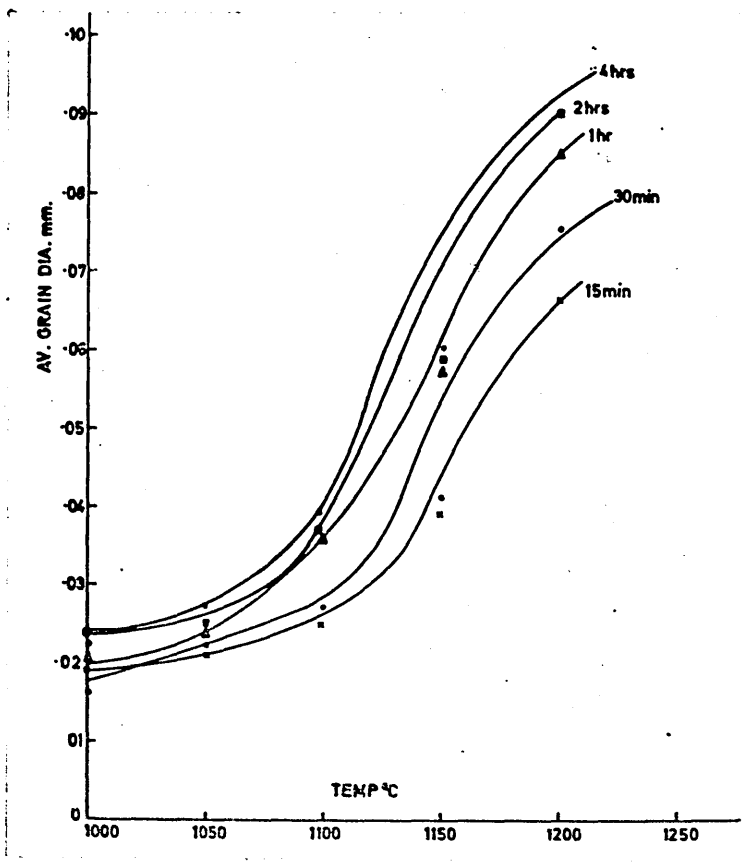

Fig 27
Grain coarsening characteristics of Alloy 8 (Strip)

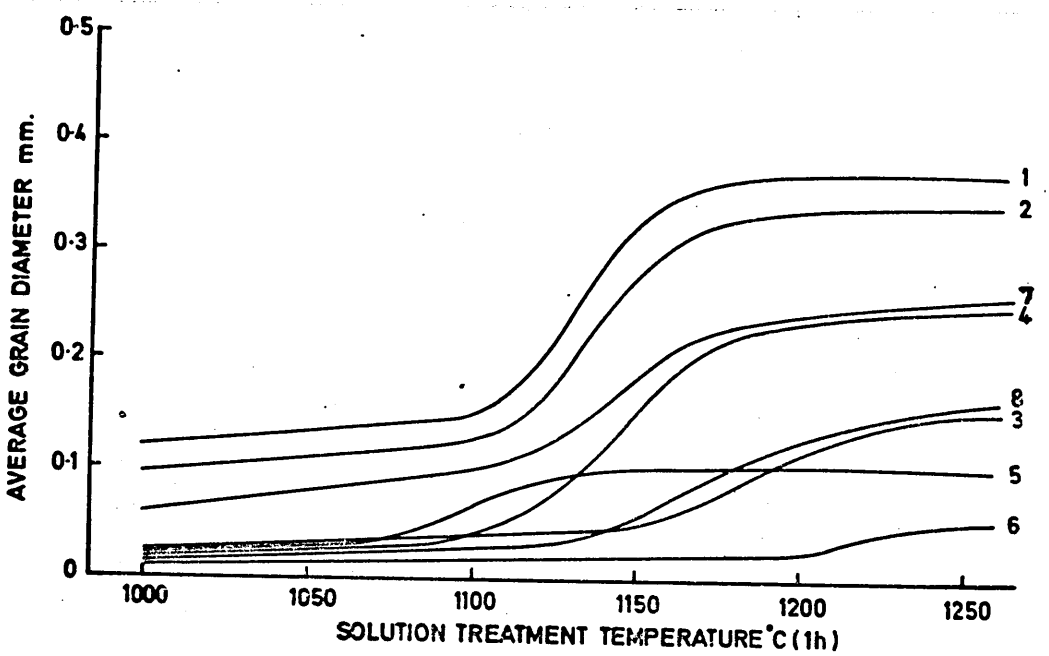

FIG. 28 GRAIN COARSENING CHARACTERISTICS

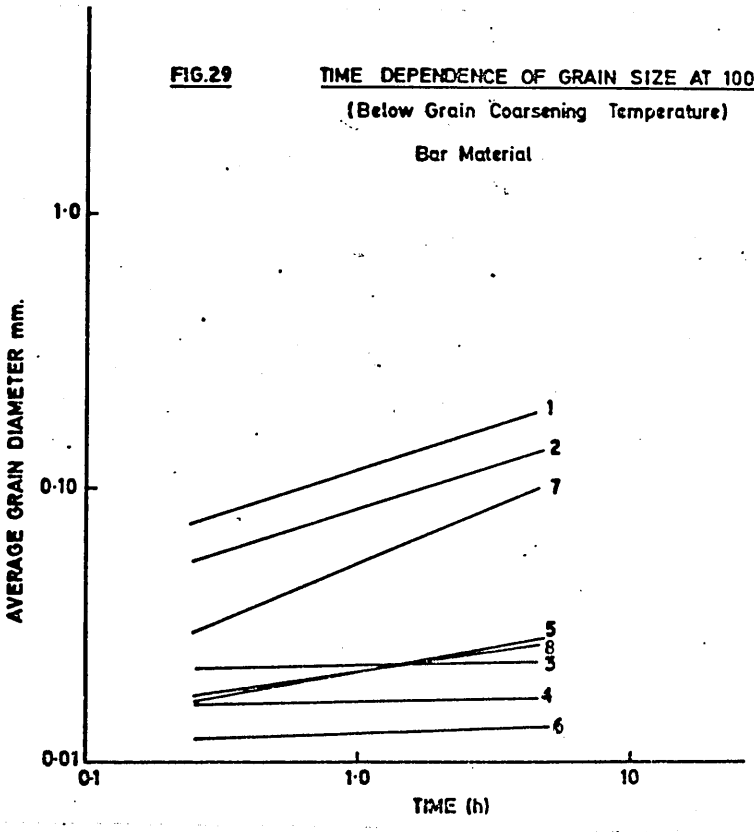

FIG. 29 TIME DEPENDENCE OF GRAIN SIZE AT 1000°C
(Below Grain Coarsening Temperature)
Bar Material

FIG.30 TIME DEPENDENCE OF GRAIN SIZE AT 1200/1250°C

(Above Grain Coarsening Temperature)

Bar Material

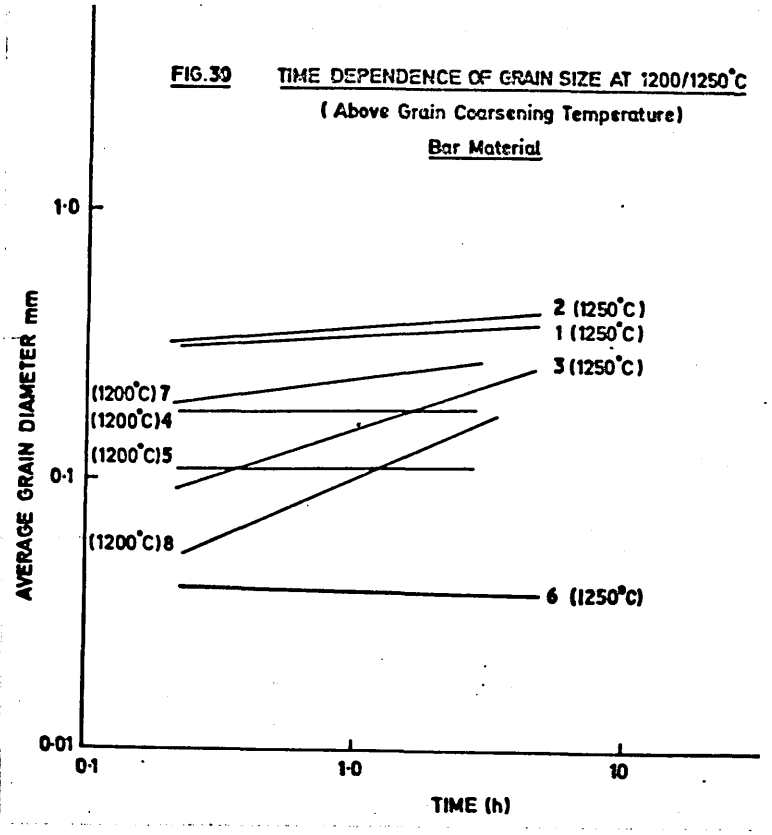

FIG31 AGEING CURVES FOR ALLOY 1

(Fe-Ni-Cr-0·0096 %C)

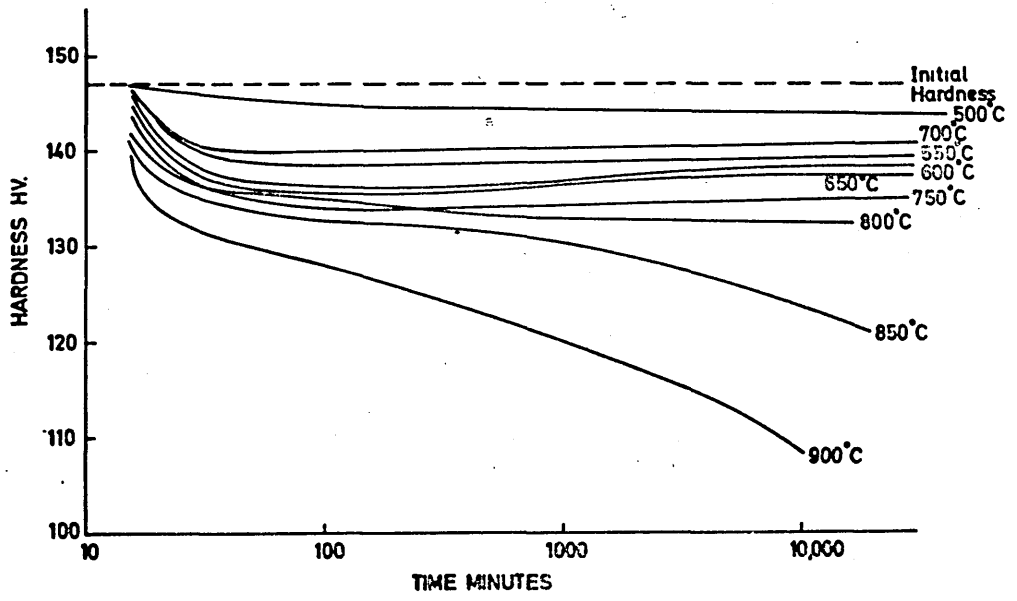

FIG 32 AGEING CURVES FOR ALLOY 2

(Fe-Ni-Cr-0·049% C)

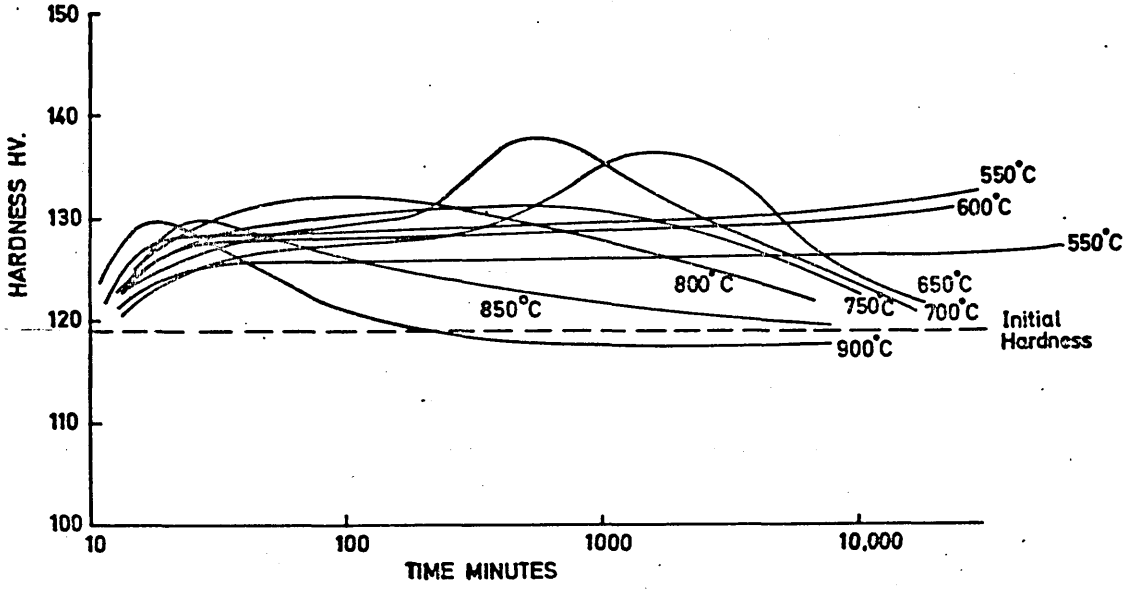

FIG 33 AGEING CURVES FOR ALLOY 3

(Fe-Ni-Cr-0·10% C)

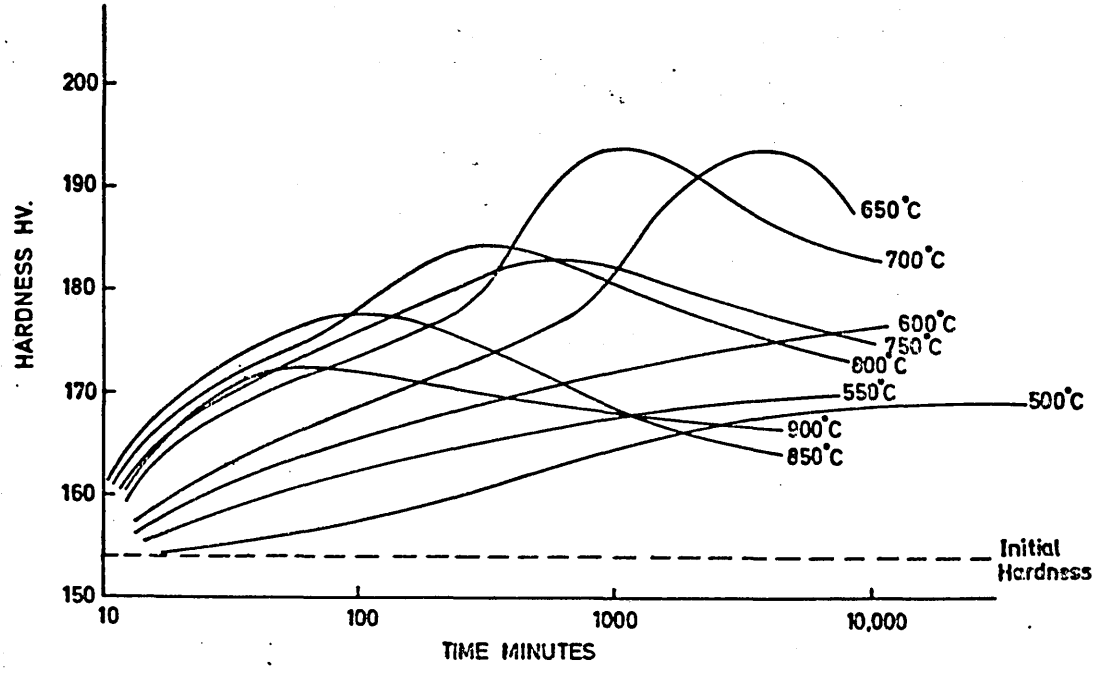

FIG.34 AGEING CURVES FOR ALLOY 4

(Fe-Ni-Cr - 0·1% C - 3·5% Mo)

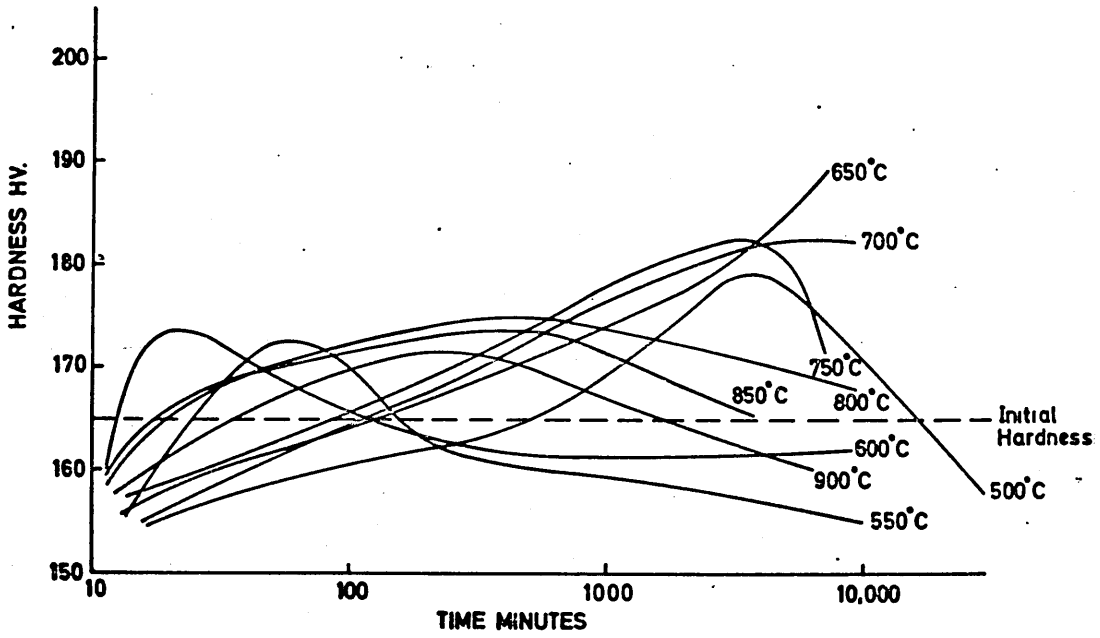

FIG.35 AGEING CURVES FOR ALLOY 5

(Fe-Ni-Cr- 0·14% C - 3·57% Mo - 1·18% Ti)

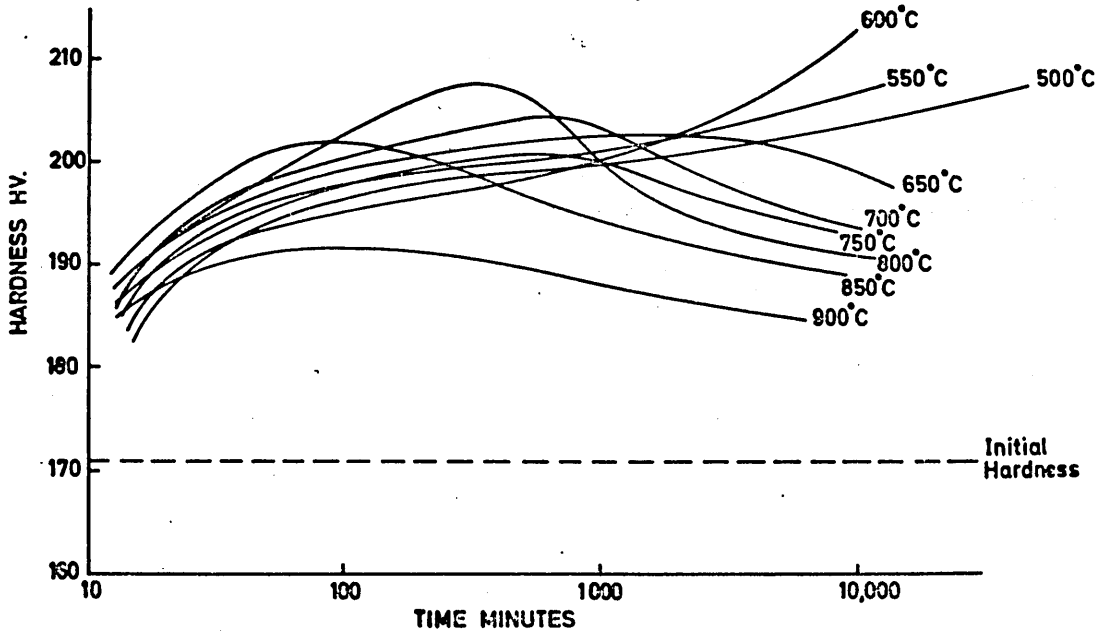

FIG.36 AGEING CURVES FOR ALLOY 6

(Fe – Ni – Cr – 0·35% C – 3·65% Mo – 1·11% Ti)

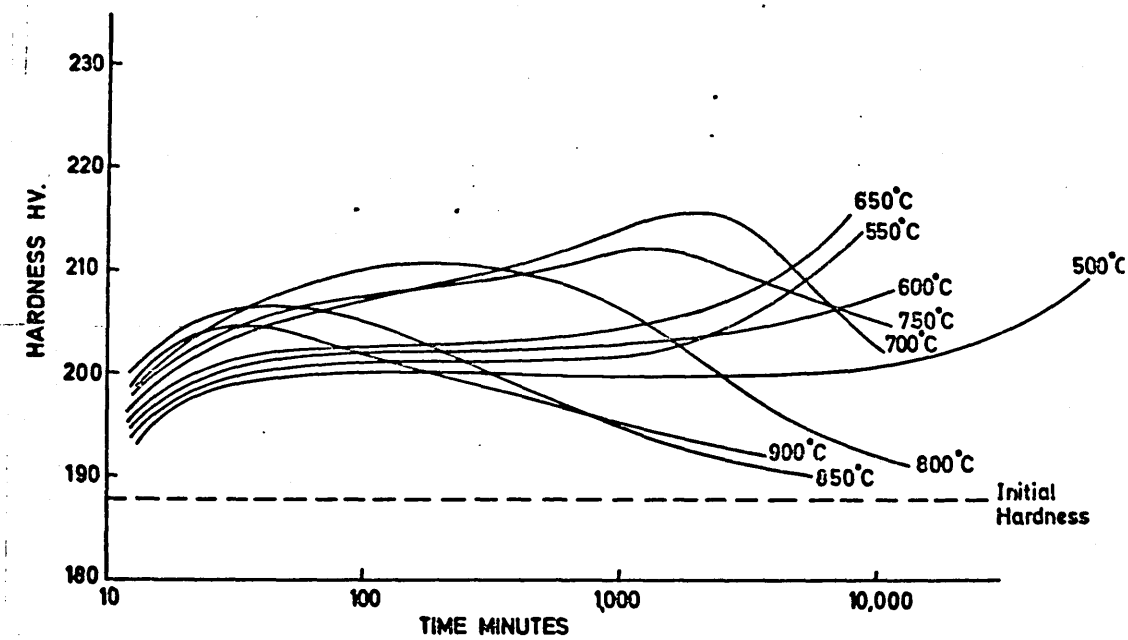

FIG.37 AGEING CURVES FOR ALLOY 7. (P.E.16 – 0·012 % C)

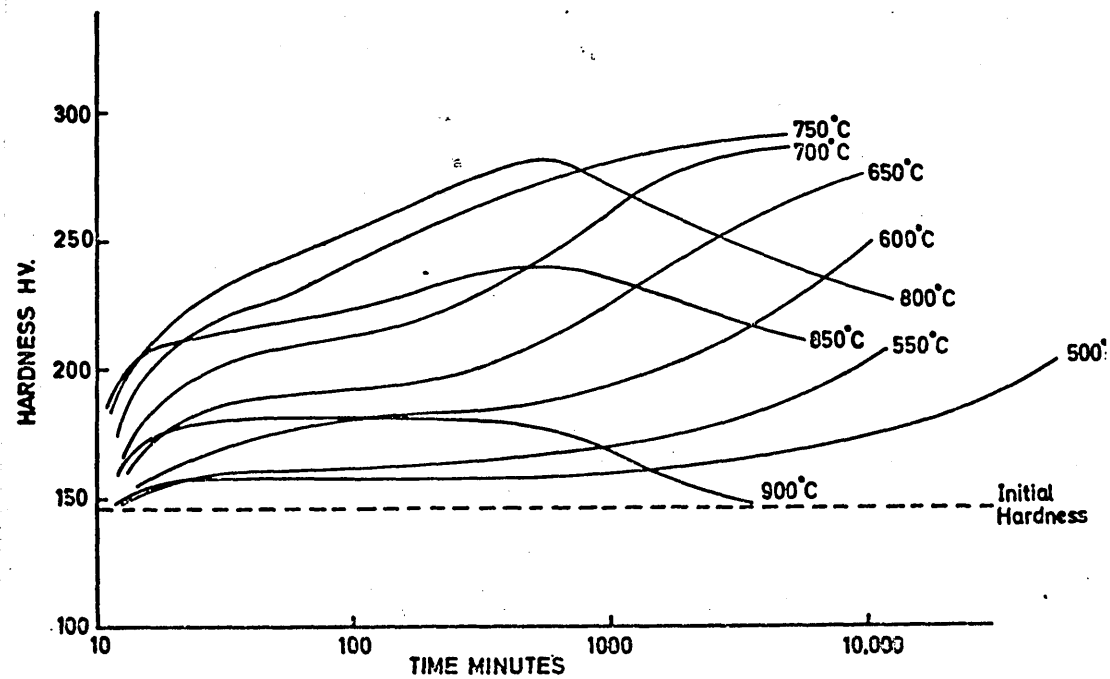

FIG.38 AGEING CURVES FOR ALLOY 8.

(P.E. 16 – 0·12% C)

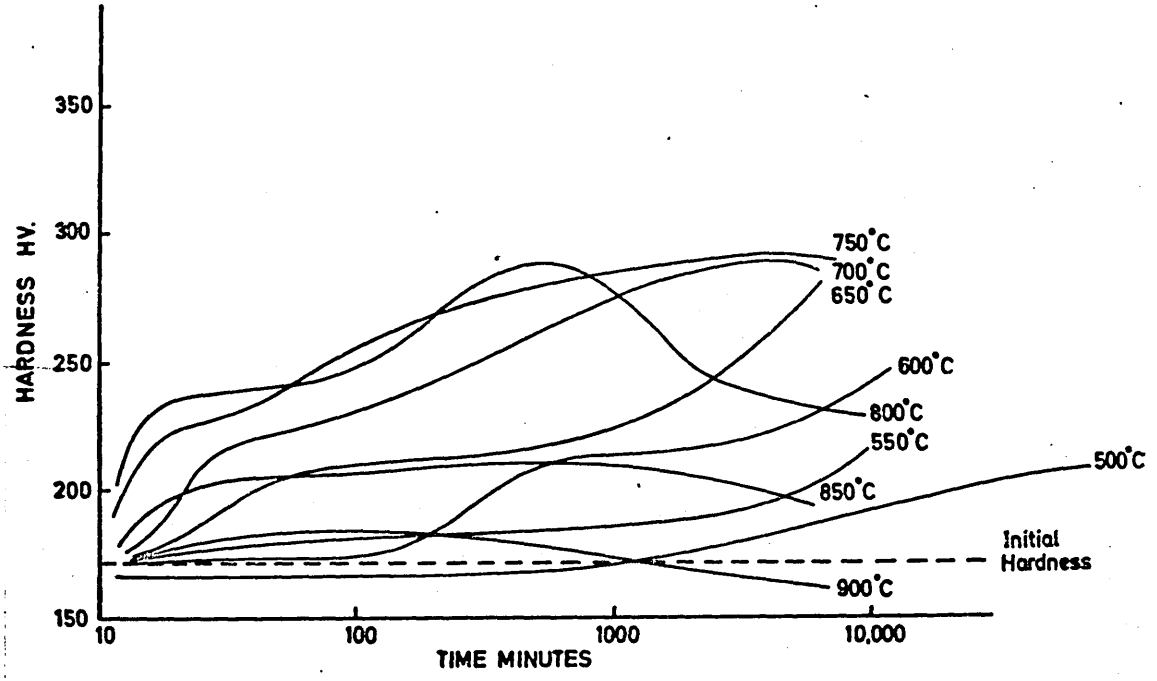

FIG.39 TENTATIVE "C CURVES" FOR START OF CARBIDE PRECIPITATION.

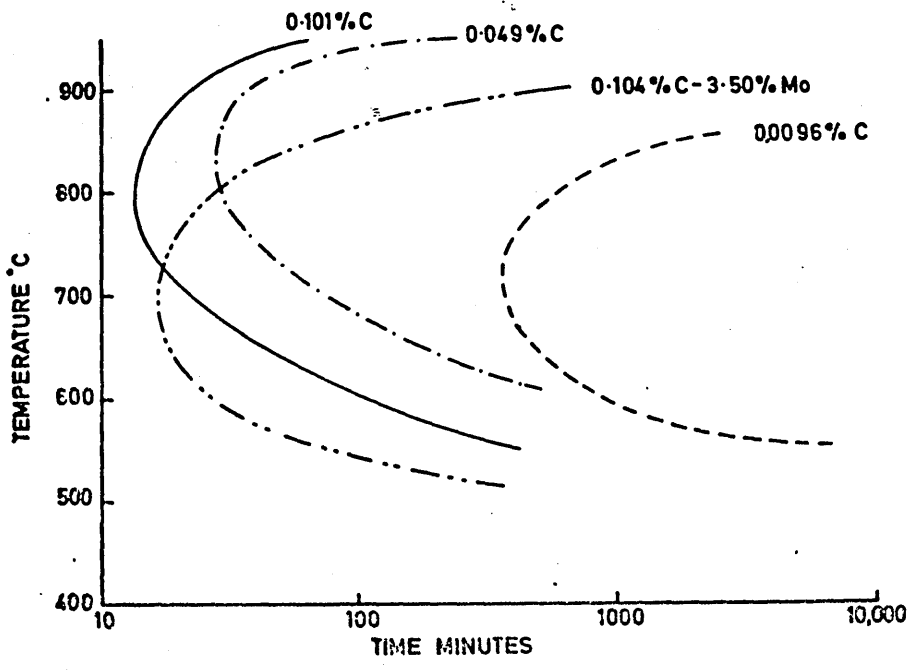

FIG.40 EFFECT OF CARBON ON AGE - HARDENING DUE TO $M_{23}C_6$ PRECIPITATION

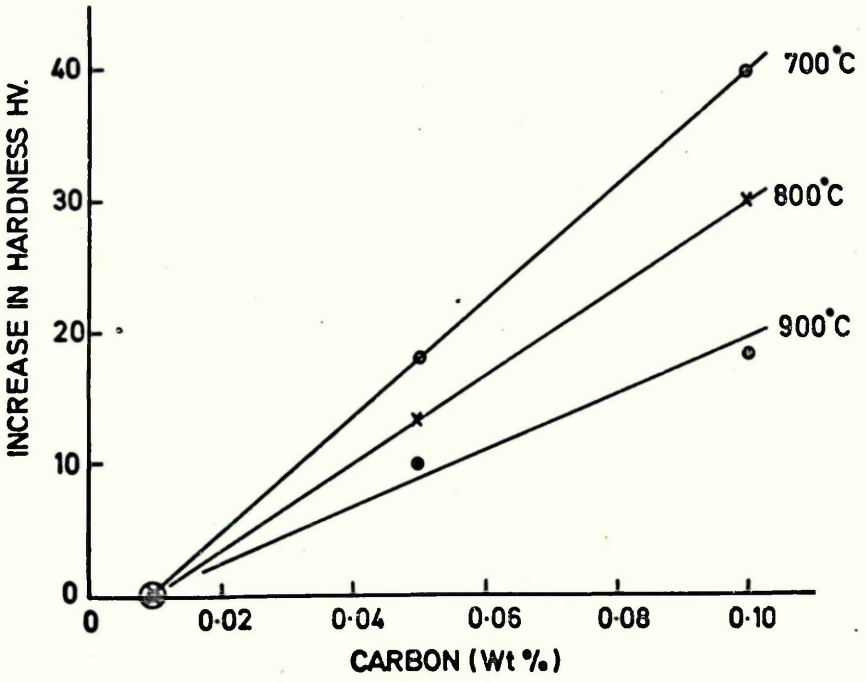

FIG.41. EFFECT OF AGEING TEMPERATURE ON MAXIMUM INCREASE IN HARDNESS.

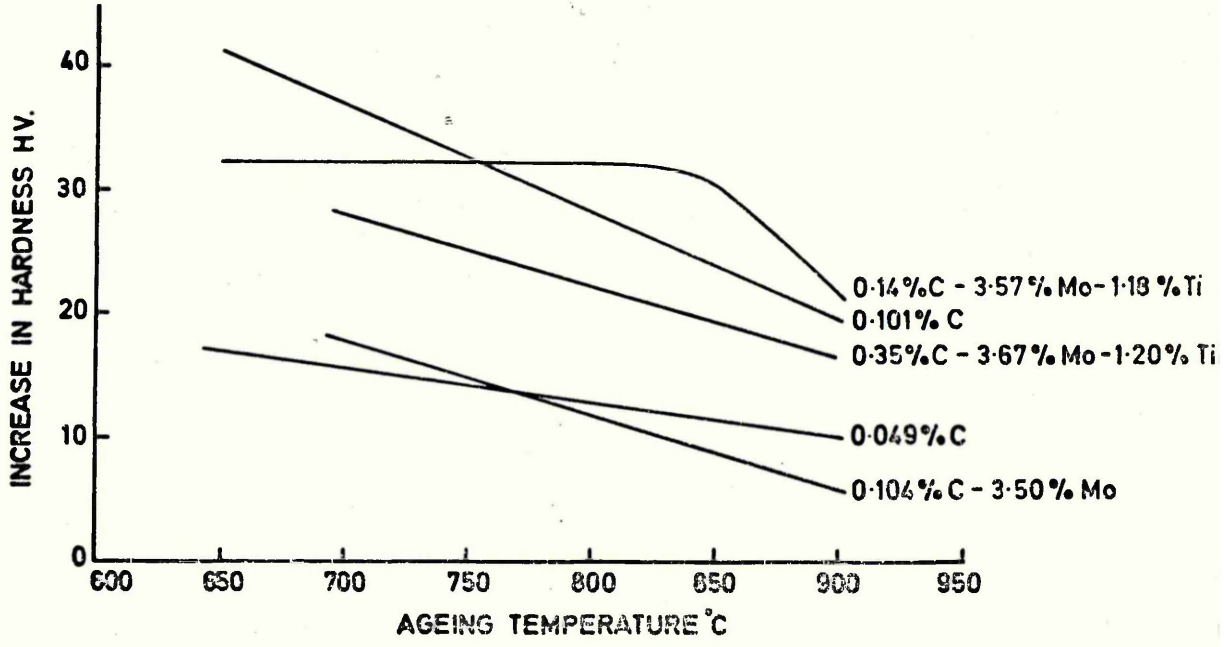

FIG.42 COMPARISON OF AGEING OF P.E. 16 ALLOYS WITH ALLOYS PRECIPITATING CARBIDE

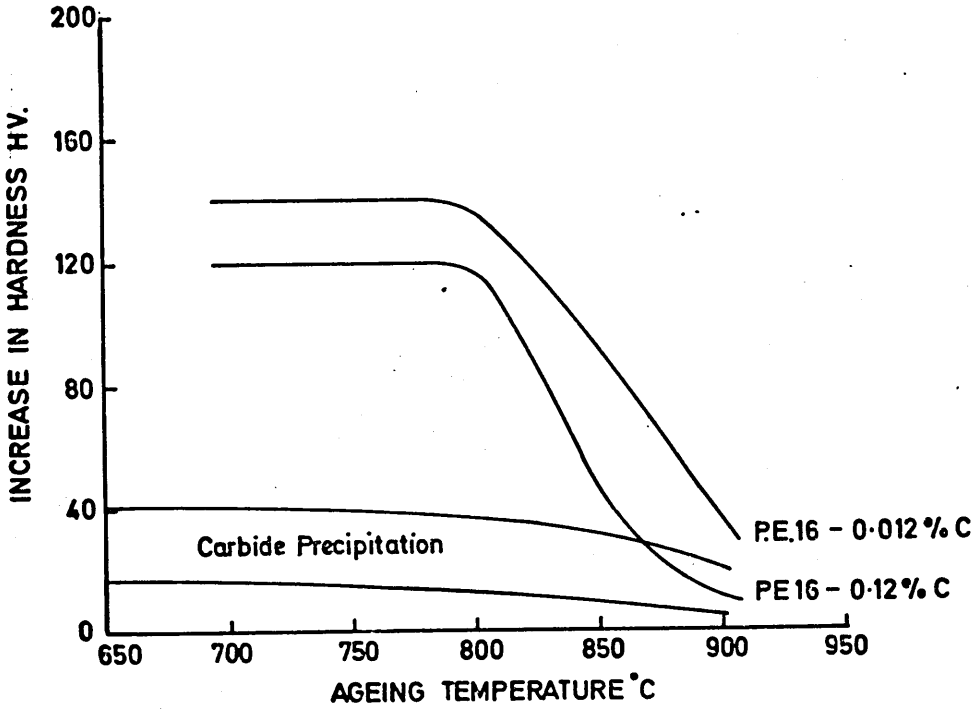

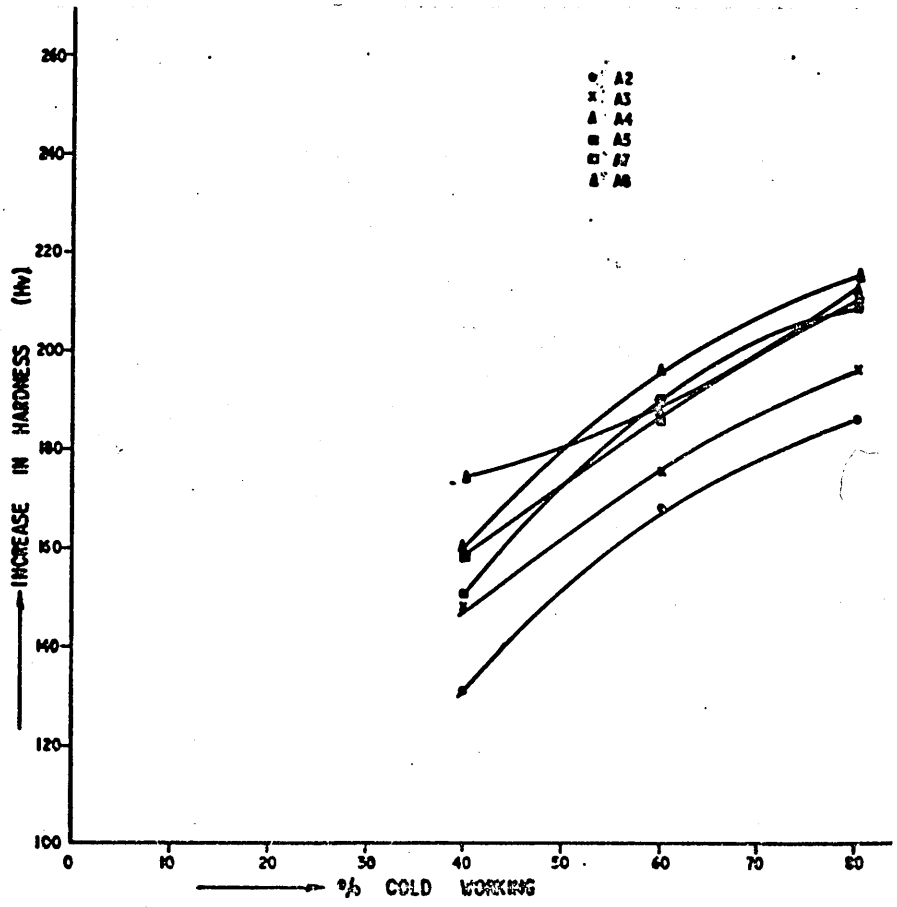

FIG. 43. WORK HARDENING CHARACTERISTICS

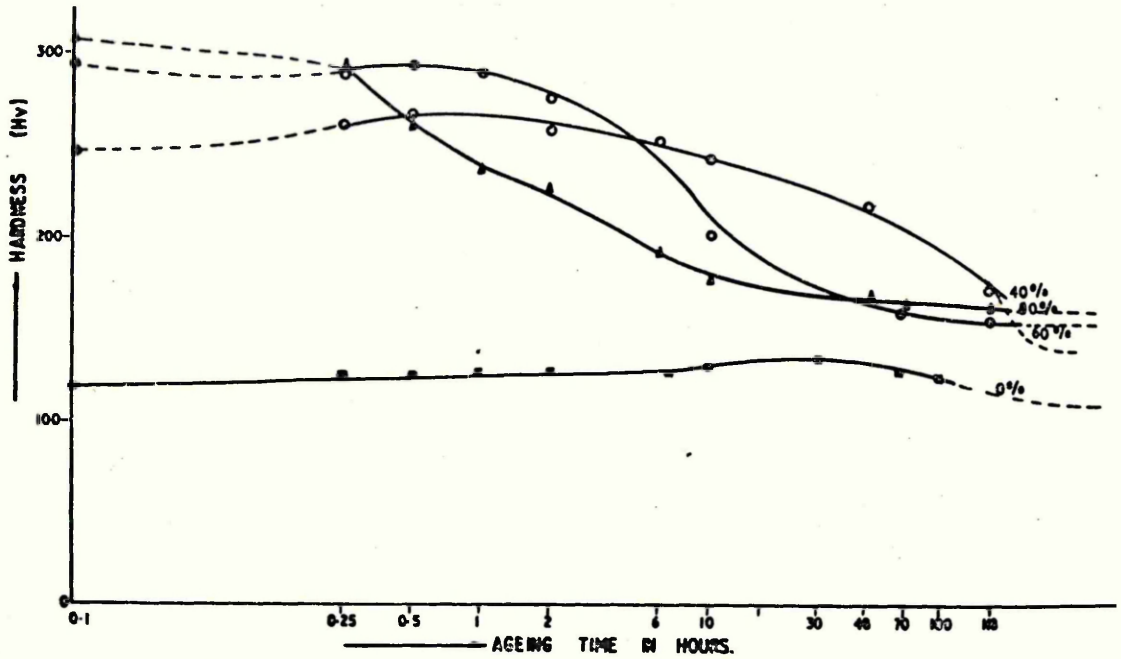

FIG. 44. RECRYSTALLIZATION CHARACTERISTICS OF ALLOY No. 2 AT 650°C.

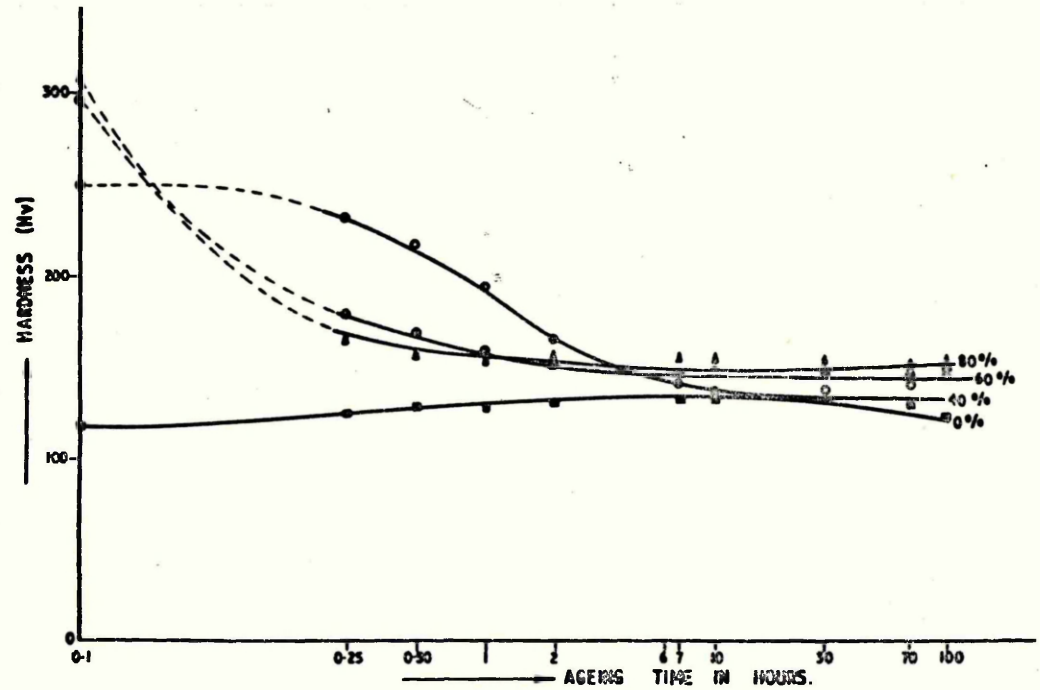

FIG. 45. RECRYSTALLIZATION CHARACTERISTICS OF ALLOY No. 2 AT 750°C.

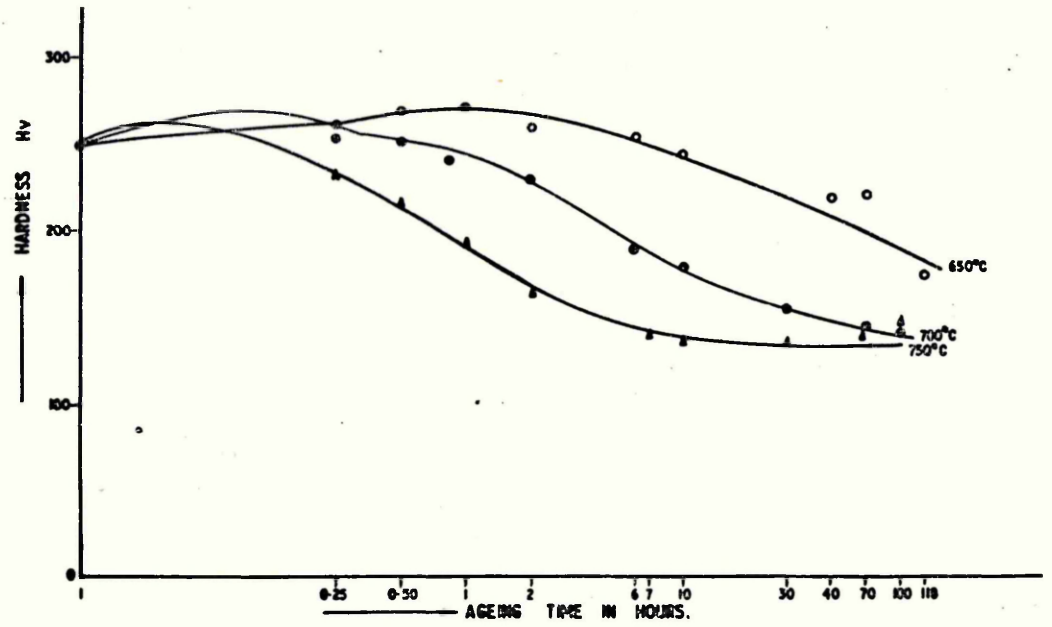

FIG. 46 RECRYSTALLIZATION CHARACTERISTICS OF ALLOY No. 2 AT 40% COLD WORKING.

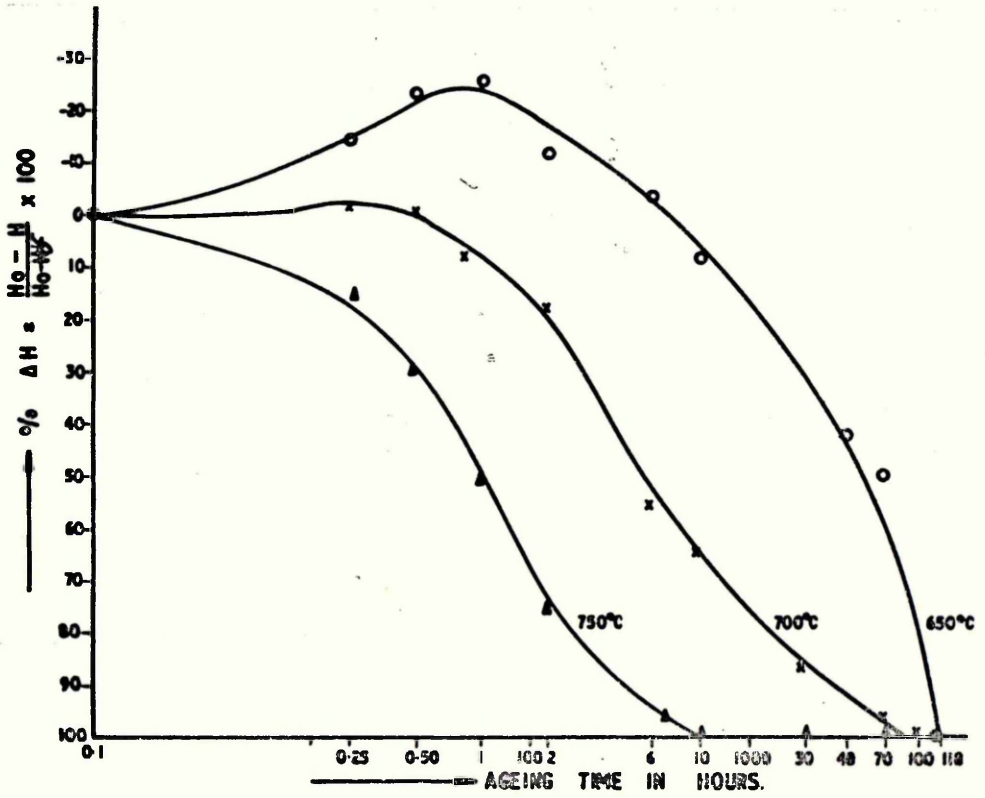

FIG. 47 SOFTENING CURVES OF ALLOY 2 AT 40% COLD WORKING.

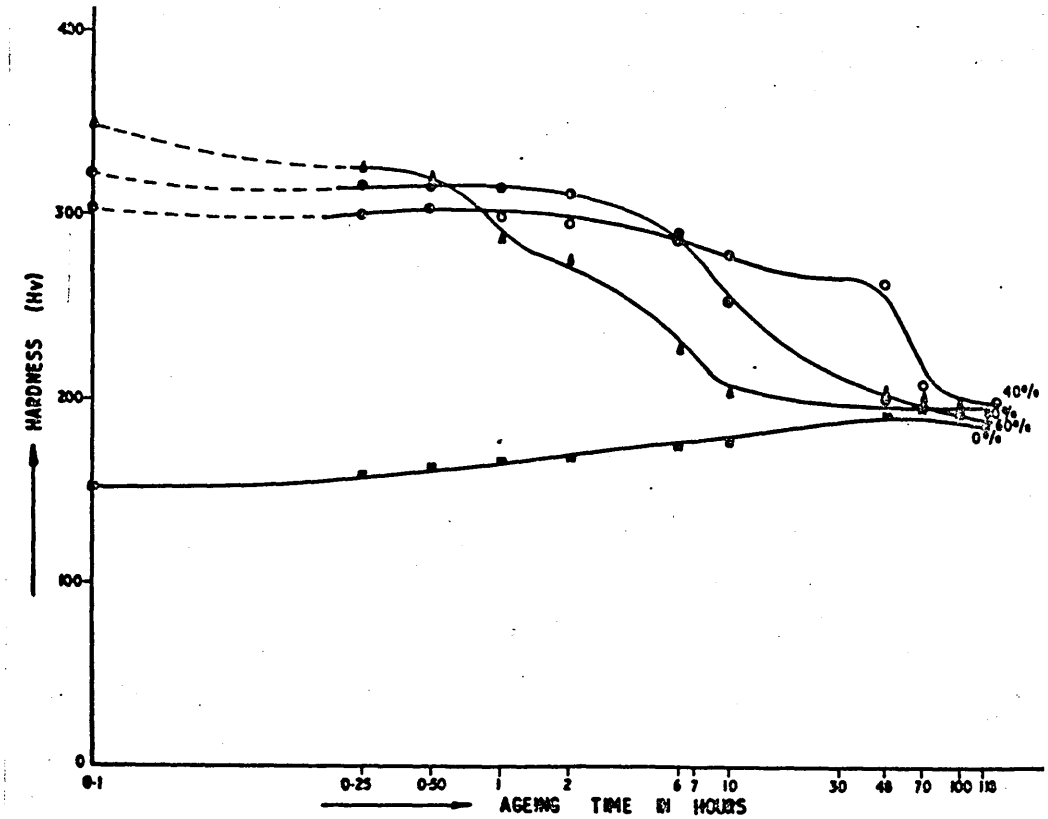

FIG. 48 RECRYSTALLISATION CHARACTERISTICS OF ALLOY No.3 AT 650°C

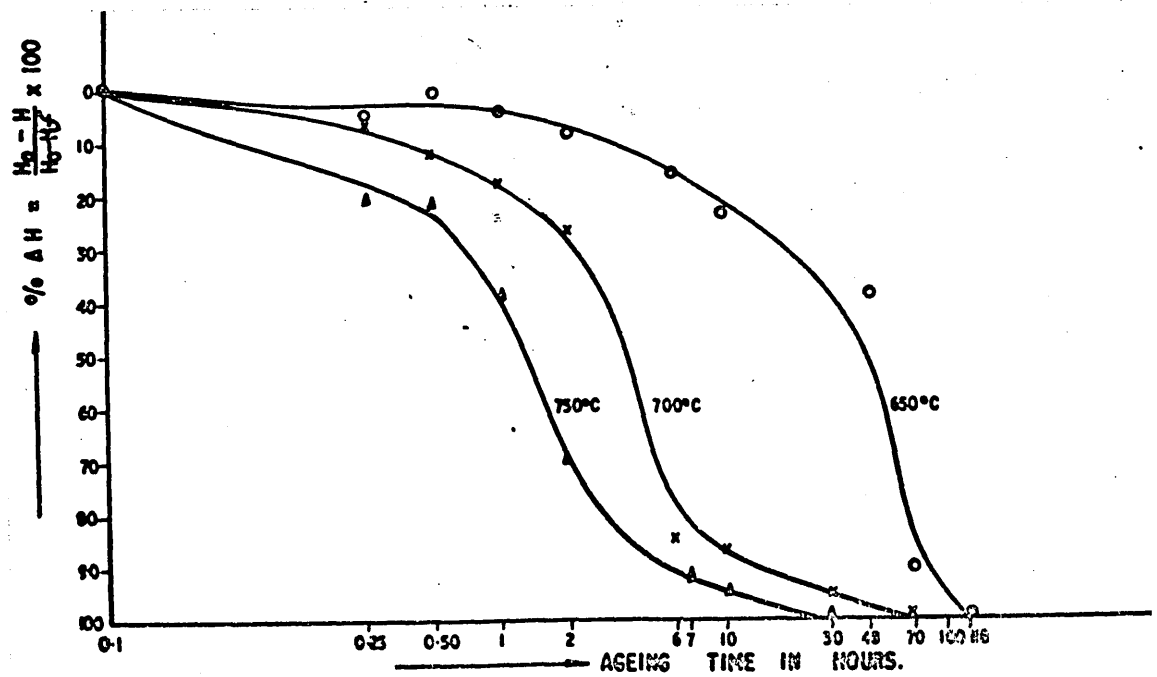

FIG. 49. SOFTENING CURVES OF ALLOY No.3 AT 40% COLD WORKING.

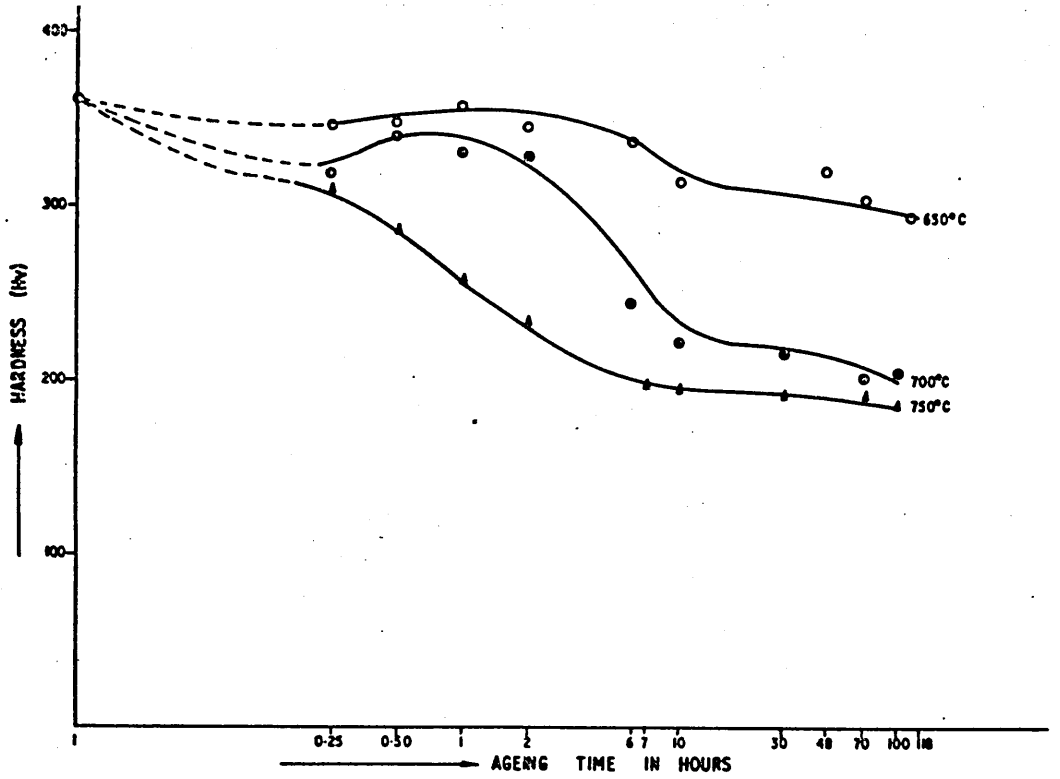

FIG. 50 RECRYSTALLIZATION CHARACTERISTICS OF ALLOY No. 4 AT 60 % COLD WORKING.

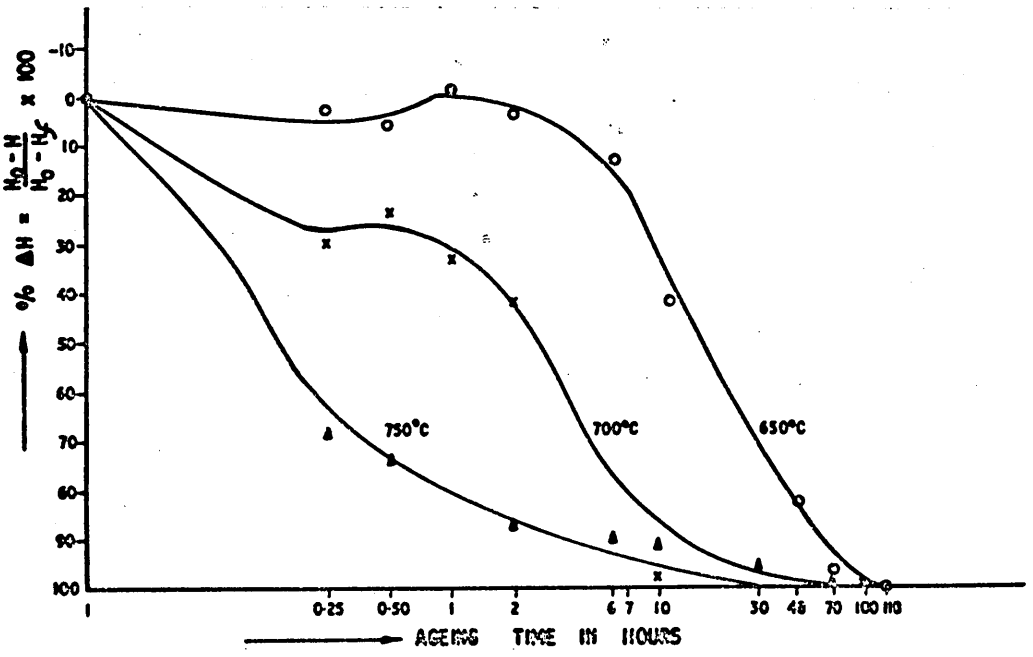

FIG. 51 SOFTENING CURVES OF ALLOY No. 4 AT 60% COLD WORKING.

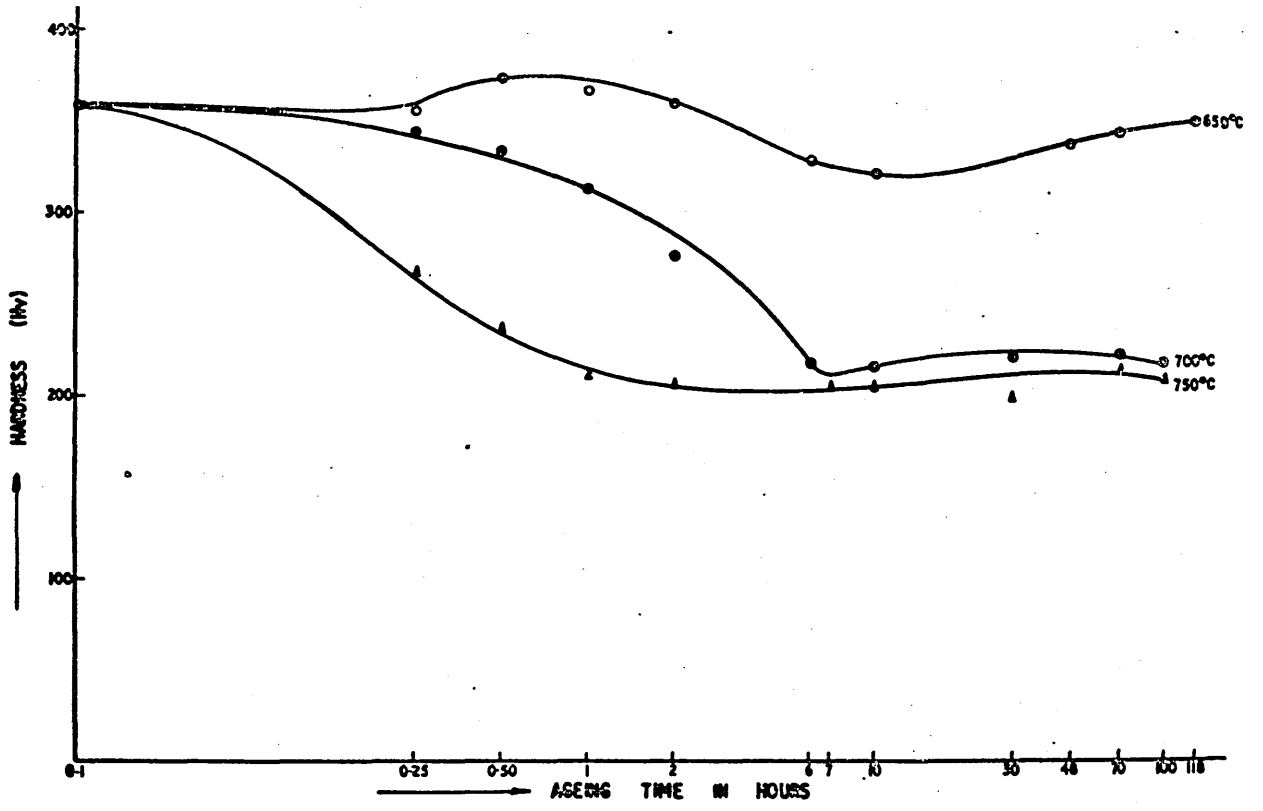

FIG. 52 RECRYSTALLIZATION CHARACTERISTICS OF ALLOY No.5 AT 60% COLD WORKING.

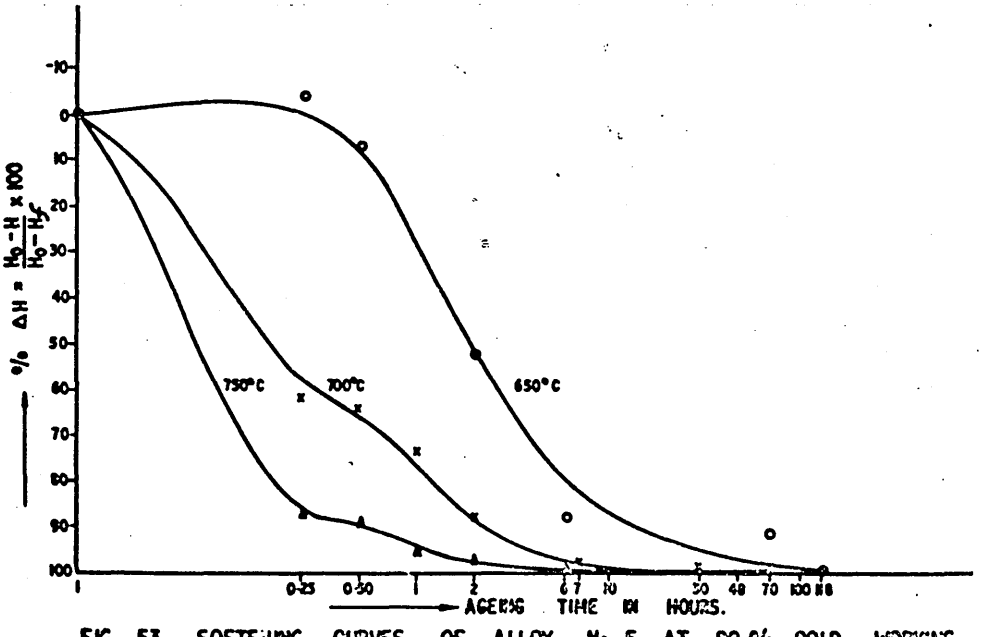

FIG. 53 SOFTENING CURVES OF ALLOY No. 5 AT 80 % COLD WORKING.

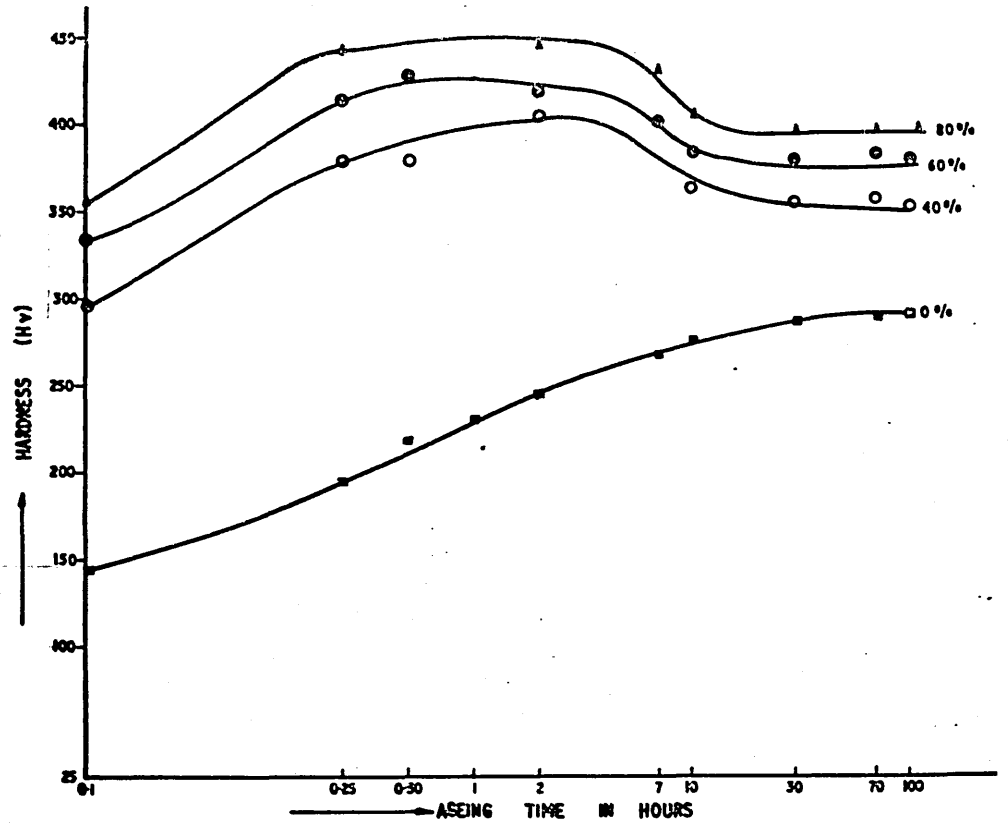

FIG. 54. RECRYSTALLISATION CHARACTERISTICS OF ALLOY No. 7 AT 750°C.

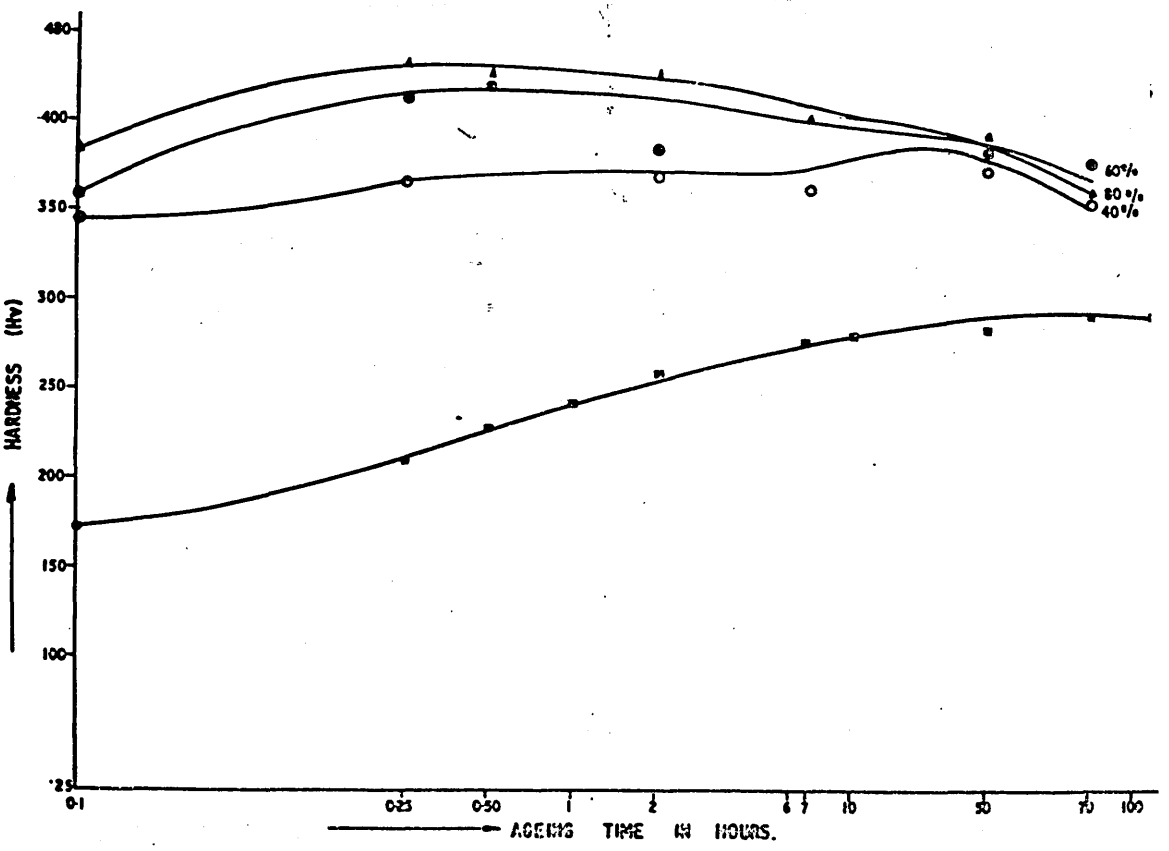

FIG. 55 RECRYSTALLIZATION CHARACTERISTICS OF ALLOY No. 8 AT 750° C.

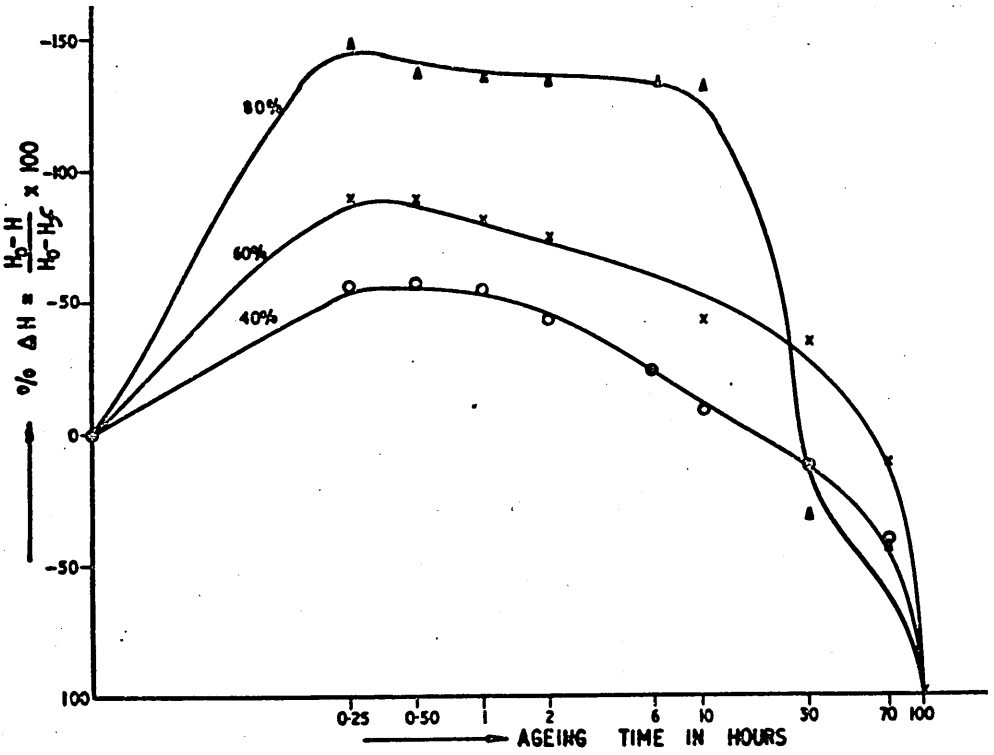

FIG. 56. SOFTENING CURVES OF ALLOY No. 7 AT 650°C.

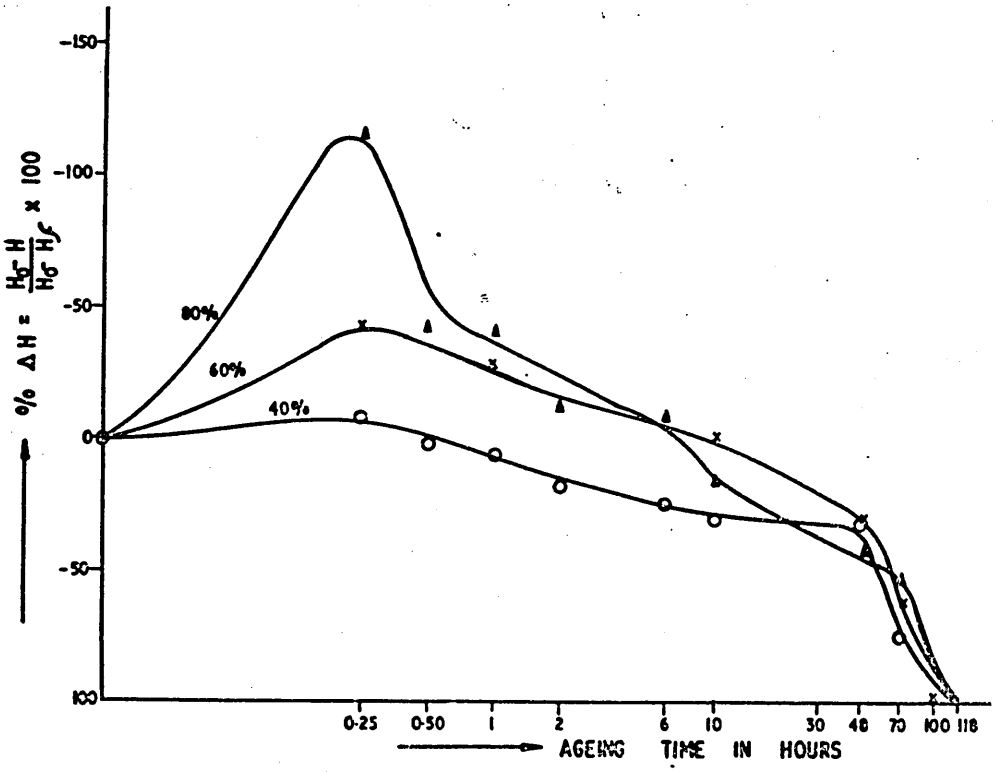

FIG. 57 SOFTENING CURVES OF ALLOY No. 8 AT 650°C.

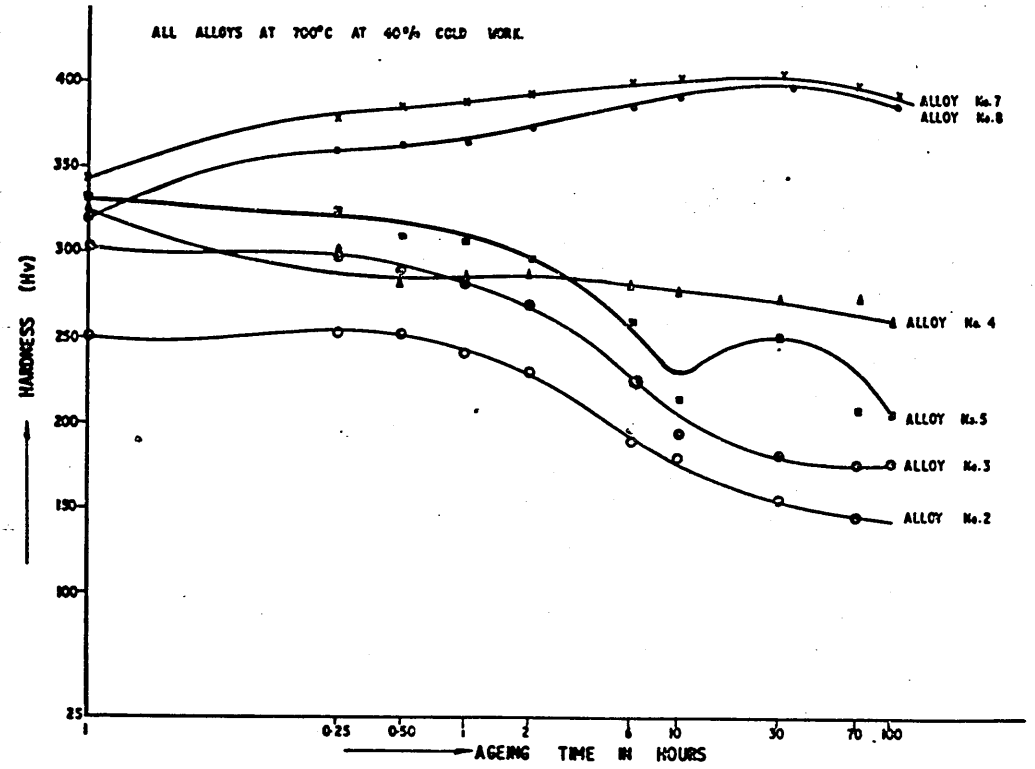

FIG. 58. RECRYSTALLIZATION CHARACTERISTICS OF ALL ALLOYS AT 700° C AT 40% COLD WORKING.

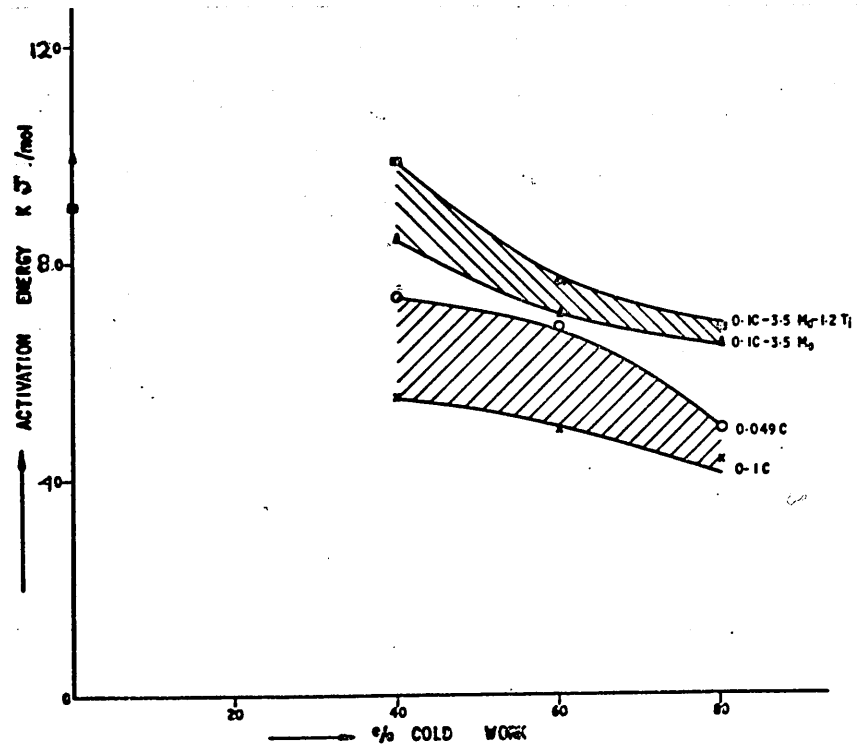

FIG. 59 ACTIVATION ENERGIES FOR 50% SOFTENING FOR CARBIDE FORMING ALLOYS

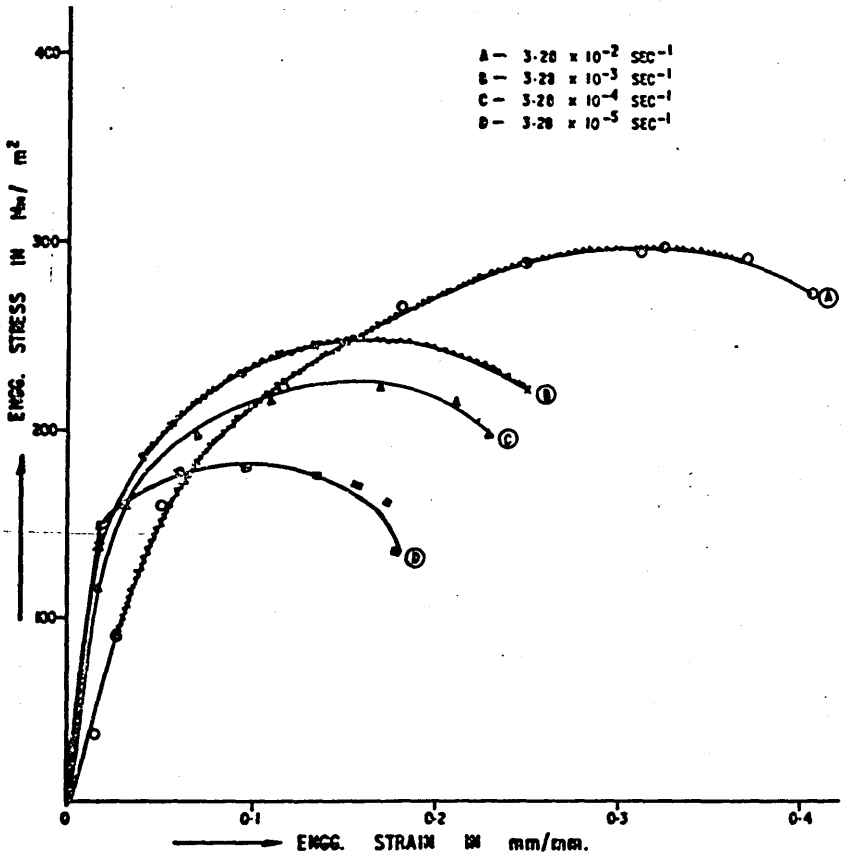

FIG. 60. TENSILE BEHAVIOUR OF LOW CARBON BASE COMPOSITION (ALLOY No. 1)

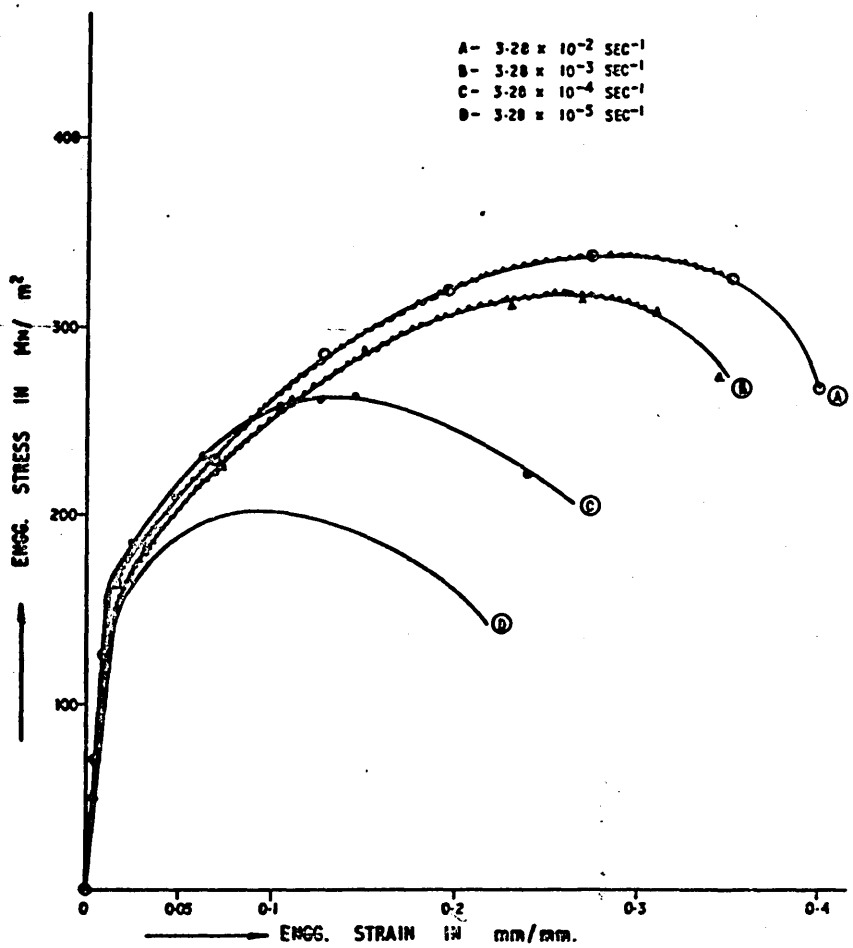

FIG. 61 TENSILE BEHAVIOUR OF MEDIUM CARBON BASE COMPOSITION. (ALLOY No2)

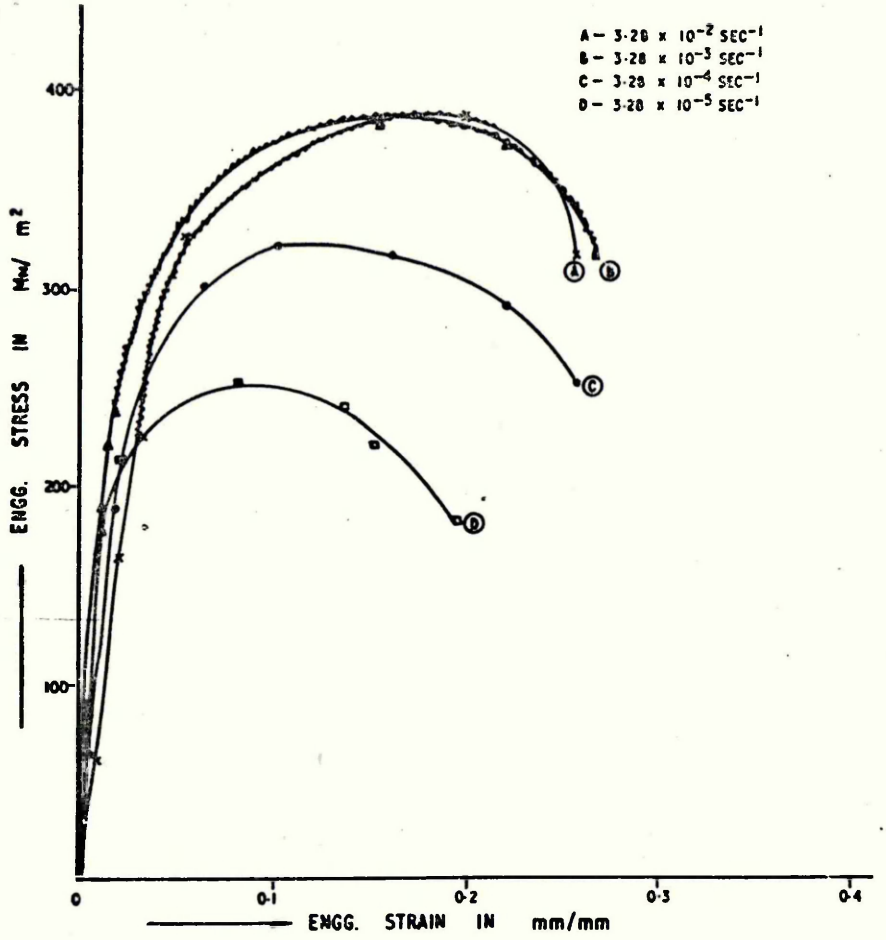

FIG. 62. TENSILE BEHAVIOUR OF HIGH CARBON BASE COMPOSITION (ALLOY No. 3)

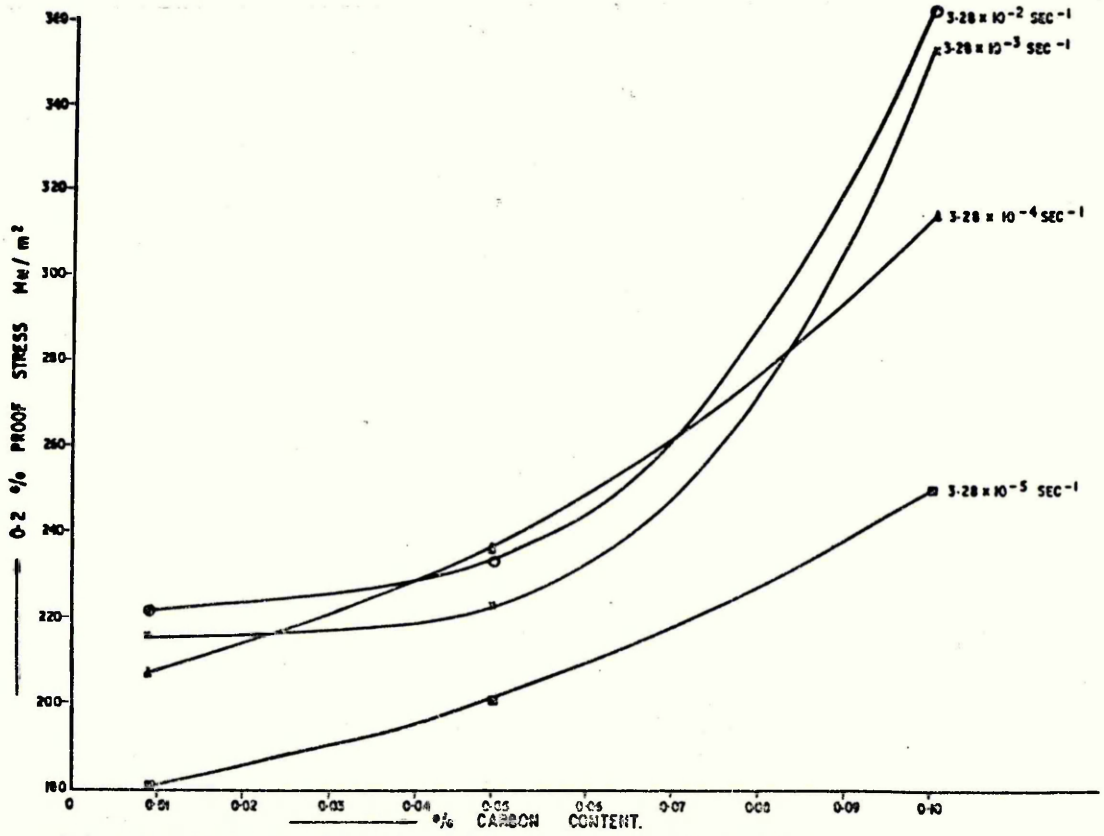

FIG. 63 EFFECT OF Cr 23 C_6 CARBIDES ON 0·2 % PROOF STRESS.

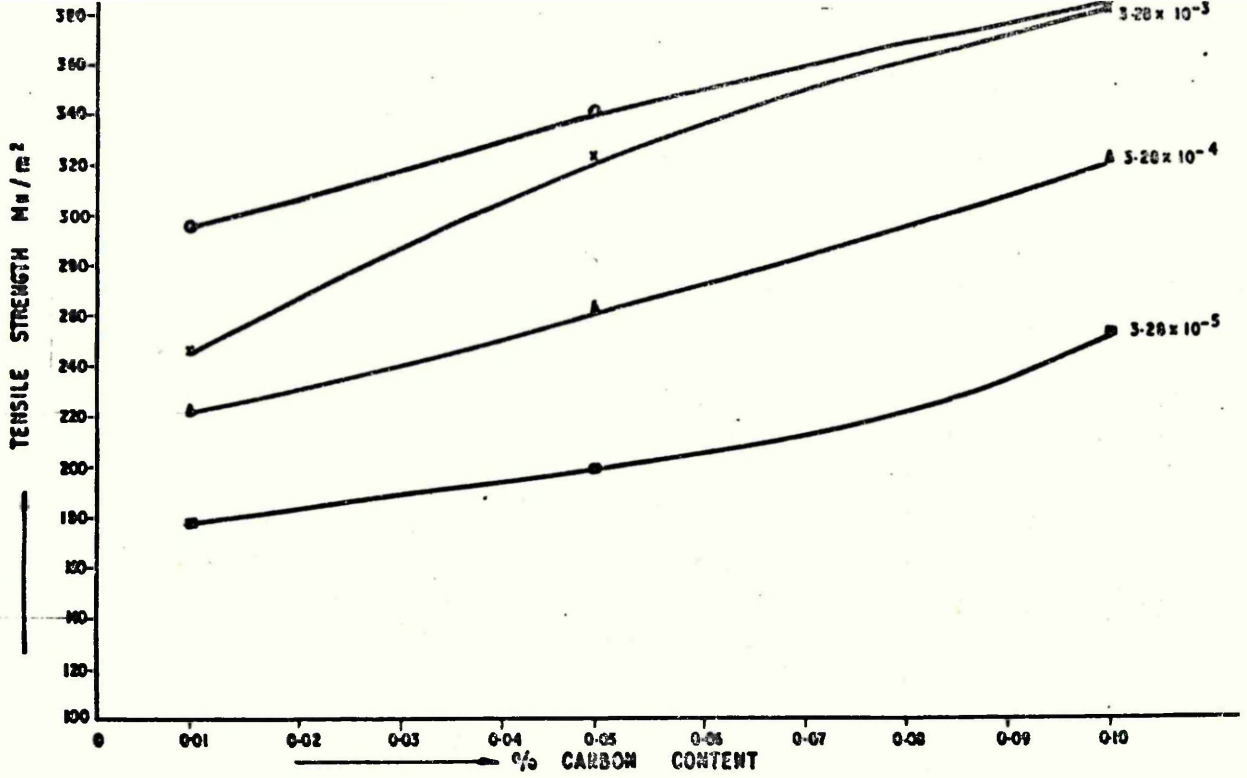

FIG. 64. EFFECT OF Cr 23 C_6 CARBIDE DISTRIBUTION ON TENSILE STRENGTH.

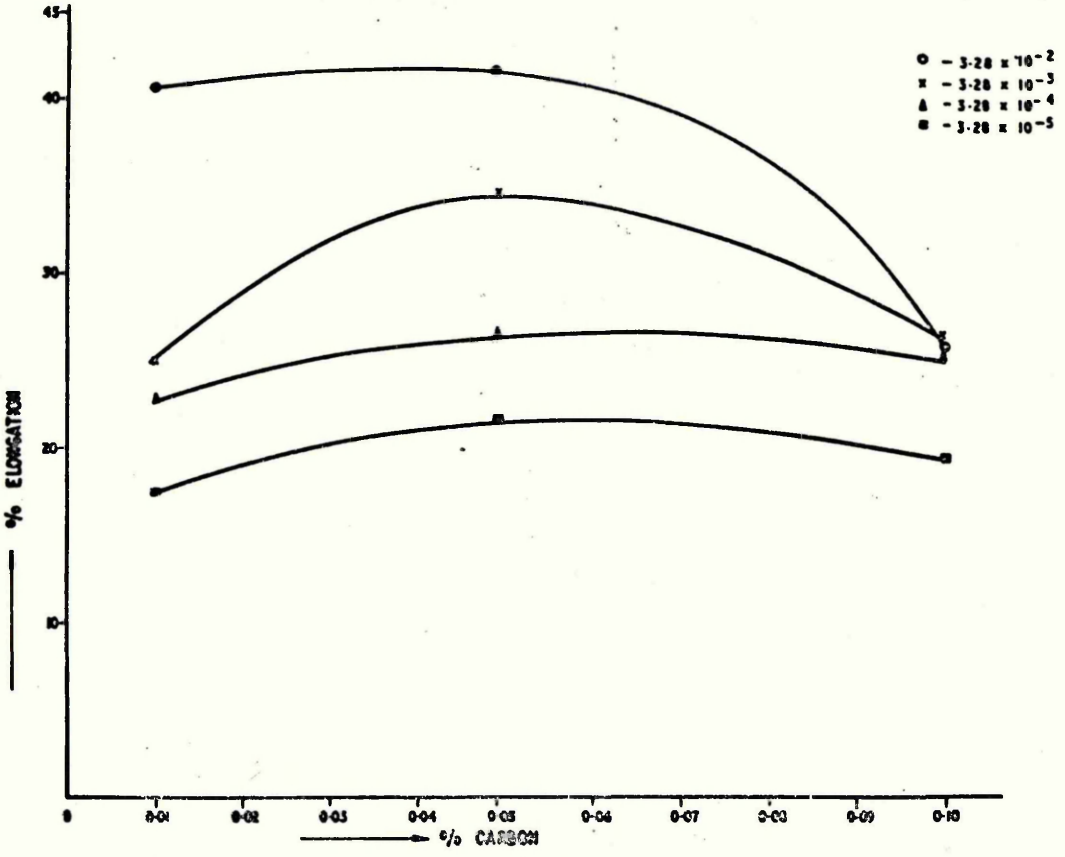

FIG. 65. EFFECT OF Cr 23 C_6 CARBIDE DISTRIBUTION ON HIGH TEMPERATURE DUCTILITY.

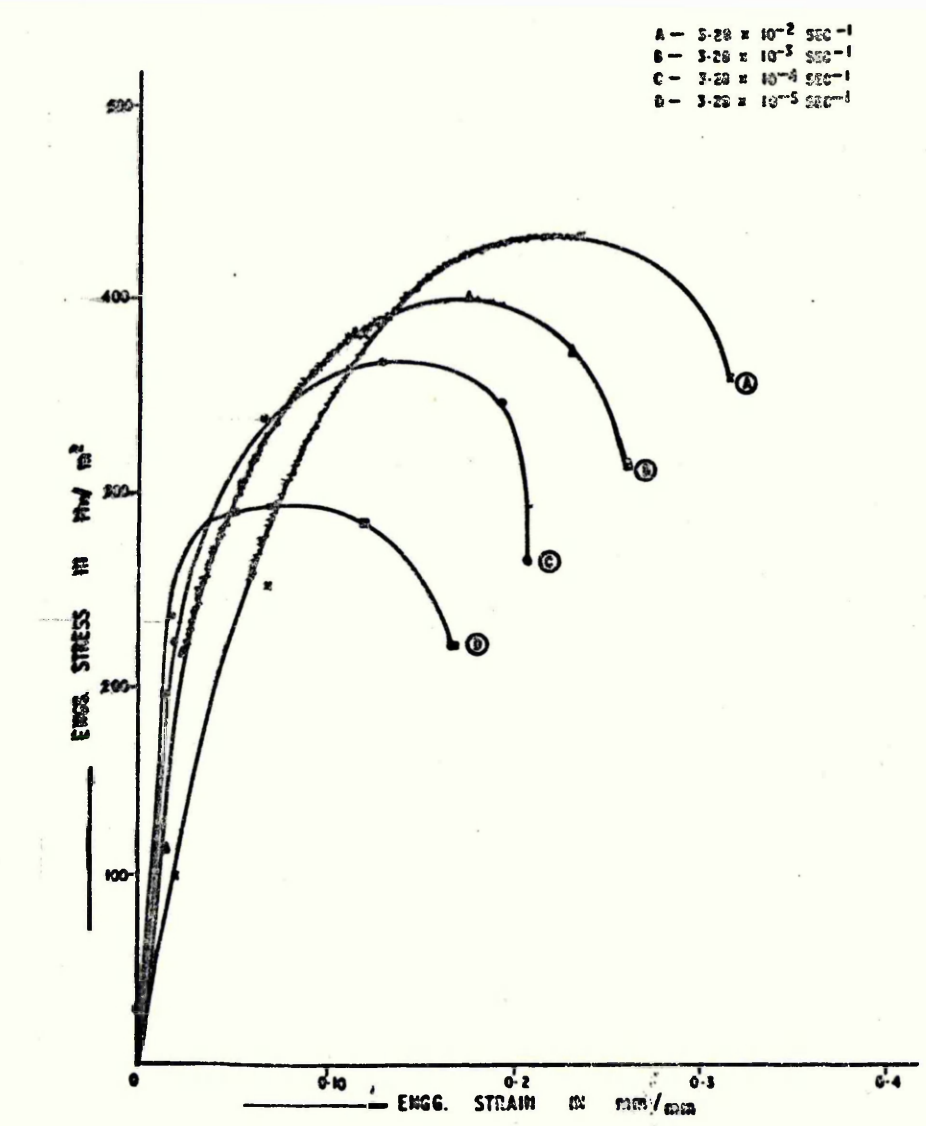

FIG. 66. TENSILE BEHAVIOUR OF HIGH CARBON MOLYBDENUM (ALLOY No. 4)

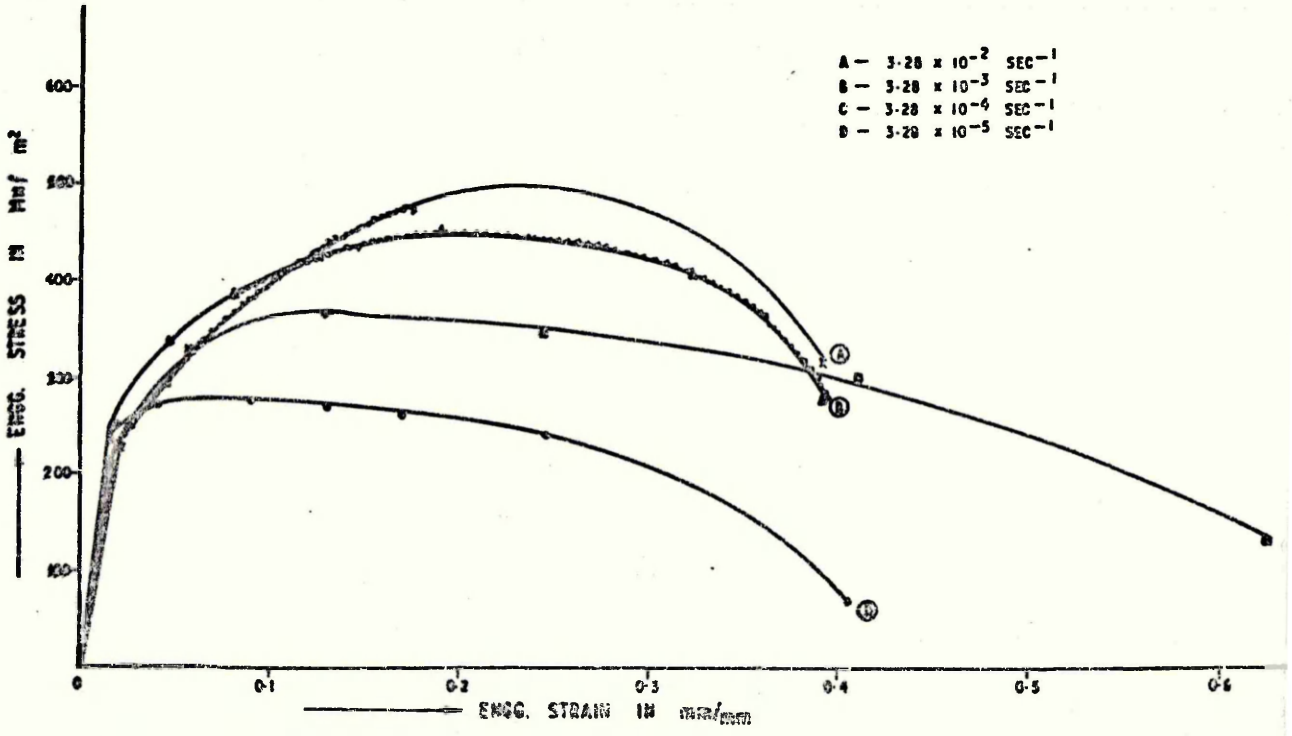

FIG. 67. TENSILE BEHAVIOUR OF HIGH CARBON MOLYBDENUM / TITANIUM CONTAINING ALLOY WITH $M_{23}C_6$ AT GRAIN BOUNDARIES (N.T. No.2) (ALLOY No.5)

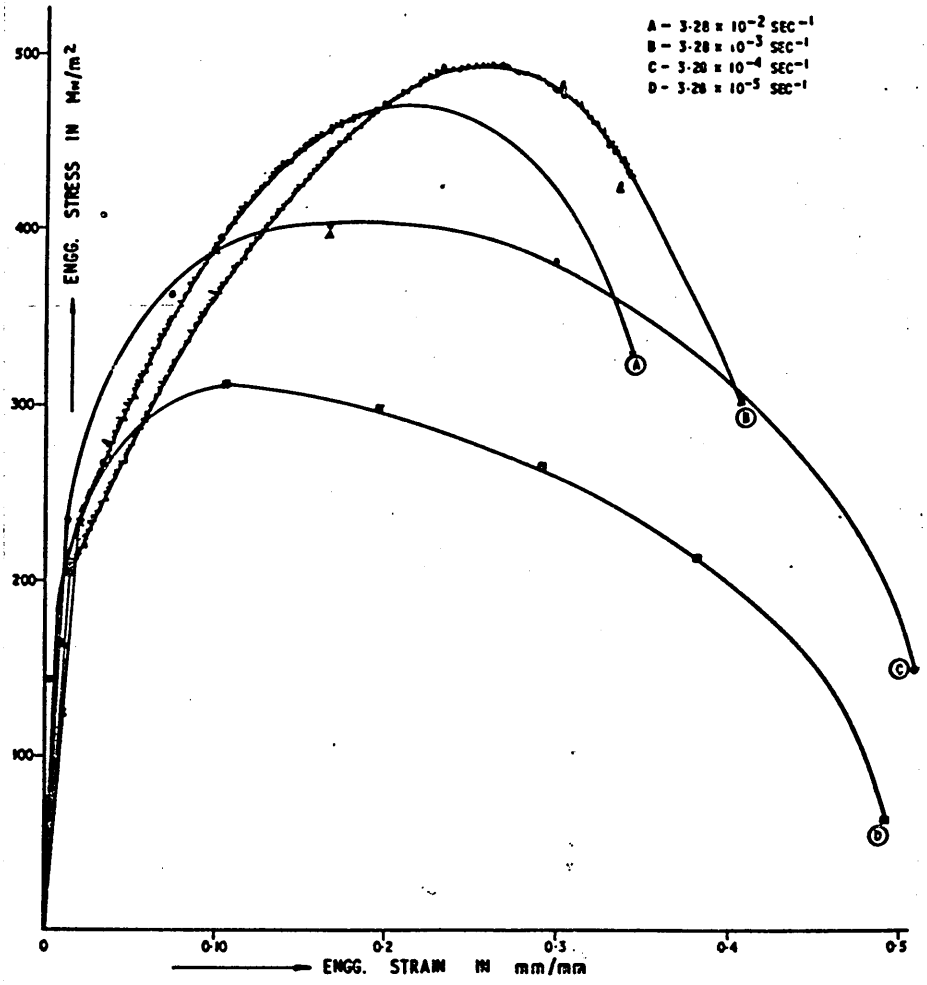

FIG. 68 HIGH CARBON MOLYBDENUM/TITANIUM BEARING ALLOY CONTAINING $M_{23}C_6$/TiC AT GRAINBOUNDARIES. (H.T. No. 1) ALLOY No. 5.

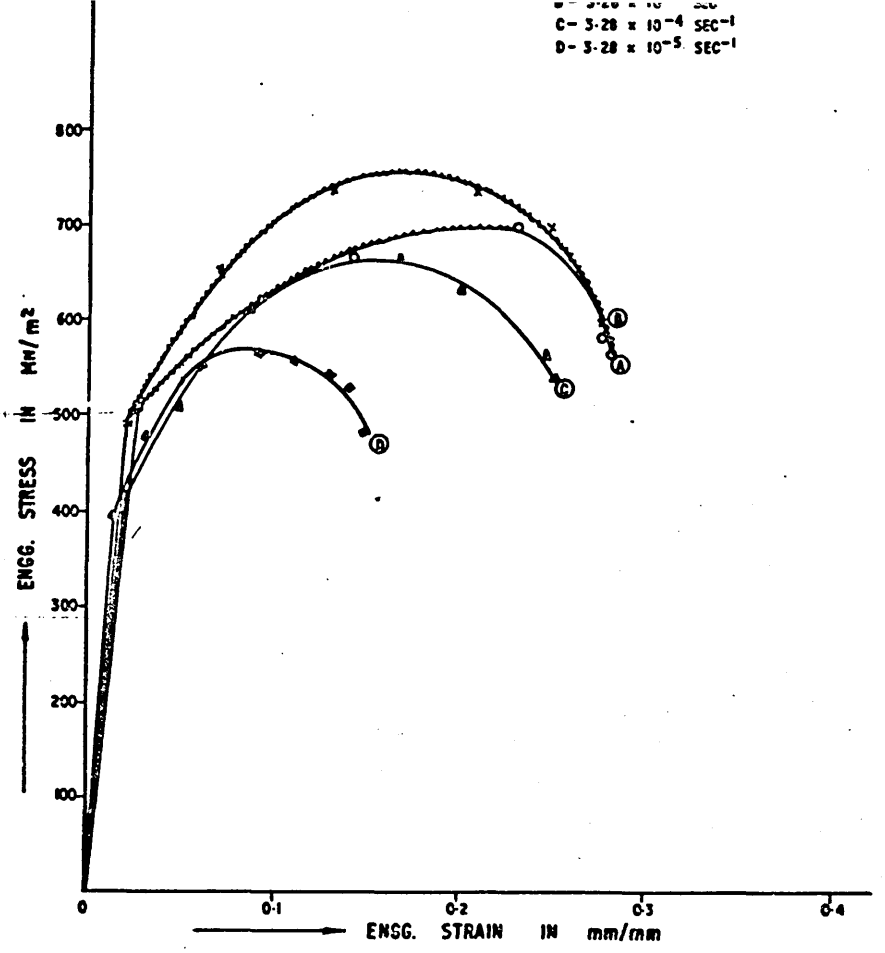

FIG. 69 LOW CARBON PE 16 CONTAINING γ' ZONES. (H.T. No.1)
ALLOY No. 7.

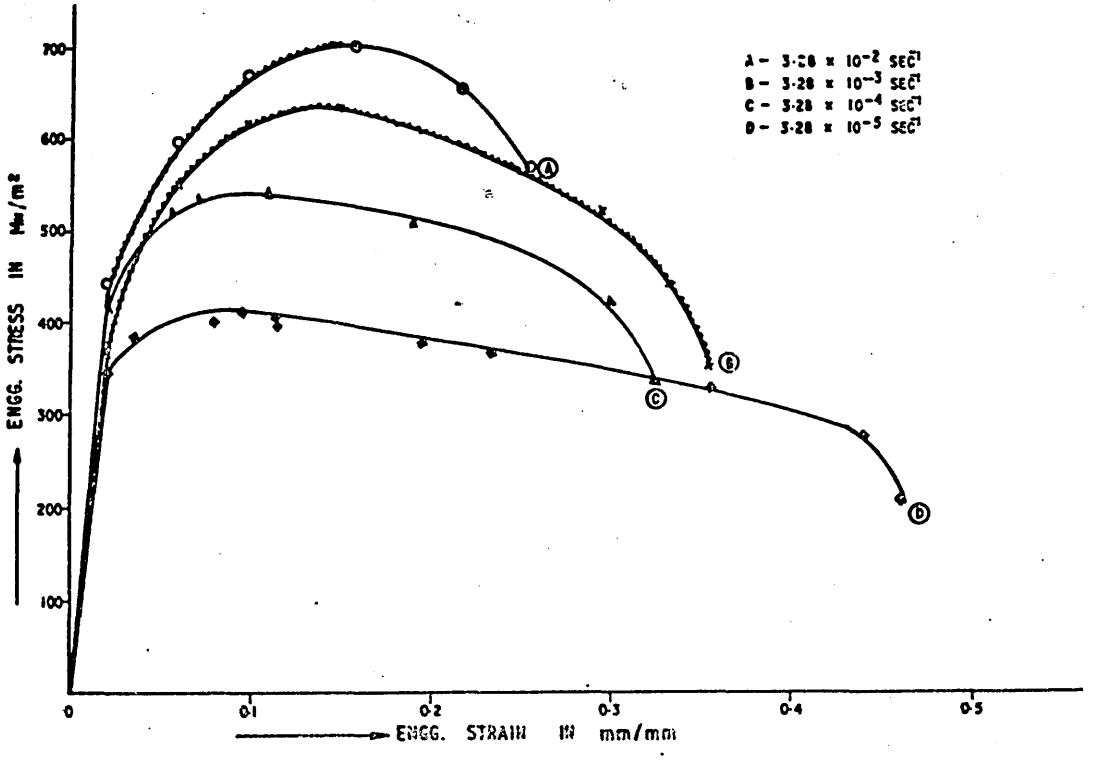

FIG. 70 LOW CARBON P.E.16 CONTAINING SEMICOHERENT γ' PARTICLES (H.T. No.2)
ALLOY No. 7

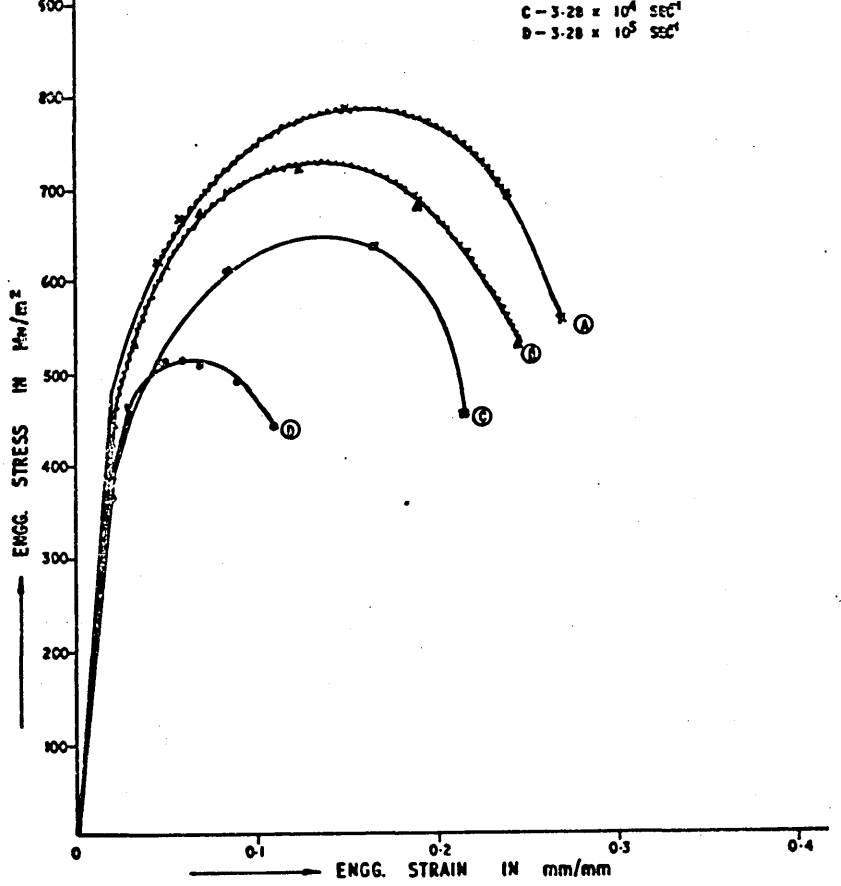

FIG. 71. HIGH CARBON PE 16 ALLOY CONTAINING γ' ZONES (H.T No. 1.) ALLOY No 8.

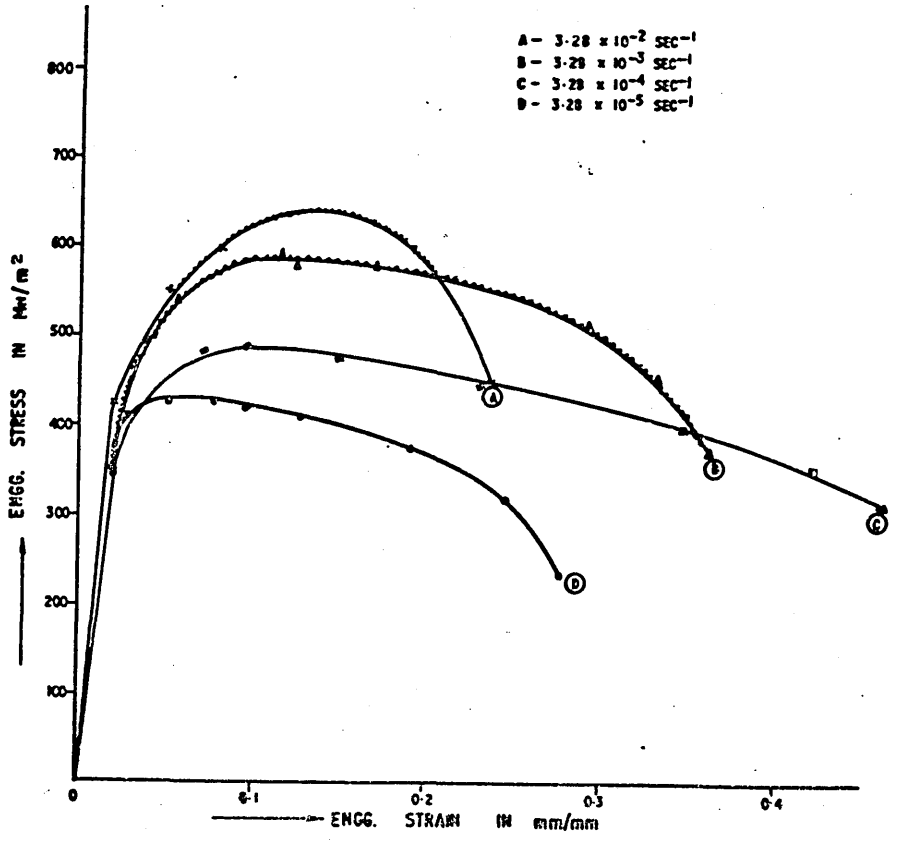

FIG. 72 HIGH CARBON PE. 16 ALLOY CONTAINING SEMICOHERENT γ' (H.T. No. 2) ALLOY No 8.

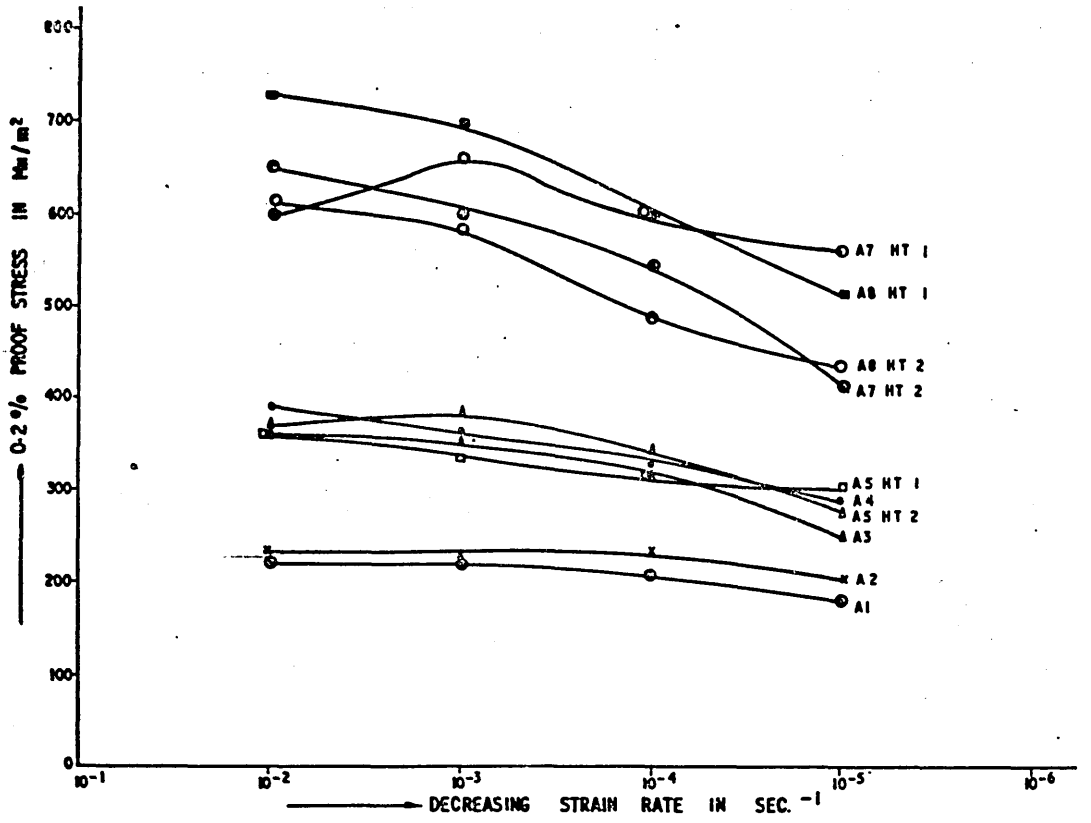

FIG. 73. STRAIN RATE SENSITIVITY OF 0·2% PROOF STRESS AT 700°C.

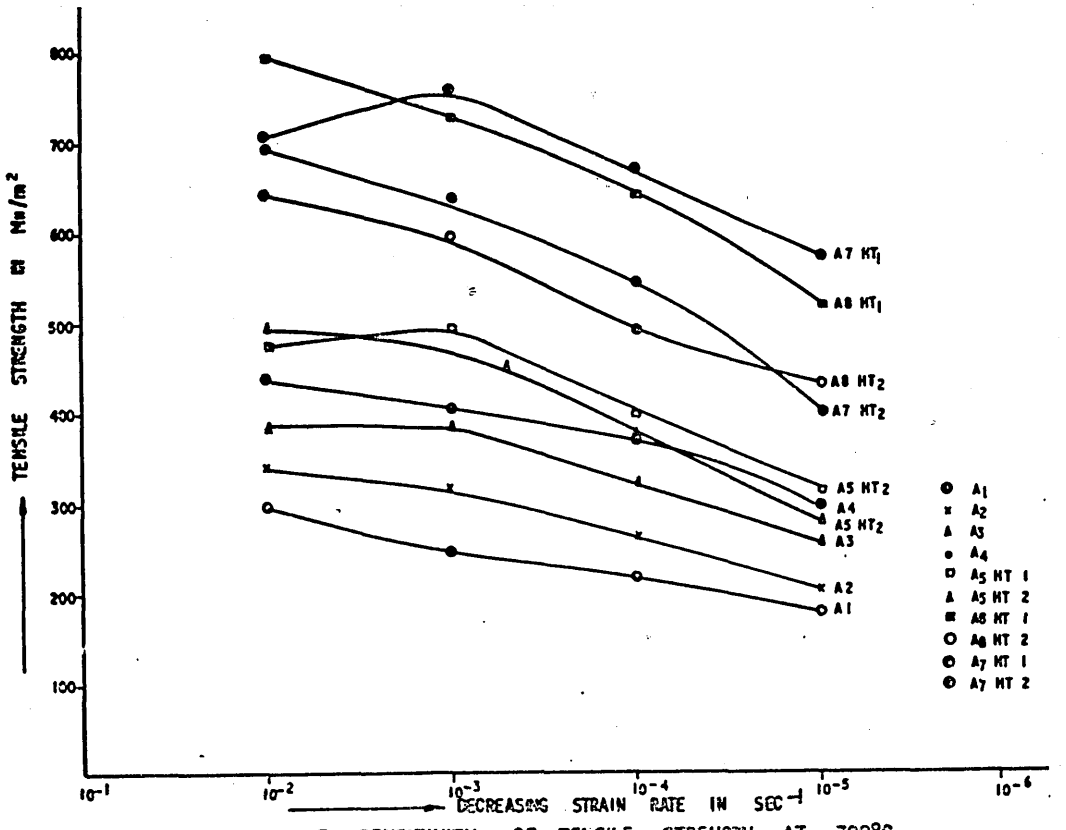

FIG. 74 STRAIN RATE SENSITIVITY OF TENSILE STRENGTH AT 700°C.

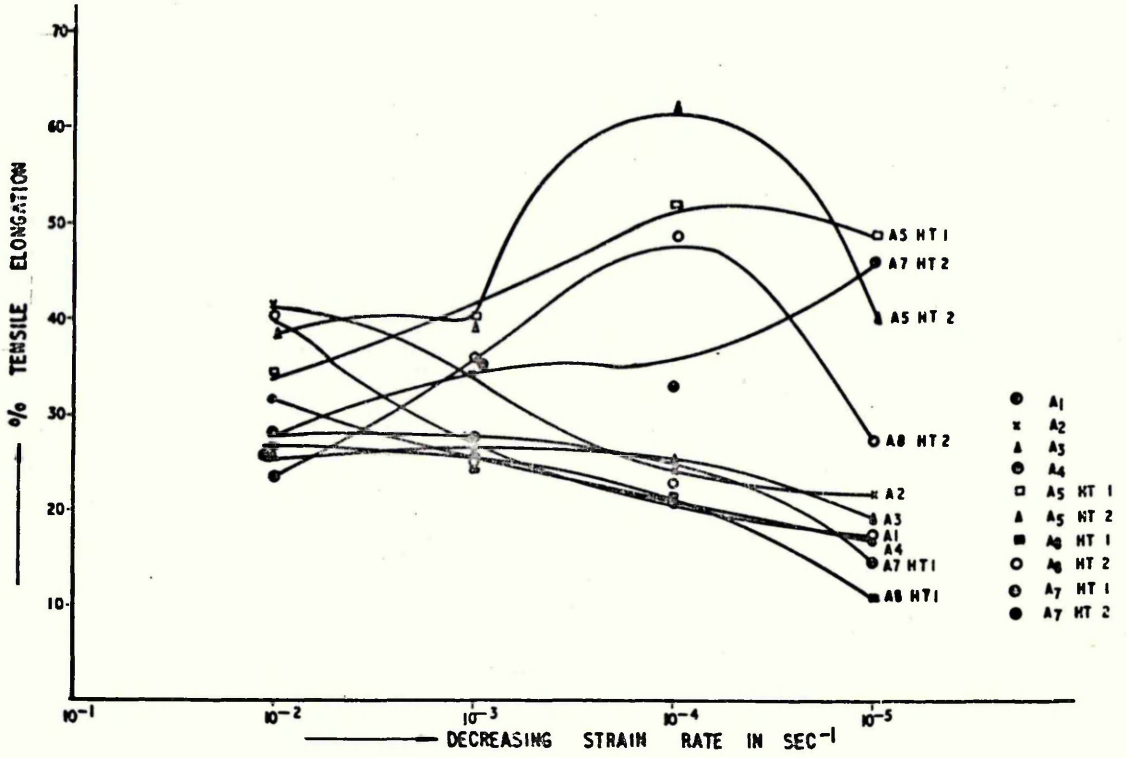

FIG. 75. STRAIN RATE SENSITIVITY OF TENSILE DUCTILITY AT 700° C.

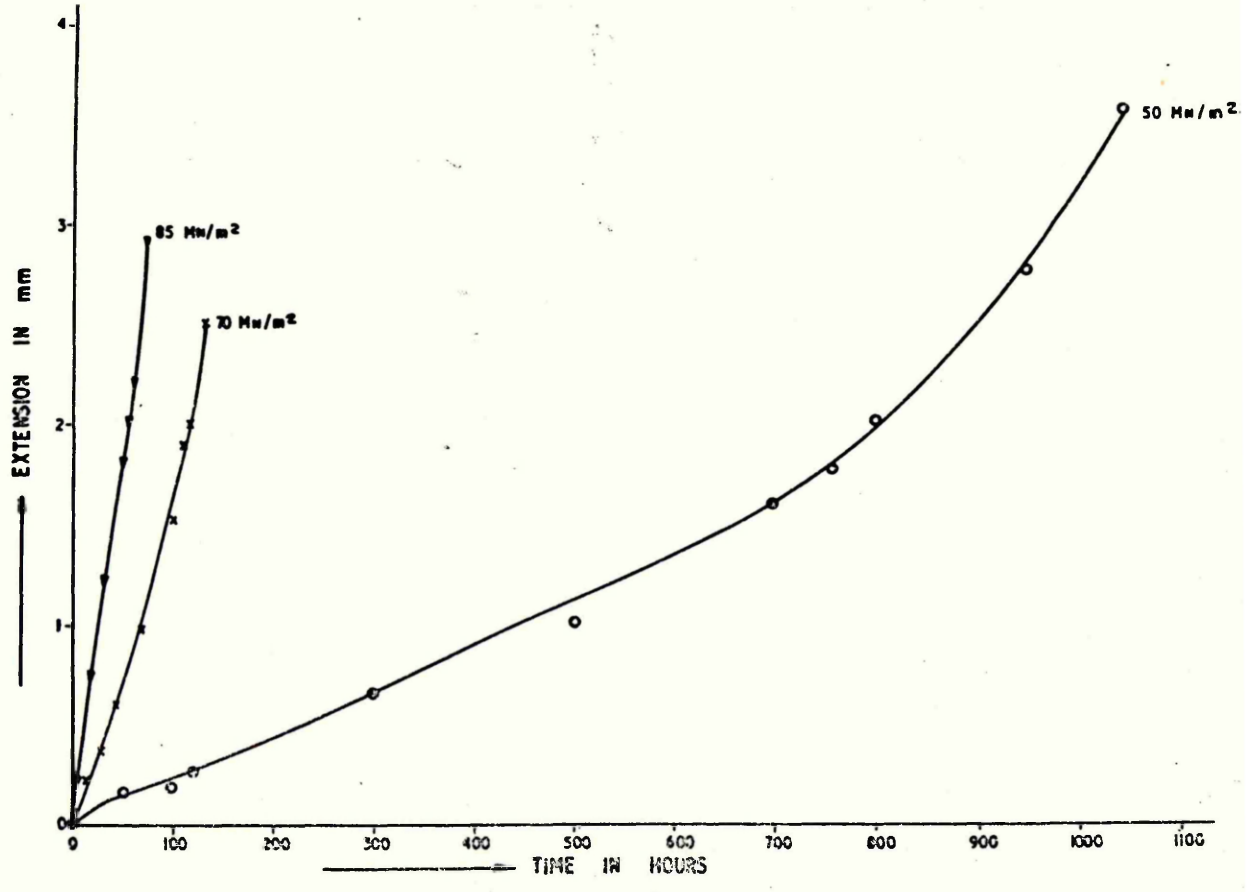

FIG. 76. CREEP BEHAVIOUR OF LOW CARBON BASE COMPOSITION AT 700°C.

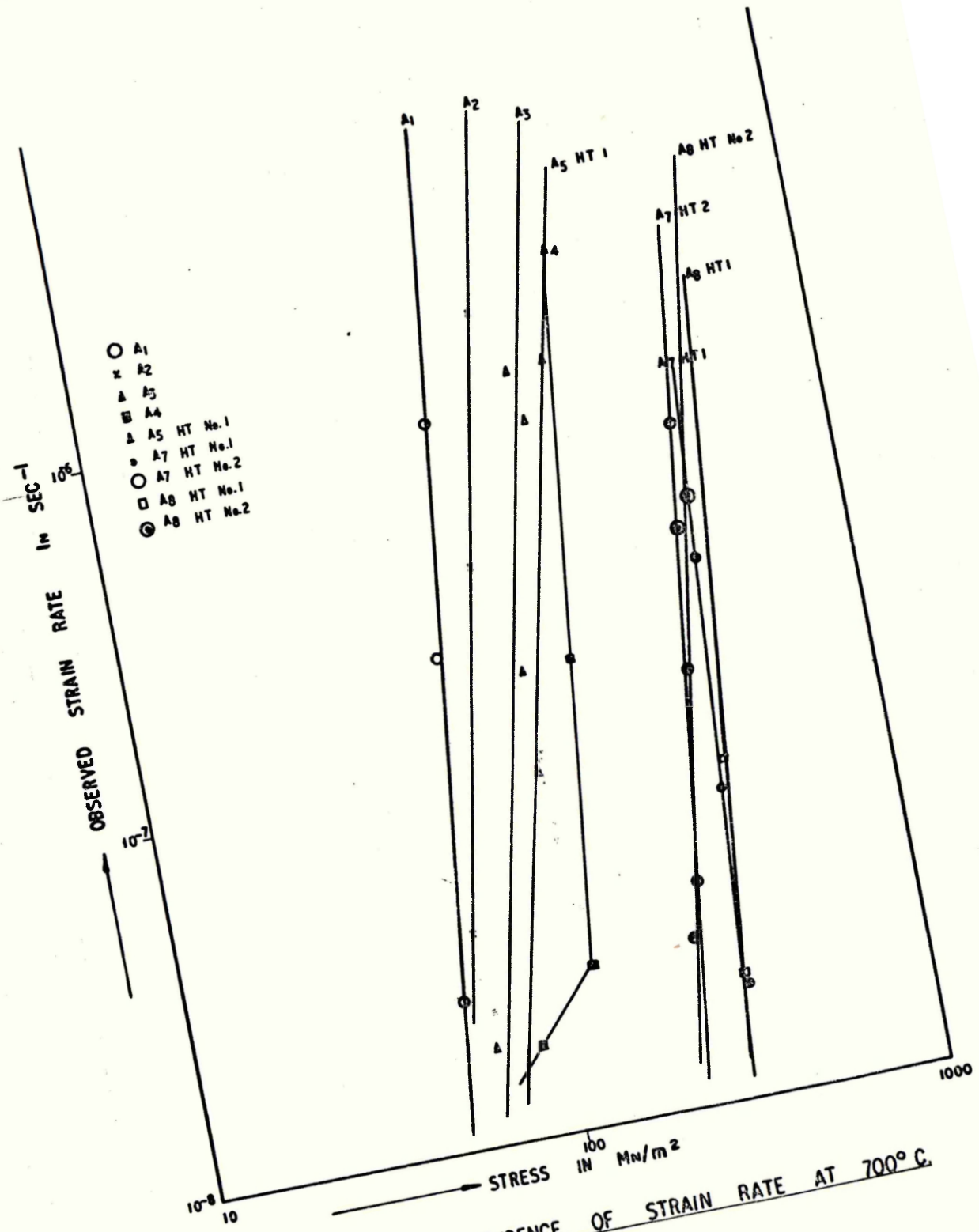

FIG. 77 STRESS DEPENDENCE OF STRAIN RATE AT 700° C.

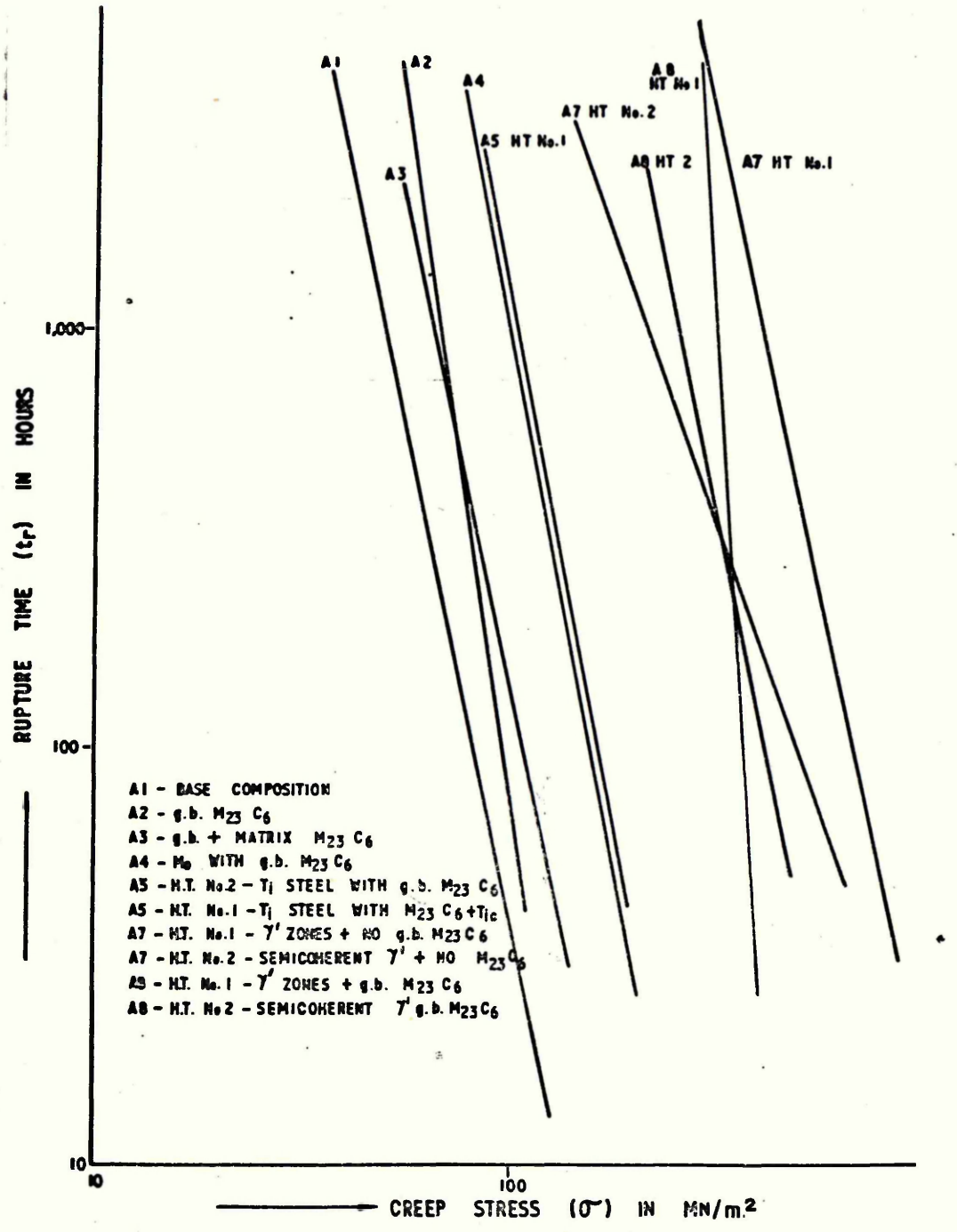

FIG. 78 STRESS EXPONENT FOR ALL ALLOYS AT 700°C.

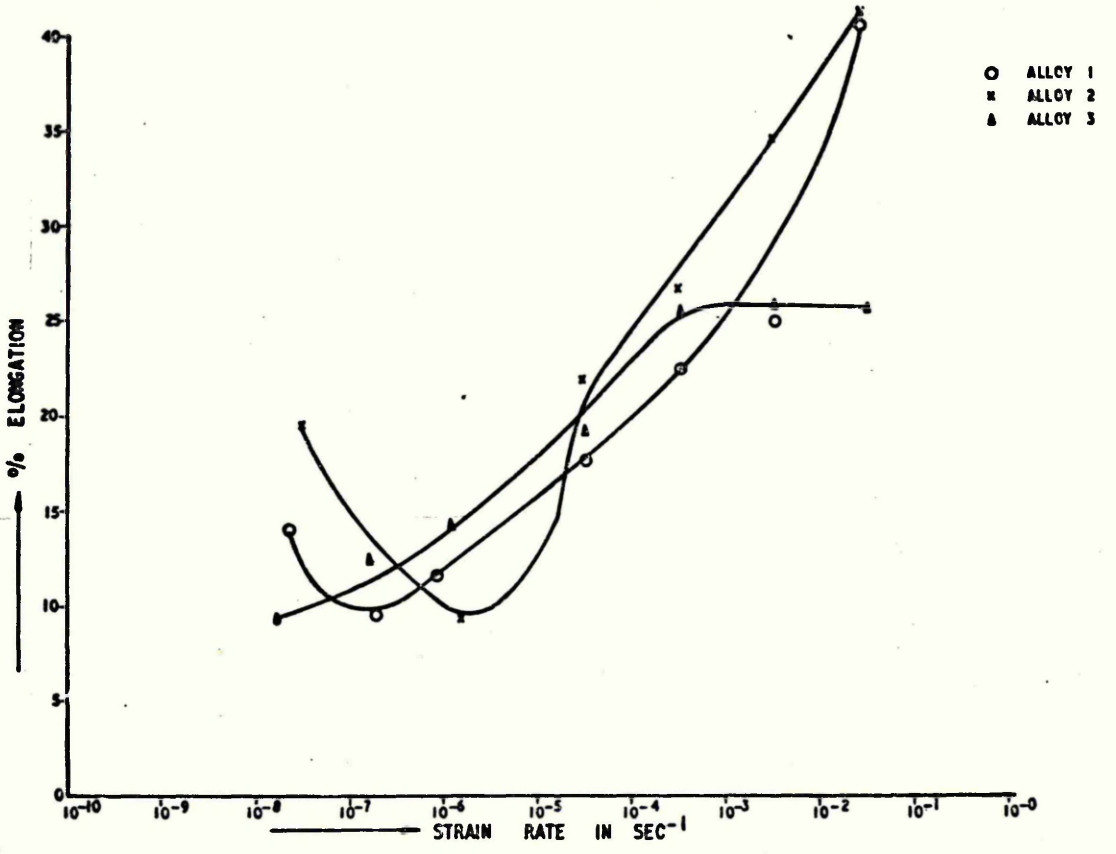

FIG. 79.(a) CARBON VARIATIONS IN BASE COMPOSITION.

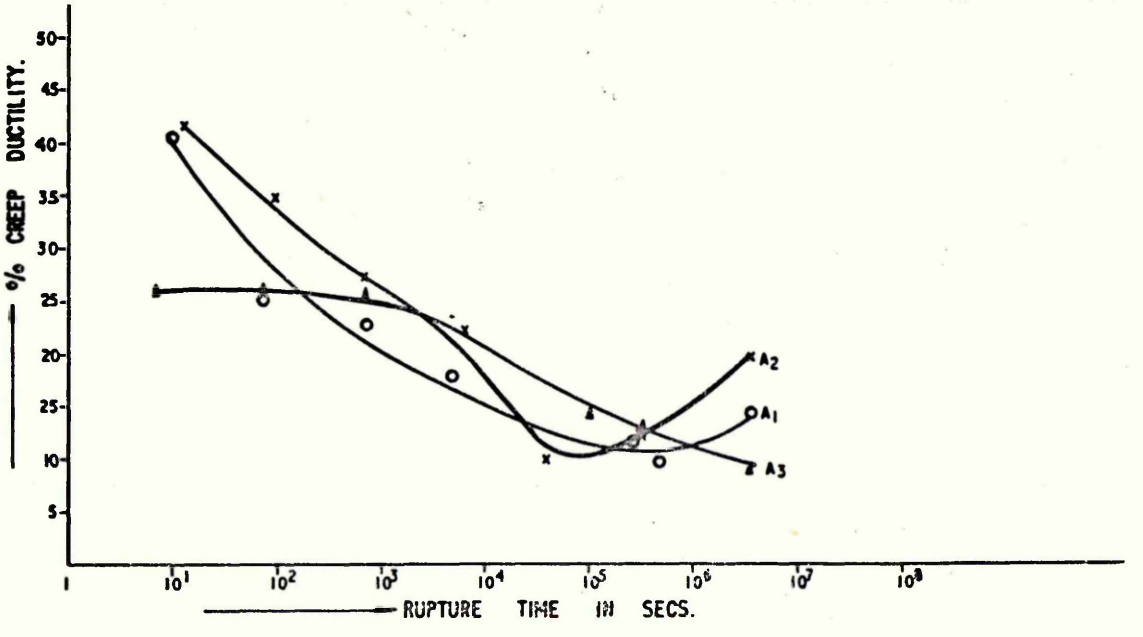

FIG. 79 (b) RUPTURE TIME v/s CREEP DUCTILITY FOR ALLOYS CONTAINING Cr.23 C6.

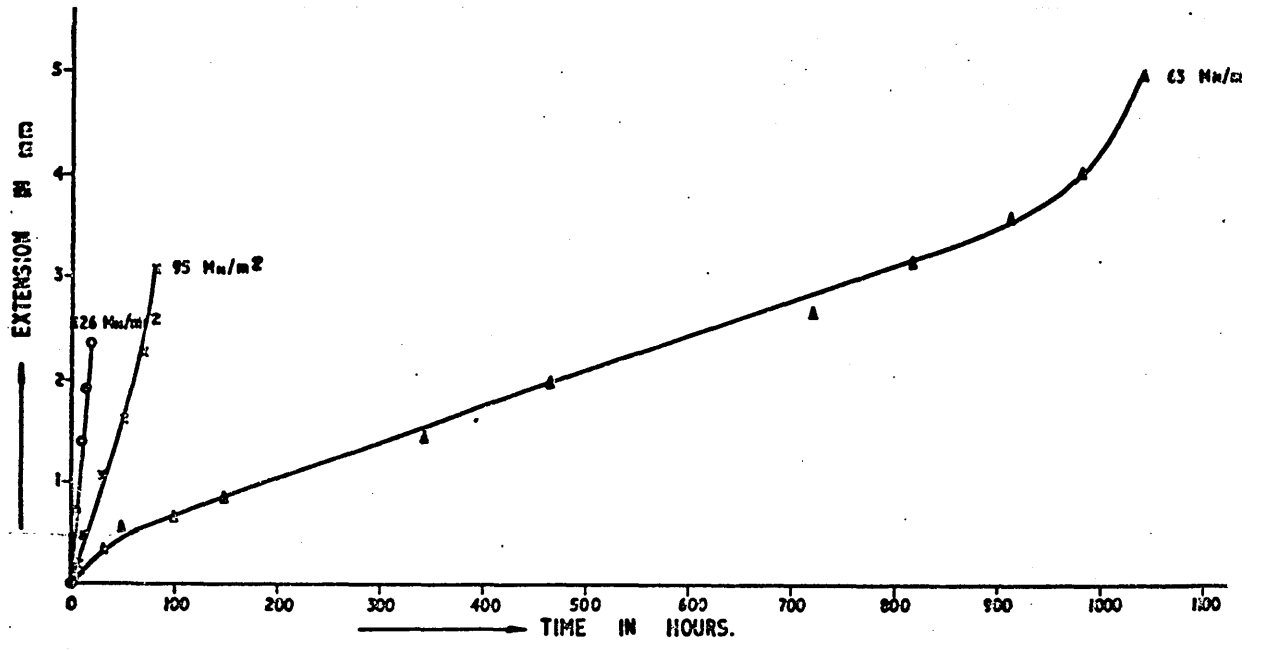

FIG. 80 CREEP BEHAVIOUR OF MEDIUM CARBON BASE COMPOSITION AT 700°C.

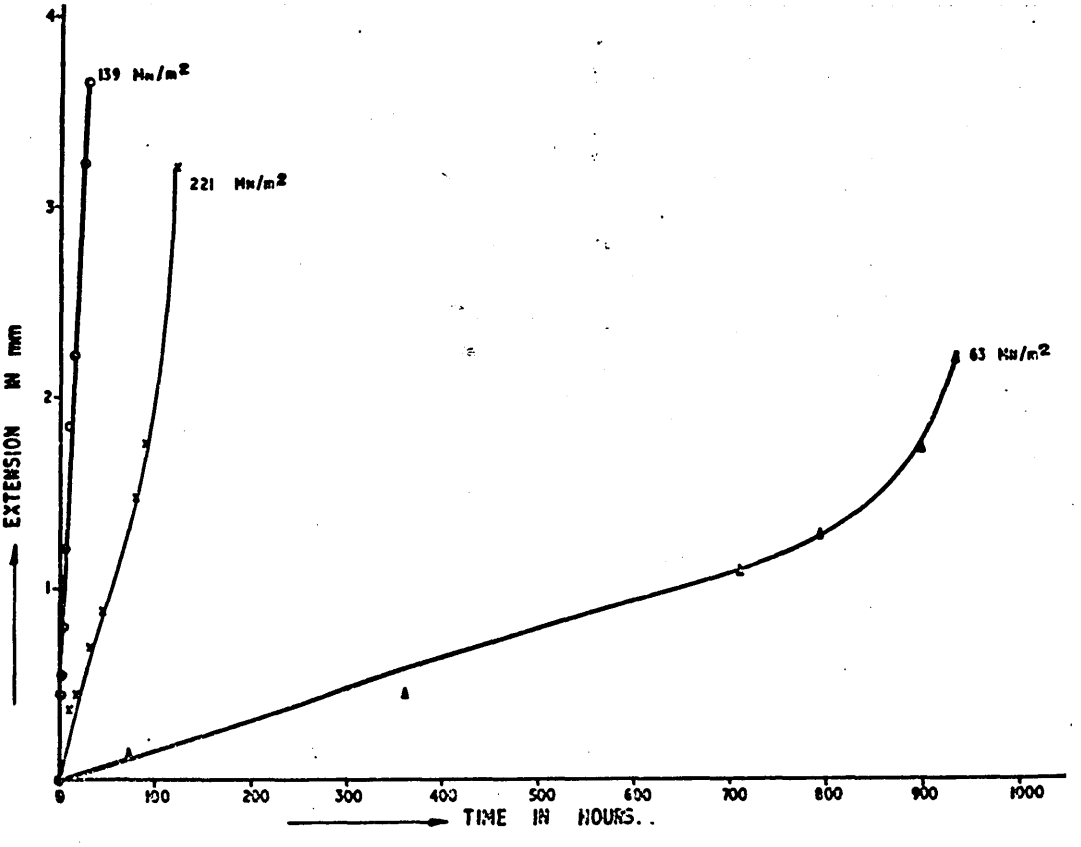

FIG. 81 CREEP BEHAVIOUR OF HIGH CARBON BASE COMPOSITION AT 700°C.

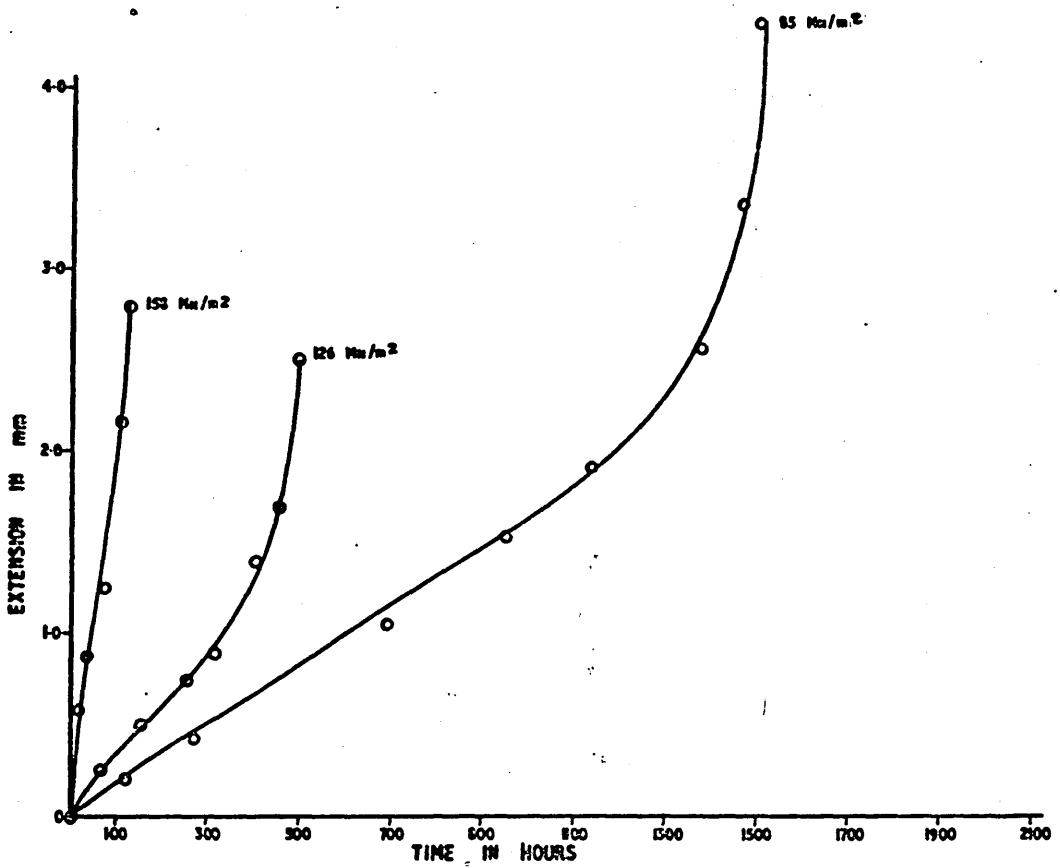

FIG. 82 CREEP BEHAVIOUR OF HIGH CARBON MOLYBDENUM BEARING ALLOY AT 700°C.

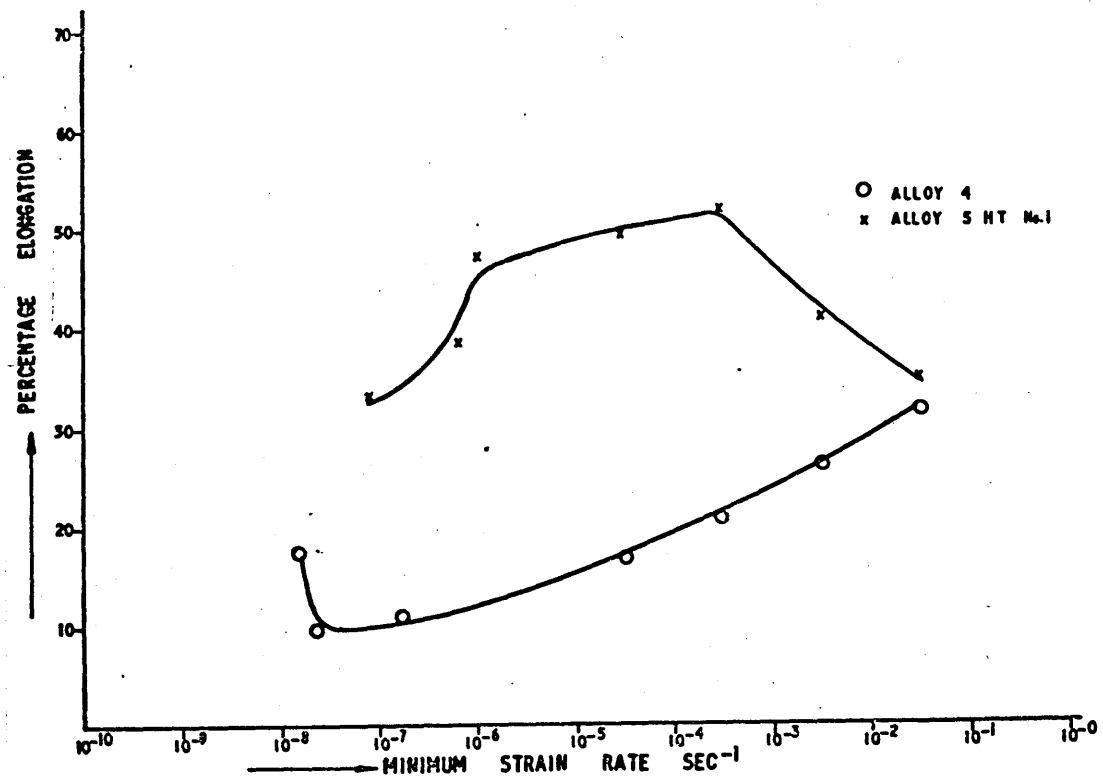

FIG. 83 (a) MOLYBDENUM AND TITANIUM EFFECT.

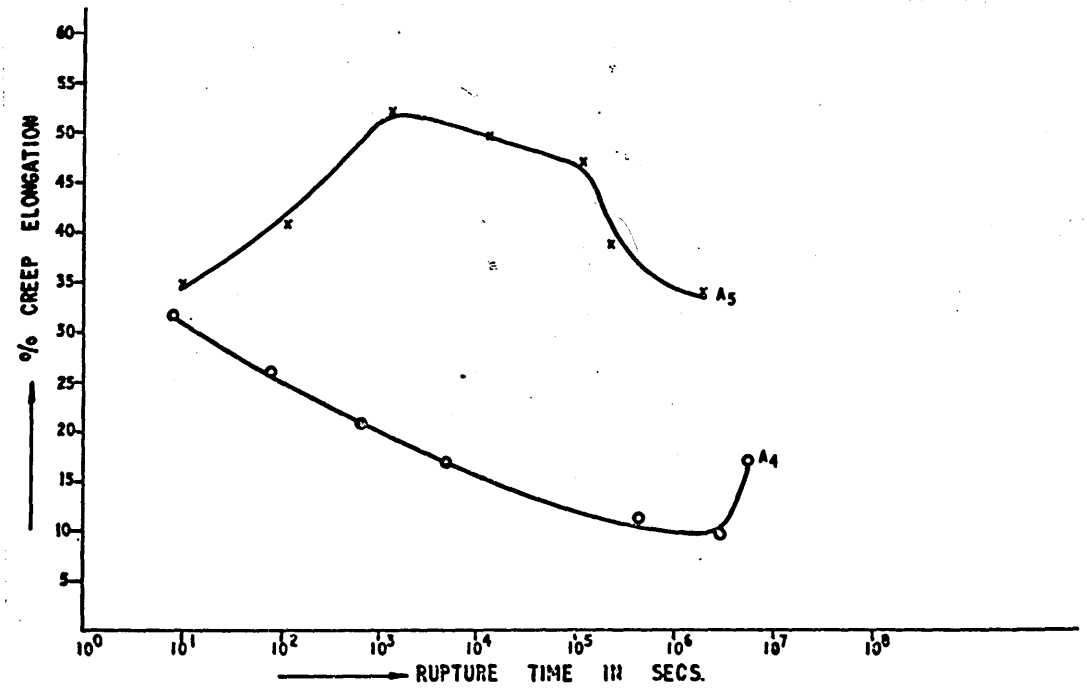

FIG. 83 (b) RUPTURE TIME v/s CREEP ELONGATION EFFECT OF MOLYBDENUM AND TITANIUM.

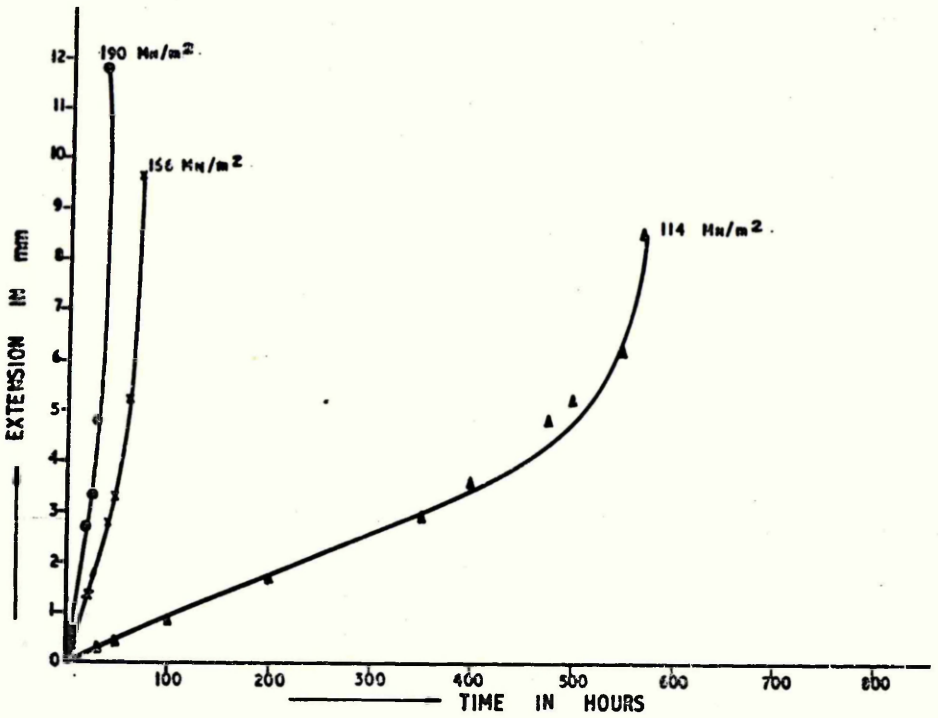

FIG. 84. CREEP BEHAVIOUR OF M_o/T_i ALLOY AT 700°C.

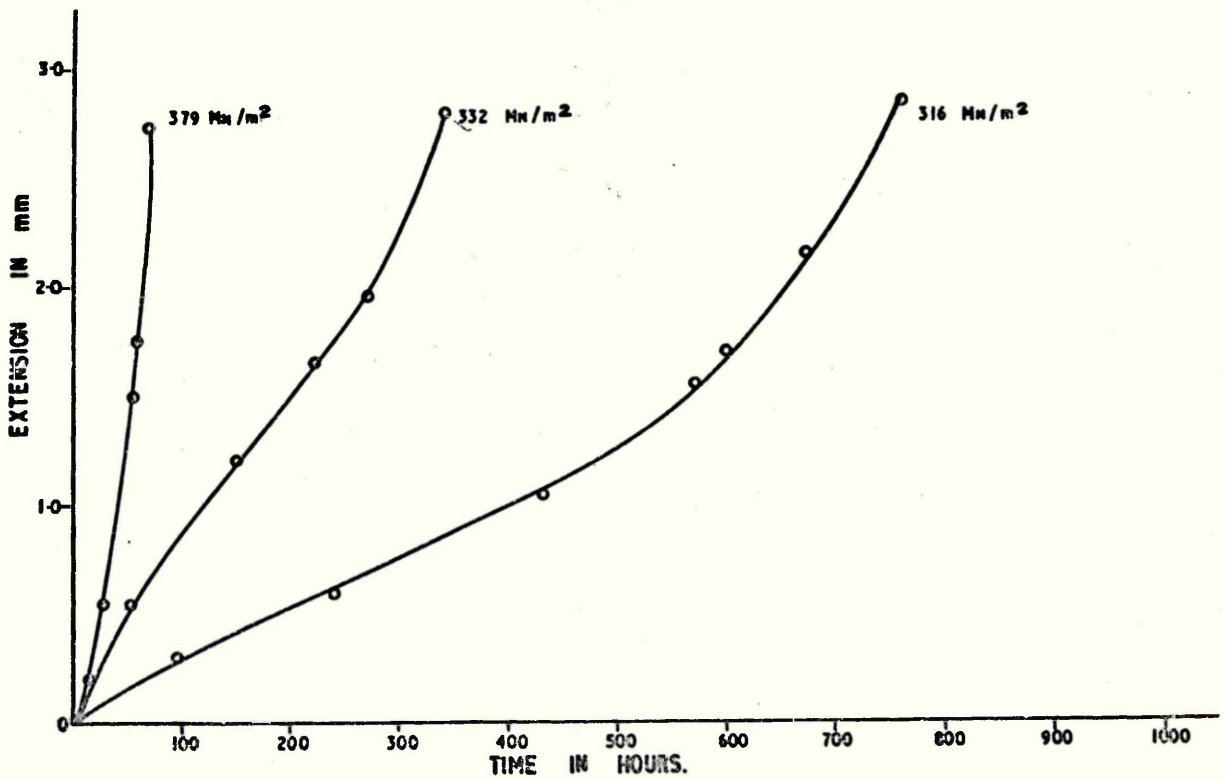

FIG. 85 CREEP BEHAVIOUR OF LOW CARBON PE 16 CONTAINING γ' ZONES AT 700°C.

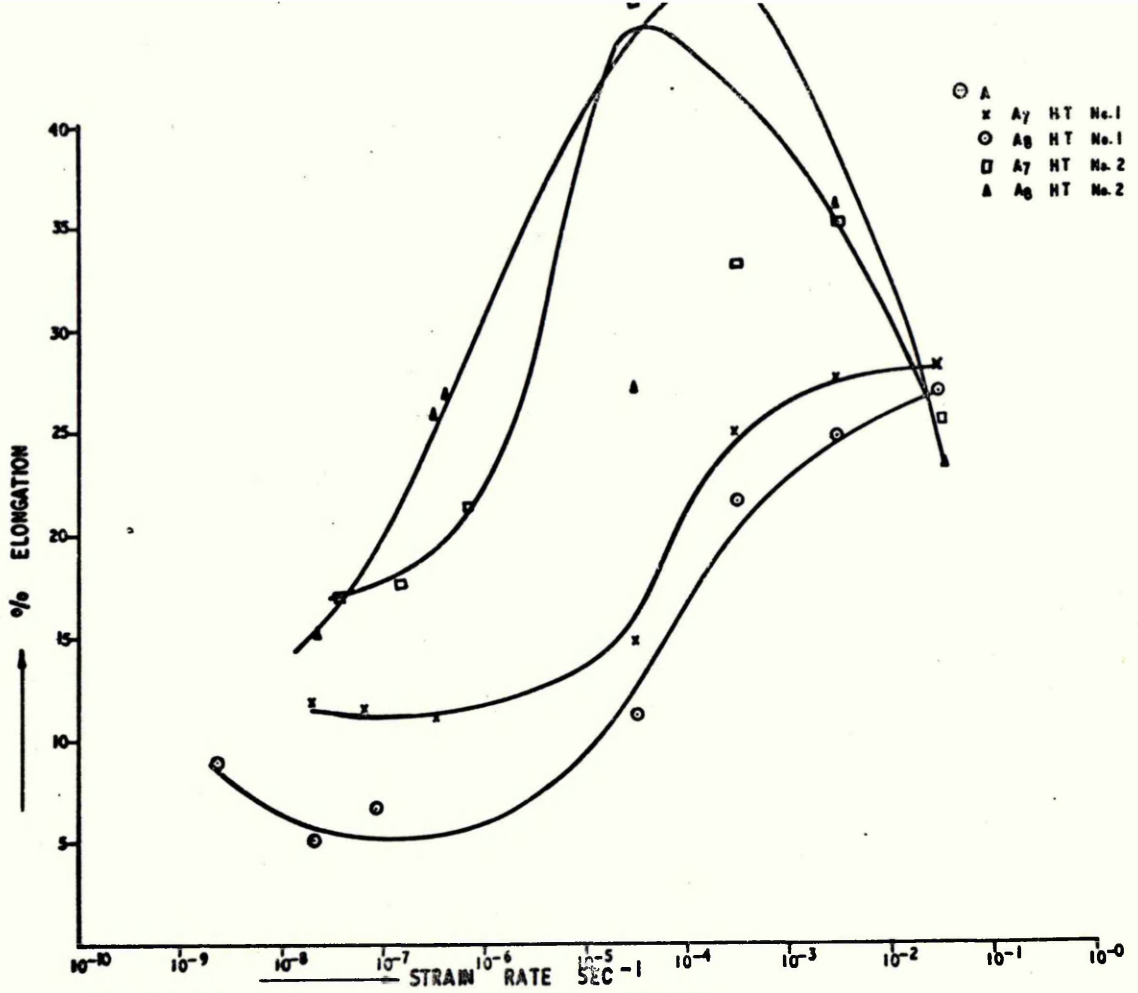

FIG. 86 (a) GAMMA PRIME FORMING ALLOYS.

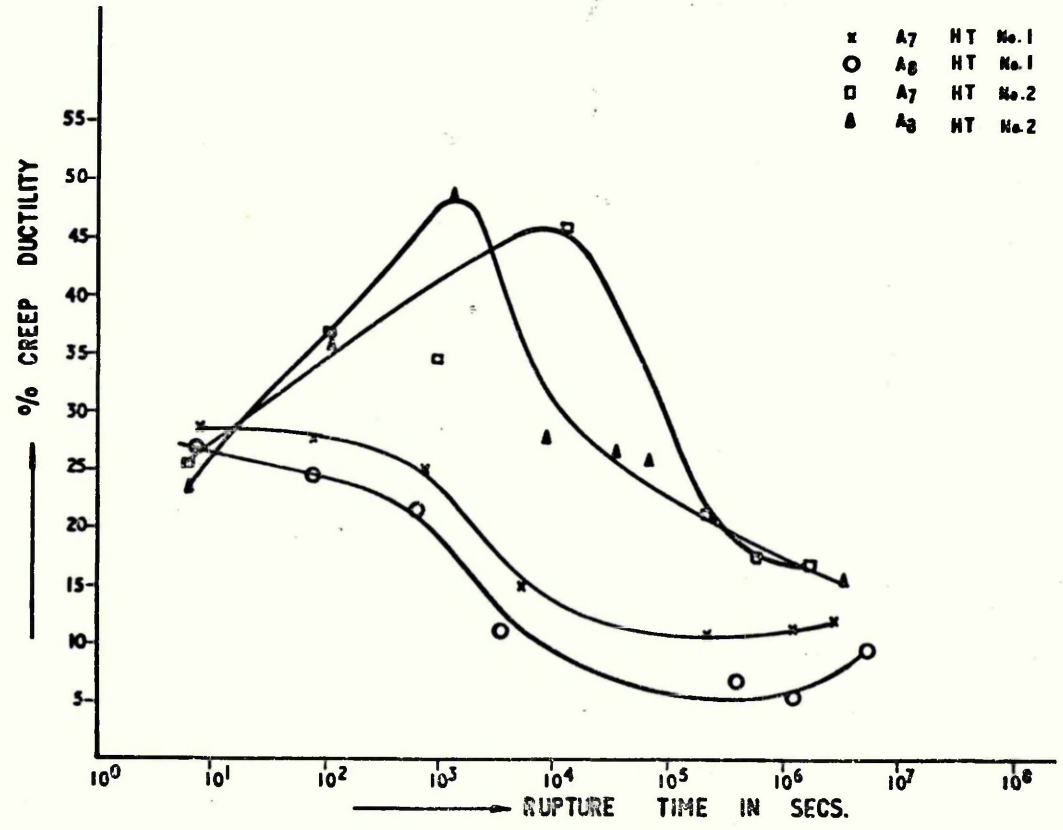

FIG. 86 (b) γ' FORMING ALLOYS.

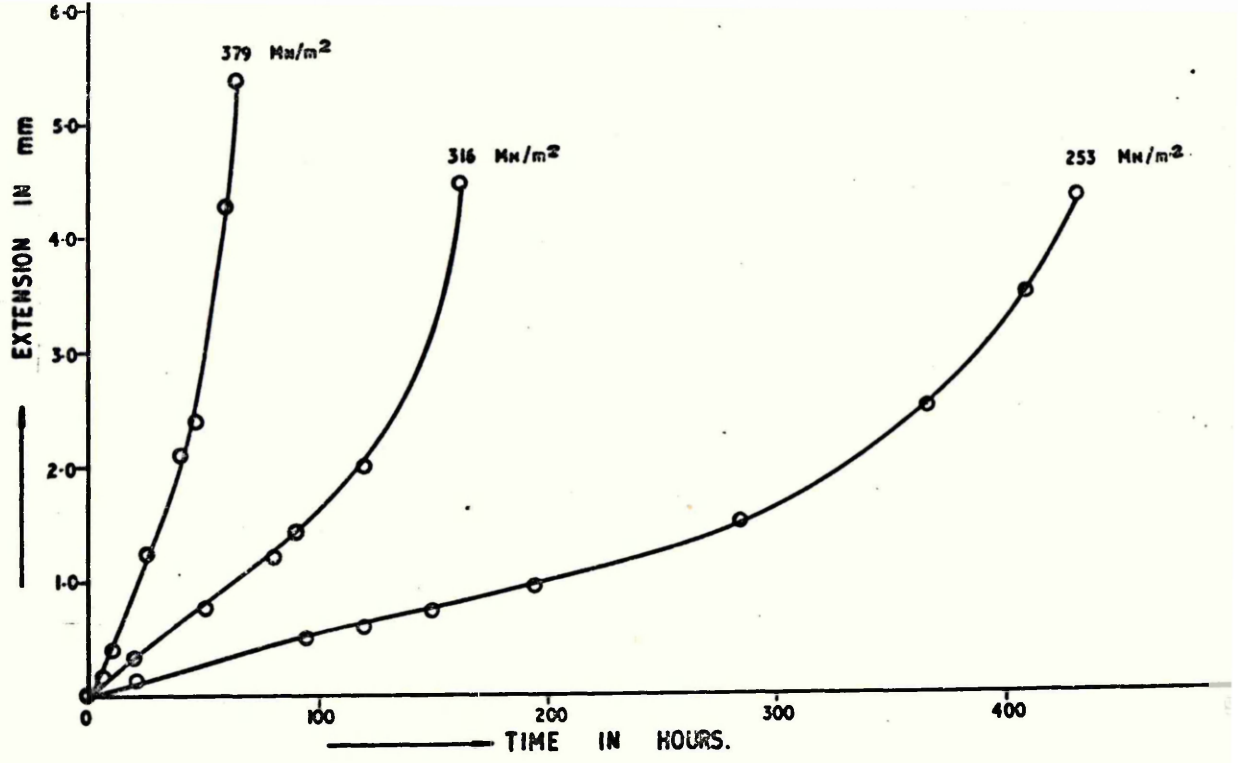

FIG. 87. CREEP BEHAVIOUR OF LOW CARBON PE16 CONTAINING SEMICOHERENT γ' AT 700°C.

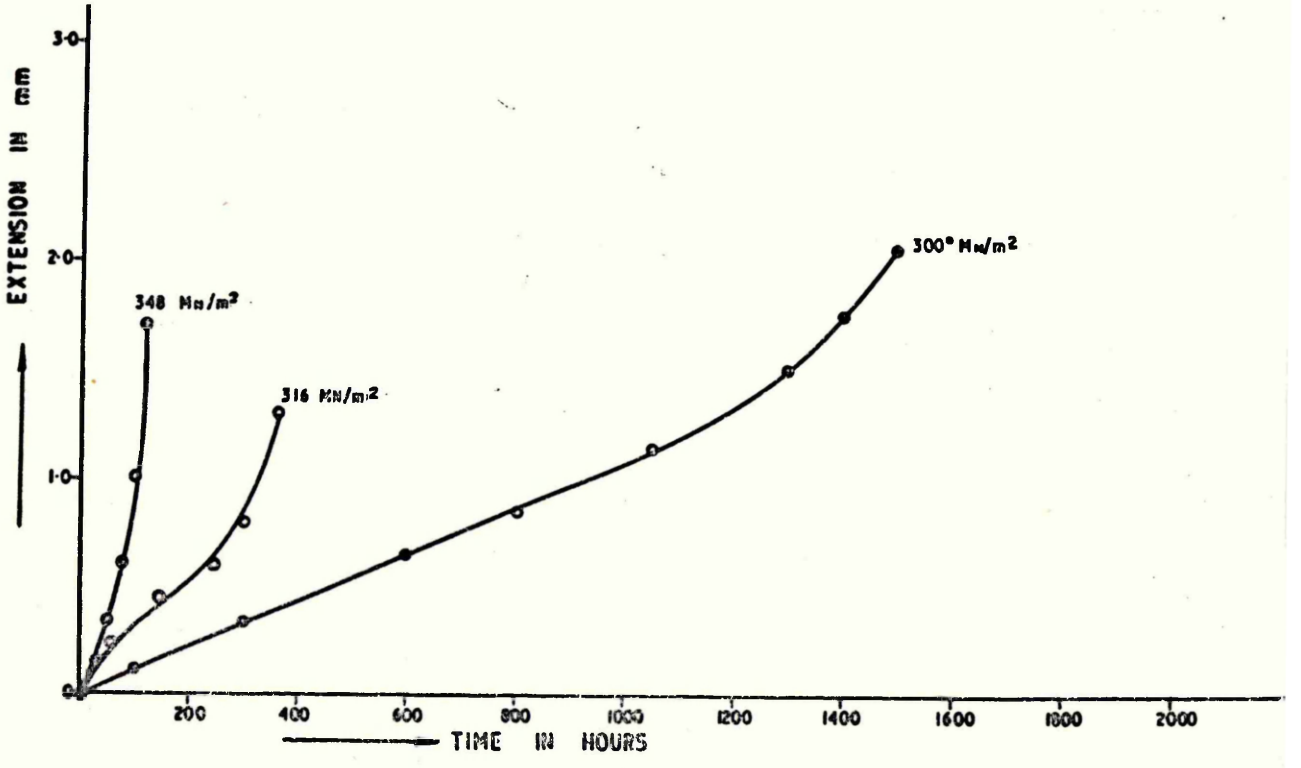

FIG. 88. CREEP BEHAVIOUR OF HIGH CARBON PE16 CONTAINING γ' ZONES AT 700°

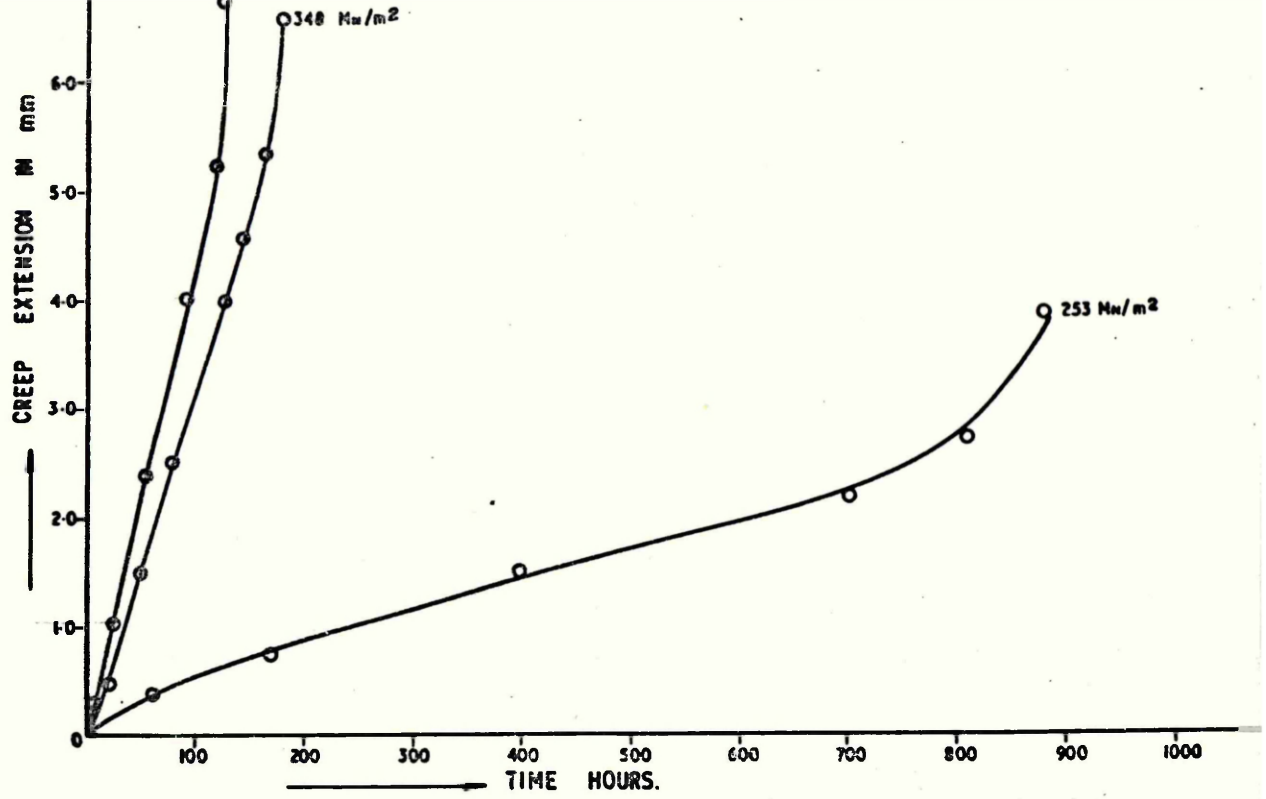

FIG. 89. CREEP BEHAVIOUR OF HIGH CARBON PE 16 CONTAINING SEMICOHERE
γ' AT 700° C.

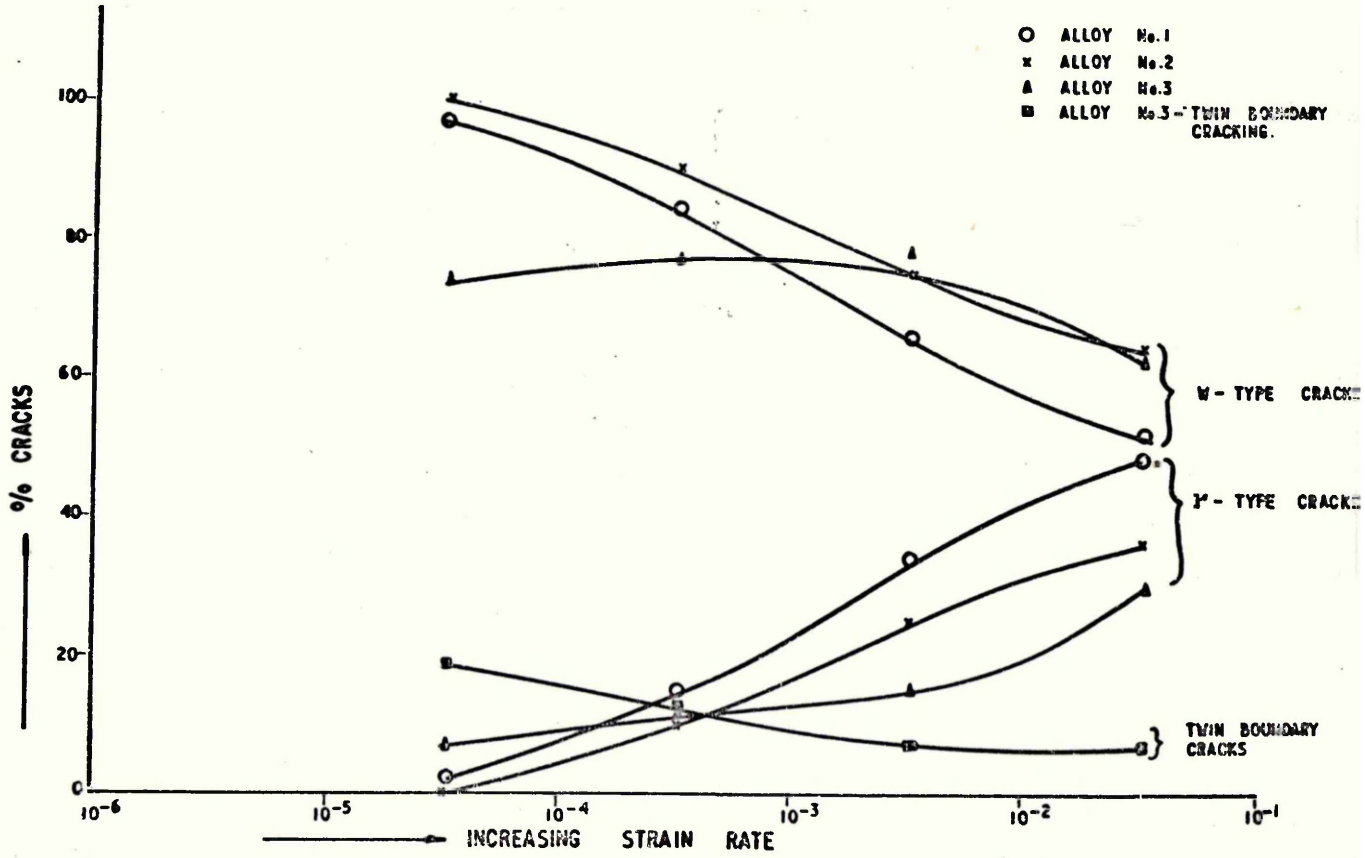

FIG. 90 NATURE OF CRACKS IN $Cr_{23}C_6$ FORMING ALLOYS.

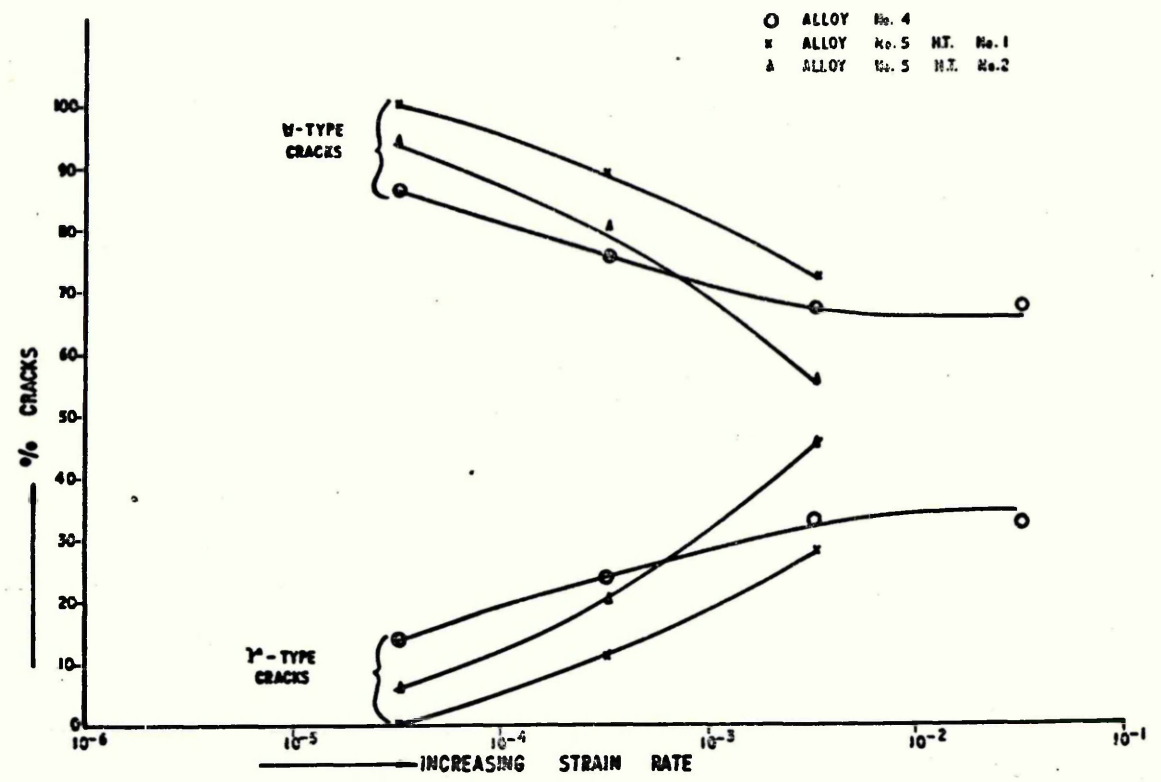

FIG. 91 EFFECT OF Mo/Ti ON NATURE OF CRACKING.

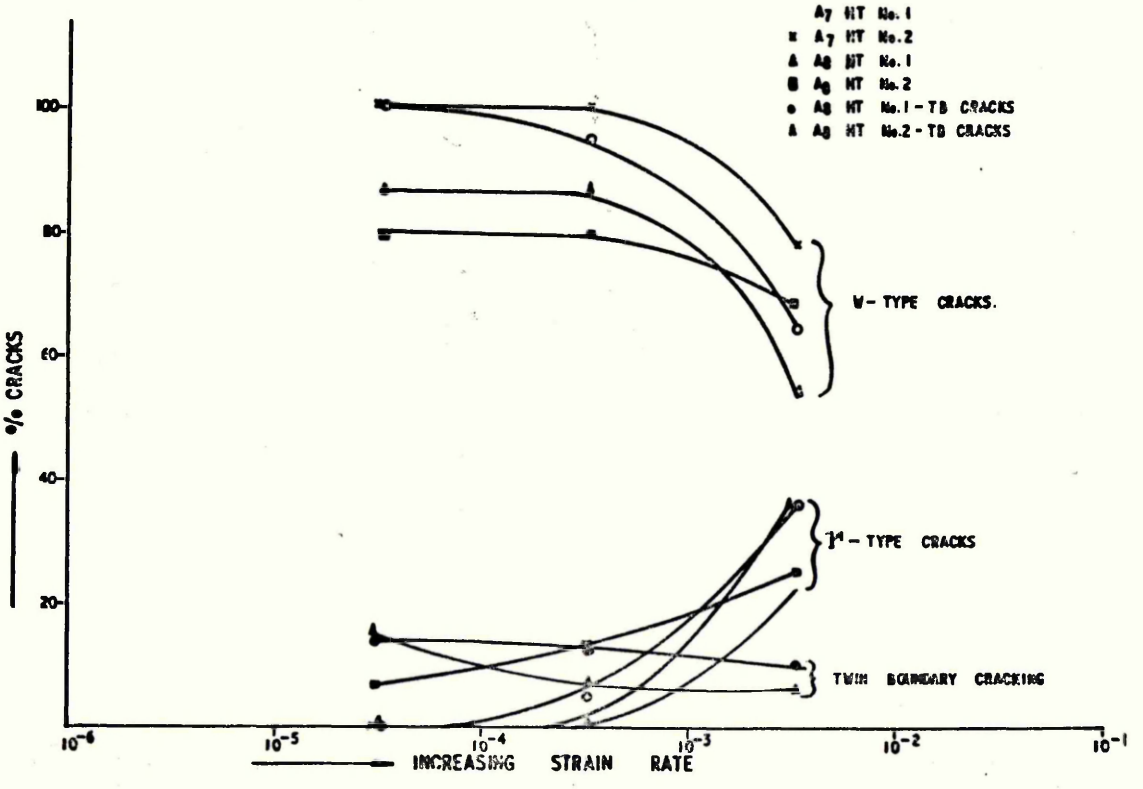

FIG. 92. NATURE OF CRACKING IN γ' FORMING ALLOYS.

PLATE 1

(a) General features of the cast structure, showing coring effects. (Alloy 4) X 100

(b) General features of the hot-rolled bar showing a very fine grained structure. (Alloy 3) X 500

(c) Dislocation structure of the base composition after solution treatment and quenching. (Alloy 1) X 28000

(d) Solution treated structure of high carbon - molybdenum bearing steel showing stringers of undissolved carbides. (Alloy 4) X 650

(e) Solution treated structure of high carbon-molybdenum alloy showing undissolved $(Cr_{15}\ Fe_4\ Ni_2\ Mo_2)\ C_6$ precipitates within the matrix. (Alloy 4) X 24500

(f) Optical micrograph of solution treated high carbon titanium bearing alloy, showing a considerable amount of undissolved carbides (Alloy 5) X 640

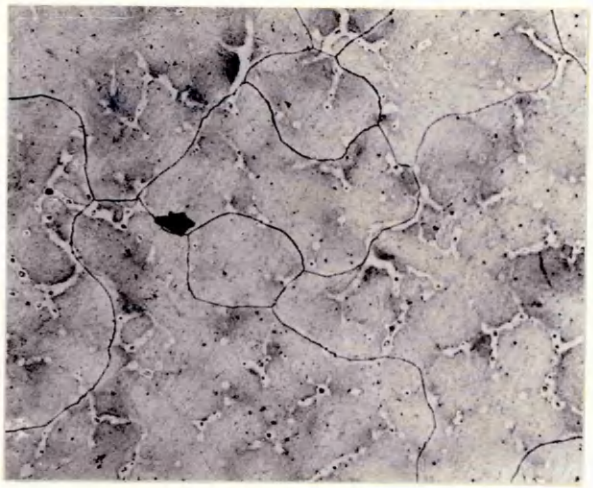

(a)

(b)

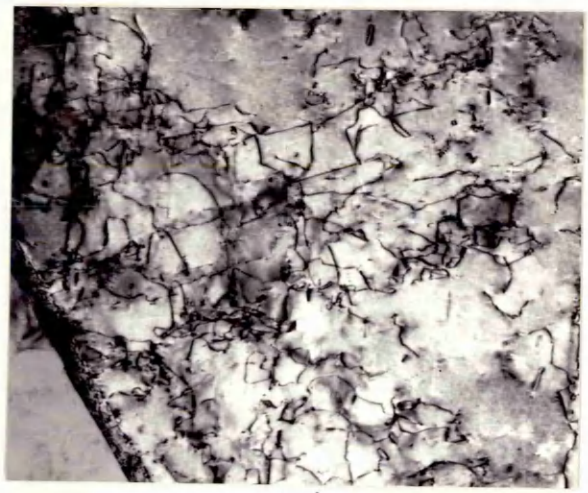

(c)

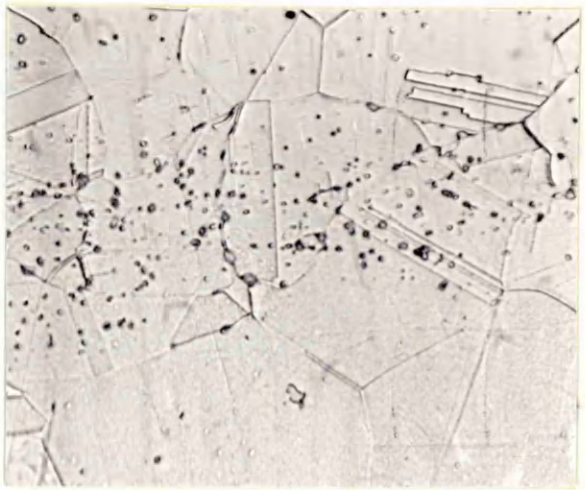

(d)

(e)

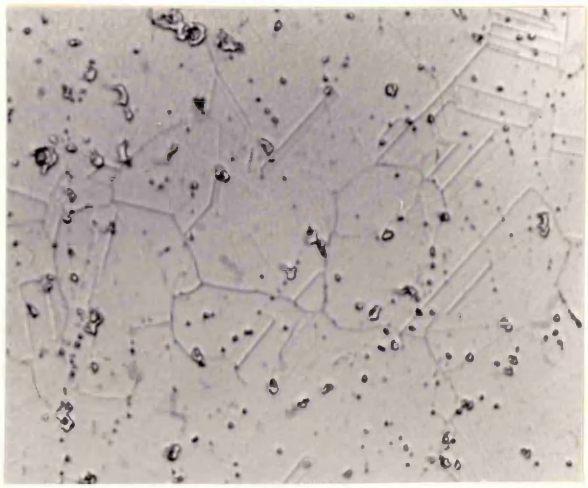

(f)

PLATE 2

(a) Electron micrograph of solution treated high carbon titanium bearing alloy, showing undissolved TiC within the grains and grain boundaries free from such precipitates. (Alloy 5) X 11900

(b) Optical micrograph of solution treated extra-high carbon titanium bearing alloy, showing a considerable amount of undissolved TiC both within the grains and at grain boundaries. (Alloy 6) X 640

(c) Optical micrograph of medium carbon base composition, aged at 700°C for 100 hours, showing grain boundary $M_{23}C_6$ precipitates. (Alloy 2) X 640

(d) Medium carbon base composition, aged at 800°C for 6 hours, showing increased $M_{23}C_6$ precipitation. (Alloy 2) X 640

(e) High carbon base composition, aged at 650°C for 0.5 hours, showing grain boundary carbide precipitation. (Alloy 3) X 640

(f) High carbon base composition, aged at 700°C for 10 hours, showing massive grain/twin boundary carbide precipitation and some precipitation within the grains. (Alloy 3) X 640

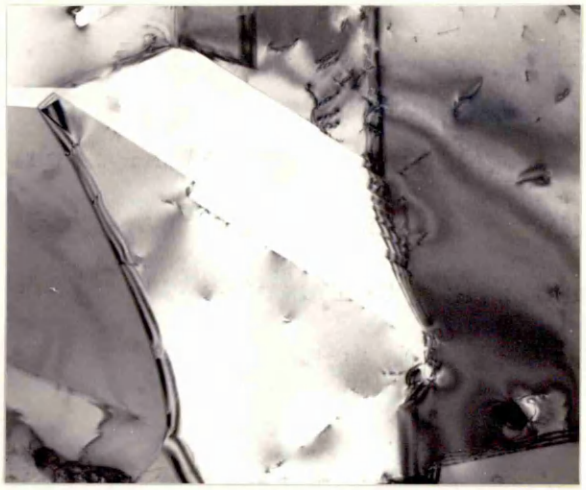

(a)

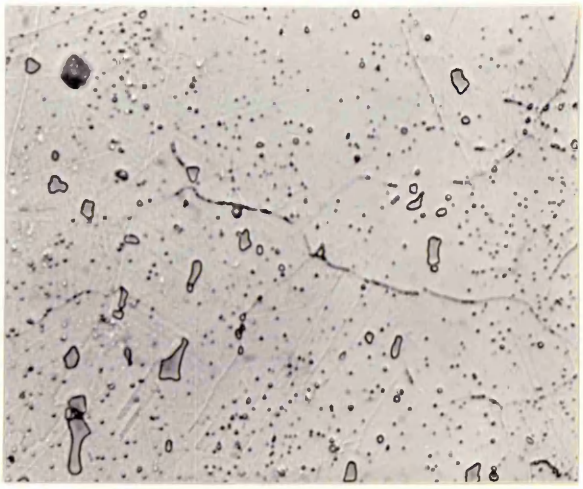

(b)

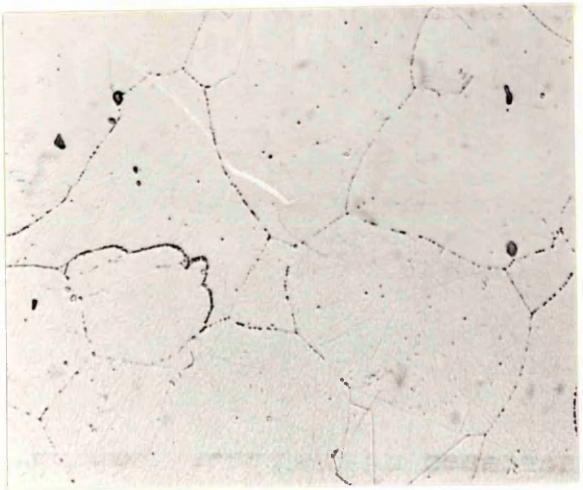

(c)

(d)

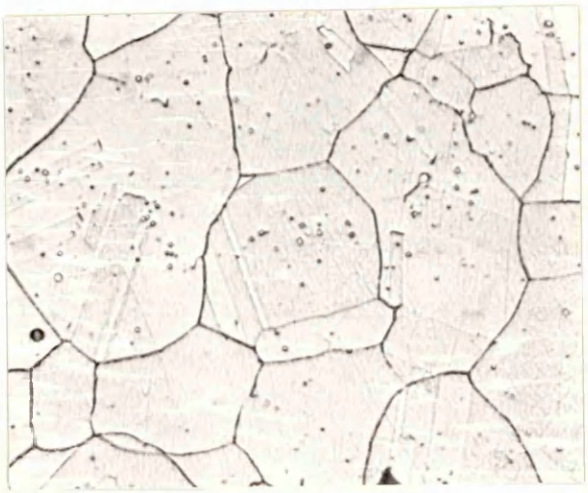

(e)

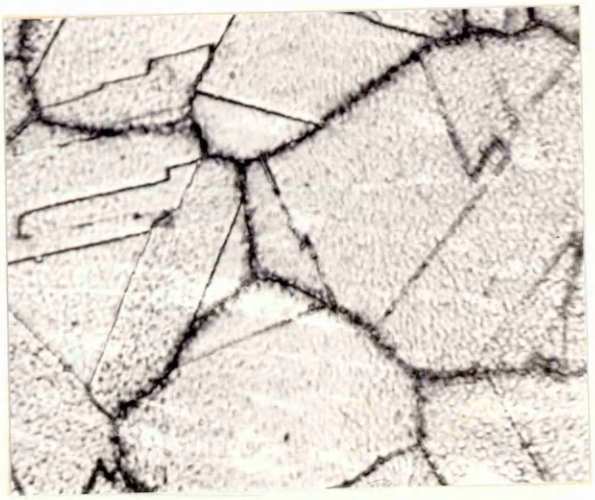

(f)

PLATE 3

(a) Massive grain boundary $M_{23}C_6$ precipitation in high carbon base composition, aged at 550°C for 100 hours. (Alloy 3) X 56000

(b) Widmanstatten type $M_{23}C_6$ precipitation in high carbon base composition, aged at 600°C for 100 hours. (Alloy 3) X 42000

(c) Incoherent twin boundary $M_{23}C_6$ precipitation in high carbon base composition, aged at 700°C for 16 hours. (Alloy 3) X 21000

(d) Dark field of Plate 3(c). (Alloy 3) X 21000

(e) Coherent twin boundary $M_{23}C_6$ precipitation in high carbon base composition, aged at 750°C for 100 hours. (Alloy 3) X 42000

(f) Decreased grain boundary $M_{23}C_6$ precipitation with little or no precipitates within the grains in high carbon base composition, aged at 800°C for 100 hours. (Alloy 3) X 24500

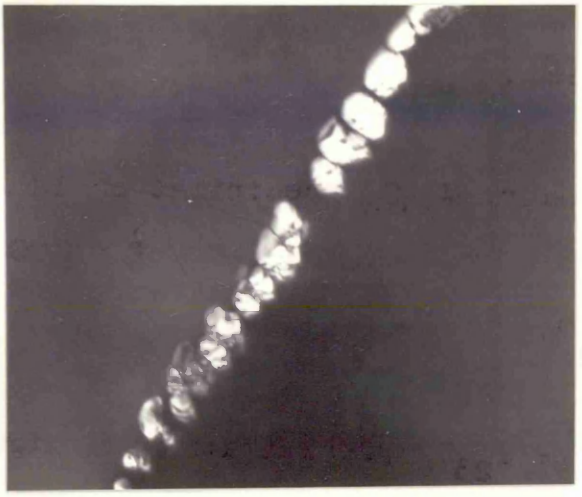

(a)

(b)

(c)

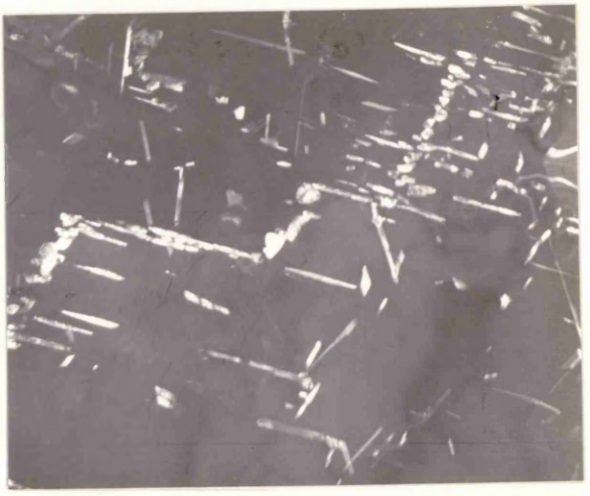

(d)

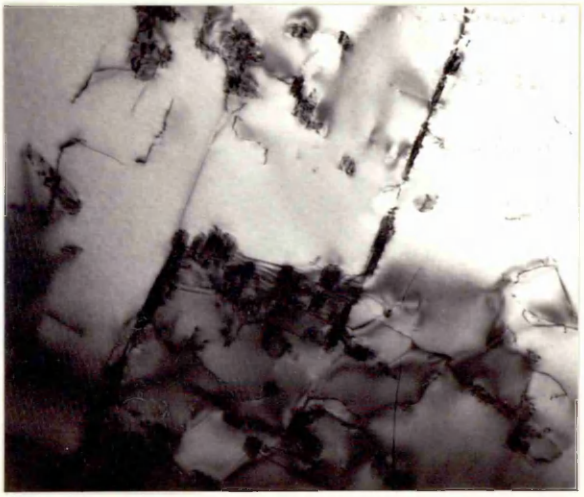

(e)

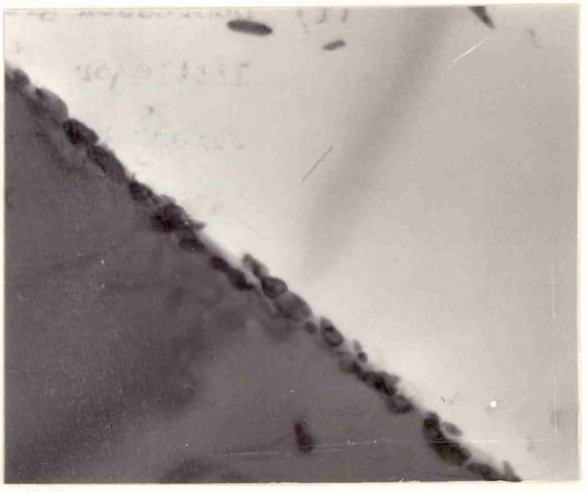

(f)

PLATE 4

(a) $M_{23}C_6$ precipitation on dislocation in high carbon molybdenum bearing alloy, aged at 550°C for 100 hours. (Alloy 4) X 28000

(b) Triple point junction $M_{23}C_6$ precipitation in high carbon molybdenum alloy, aged at 650°C for 70 hours. (Alloy 4) X 21000.

(c) Massive $M_{23}C_6$ carbide precipitation at grain boundaries in high carbon molybdenum bearing alloy, aged at 650°C for 70 hours. (Alloy 4) X 10500

(d) Massive plates of $M_{23}C_6$ carbide precipitates along incoherent twin boundaries and within the grains. (Alloy 4) X 24500

(e) Optical micrograph of high carbon molybdenum bearing alloy showing a continuous grain boundary carbides and a considerable amount of undissolved carbides, aged at 700°C for 2 hours (Alloy 4). X 640

(f) Precipitation of carbides along coherent twin boundary aged at 750°C for 100 hours. (Alloy 4) X 24500

(a)

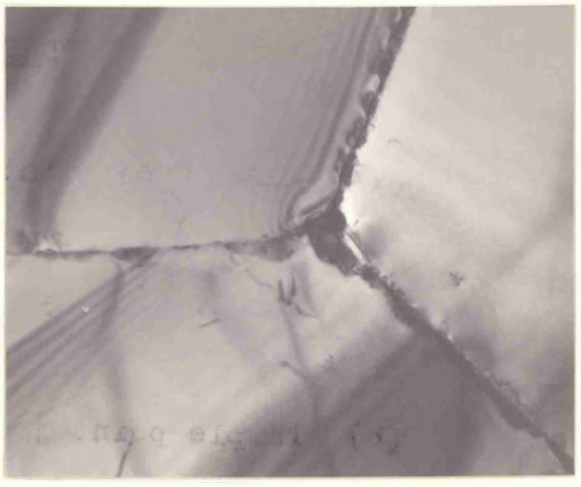

(b)

(c)

(d)

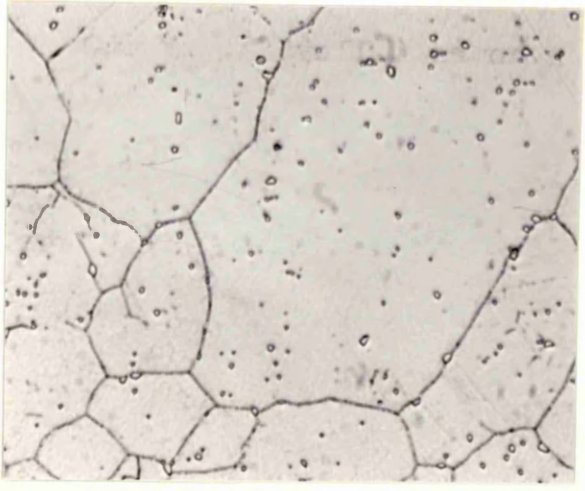

(e)

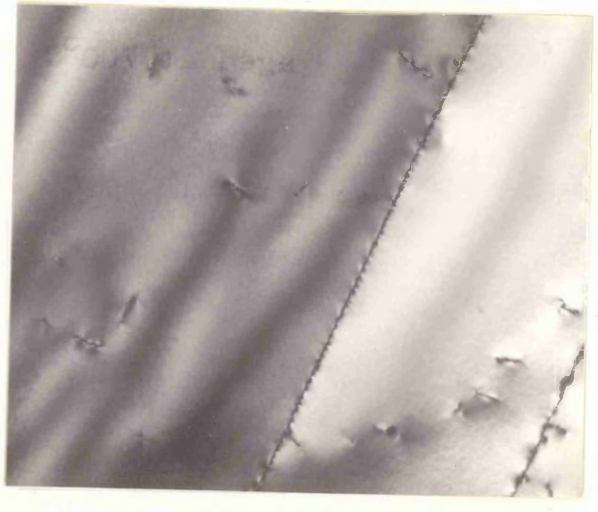

(f)

PLATE 5

(a) Dark field of huge $M_{23}C_6$ Widmanstatten type platelets within the matrix, aged at 800°C for 2 hours. (Alloy 4) X 11900

(b) Massive $M_{23}C_6$ particles along incoherent twin-boundary aged at 800°C for 2 hours. (Alloy 4) X 28000

(c) High carbon titanium bearing alloy, aged at 650°C for 30 hours, showing very little carbide precipitation on grain boundaries. (Alloy 5) X 640

(d) Optical micrograph of high carbon titanium alloy, aged at 700°C for 100 hours, showing fine carbide precipitation along grain boundaries. (Alloy 5) X 640

(e) High carbon titanium bearing alloy, aged at 850°C for 70 hours showing massive grain boundary carbide precipitation. (Alloy 5) X 640

(f) Dark field micrograph of titanium bearing alloy, aged at 700°C for 10 hours, revealing fine $M_{23}C_6$ precipitates along grain boundaries. (Alloy 5) X 11900

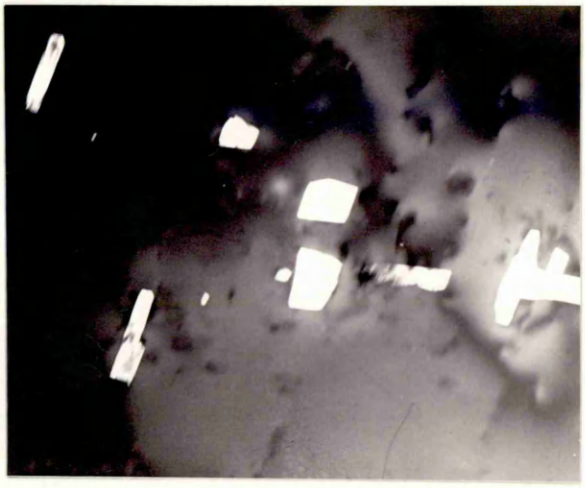

(a)

(b)

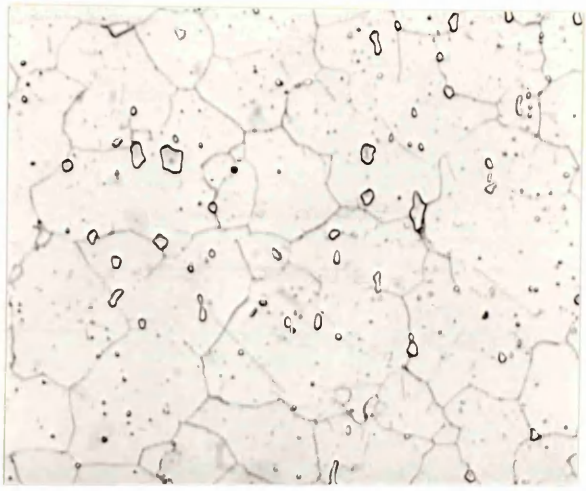

(c)

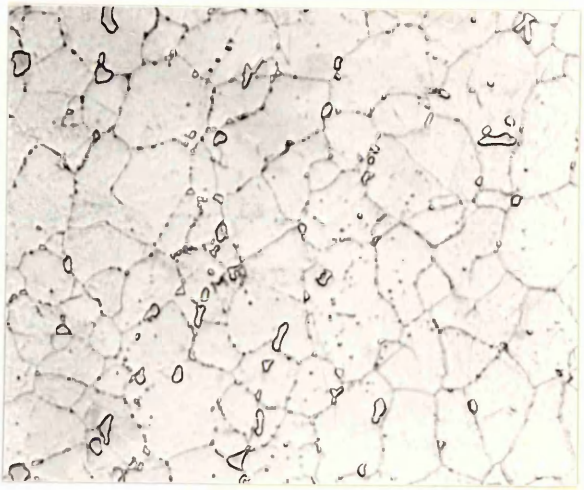

(d)

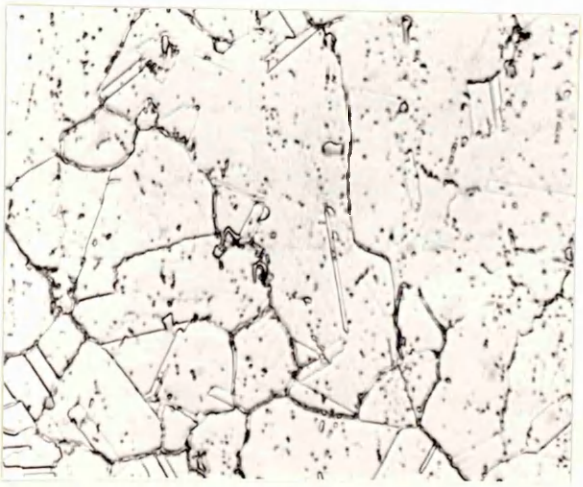

(e)

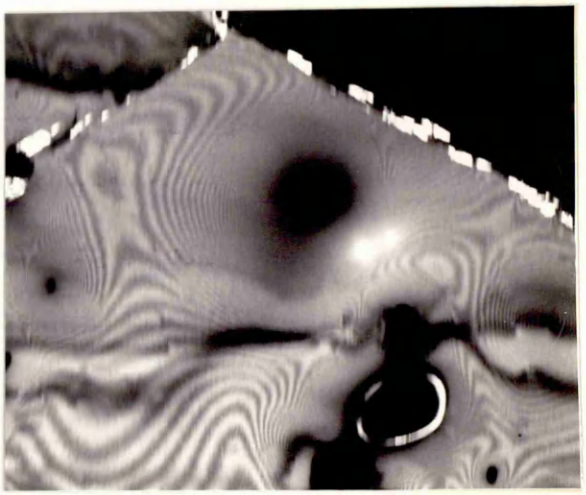

(f)

PLATE 6

(a) Very fine $M_{23}C_6$ precipitation along grain-boundaries in titanium bearing alloy, aged at 750°C for 16 hours. (Alloy 5) X 14000

(b) Dark field micrograph of the above carbides, aged at 750°C for 16 hours. (Alloy 5) X 14000

(c) Dark field micrograph of titanium bearing alloy, showing fine TiC precipitation along dislocations, aged at 750°C for 16 hours. (Alloy 5) X 10500

(d) Dark field micrograph showing TiC precipitation along grainboundaries, aged at 800°C for 6 hours. (Alloy 5) X 14000

(e) Grain boundary carbide precipitation in extra-high carbon titanium bearing steel, aged at 800°C for 10 hours. (Alloy 6) X 640

(f) Low carbon PE16 composition showing occasional carbide precipitation along grain-boundaries, aged at 650°C for 100 hours. (Alloy 7) X 640

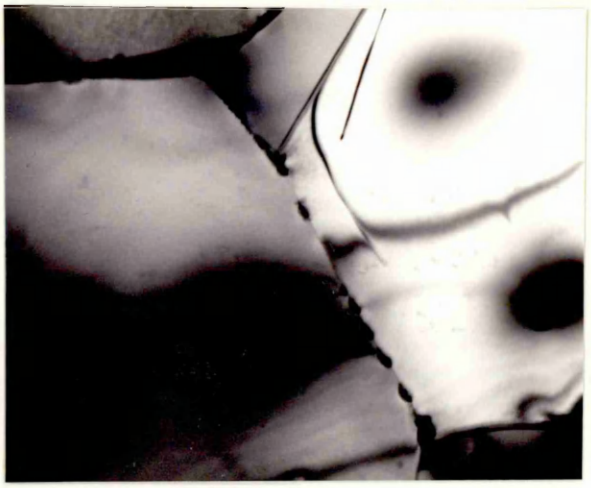

(a)

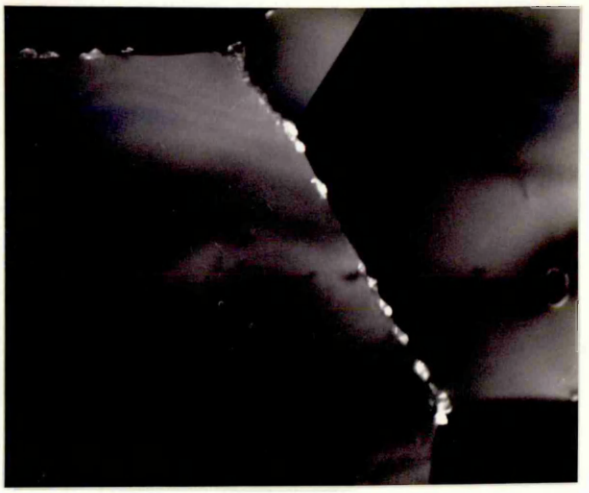

(b)

(c)

(d)

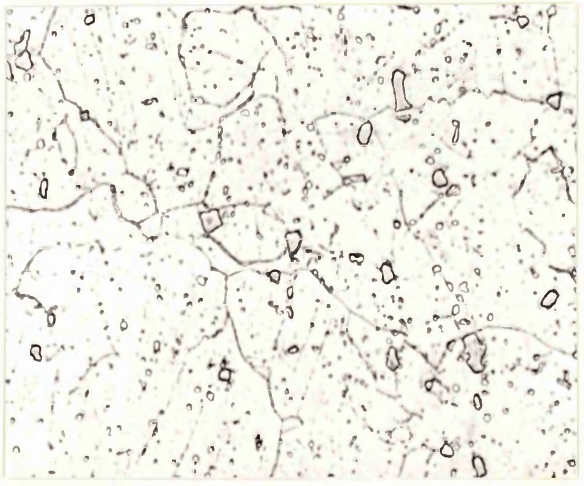

(e)

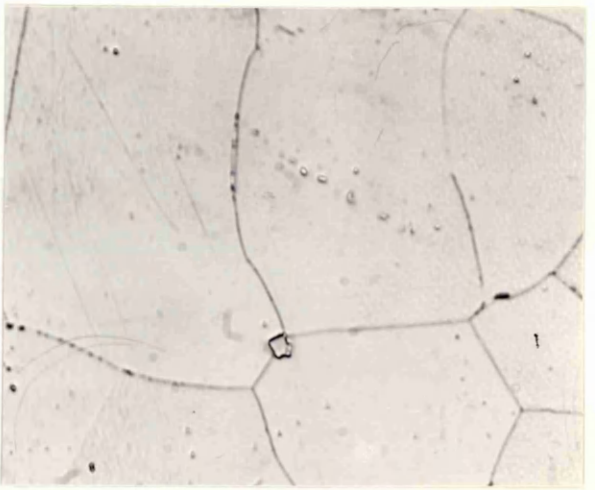

(f)

PLATE 7

(a) Low carbon PE16 aged at 900°C for 6 hours, showing carbides at grain boundaries and an etching effect within the grains due to γ' precipitation. (Alloy 7) X 640

(b) Low carbon PE16 aged at 500°C for 100 hours, showing super dislocations and some dislocation pairs within the matrix. (Alloy 7) X 14000

(c) Electron micrograph of low carbon PE16. aged at 550°C for 100 hours showing mottling effect due to γ' zone formation within the grains. (Alloy 7) X 31500

(d) Low carbon PE16 aged at 700°C for 30 hours, revealing increased mottling effect due to γ' zone formation. (Alloy 7) X 63000

(e) Electron micrograph of PE16 aged at 700°C for 30 hours showing a few grain boundary $M_{23}C_6$ precipitates. (Alloy 7) X 14000

(f) Low carbon PE16 composition aged at 750°C for 70 hours, showing a uniform distribution of semicoherent γ' precipitates. (Alloy 7) X 24500

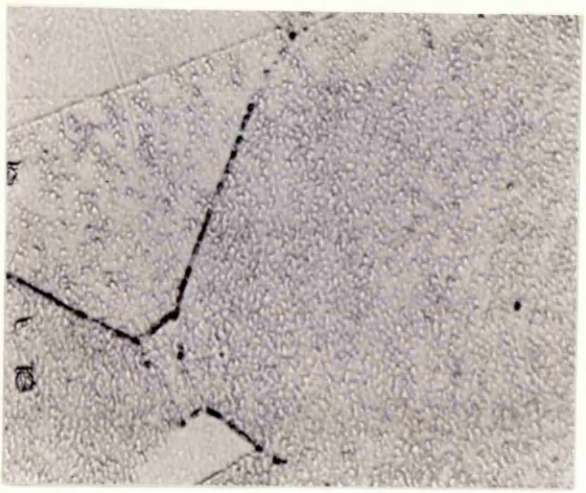

(a)

(b)

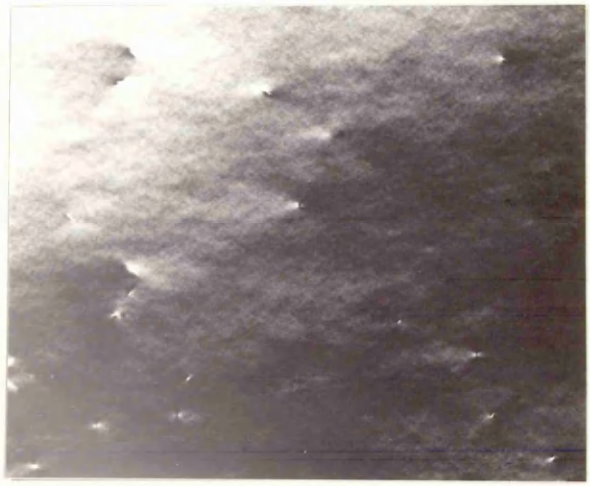

(c)

(d)

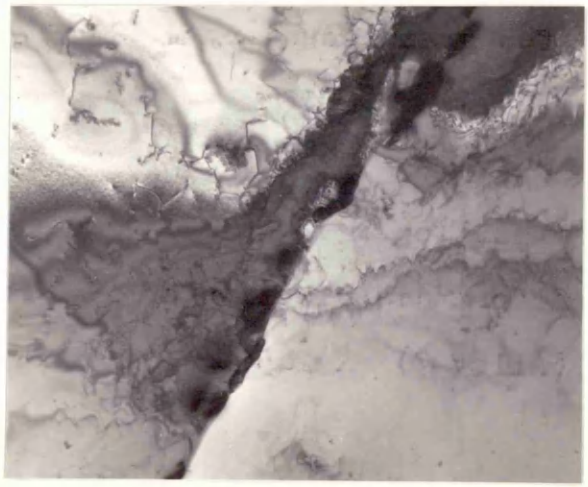

(e)

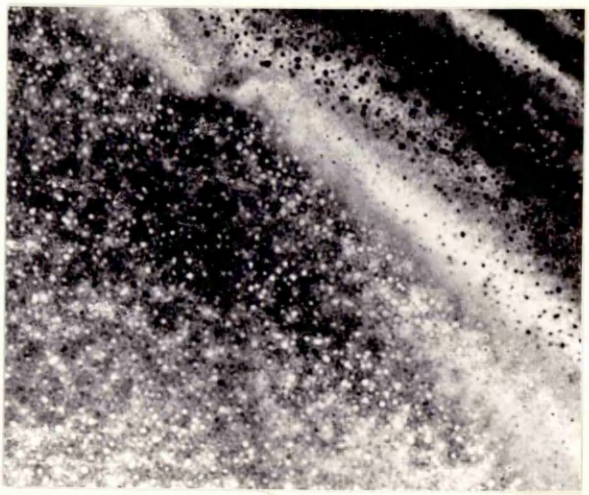

(f)

PLATE 8

(a) Increased size of semicoherent γ' precipitates, aged at 800°C for 30 hours. (Alloy 7) X 56000

(b) Optical micrograph of high carbon PE16 composition, showing continuous grain boundary carbide precipitation, aged at 700°C for 2 hours. (Alloy 8) X 640

(c) Electron micrograph of high carbon PE16, showing mottling effect due to γ' zone formation, aged at 700°C for 6 hours. (Alloy 8) X 17500

(d) Continuous grain boundary $M_{23}C_6$ precipitation in high carbon PE16, aged at 700°C for 30 hours. (Alloy 8) X 14000

(e) Dark field of the above $M_{23}C_6$ precipitates. (Alloy 8) X 14000

(f) High carbon PE16 composition aged at 750°C for 30 hours, showing γ' particles coherent with the matrix, including coherency strains. (Alloy 8) X 63000

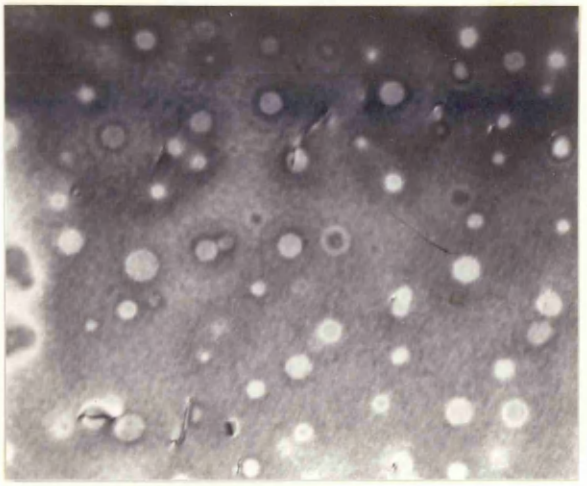

(a)

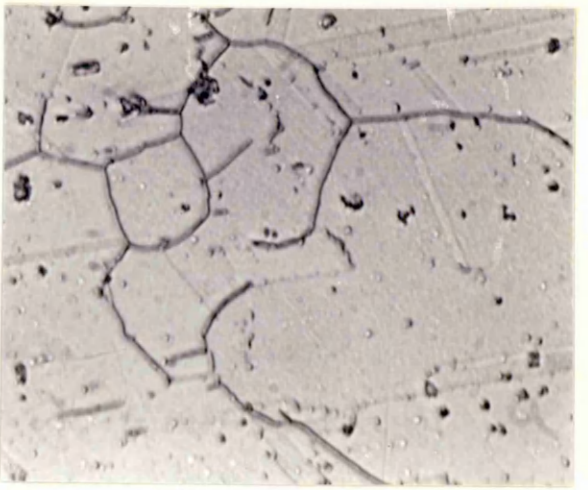

(b)

(c)

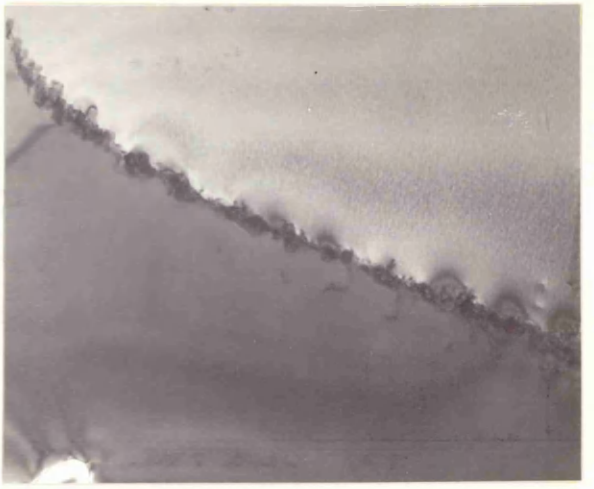

(d)

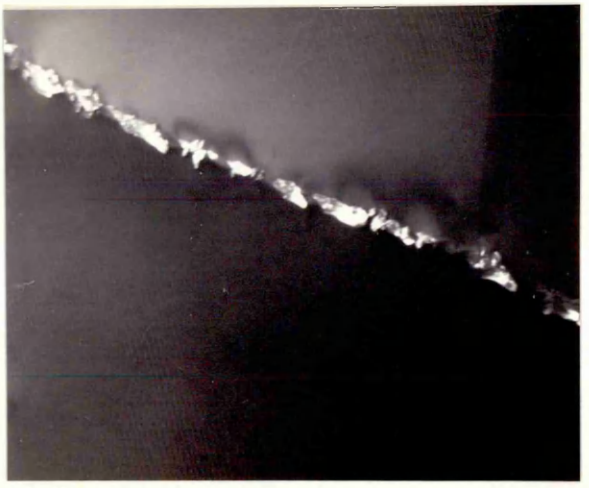

(e)

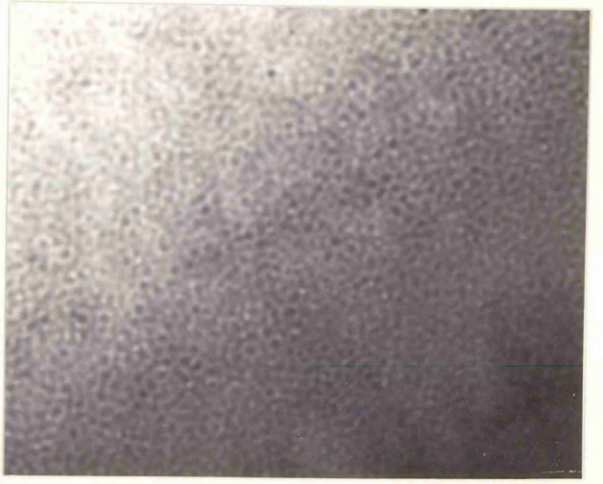

(f)

PLATE 9

(a) High carbon PE16 composition, aged at 750°C for 30 hours, revealing $M_{23}C_6$ precipitates along the undissolved TiC/matrix interface. (Alloy 8) X 28000

(b) Dark field micrograph of the above, showing a uniform distribution of $M_{23}C_6$ along carbide/matrix interface. (Alloy 8) X 28000

(c) Semicoherent γ' precipitates uniformly distributed throughout the matrix, aged at 750°C for 100 hours. (Alloy 8) X 84000

(d) Increased size of semicoherent γ' precipitates on ageing at 800°C for 70 hours. (Alloy 8) X 28000

(e) Dark field micrograph of massive $M_{23}C_6$ precipitation along grain boundaries on ageing at 800°C for 70 hours (Alloy 8) X 28000

(f) Bright field micrograph of above carbides ageing at 800°C for 70 hours (Alloy 8) X 2800

(a)

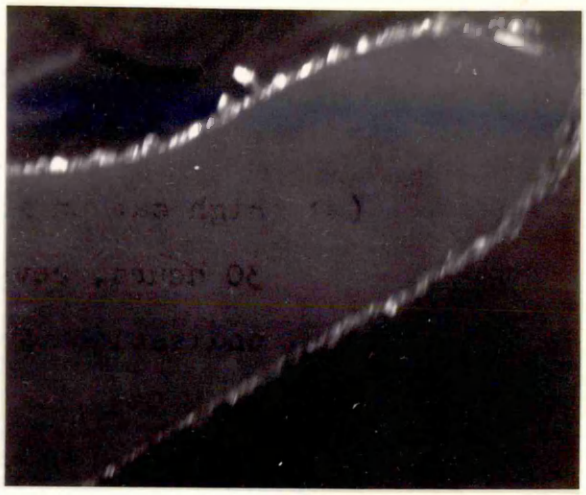

(b)

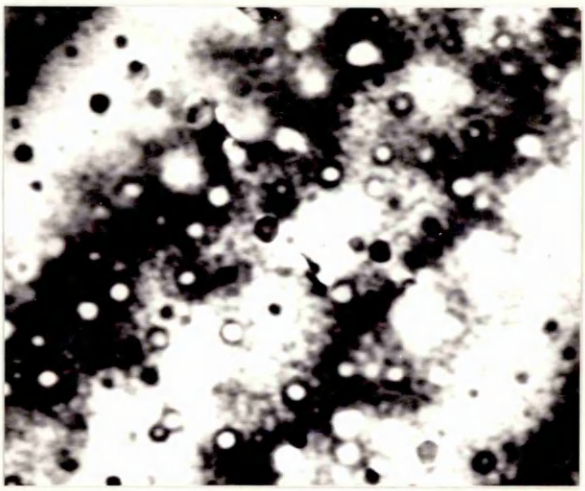

(c)

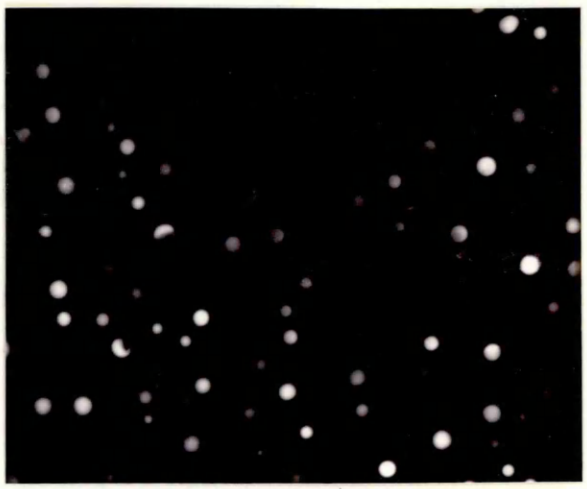

(d)

(e)

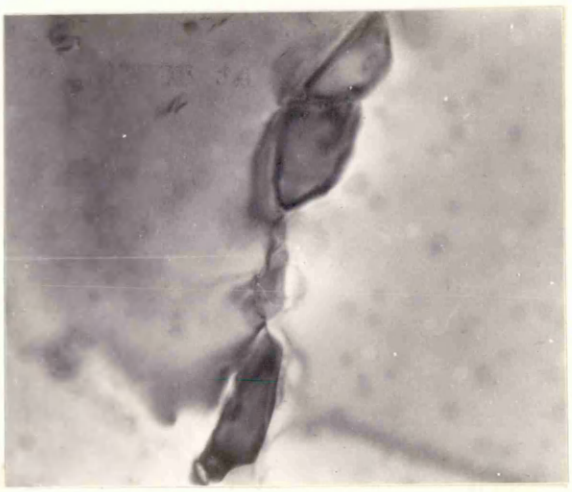

(f)

PLATE 10

(a) Optical micrograph of medium carbon base composition, aged at 750°C for ½ hours after 40% cold working. (Alloy 2) X 600

(b) Optical micrograph of medium carbon base composition, aged at 650°C for 70 hours after 40% cold working. (Alloy 2) X 600

(c) Electron micrograph of medium carbon base composition, aged at 700°C for ½ hour after 40% cold working, showing the recrystallized grain formation along a deformed grain boundary. (Alloy 2) X 56000

(d) Optical micrograph showing increased carbide precipitation on ageing at 700°C for ½ hour after 80% cold working. (Alloy 2) X 600

(e) Electron micrograph of medium carbon base composition showing recrystallized structure and $M_{23}C_6$ precipitation along a deformation band, aged at 700°C for ½ hours after 80% cold working. (Alloy 2) X 11900

(f) Recovered regions on ageing at 700°C for ½ hours after 80% cold working. (Alloy 2) X 63000

(a)

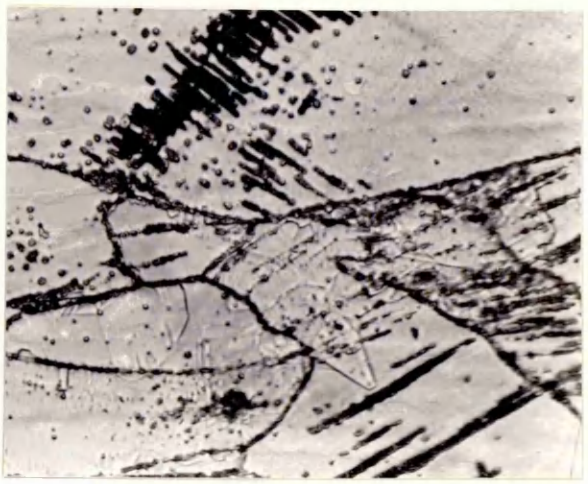

(b)

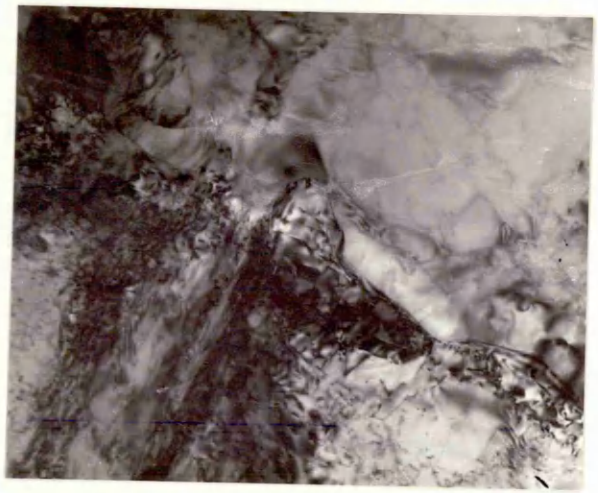

(c)

(d)

(e)

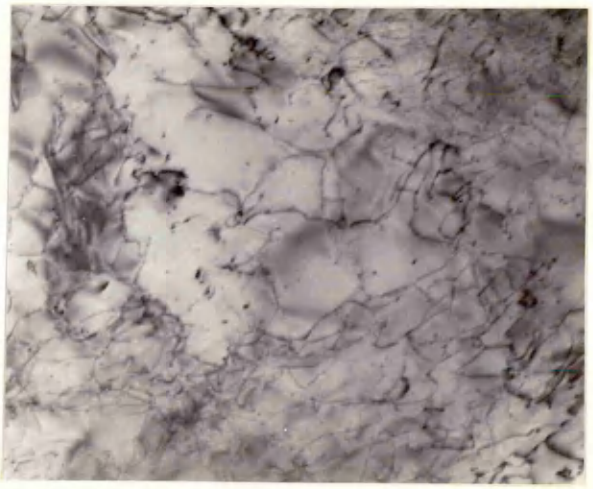

(f)

PLATE 11

(a) High carbon base composition on ageing at 700°C for ½ hours, after 40% cold working. (Alloy 3) X 600

(b) Dark field of $M_{23}C_6$ precipitates along deformed grain boundaries, aged at 700°C for ½ hours, after 40% cold working. (Alloy 3) X 28000

(c) Recrystallized grains around an undissolved $M_{23}C_6$ precipitates, aged at 700°C for ½ hours after 80% cold working. (Alloy 3) X 35000

(d) Grainboundary pinning effect of precipitated $M_{23}C_6$ particles on growing recrystallized grains, aged at 700°C for ½ hour, after 80% cold working. (Alloy 3) X 11900

(e) High carbon molybdenum bearing alloy showing dislocation rearrangement on ageing at 700°C for 1 hour, after 40% cold working. (Alloy 4) X 56000

(f) Molybdenum bearing alloy showing recrystallized structure with $M_{23}C_6$ precipitation along a definite direction. Aged at 700°C for 1 hour after 80% cold working. (Alloy 4) X 14000

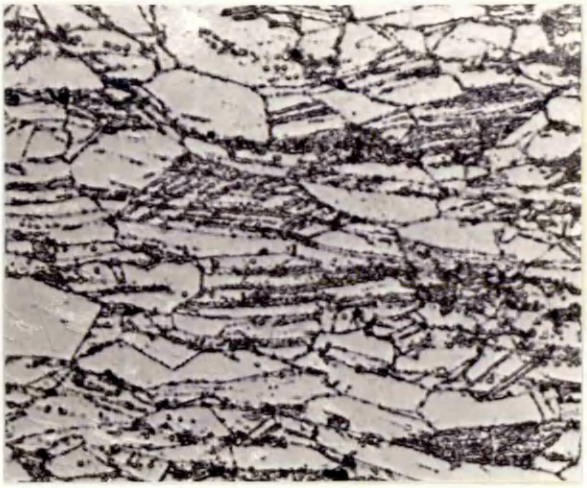

(a)

(b)

(c)

(d)

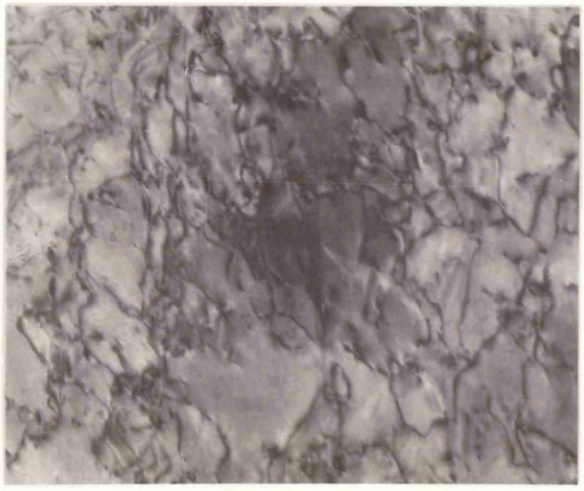

(e)

(f)

PLATE 12

(a) Titanium bearing steel showing a completely recrystallized structure on ageing at 700°C for ½ hour after 80% cold working. (Alloy 5) X 11900

(b) A recrystallized grain growing in the deformed matrix. Aged at 700°C for ½ hour after 80% cold working. (Alloy 5). X 24500

(c) Recrystallized structure with $M_{23}C_6$ precipitates uniformly distributed. Aged at 750°C for 30 hours after 80% cold working. (Alloy 5) X 5600

(d) TiC precipitated on dislocations within a recrystallized grain. Aged at 750°C for 30 hours after 80% cold working. (Alloy 5) X 17500

(e) Coarsened $M_{23}C_6$ precipitates on ageing at 750°C for 100 hours after 80% cold working. (Alloy 5) X 14000

(f) Intense mottling due to γ' zone formation on ageing at 650°C for 1 hour after 80% cold working. (Alloy 7) X 70000

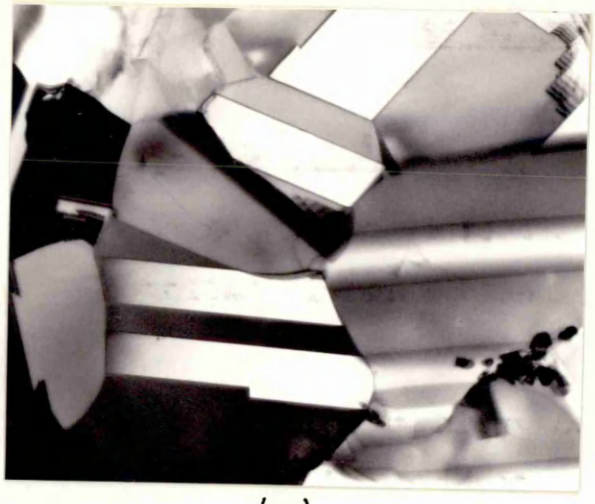

(a)

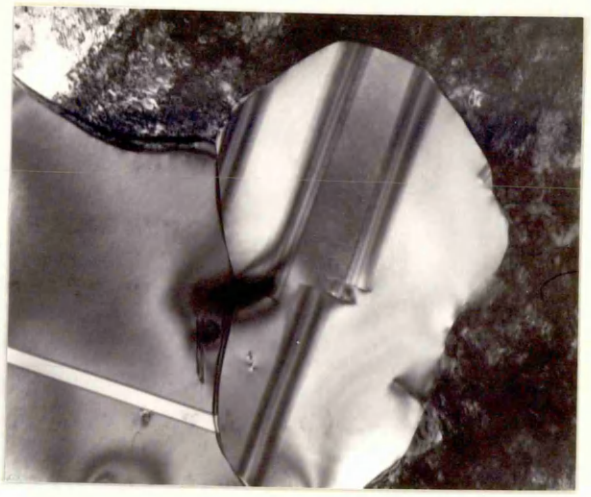

(b)

(c)

(d)

(e)

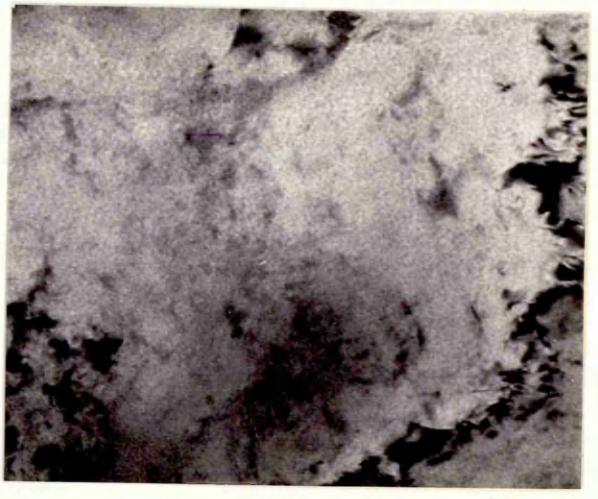

(f)

PLATE 13

(a) Dark field micograph showing semicoherent γ' precipitates, on ageing at 750°C for 30 hours after 80% cold working. (Alloy 7) X 35000

(b) Recovered structure of low carbon PE16 composition on ageing 750°C for $\frac{1}{2}$ hour after 80% cold working. (Alloy 7) X 70000

(c) Partially recrystallized structure on ageing at 750°C for 30 hours after 80% cold working. (Alloy 7) X 42000

(d) Recrystallized grain growing within the deformed structure, on ageing at 750°C for 30 hours, after 80% cold working. X 28000 (Alloy 7)

(e) Recrystallized regions along with $M_{23}C_6$ precipitation in high carbon PE16 composition. Aged at 750°C for 30 hours after 80% cold working. (Alloy 8) X 35000

(f) Partially recrystallized structure on ageing at 750°C for 30 hours after 80% cold working. (Alloy 8) X 7400

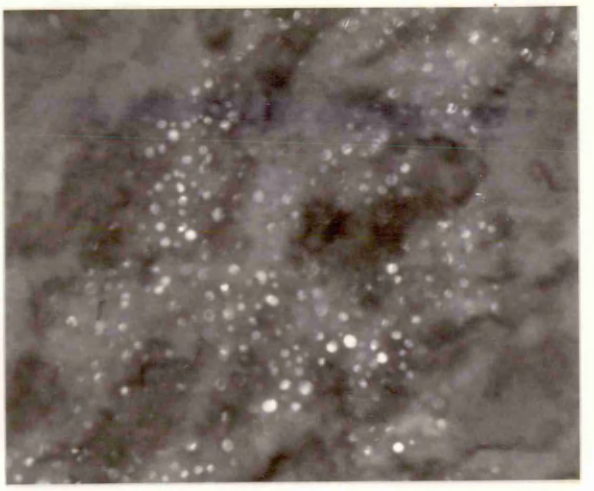

(a)

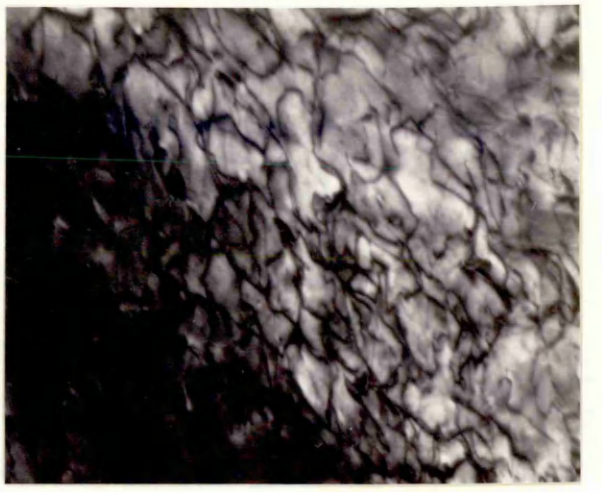

(b)

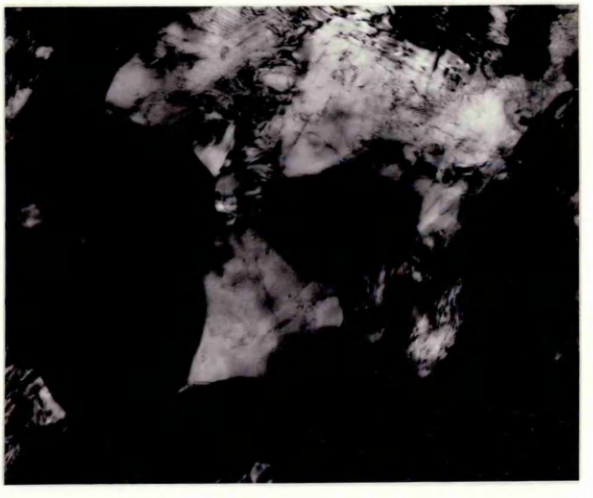

(c)

(d)

(e)

(f)

PLATE 14

(a) Grain boundary dislocation structure of low carbon base composition after creep testing at 700°C. (Alloy 1) X 30240

(b) Dislocation generation near a twinboundary ledge after creep testing at 700°C. (Alloy 1) X58320

(c) A general area picture showing deformation within the grains after creep testing at 700°C. (Alloy 5 H.T.No.1) X 18360

(d) Grain boundary migration near $M_{23}C_6$ carbides on creep testing at 700°C. (Alloy 5 H.T.No.1) X 13800

(e) Low angle sub-boundary formation on creep testing at 700°C (Alloy 5 H.T.No.1) X 22680

(f) High dislocation density within the grains on creep testing at 700°C (Alloy 7 H.T.No.1) X 14690

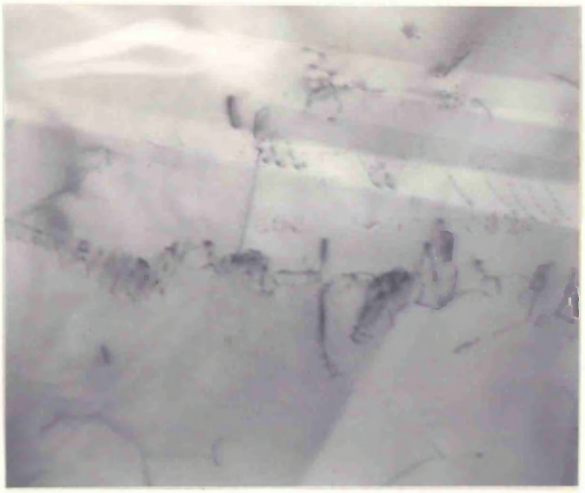

(a)

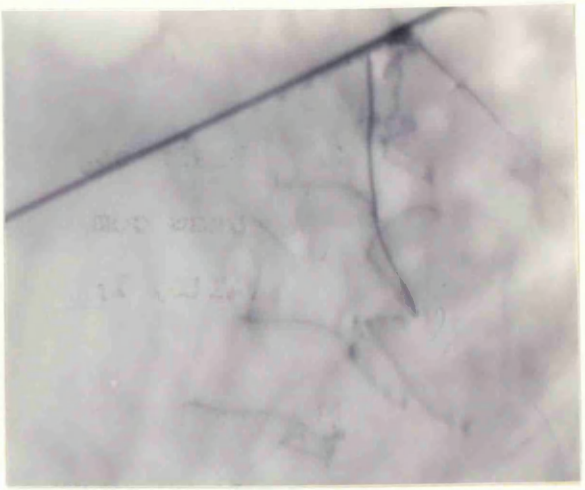

(b)

(c)

(d)

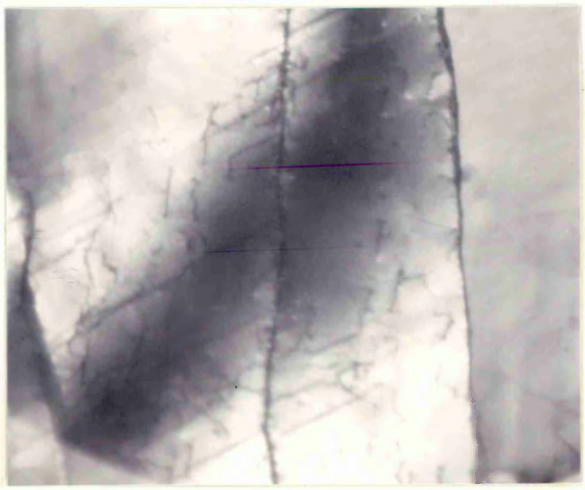

(e)

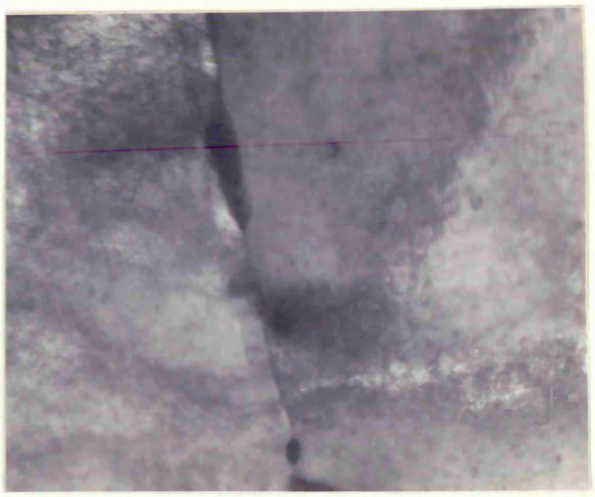

(f)

PLATE 15

(a) Semicoherent γ' precipitate formation and a general dislocation structure on creep testing at 700°C. (A7 H.T.No.1) X 88560

(b) General dislocation/particle interactions on creep testing at 700°C. (A7 H.T.No.2) X 71280

(c) Orowon looping around semicoherent γ' particles, on creep testing at 700°C. (A7 H.T.No.2) X 85000

(d) Grain boundary migration on creep testing at 700°C. (A7 H.T.No.2) X 18360

(e) Grainboundary area in presence of massive $M_{23}C_6$ precipitates, creep tested at 700°C. (A7 H.T.No.2) X 71280

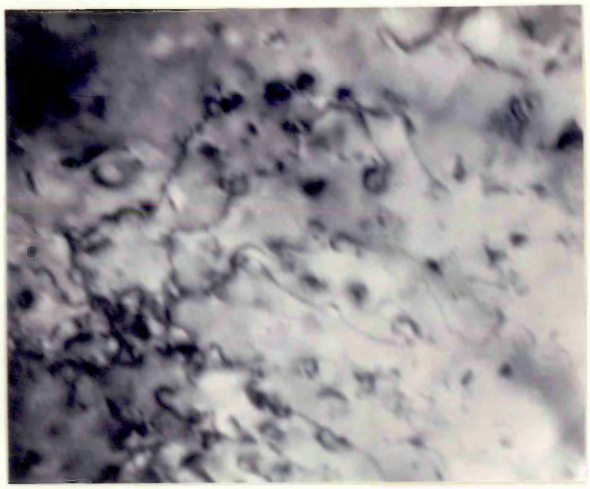

(a)

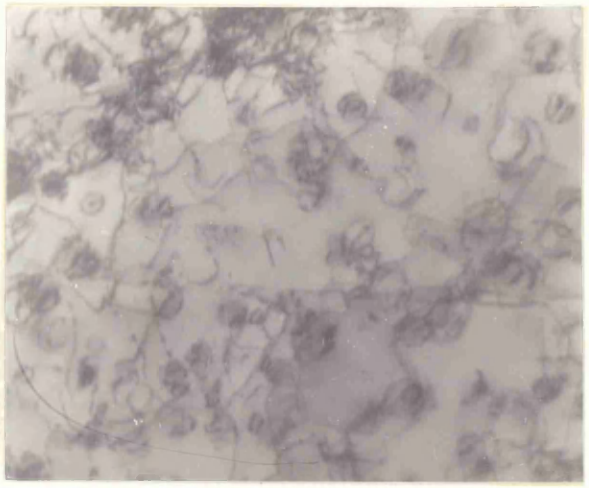

(b)

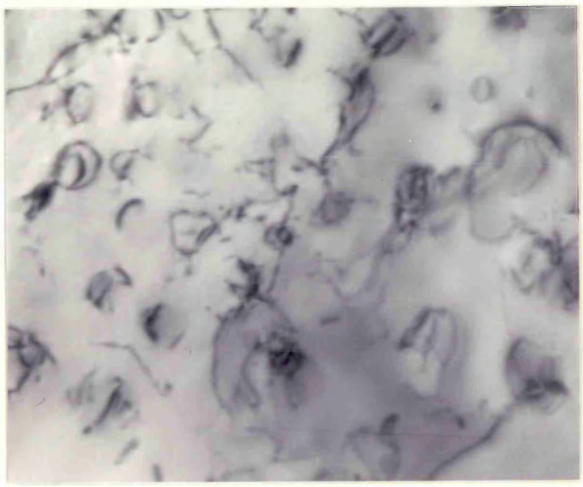

(c)

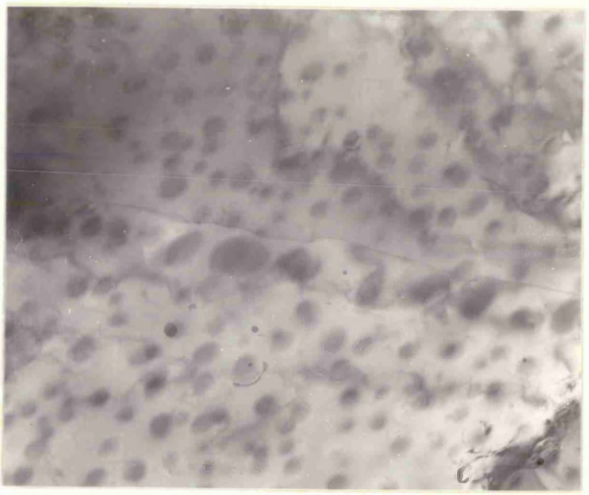

(d)

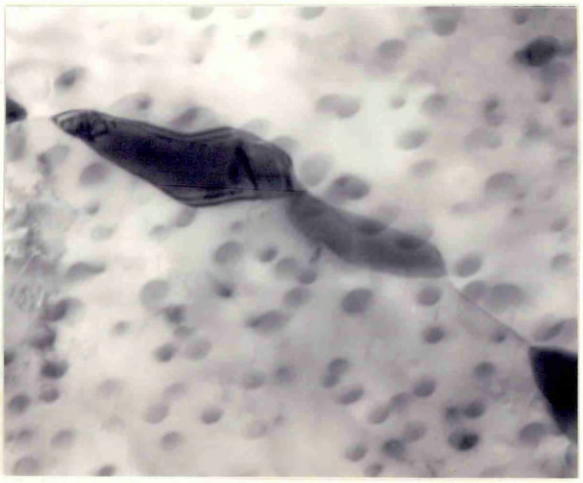

(e)

PLATE 16

(a) Cavity formation around chromite particles, tested at a strain rate of 3.28×10^{-1}/sec at 700°C. (Alloy 1) X 640

(b) Areas showing partial intergranular failure, tested at a strain rate of 3.28×10^{-2}/sec. at 700°C (Alloy 1) X 320

(c) Increased areas of intergranular appearance, tested at a strain rate of 3.28×10^{-3}/sec at 700°C (Alloy 1) X 200

(d) Combined intergranular/ductile fracture, tested at a strain rate of 3.28×10^{-4}/sec at 700°C (Alloy 1) X 200

(e) Oxide formation on creep testing at 700°C (Alloy 1) X 1600

(f) Grainboundary area showing transgranular ductile failure (Alloy 2) X 3200

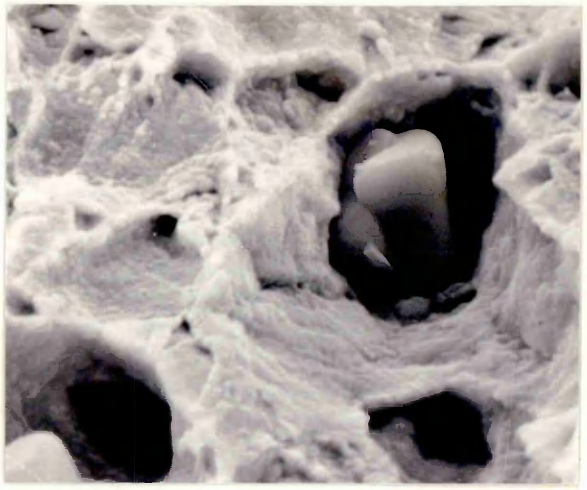

(a)

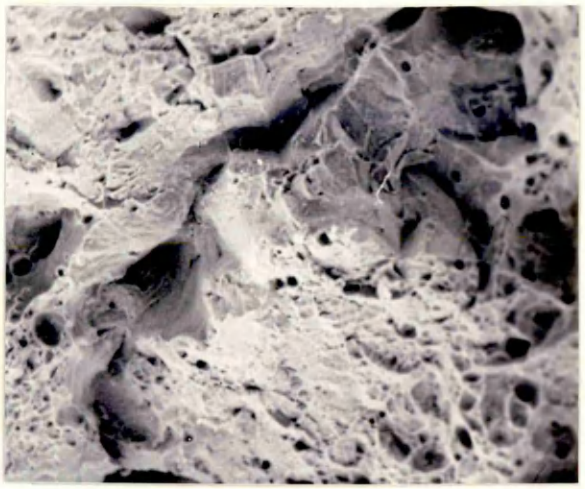

(b)

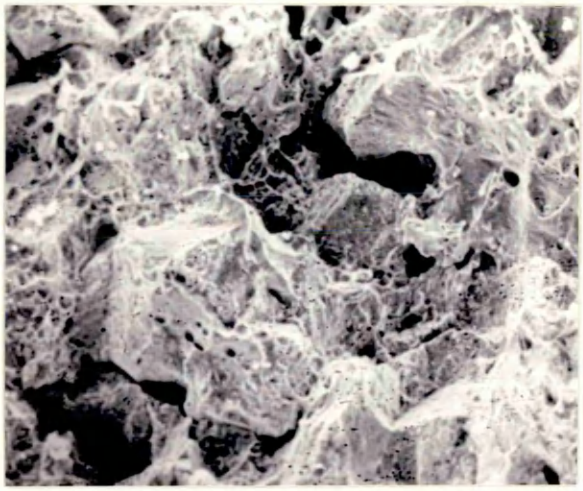

(c)

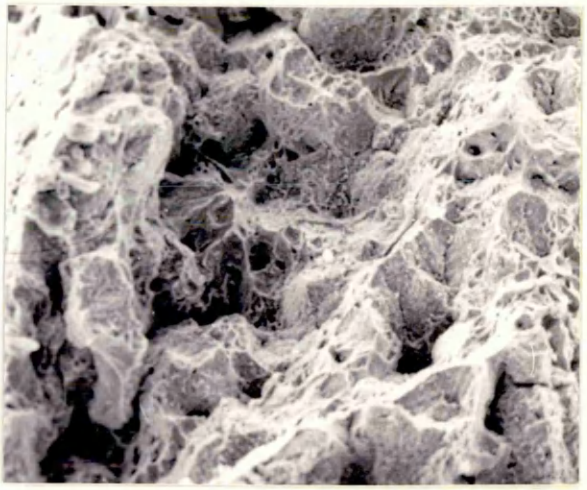

(d)

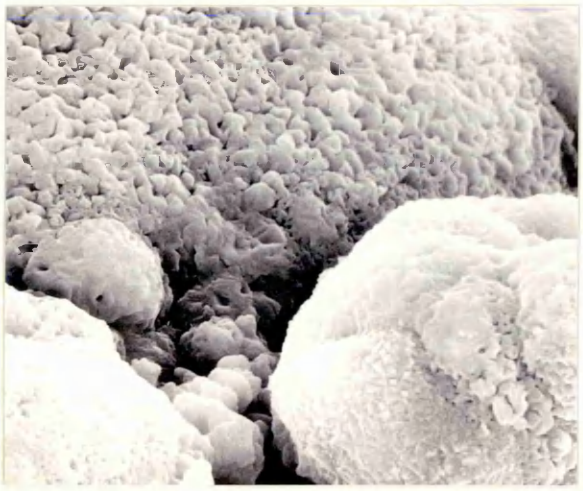

(e)

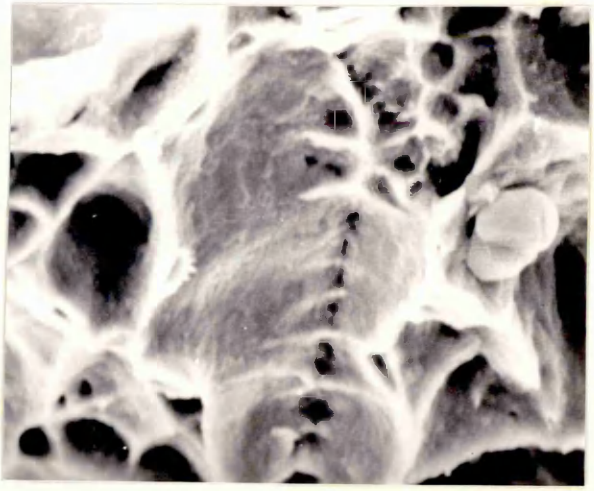

(f)

PLATE 17

(a) General fracture of medium carbon base composition, creep tested at 700°C. (Alloy 2) X 80

(b) Triple point junction on fracture showing crack nucleation and propagation, creep tested at 700°C. (Alloy 2) X 5000

(c) Grainboundary crack along $M_{23}C_6$ precipitates, creep tested at 700°C. (Alloy 2). X 5000

(d) Chromium distribution map of the above boundary containing $M_{23}C_6$ carbides, creep tested at 700°C. (Alloy 2). X 5000

(e) Twin boundary cracks along precipitated $M_{23}C_6$ carbides, tested at 3.28×10^{-5}/sec at 700°C. (Alloy 3) X 1600

(f) Chromium distribution map of the above twinboundary cracking area. (Alloy 3) X 1600

(a)

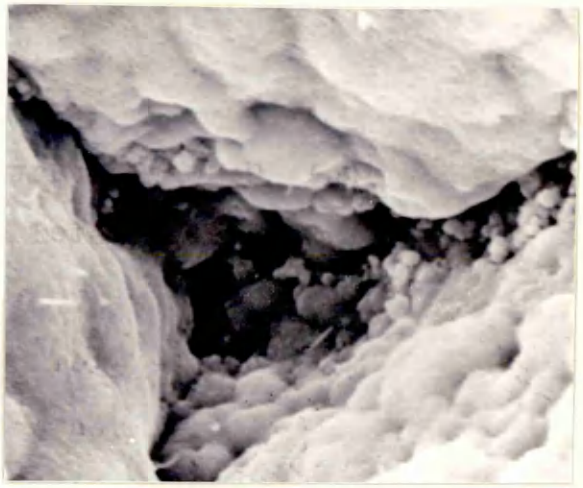

(b)

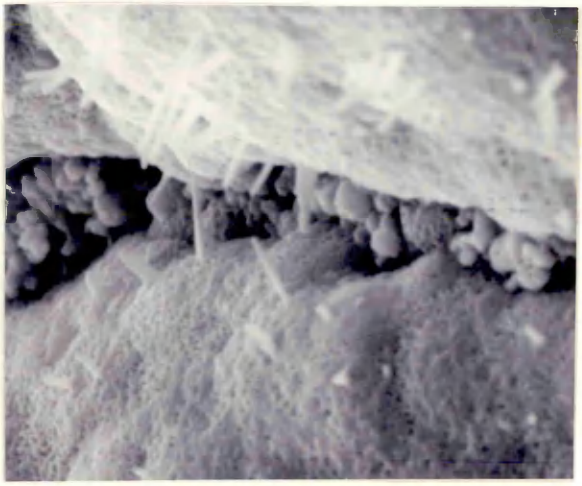

(c)

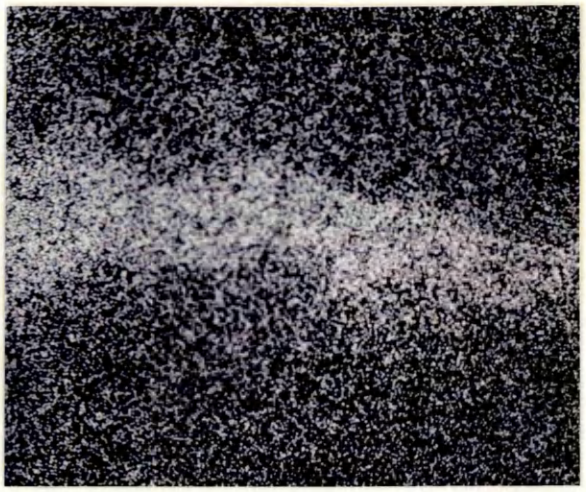

(d)

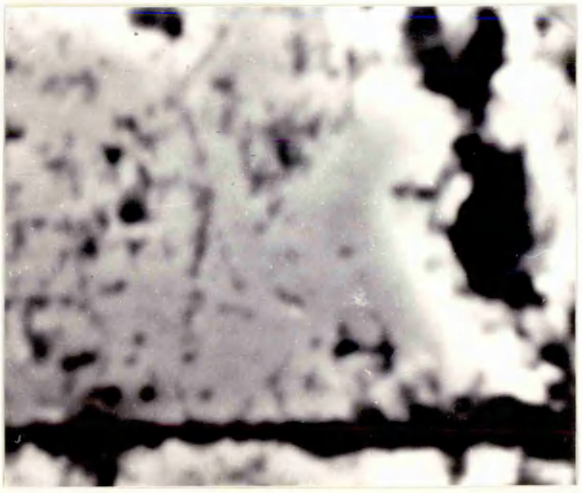

(e)

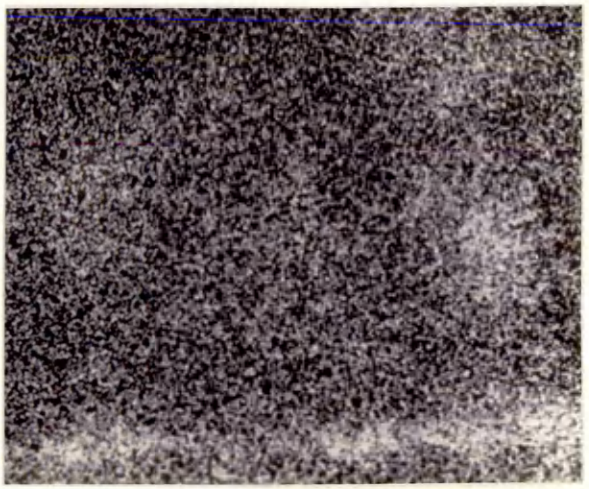

(f)

PLATE 18

(a) General area fracture of molybdenum bearing alloy, tested at a strain rate of 3.28×10^{-4}/sec at 700°C. (Alloy 4) X 400

(b) Fractured specimen of titanium bearing alloy, showing typical cup and cone appearance, tested at 3.28×10^{-1}/sec at 700°C. (Alloy 5 H.T.No.1) X 25

(c) Ductile fracture and some necking on testing at a strain rate of 3.28×10^{-4}/sec at 700°C. (Alloy 5 H.T.No.1) X 25

(d) Ductile fracture with profound necking on testing at a strain rate of 3.28×10^{-5}/sec at 700°C. (Alloy 5 H.T.No.1) X 25

(e) Typical ductile failure with no intergranular appearance at a strain rate of 3.28×10^{-5}/sec at 700°C. (Alloy 5 H.T.No.1) X 200

(f) Oxide formation on the fractured surface on creep testing at 700°C. (Alloy 5 H.T.No.1) X 3200

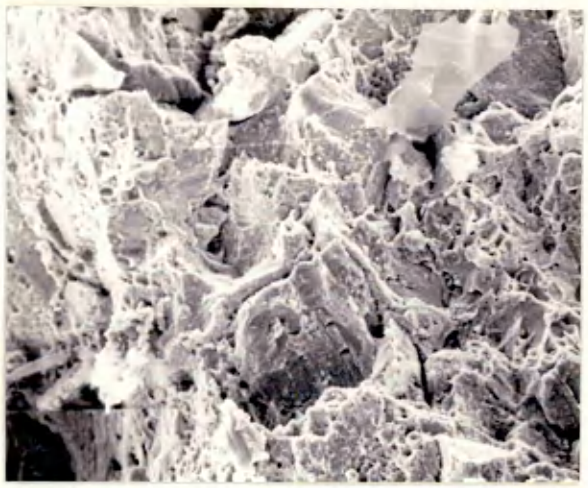

(a)

(b)

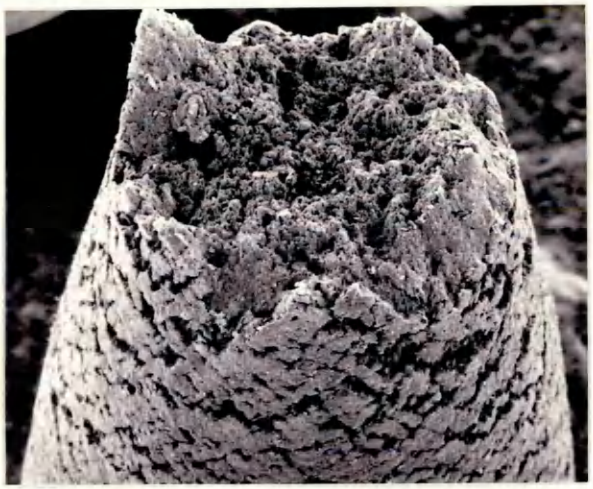

(c)

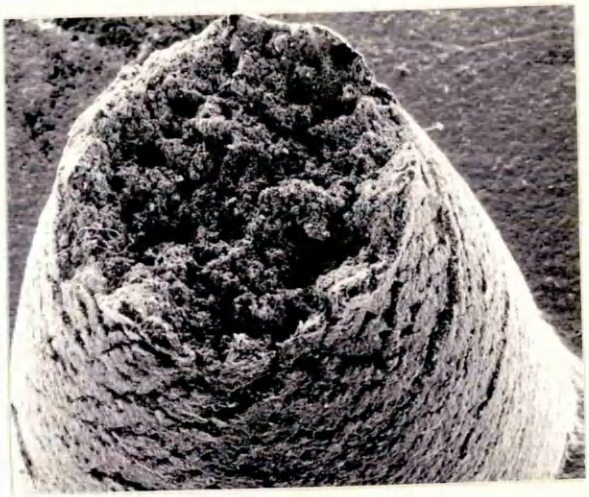

(d)

(e)

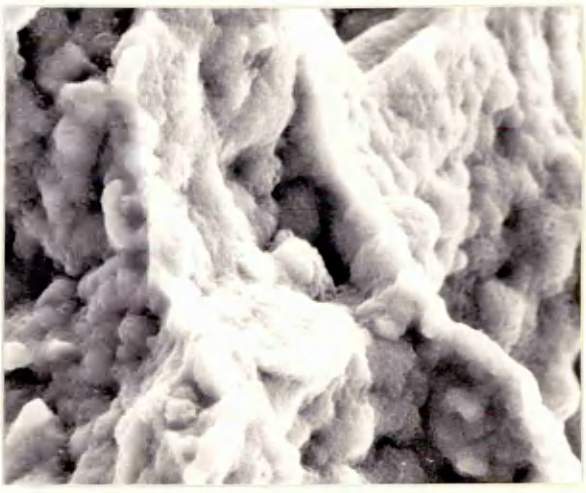

(f)

PLATE 19

(a) Intergranular facets with ductile areas on testing at a strain rate of 3.28×10^{-3}/sec at 700°C. (A7 H.T.No.1) X 200

(b) Typical ductile areas showing dimples, tested at a strain rate of 3.28×10^{-3}/sec at 700°C. (A7 H.T.No.1) X 800

(c) Ductile appearance of the fractured surface at a strain rate of 3.28×10^{-4}/sec at 700°C testing temperature. (A7 H.T.No.2) X 25

(d) General fracture surface, tested at a strain rate of 3.28×10^{-1}/sec, at 700°C. (A8 H.T.No.1) X 25

(e) General area fracture at a slower strain rate of 3.28×10^{-5}/sec at 700°C (A8 H.T.No.1) X 25

(f) Ductile areas with intergranular facets, tested at a strain rate of 3.28×10^{-5}/sec at 700°C. (A8 H.T.No.1) X 800

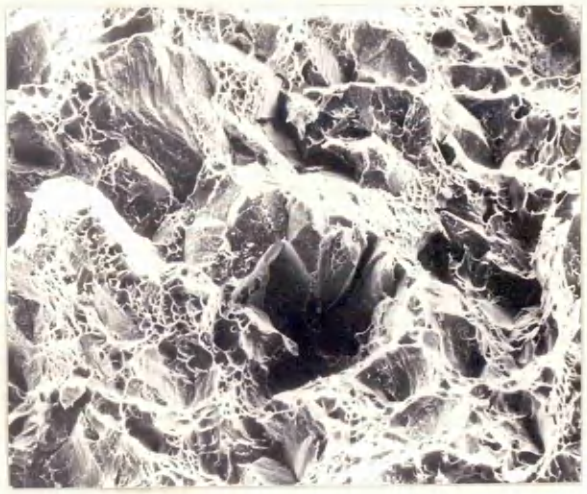

(a)

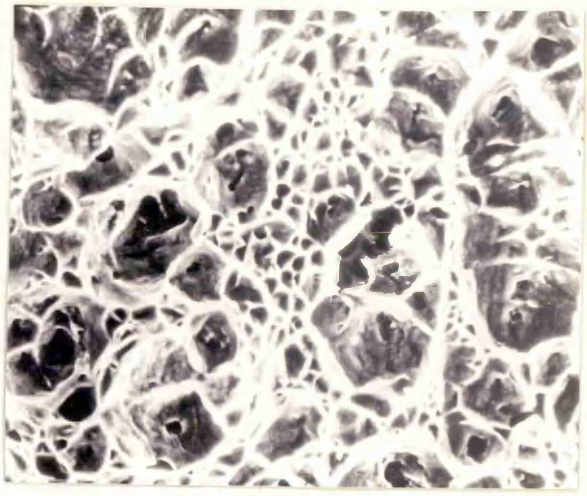

(b)

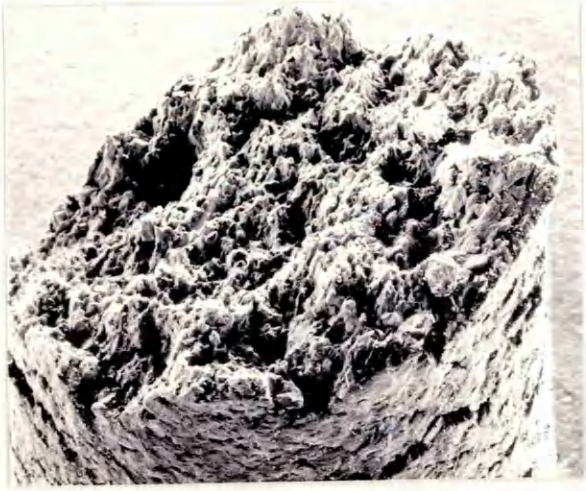

(c)

(d)

(e)

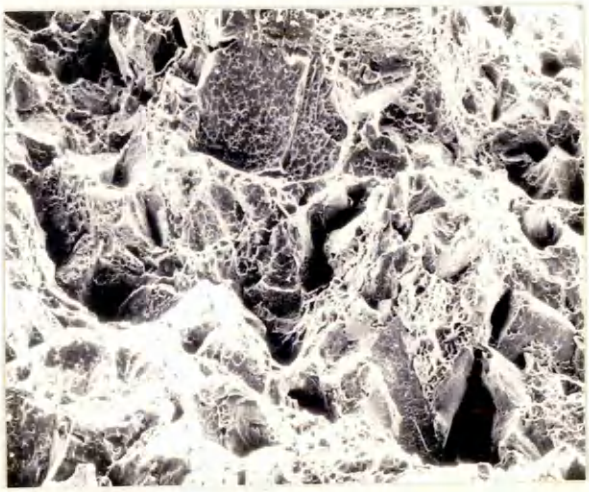

(f)

PLATE 20

(a) Whole specimen showing ductile appearance of the fracture. Tested at a strain rate of 3.28×10^{-4}/sec at 700°C. (A8 H.T. No. 2) X25

(b) Intergranular facets with ductile dimples at a strain rate of 3.28×10^{-4}/sec at 700°C. (A8 H.T. No. 2) X100

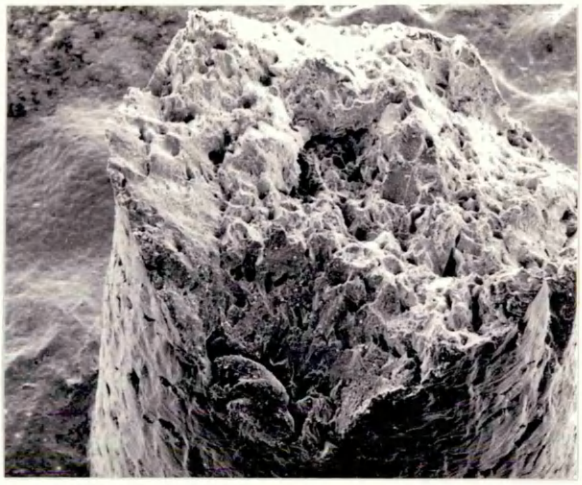

(a)

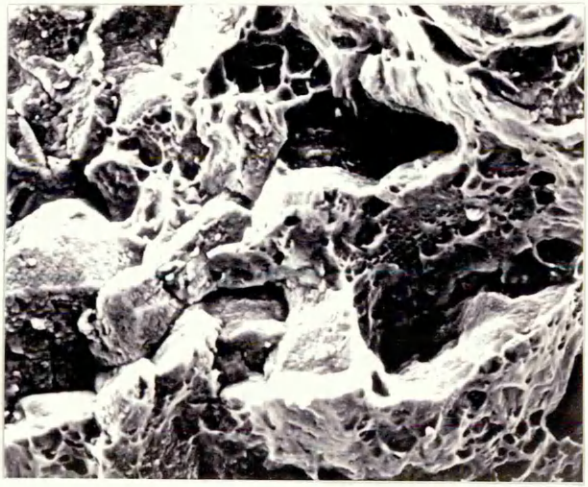

(b)